

# FUNDAMENTALS OF SOLID-PROPELLANT COMBUSTION

**Edited by**

**Kenneth K. Kuo**

The Pennsylvania State University  
University Park, Pennsylvania

**Martin Summerfield**

Princeton Combustion Research Laboratories, Inc.  
Monmouth Junction, New Jersey

Volume 90

Progress in

Astronautics and Aeronautics

**Martin Summerfield, Series Editor-in-Chief**

Princeton Combustion Research Laboratories, Inc.  
Monmouth Junction, New Jersey

Published by the American Institute of Aeronautics and Astronautics, Inc.  
1633 Broadway, New York, N.Y. 10019

American Institute of Aeronautics and Astronautics, Inc.  
New York, New York

**Library of Congress Cataloging in Publication Data**

Main entry under title:

Fundamentals of solid-propellant combustion.

(Progress in astronautics and aeronautics; v. 90)

Bibliography: p.

Includes index.

1. Solid propellants—Combustion. I. Kuo, Kenneth K.

II. Summerfield, Martin. III. Series.

TL507.P75 vol. 90 [TL785] 629.1s [629.47'524]

84-11007 ISBN 0-915928-84-1

**Third Printing**

Copyright © 1984 by the American Institute of Aeronautics and Astronautics, Inc. All rights reserved. Printed in the United States of America. No part of this publication may be reproduced, distributed, or transmitted, in any form or by any means, or stored in any data base or retrieval system, without the prior written permission of the publisher.

## Preface

There is a broad usage of solid propellants in various propulsion and gas-generation systems. Engineers and scientists working on such systems are continuously challenged by problems involving complicated aerothermochemical processes. Solution of these complicated processes requires a good understanding of many branches of science and engineering, including chemistry, fluid mechanics, heat transfer, turbulence, thermodynamics, solid mechanics, rocket propulsion, material sciences, mathematics, and numerical methods for partial and ordinary differential equations.

The specific objectives for publishing this new volume in the *AIAA Progress in Astronautics and Aeronautics* series are: 1) to present historical and state-of-the-art developments of various aspects of solid-propellant combustion studies so that this volume can be used as a basic reference; 2) to develop a systematic textbook that serves as tutorial material for beginners learning the necessary fundamentals of solid-propellant combustion processes; 3) to suggest future research areas and directions by identifying technological gaps in different areas of solid-propellant combustion; and 4) to encourage further advancements in solid-propellant propulsion systems so that future systems can be designed and developed with higher efficiency, greater reproducibility, and maximum safety considerations.

Several outstanding books have been published in the areas of solid-propellant combustion and rocket propulsion. These include: the first volume in the AIAA Progress Series entitled *Solid Propellant Rocket Research*, edited by Martin Summerfield in 1960; *Solid Propellant Rockets* by Clayton Huggett et al., published by Princeton University Press in 1960; *Rocket Propulsion* by Marcel Barrère et al., published by Elsevier Publishing Company in 1960; and an AGARDograph entitled *Fundamental Aspects of Solid Propellant Rockets*, by Forman A. Willams et al., published in 1969. George Sutton et al. have also presented several editions of *Rocket Propulsion Elements*, published by John Wiley & Sons from 1949 through 1976. All of these books have been useful, especially when first published; however, due to significant advancements in the

solid-propellant combustion field during the last three decades, there is a definite need for a new book containing the most up-to-date information on this subject.

Several other books treat the subject of solid-propellant combustion in the context of special applications, in particular, guns. The earliest well-known book on gun ballistics, *The Theory of the Interior Ballistics of Guns*, was written by J. Corner and published by John Wiley & Sons in 1950. Other books in the area of gun ballistics include: *Internal Ballistics* by F. R. W. Hunt, published by His Majesty's Printing Office, London, in 1951; *The Theory of High Speed Guns* by A. E. Siegel, published as an AGARDograph in Paris in 1965; and *Interior Ballistics of Tube Weapons and Solid Propellant Rockets* by M. E. Serebryakov, published by the State Scientific and Technical Publishing House, Moscow, from 1942 to 1962. The most recent book in this area, edited by Herman Krier and Martin Summerfield, is *Interior Ballistics of Guns*, published as Vol. 66 of the *AIAA Progress in Astronautics and Aeronautics* series in 1979. Even though these books contain material on solid-propellant combustion, they emphasize the interior ballistic performance of gun systems rather than fundamental aspects of solid-propellant combustion.

In the specialized area of deflagration-to-detonation transition, A. F. Belyaev et al. have written a book entitled *Transition from Deflagration to Detonation in Condensed Phases*, published by the Academy of Sciences of the USSR in 1973. This book deals specifically with transient phenomenon and is useful in that application; however, it does not provide a general background of solid-propellant combustion. In view of the status and objectives of the existing books, it is obvious that this new book is needed and will be important as a reference document for the future advancement of solid-propellant propulsion devices.

Due to the diversity and breadth of the field, this volume contains contributions from many distinguished researchers who speak from their respective areas of expertise in solid-propellant combustion. Each of the fifteen chapters provides a survey of previous work in the subject area, a detailed description of important theoretical formulation and experimental methods, relevant experimental and theoretical results, and technological gaps and future research directions.

The first chapter, contributed by *N. Kubota*, provides an excellent tutorial introduction of the performance of solid-propellant rocket



motors and a general survey of solid-propellant combustion characteristics. The next three chapters deal with different aspects of the chemistry of pyrolysis, ignition, and combustion of solid propellants. Chapter 2, authored by *K. Kishore* and *V. Gayathri* presents the basic chemistry of ignition and combustion of AP-based propellants as well as the roles of oxidizers, binders, catalysts, and ambient conditions in ignition and combustion. The third chapter, by *T. L. Boggs*, consists of pertinent information on the thermal behavior of RDX and HMX and a clear delineation of the sublimation, pyrolysis, ignition, and self-deflagration of these nitramine ingredients. Detailed kinetics of NC, HMX, and RDX decomposition, catalysis of nitramine propellants, and an interesting discussion of flame-zone chemistry appear in the fourth chapter, written by *R. A. Fifer*.

Chapters 5 and 6 cover ignition and flame spreading in solid propellants. Chapter 5, contributed by *C. E. Hermance*, gives a detailed description of various types of ignition experiments and theories, including solid-phase, heterogeneous, and gas-phase theories. Numerous ignition phenomena and criteria are also explained thoroughly. Information on ignition and thrust transients in solid-propellant rocket motors is given in Chap. 6, authored by *M. Kumar* and *K. K. Kuo*. Detailed discussions on flame spreading over the surfaces of solid propellants and into the defects of propellant grains are included.

Four chapters in this volume cover different aspects of steady-state burning of solid propellants. In Chap. 7, *G. Lengellé*, *A. Bizot*, *J. Duterque*, and *J. F. Trubert* present important information on the flame structure and combustion mechanisms of homogeneous propellants. This chapter also contains interesting discussions on mechanisms of super rates and plateau or mesa effects. *K. N. R. Ramohalli* gives a detailed treatment in Chap. 8 of various models developed for heterogeneous propellants, including the Guirao-Williams' model for AP combustion, Summerfield's granular diffusion flame model, the Hermance model, the Beckstead-Derr-Price model, and the petite ensemble model of Osborn and his co-workers. In Chap. 9, *E. W. Price* offers extensive descriptions and interpretations of the combustion phenomena of metalized propellants. Metal and oxide properties as well as the effect of metal additives on burning rates are discussed in detail, with appropriate photographs. The study of erosive burning of solid propellants is presented in Chap. 10 by *M. K. Razdan* and *K. K. Kuo*. Various

theoretical models are grouped into different categories based upon the method of approach. Experimental measurements and observations on erosive burning phenomena as well as the basic mechanisms involved are described in detail.

There are four chapters that address the problems of transient burning and combustion instability. Chapter 11, authored by *K. K. Kuo, J. P. Gore, and M. Summerfield*, discusses transient burning of solid propellants and provides basic mechanisms, theoretical models, experimental observations, and the effects of physico-chemical parameters and operating conditions on transient burning rates. Extinction theories and experiments are treated specifically in Chap. 12, contributed by *L. De Luca*. Dynamic extinction of fast depressurization, deradiation, and various quenching techniques are covered in detail. Nonlinear burning stability mechanisms and theories are also fully described. Chapter 13, authored by *E. W. Price*, covers experimentally observed combustion instabilities in rocket motors. Techniques for the measurement of combustion response functions, various modes of instabilities, and the effect of propellant characteristics on combustion instabilities are some of the topics covered. *J. S. T'ien* contributed Chap. 14, which deals with the theoretical analysis of combustion instability. This chapter includes discussions on the linear analysis of wave motion, acoustic amplification and damping, nonacoustic nonstability, nonlinear analysis, and predictive capabilities of various theories.

In Chap. 15, *E. Miller* covers the subject of smokeless propellants. This chapter contains detailed discussions of the chemical origins of smoke, secondary smoke formation and its modeling, homogeneous and heterogeneous nucleation of smoke, and various methods of reducing smoke of propellant products.

Although technology in the solid-propellant field has advanced significantly over the past thirty years, there are still many unresolved problems and new applications. As a personal view, derived from long participation in the field, we can point to at least four areas of research we believe will receive increasing attention in the future. One of these areas will be the application of advanced nonintrusive fast-response diagnostic techniques for the measurement of the flame structure and properties of the flowfield adjacent to burning solid propellants. Such techniques provide solid-propellant combustion scientists with the means for measurement of velocities, species concentrations, temperatures, and densities with high spatial and time resolutions. These techniques include laser

Doppler anemometry, coherent anti-Stokes Raman spectroscopy, laser spark spectroscopy, fast wavelength tracking Michelson interferometry, laser-induced fluorescence, high-speed flow visualization, high-powered x-ray cineradiography, etc. Many of these techniques can be applied in the studies of the ignition of solid propellants, transient burning phenomena, two-phase reacting flows, combustion instabilities, and the development of various propulsive devices. We look forward, as findings emerge, to a substantial revision of our ideas.

A second area for future research may be expected to develop as the realization grows that the many limitations of present-day understanding and of present-day mathematical theories of solid-propellant combustion, which have been largely thermophysical in character, are due to the lack of appreciation of the governing chemical processes. Thus, instability theories that ignore the role of gas-phase chemistry and finite-rate gas-phase kinetics in the rocket motor may be too simplified, too purely thermophysical, and therefore of limited validity. As another example, conventional burning rate theories cannot explain the specific chemical effects of the formation of plateaus in solid-propellant burning. The effects of chemistry are many and they deserve experimental and theoretical exploration. The newly developed experimental techniques mentioned in the previous paragraph will surely help to elucidate the underlying processes.

A third area for future research that may be expected to grow is the high-pressure combustion field. Much of what is known from experiments, providing the basis for this book, was learned historically by research performed at conventional pressures, e.g., up to 100 atm. However, designers are developing applications of solid-propellant rocketry at still higher pressures, and guns have always operated at pressures at least tenfold higher than conventional solid-propellant rockets, forcing the combustion scientist to resort to speculative extrapolation of current theories in order to cope with the phenomena of ignition and burning.

The fourth area of future research will be the application of fuel-rich solid propellants in airbreathing propulsion systems. Solid-fuel ramjets offer the advantage of high specific impulse and long-range flight. In these solid-fuel ramjets, the combustion zone could be altered considerably by the flow of ram air containing oxygen. This, in turn, could greatly affect the burning rate of fuel-rich solid propellants, ignition processes, extinction phenomena, and many

aspects of combustion. Much can be learned from the research that has been and is being performed in the broad field of fire research, but there is much that is new in solid-fuel ramjet combustion.

---

In addition to major contributions made by the authors of the chapters in this volume, the editors would also like to acknowledge important contributions made by a number of outstanding reviewers who specialize in the various areas of solid-propellant combustion. These reviewers are: R. S. Brown, S. Bulusu, J. P. Coughlin, J. Crump, R. L. Derr, M. Farber, R. A. Fifer, B. B. Goshgarian, C. E. Hermance, H. Hoshizaki, K. J. Kraeutle, N. Kubota, A. K. Kulkarni, J. N. Levine, H. B. Mathes, C. L. Merkle, J. W. Meyer, M. M. Micci, M. S. Miller, A. Peretz, C. F. Price, M. A. Schroeder, W. A. Sirignano, A. C. C. Tao, J. S. T'ien, F. A. Williams, and X. Wu. Their valuable comments and constructive suggestions were greatly beneficial to the high quality of this volume.

Finally, we would like to acknowledge the help of Camille S. Koorey, Brenda Hio, and Ruth F. Bryans of AIAA for their invaluable assistance in the production of this volume. We would also like to thank Mary Jane Coleman for handling numerous correspondence between editors, authors, and reviewers, and for typing three chapters of this volume.

Kenneth K. Kuo  
Martin Summerfield  
January 1984

## Table of Contents

<b>Authors</b> .....	<b>xi</b>
<b>Preface</b> .....	<b>xiii</b>
<b>Acknowledgments</b> .....	<b>xix</b>
<b>Chapter 1. Survey of Rocket Propellants and Their Combustion Characteristics</b> .....	<b>1</b>
<i>by N. Kubota</i>	
Performance of a Solid-Propellant Rocket Motor .....	4
Stable Combustion of a Rocket Motor .....	12
Temperature Sensitivity of Burning Rate .....	13
Thermochemical Properties of Propellant Ingredients .....	16
Thermochemical Properties of Propellant Combustion Products .....	20
Combustion Processes of Various Types of Solid Propellants .....	26
Double-Base Propellants .....	27
Ammonium Perchlorate Composite Propellants .....	28
Composite Modified Double-Base Propellants .....	29
Nitramine Composite Propellants .....	32
Burning Rate Controlling Factors of Solid Propellants .....	33
Combustion Characteristics Required for Solid Propellants and Gen- eral Description of the Combustion Wave .....	33
Heat-Transfer Mechanism in Combustion Waves .....	36
Heat Transfer in Solid Phase .....	38
Heat Transfer in Gas Phase .....	40
Reaction Rate in Gas Phase .....	43
Burning Rate of Solid Propellant Calculated by a Simplified Gas-Phase Model .....	47
<b>Chapter 2. Chemistry of Ignition and Combustion of Ammonium- Perchlorate-Based Propellants</b> .....	<b>53</b>
<i>by K. Kishore and V. Gayathri</i>	
Chemistry of Ignition .....	55
Sequence of Ignition .....	55
Theories of Ignition .....	57
Role of Oxidizer and Binder .....	58
Effect of Pressure .....	60
Effect of Oxidizing Atmosphere .....	61
Ignition of Composite Propellant Fuels by $\text{HClO}_4$ Vapor .....	63
Preignition Reactions .....	64
Effect of Catalysts on Ignition .....	66

Chemistry of Combustion . . . . .	68
Introduction to Combustion Mechanism . . . . .	68
Surface Reactions . . . . .	70
Subsurface Reactions . . . . .	75
Gas-Phase Reactions . . . . .	94
Effect of Catalysts on Propellant Combustion . . . . .	98
Future Research Directions . . . . .	106
 <b>Chapter 3. The Thermal Behavior of Cyclotrimethylenetrinitramine (RDX) and Cyclotetramethylenetetranitramine (HMX) . . . . .</b>	<b>121</b>
<i>by T. L. Boggs</i>	
Crystallography . . . . .	123
Sublimation of HMX . . . . .	126
Decomposition of the Solid RDX and HMX . . . . .	127
Liquefaction . . . . .	142
Decomposition of Liquid . . . . .	144
Pyrolysis of HMX . . . . .	150
Shock Tube Studies . . . . .	157
Ignition of HMX . . . . .	160
Self-Deflagration of HMX and RDX . . . . .	161
Self-Deflagration Rate as a Function of Pressure . . . . .	161
Self-Deflagration Rate as a Function of Pressure and Initial Sample Temperature . . . . .	164
Surface Structure of Self-Deflagrating HMX . . . . .	165
 <b>Chapter 4. Chemistry of Nitrate Ester and Nitramine Propellants . . . .</b>	<b>177</b>
<i>by R. A. Fifer</i>	
Decomposition of Nitrocellulose . . . . .	181
Kinetics of Nitrocellulose Decomposition . . . . .	182
Products and Mechanism of Nitrocellulose Decomposition . . . . .	184
Plasticizers and Stabilizers in Nitrocellulose Decomposition . . . . .	189
Catalysis of Nitrate Ester Propellants . . . . .	191
Decomposition of Nitramines . . . . .	202
Kinetics of HMX and RDX Decomposition . . . . .	203
Products and Mechanism of HMX and RDX Pyrolysis . . . . .	207
Catalysis of Nitramine Propellants . . . . .	215
Flame Zone Chemistry . . . . .	219
 <b>Chapter 5. Solid-Propellant Ignition Theories and Experiments . . . .</b>	<b>239</b>
<i>by C. E. Hermance</i>	
Introduction . . . . .	241
Radiant Energy Ignition Sources . . . . .	246
Shock Tube and Other Ignition Experiments . . . . .	259
Theoretical Models of Solid-Propellant Ignition and Related Theory . . . . .	266
Comments on Solution Methods . . . . .	275
Solid-Phase Reaction Mechanism Theory . . . . .	278
Theory of Ignition by Heterogeneous Reaction with External Oxidizer . . . . .	281

Gas-Phase Theory of Solid-Propellant Ignition . . . . .	285
Gas-Phase Theory—Shock Tube Cases . . . . .	286
Gas-Phase Theory—Radiant Heat Input . . . . .	289
<b>Chapter 6. Flame Spreading and Overall Ignition Transient . . . . .</b>	<b>305</b>
<i>by M. Kumar and K. K. Kuo</i>	
Ignition and Thrust Transients in Solid-Propellant Rocket Motors . . . . .	309
Ignition Devices or Igniters . . . . .	309
Physical Processes during Ignition Transient . . . . .	312
Ignition Transient Models and Experiments . . . . .	315
Flame Spreading over Solid Propellants and Fuels . . . . .	327
Flame-Spreading Mechanisms . . . . .	327
Flame-Spreading Theories and Experiments . . . . .	330
Flame Spreading into Solid-Propellant Cracks and Flaws . . . . .	339
Physical Processes during Flame Spreading and Combustion in Propellant Defects . . . . .	340
Theories and Experiments on Flame Spreading in Propellant Cracks . . . . .	341
<b>Chapter 7. Steady-State Burning of Homogeneous Propellants . . . . .</b>	<b>361</b>
<i>by G. Lengellé, A. Bizot, J. Duterque, and J. F. Trubert</i>	
General Behavior and Flame Structure of Homogeneous Propellants . . . . .	367
Burning Rate Laws: Influence of Additives . . . . .	371
Detailed Study of the Combustion Mechanisms in the Condensed Phase . . . . .	375
Degradation of the Propellant . . . . .	375
Condensed-Phase Degradation Gases . . . . .	384
Condensed-Phase Behavior of the Additive . . . . .	387
Detailed Study of the Combustion Mechanisms in the Gas Phase . . . . .	387
Primary and Secondary Flame Regimes . . . . .	389
Primary Flame Structure with/without Additives . . . . .	392
Mechanisms of Super-Rate and Plateau or Mesa Effects . . . . .	398
<b>Chapter 8. Steady-State Burning of Composite Propellants under Zero Cross-Flow Situation . . . . .</b>	<b>409</b>
<i>by K. N. R. Ramohalli</i>	
Various Combustion Models of Composite Solid Propellants . . . . .	415
The Guirao-Williams Model for AP Combustion . . . . .	420
The Granular Diffusion Flame Model . . . . .	427
The Hermance Model for Propellant Combustion . . . . .	434
The Beckstead-Derr-Price Model or the Model of Multiple Flames . . . . .	443
Petite Ensemble Model . . . . .	451
The Statistical Flame Description . . . . .	458
Summary of the PEM Equation (Applied to Each Pseudopropellant) . . . . .	465
Future Developments . . . . .	471
<b>Chapter 9. Combustion of Metalized Propellants . . . . .</b>	<b>479</b>
<i>by E. W. Price</i>	
Metals as Fuel Ingredients in Propellants . . . . .	479
Metal and Oxide Properties . . . . .	481

Results of Controlled Experiments with Aluminum. . . . .	484
Propellant Combustion. . . . .	496
Effect of Aluminum on Propellant Burning Rate . . . . .	501
Combustion Products . . . . .	503
Future Developments . . . . .	505
<b>Chapter 10. Erosive Burning of Solid Propellants . . . . .</b>	<b>515</b>
<i>by M. K. Razdan and K. K. Kuo</i>	
Theoretical Approaches to Erosive Burning . . . . .	521
Classification of Erosive Burning Theories . . . . .	521
Models Based on Phenomenological Heat-Transfer Theories . . . .	522
Models Based on Integral Boundary-Layer Analysis. . . . .	523
Models Based on a Modification of the Propellant	
Combustion Mechanism . . . . .	526
Models Based on a Chemically Reacting Boundary-Layer	
Analysis . . . . .	527
Other Models . . . . .	528
Recent Theoretical Approaches . . . . .	529
Summary of Theoretical Work. . . . .	541
Experimental Work on Erosive Burning . . . . .	541
Experimental Methods. . . . .	541
Recent Experimental Work . . . . .	559
Summary of Experimental Work . . . . .	563
Important Results of Erosive Burning Studies. . . . .	575
Generally Observed Effects of Various Parameters . . . . .	575
Physical Mechanism of Erosive Burning Phenomena . . . . .	588
Recommendation for Future Work . . . . .	590
<b>Chapter 11. Transient Burning of Solid Propellants . . . . .</b>	<b>599</b>
<i>by K. K. Kuo, J. P. Gore, and M. Summerfield</i>	
Mechanism of Transient Burning . . . . .	602
Mathematical Description of the Transient Burning Phenomena. . . . .	606
Description of the Existing Models . . . . .	614
$dp/dt$ Models. . . . .	622
Flame Description Approach . . . . .	624
Zel'dovich Approach . . . . .	631
Unsteady State Gas-Phase Models . . . . .	635
Experimental Work in Transient Combustion of Solid Propellants . . . . .	635
Experimental Apparatus Used by Various Researchers . . . . .	636
Results of Parametric Studies. . . . .	648
Future Direction . . . . .	651
<b>Chapter 12. Extinction Theories and Experiments. . . . .</b>	<b>661</b>
<i>by L. De Luca</i>	
Technical Background. . . . .	666
Literature Survey on Dynamic Extinction . . . . .	669
Theoretical Results on Dynamic Extinction by Fast Depressurization .	670
Experimental Results on Dynamic Extinction by Fast	
Depressurization . . . . .	674
Dynamic Extinction by Fast Deradiation . . . . .	680



Extinction by Other Quenching Techniques . . . . .	685
Injection of Flame Inhibitors . . . . .	685
Heat Sink . . . . .	687
Miscellaneous Quenching Techniques . . . . .	688
Mathematical Formulation of the Problem . . . . .	689
Nonlinear Burning Stability of Solid Propellants . . . . .	702
Nonlinear Static Burning Stability . . . . .	707
Nonlinear Dynamic Burning Stability . . . . .	715
Numerical and Experimental Validation . . . . .	719
Conclusions and Future Work . . . . .	725

### **Chapter 13. Experimental Observations of Combustion Instability . . . 733**

*by E. W. Price*

General Features of Instability . . . . .	736
Gains and Losses . . . . .	741
Processes Contributing to Stability . . . . .	741
Combustion Response . . . . .	742
Measuring Combustion Response . . . . .	749
Particulate Damping . . . . .	754
Other Gains and Losses . . . . .	757
Rocket Motor Instabilities . . . . .	759
Bulk Mode Instability . . . . .	759
Transverse Mode Instability . . . . .	765
Axial Mode Instability . . . . .	767
Fluid Dynamically Excited Oscillations . . . . .	774
Effect of Propellant Characteristics on Combustion Instability . . . . .	775
Summary and Recommendations . . . . .	778

### **Chapter 14. Theoretical Analysis of Combustion Instability . . . . . 791**

*by J. S. T'ien*

Linear Analysis of Wave Motion . . . . .	795
Governing Equations . . . . .	795
Acoustic Energy in a Sound Field . . . . .	796
Acoustic Admittance Function . . . . .	798
Linear Analysis . . . . .	800
Acoustic Amplification: Propellant Response Function . . . . .	805
Estimate of Time Scales . . . . .	805
Quasisteady Gas-Phase and Unsteady Solid-Phase Models . . . . .	808
Nonsteady Gas-Phase Model . . . . .	816
Velocity Coupling . . . . .	819
Others . . . . .	820
Acoustic Damping . . . . .	821
Nozzle Response . . . . .	821
Particle Damping . . . . .	823
Others . . . . .	824
Examples of Computing Linear Stability Boundaries . . . . .	825
Nonacoustic Instability . . . . .	828

Nonlinear Analysis . . . . .	830
Comparison of Theory and Experiments. . . . .	832
<b>Chapter 15. Smokeless Propellants . . . . .</b>	<b>841</b>
<i>by E. Miller</i>	
Chemical Origin of Smoke . . . . .	844
Homogeneous and Heterogeneous Nucleation of Smoke. . . . .	847
Modeling of Secondary Smoke . . . . .	849
The Dynamics of Secondary Smoke Formation . . . . .	849
Opacity Theory for Visible Light . . . . .	854
Light Scattering . . . . .	854
Plume Visibility . . . . .	856
Experiments in Secondary Smoke Formation . . . . .	860
Facilities . . . . .	860
SCF Results and Comparison with Models. . . . .	862
Condensation Nuclei. . . . .	862
Smoke Measurements . . . . .	866
AEDC Results and Comparison with Models. . . . .	868
Full-Scale Rocket Motor Tests . . . . .	868
Methods for Reducing Smoke . . . . .	877
Future Research Directions . . . . .	879
<b>Index to Contributors to Volume 90. . . . .</b>	<b>885</b>

## Chapter 1

# Survey of Rocket Propellants and Their Combustion Characteristics

Naminosuke Kubota\*  
*Japan Defense Agency, Tokyo, Japan*

### Abstract

The combustion phenomena of solid propellants are largely dependent on the propellant ingredients, pressure, propellant initial temperature, and various parameters of aerothermochemistry in rocket motors. This chapter presents the fundamental principles of rocket motors and an introduction to the combustion phenomena of solid propellants for a better understanding of rocketry. The thermochemical properties, combustion wave structures, burning processes, and rate-control steps of the burning rate for various types of solid propellants are discussed. The heat feedback process from the gas phase to the burning surface plays a dominant role in the burning rate characteristics of propellants. Simplified burning rate models and chemical reaction schemes in the gas phase are outlined to lead to the development of more definitive burning rate models.

### Nomenclature

- A = area
- a = constant defined in Eq. (15)
- c = specific heat
- $c_D$  = mass discharge coefficient
- $c_F$  = thrust coefficient
- D = mass diffusion coefficient
- E = activation energy
- F = thrust
- $g_0$  = normal gravitational acceleration at sea level

---

Copyright © American Institute of Aeronautics and Astronautics, Inc., 1982. All rights reserved.

\*Chief, Rocket Propulsion Laboratory, Third Research Center, Technical Research and Development Institute.

$H$	= enthalpy
$\Delta H_f$	= heat of formation
$h$	= heat defined in Eq. (41)
$I_{sp}$	= specific impulse
$k_b$	= backward reaction rate constant
$k_f$	= forward reaction rate constant
$M_w$	= molecular weight
$\dot{m}_d$	= rate of mass discharge
$\dot{m}_g$	= rate of mass generation
$N$	= number of elementary chemical reaction
$n$	= pressure exponent of burning rate or number of chemical species
$p$	= pressure
$Q$	= heat of reaction
$R$	= universal gas constant
$\bar{R}$	= gas constant
$T$	= temperature
$T_f$	= flame temperature
$t$	= time
$u$	= gas flow velocity
$V_c$	= chamber volume
$\mathbf{v}$	= mass-averaged velocity vector
$x$	= distance
$Y$	= molar concentration
$\bar{Y}$	= mass fraction
$Z$	= pre-exponential factor
$\alpha^*$	= coefficient of reactant
$\alpha^{**}$	= coefficient of product
$\gamma$	= specific heat ratio
$\delta$	= thermal wave thickness
$\lambda$	= thermal conductivity
$\pi_K$	= temperature sensitivity of chamber pressure
$\rho$	= density
$\sigma_p$	= temperature sensitivity of burning rate
$\omega$	= reaction rate

### Subscripts

$a$	= ambient condition
$b$	= burning surface of propellant
$c$	= chamber or condensed phase
$e$	= exit of nozzle
$F$	= fuel
$g$	= gas phase
$i$	= $i$ th chemical species
$j$	= $j$ th chemical reaction

- O = oxidizer
- p = propellant or product
- s = burning surface of propellant
- s<sup>+</sup> = gas phase at burning surface of propellant
- s<sup>-</sup> = condensed phase at burning surface of propellant
- t = nozzle throat
- x = distance
- 0 = reference state at 0
- 1 = reference state at 1

## Introduction

Combustion is an exothermic reaction involving rapid oxidizing reactions. For the past 20 years, combustion phenomena have been studied extensively to elucidate the combustion mechanisms of various types of propellants. In recent years, the theoretical and experimental aspects of chemical kinetics and the fluid dynamical nature of combustion have been understood through the use of high-speed computers and modern types of optical equipment. Because the reaction rates during combustion are much faster than those of commonly observed chemical reactions and because physical changes, such as velocity, temperature, and pressure, accompany combustion, a knowledge of aerothermochemistry is needed to understand combustion phenomena.

The combustion phenomena of a solid are much more complex than those of a gas because of the phase changes involved in going from a solid to a liquid to a gas. Examples of solid combustion are rockets and guns. Since solid propellants for rockets and guns burn at high pressures, experimental observations and measurements are far more difficult than those of other combustion phenomena. Since the 1950s, numerous experimental and theoretical models to predict steady and unsteady combustion have been put forth, with the result that overall combustion mechanisms of solid propellants are beginning to be understood.

Propellants are defined as the material which generates a large number of gaseous molecules at high temperature during combustion and which can self-sustain without the presence of ambient oxidizer combustion. Since combustion is a self-sustaining exothermic rapid-oxidizing reaction, both oxidizers and fuels are needed to form propellants. Propellants are classified by their physical state. When a propellant is liquid, it is called a liquid propellant. When the propellant is in a solid state, it is called a solid propellant. When the oxidizer and fuel ingredients are mixed and combined physically for a solid propellant, the pair of the materials is called a heterogeneous propel-

lant. When the oxidizer and the fuel molecules are linked chemically, and are made of one material, the material is called a homogeneous propellant.

Since both solid propellants and explosives contain fragments of oxidizer and fuel in their chemical structures and can self-sustain combustion, there are no clear differences between these two materials. Thus, in general, propellants and explosives are listed in the same category of combustion materials. However, the distribution between propellants and explosives is evident in their applications. For instance, propellants generate combustion gases by deflagration phenomena, whereas explosives generate combustion gases by explosion or detonation phenomena. This means that the combustion process of propellants is usually subsonic, whereas that of explosives is usually supersonic. Propellants use their combustion gases to generate propulsive forces, whereas explosives generate destructive forces through the shock waves. The chemical compositions of propellants and explosives are fundamentally the same, with the result that some propellants can also be used as explosives, and vice versa. Explosives and some propellants can be detonated by a strong external force such as mechanical shock or friction. When these materials are used under a limited range of external forces, detonation can be avoided and the materials used as propellants.

Propellants are used for rockets, guns, gas generators, and pressure generators. Most of these applications require high-pressure combustion gases in an open or a closed chamber. The operating pressure and time are dependent on the intended applications. Different operating conditions result in different combustion rates. Major applications of propellants are in rockets and guns, both of which use gas at high temperature and pressure to generate propulsive forces. However, there are fundamental differences between rockets and guns. Rockets consist of propellant and combustion chambers within their projectiles, whereas gun projectiles usually do not. The difference results in different operating pressure levels for both rockets and guns, with rockets operating between 10 and 300 atm and guns between 500 and 5000 atm.

#### Performance of a Solid-Propellant Rocket Motor

A rocket motor is a typical example of an energy-transfer system which can be directly explained by thermodynamics and Newton's second law: a pressurized high-temperature gas generated in the system is expanded adiabatically, and the sensible energy of the gas is converted to kinetic energy.

Thus, the system produces a reaction force. Therefore, the thermodynamic requirement for a rocket motor is to get a high-pressure and high-temperature gas in the motor, and to convert the sensible energy effectively into the kinetic energy through physicochemical processes.

The thrust generated by a rocket motor is produced by the pressure distribution in the motor. If one can determine the pressure distribution acting on the interior surface of the motor, the thrust can be calculated by

$$F = \oint p dA \quad (1)$$

where  $p$  is pressure,  $A$  is the interior surface of the motor, and the integration must be done along the whole surface area. Equation (1) is just the momentum change resulting from the ejection of combustion gases from the rocket motor.

Figure 1 is a schematic drawing of a rocket motor. The motor consists of a combustion chamber and a convergent-divergent nozzle. High-pressure combustion produces gases and sometimes a small fraction of condensed particles is generated in the chamber by the propellant burning. During the time interval of steady-state operation, the pressure is approximately constant, and the flow velocity of the burned gas is usually small within the chamber. However, in the convergent part of the nozzle, the pressure decreases and the flow velocity increases. At the throat of the nozzle the flow velocity becomes sonic. As the burned gas flows to the downstream side of the divergent part of the nozzle, the velocity goes supersonic while the pressure decreases. At the nozzle exit, the flow velocity reaches the maximum, and the pressure becomes approximately the ambient pressure.

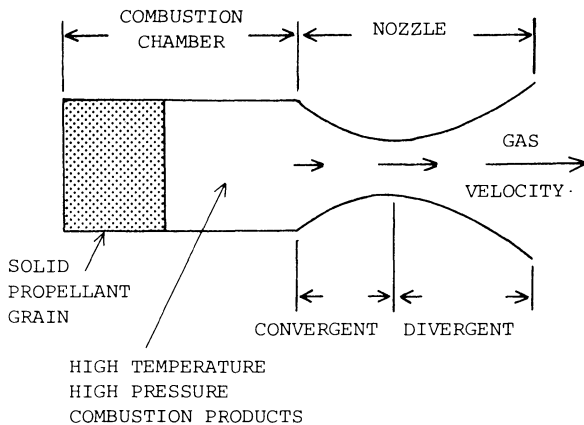


Fig. 1 Schematic diagram of a rocket motor.

The distribution of pressure  $p$ , velocity  $u$ , temperature  $T$ , and pressure acting on the axial direction of the motor  $p_\eta$  are shown in Fig. 2.

The resultant pressure acting on the entire surface of a rocket motor is calculated using Eq. (1). Thus the thrust can be written as

$$F = c_F A_t p_c \quad (2)$$

where  $c_F$  is the dimensionless thrust coefficient which is an important parameter determined by the nozzle flow,  $A_t$  is the nozzle throat area, and  $p_c$  is the pressure in the combustion chamber. Since the cross-sectional area of the combustion chamber is larger than the throat area, it is evident from the pressure distribution shown in Fig. 2 that  $c_F$  is always larger than unity. For example, for a convergent nozzle the

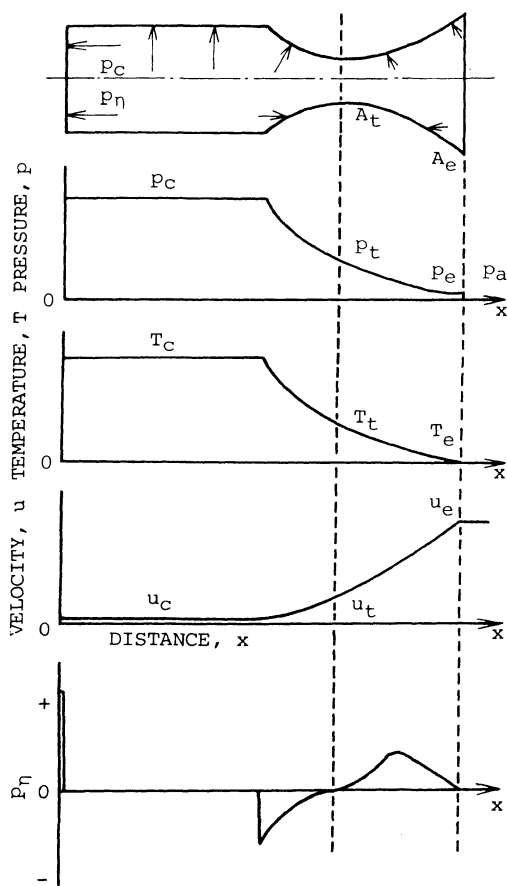


Fig. 2 Distributions of pressure, temperature, velocity, and pressure acting on the direction of motor axis.



$c_F$  is approximately 1.2. In the convergent section the flow velocity increases and the pressure decreases, resulting in a continuous decrease of  $p_\eta$  acting on the convergent part of the nozzle. Therefore, there is a net contribution of thrust due to the difference between the values of  $p_\eta$  at the head end of the motor and that at the convergent section. When a nozzle consists of convergent and divergent sections, the  $c_F$  can increase to approximately 1.7, owing to the effect of  $p_\eta$  acting on the divergent section. It is evident from Fig. 2 that thrust varies with the shape of the divergent section of the nozzle, even when the chamber pressure is kept constant. In other words, the thrust does not depend solely on the combustion process of the propellants in the motor.

The important parameters for rocket motor design, such as  $c_F$ ,  $p_x$ ,  $u_x$ , and  $T_x$ , can be calculated using the one-dimensional isentropic flow equations,<sup>1-4</sup> which are summarized as follows:

$$c_F = \sqrt{\frac{2\gamma^2}{\gamma - 1} \left( \frac{2}{\gamma + 1} \right)^{\gamma-1} \left( 1 - \left( \frac{p_e}{p_c} \right)^{\frac{\gamma-1}{\gamma}} \right)} + \frac{p_e - p_a}{p_c} \frac{A_e}{A_t} \quad (3)$$

$$\frac{A_t}{A_x} = \left( \frac{\gamma + 1}{2} \right)^{\frac{1}{\gamma-1}} \left( \frac{p_x}{p_c} \right)^{\frac{1}{\gamma}} \sqrt{\frac{\gamma + 1}{\gamma - 1} \left( 1 - \left( \frac{p_x}{p_c} \right)^{\frac{\gamma-1}{\gamma}} \right)} \quad (4)$$

$$\frac{u_x}{u_t} = \sqrt{\frac{\gamma + 1}{\gamma - 1} \left( 1 - \left( \frac{p_x}{p_c} \right)^{\frac{\gamma-1}{\gamma}} \right)} \quad (5)$$

$$\frac{T_x}{T_c} = \left( \frac{p_x}{p_c} \right)^{\frac{\gamma-1}{\gamma}} \quad (6)$$

where  $\gamma$  is the specific heat ratio of the gas, and the subscripts c, t, and x are chamber, throat, and the distance along the motor axis, respectively. As shown in Eqs. (1) and (2), the thrust is largely dependent on the chamber pressure. The following paragraph describes how the chamber pressure is determined by the combustion of the propellant in the chamber.

Since the mass generation in the chamber is a function of the propellant burning and the mass discharge through the

nozzle, the mass balance in the rocket motor can be written as

$$\frac{d(\rho_g V_c)}{dt} = \dot{m}_g - \dot{m}_d \quad (7)$$

where  $V_c$  is the chamber volume and  $\rho_g$  is the density of the burned gas in the chamber. Under a nearly steady-state condition with constant chamber pressure, the term on the left-hand side of Eq. (7) may be negligible. However, this term plays an important role in nonsteady burning such as that which occurs in ignition transients, oscillatory burning, and combustion termination. The rate of mass discharge from a choked nozzle is proportional to the chamber pressure

$$\dot{m}_d = c_D A_t p_c \quad (8)$$

which is purely a fluid dynamical relation. The proportionality constant  $c_D$  is called the nozzle discharge coefficient which has a unit of mass flow rate/force and is dependent on thermodynamic parameters, such as temperature, molecular weight, and specific heat of the burned gas. The  $c_D$  is given by Eq. (9),

$$c_D = \sqrt{\gamma \left( \frac{2}{\gamma + 1} \right)^{\frac{\gamma+1}{\gamma-1}}} \frac{1}{R} \frac{M_w}{T_c} \quad (9)$$

where  $M_w$  is the molecular weight and  $R$  is the universal gas constant.

The rate of mass generation in the combustion chamber is equivalent to the mass burning rate of the propellant

$$\dot{m}_g = \rho_p A_b r \quad (10)$$

where  $\rho_p$  is the density of the propellant,  $A_b$  is the burning surface area of the propellant, and  $r$  is the linear burning rate which is defined as the regressing distance per unit of time perpendicular to the burning surface. For steady-state burning, the mass balance equation, using Eqs. (8) and (10), can be written as

$$\rho_p A_b r = c_D A_t p_c \quad (11)$$

and the chamber pressure is found to be

$$p_c = \rho_p A_b r / c_D A_t \quad (12)$$

Thus, the thrust can be written, using Eqs. (2) and (12), as

$$F = (c_F/c_D)\rho_p A_b r = I_{sp} \dot{m}_g g_0 \quad (13)$$

where  $c_F/(c_D g_0) = I_{sp}$  is defined as specific impulse and  $g_0$  the normal gravitational acceleration at sea level. The specific impulse is the time required to generate a unit thrust by a unit weight of propellant. Specific impulse is also a measure of the thrust obtained by the burning of a unit weight of propellant per unit time. Thus, the units of  $I_{sp}$  can be either seconds or kg/(kg/s).  $I_{sp}$  is a very useful parameter in evaluating the propellant combustion efficiency.

As shown in Eq. (13),  $I_{sp}$  is dependent not only on the discharge coefficient  $c_D$  but also on the thrust coefficient  $c_F$ . Thus,  $I_{sp}$  is a function of the chemical properties of the propellant and the expansion process through the nozzle and can be written as

$$I_{sp} = \sqrt{\frac{2\gamma}{\gamma-1} R \frac{T_c}{M_w} \left( 1 - \left( \frac{p_e}{p_c} \right)^{\frac{\gamma-1}{\gamma}} \right)} + \left( \frac{\gamma+1}{2} \right)^{\frac{\gamma+1}{2(\gamma-1)}} \sqrt{\frac{RT_c}{\gamma M_w}} \left( \frac{p_e - p_a}{p_c} \right) \frac{A_e}{A_t} \quad (14)$$

If one assumes  $p_e = p_a$ ,  $\gamma = 1.2$ , and  $M_w = 22$  g/mole, one can calculate  $c_F$  as a function of  $p_c/p_e$  as shown in Fig. 3. Although  $c_F$  always increases with increasing  $p_c/p_e$ , the degree of increase is more rapid at low  $p_c/p_e$ , typically  $< 100$ . The expansion condition  $p_e = p_a$  is the optimum expansion. When  $p_e > p_a$ , the exhaust is underexpanded and, when  $p_e < p_a$ , the exhaust is overexpanded. For both under- and overexpanded exhaust conditions,  $c_F$  decreases when compared with the  $c_F$  at  $p_e = p_a$ . The expansion ratio of the nozzle  $p_c/p_e$  is a function of the area ratio of  $A_e/A_t = \epsilon$ , as shown in Eq. (4), by taking  $A_x = A_e$  and  $p_x = p_e$ . The optimum area ratio  $\epsilon$  is dependent on  $p_c/p_e$  and  $\gamma$ . Figure 4 shows  $c_F$  vs  $\epsilon$  at  $p_c/p_e = 100$  and  $\gamma = 1.2$ . The optimum expansion occurred at  $\epsilon = 12$  with an overexpansion occurring when  $\epsilon > 12$  and an underexpansion occurring when  $\epsilon < 12$ .

Figure 5 shows a relationship between  $c_F g_0$  and  $T_c/M_w$  at  $\gamma = 1.2$ . The  $c_F$  decreases with increasing  $T_c/M_w$  as depicted by Eq. (9). As shown in Eq. (13),  $I_{sp}$  increases when  $c_D$

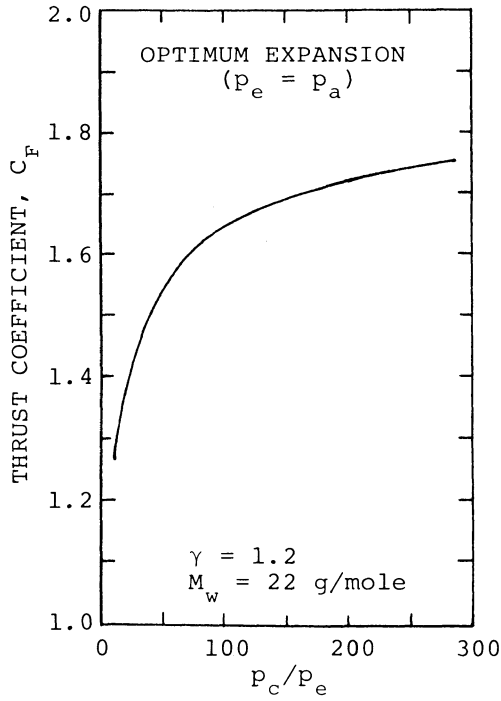


Fig. 3 Thrust coefficient vs pressure ratio.

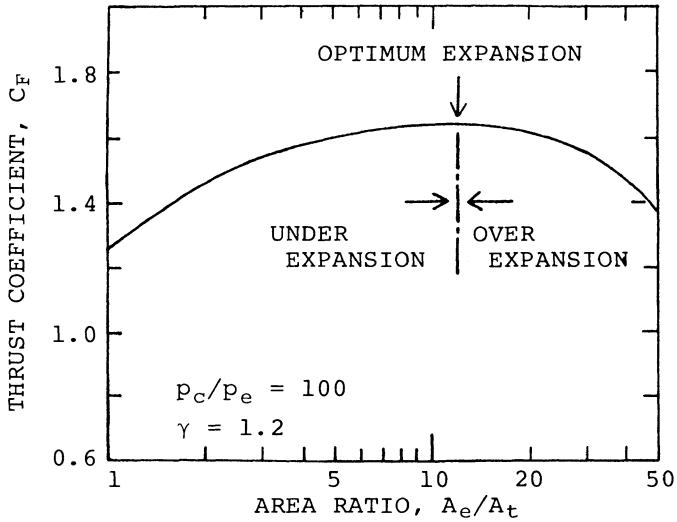


Fig. 4 Thrust coefficient vs nozzle area ratio.

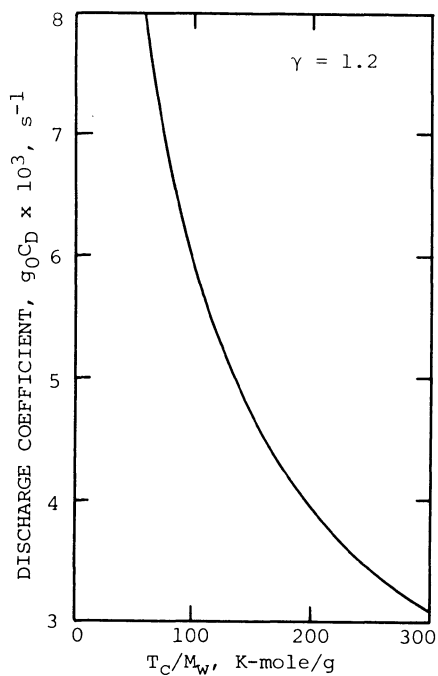


Fig. 5 Discharge coefficient vs temperature/molecular weight in a rocket motor.

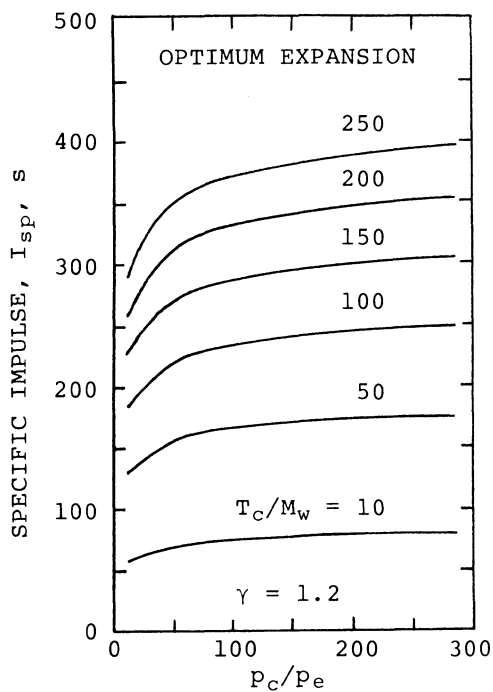


Fig. 6 Specific impulse vs pressure ratio as a function of  $T_C/M_w$ .

decreases. In other words, to increase the specific impulse, it is necessary to increase the flame temperature and/or to decrease the molecular weight of the combustion product. It is evident from Figs. 3 and 5 that  $I_{sp}$  increases with increasing  $p_c/p_e$  and/or with increasing  $T_c/M_w$ . A typical calculated example of  $I_{sp}$  as a function of  $p_c/p_e$  and  $T_c/M_w$  for  $\gamma = 1.2$  is shown in Fig. 6.

The pressure in the combustion chamber or thrust is dependent on the burning rate of propellants as shown in Eqs. (12) and (13). A large thrust occurs when the burning rate is high. However, when a long burning time is required, a lower burning propellant may be suitable. If the burning rate is assumed proportional to the  $n$ th power of pressure,

$$r = ap^n \quad (15)$$

where  $n$  is the pressure exponent of the burning rate and  $a$  is a constant. The pressure in the combustion chamber can be written by Eq. (12a),

$$p_c = \left( \frac{a \rho_p}{c_D} \frac{A_b}{A_t} \right)^{\frac{1}{1-n}} \quad (12a)$$

Equation (15) is called Vieille's law or Saint Robert's law, and  $n$  and  $a$  are dependent on the chemical composition and the initial temperature of the propellant. This burning rate equation is based on various empirical measurements and is discussed in greater detail in a later section.

#### Stable Combustion of a Rocket Motor

The pressure  $p_c$  in a combustion chamber during steady-state burning is given by Eq. (12a). However, it is necessary to determine whether or not the pressure is stable. If one plots  $\dot{m}_g$  and  $\dot{m}_d$  as a function of pressure, as shown in Fig. 7, there exists a crossover point which is the pressure given by Eq. (12a). When there is a small increase of pressure at the crossover point, the pressure can decrease only when  $\dot{m}_g < \dot{m}_d$ . When there is a small decrease of pressure at the same point, the pressure can increase only when  $\dot{m}_g > \dot{m}_d$ . Based on this, the condition for stable combustion is, at  $p = p_c$ ,

$$\frac{d}{dp}(c_D A_t p) > \frac{d}{dp}(\rho_p A_b a p^n) \quad (16)$$

Since  $c_D$  is approximately independent of pressure, the stability criterion can be written, using Eqs. (11) and (16), as

$$n < 1 \quad (17)$$

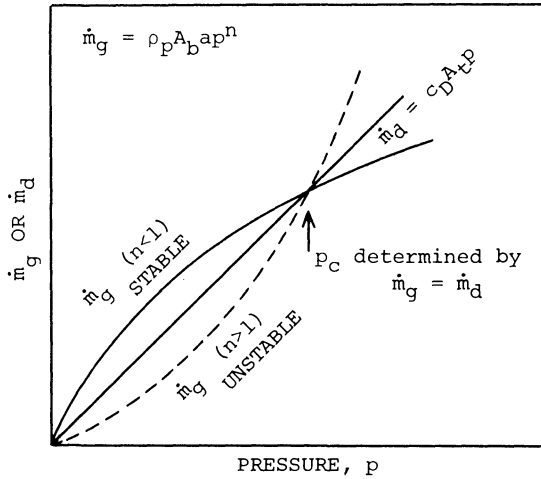


Fig. 7 Mass balance in a rocket motor showing a stable criterion of chamber pressure.

It is possible to obtain a crossover point even when  $n > 1$ , as shown in Fig. 7, and to express equilibrium pressure by Eq. (12a). However, if the pressure shifts away from the crossover point by an external disturbance, the pressure decreases to the ambient pressure or increases to infinity. Thus, the pressure exponent of burning rate must always be less than unity in the pressure range where the rocket motor operates.

#### Temperature Sensitivity of Burning Rate

As shown in Eq. (15), the burning rate is dependent on pressure. However, it is also dependent on the initial temperature of the propellant even when the pressure is kept constant. If one defines  $\sigma_p$  as the variation of the burning rate with the initial temperature change at a constant pressure,  $\sigma_p$  then can be written as

$$\sigma_p = \frac{1}{r} \frac{r_1 - r_0}{T_1 - T_0} \quad (18)$$

where  $r_0$  and  $r_1$  are the burning rates at temperatures  $T_0$  and  $T_1$ , respectively. Thus,  $\sigma_p$  represents the variation of the burning rate per unit temperature and is called the temperature sensitivity of burning rate at constant pressure. The dimension of  $\sigma_p$  is  $K^{-1}$ , and  $\sigma_p \times 100$  is %/K of the burning rate change. Equation (18) is rewritten in a more rigorous

differential form as

$$\sigma_p = \frac{1}{r} \left( \frac{\partial r}{\partial T} \right)_p = \left( \frac{\partial \ln r}{\partial T} \right)_p \quad (18a)$$

Substitution of Eq. (15) into Eq. (18a) gives

$$\sigma_p = \left( \frac{\partial \ln(ap^n)}{\partial T} \right)_p = \frac{1}{a} \left( \frac{\partial a}{\partial T} \right)_p \quad (18b)$$

When the initial temperature of a propellant in a rocket motor is changed, the burning rate of the propellant changes according to the relationship given in Eq. (18). However, the crossover point for an equilibrium pressure shown in Fig. 7 shifts to a different point at another equilibrium pressure. This is also evident from the mass balance equation of Eq. (11). Therefore, the  $\sigma_p$  given by Eq. (18) is not sufficient to express the effect of the initial temperature change on the performance of a rocket motor. Thus, the following temperature sensitivity is used to evaluate the effect of temperature:

$$\pi_k = \frac{1}{p} \frac{p_1 - p_0}{T_1 - T_0} \quad (19)$$

where  $p_0$  and  $p_1$  are the pressures in the combustion chamber at the initial temperatures  $T_0$  and  $T_1$ , respectively. Thus,  $\pi_k$  indicates the specific variation of pressure in the combustion chamber per unit temperature and is called temperature sensitivity of pressure at constant  $K_n$ .  $K_n$  is defined as  $K_n = A_p/A_t$ .  $K_n = \text{constant}$  is equivalent to a fixed physical dimension of a rocket motor. The dimension of  $\pi_k$  is given by  $K^{-1}$ , and  $\pi_k \times 100$  indicates the specific variation of chamber pressure as %/K. Similar to Eq. (18a),  $\pi_k$  is written in differential form as

$$\pi_k = \frac{1}{p} \left( \frac{\partial p}{\partial T} \right)_{K_n} = \left( \frac{\partial \ln p}{\partial T} \right)_{K_n} \quad (19a)$$

Equation (12a) is differentiated with respect to  $T$  and is substituted into Eq. (19a) to give

$$\pi_k = \frac{1}{1-n} \frac{1}{a} \left( \frac{\partial a}{\partial T} \right) = \frac{1}{1-n} \sigma_p \quad (19b)$$

Thus,  $\sigma_p$  and  $\pi_k$  are dependent only on the nature of the propellant burning rate and are determined by the combustion mechanisms of propellants.<sup>5</sup>



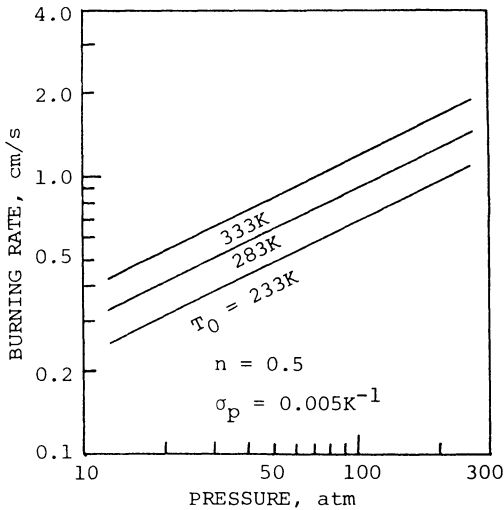


Fig. 8 Temperature sensitivity characteristics of a solid propellant

The value of  $\sigma_p$  for conventional propellants ranges between 0.002/K and 0.008/K. For example in the temperature range between 233 K and 333 K, the burning rate of a propellant with  $\sigma_p = 0.005/K$  varies 50%. When this propellant burns in a combustion chamber, the  $\pi_k$  given by Eq. (19) is  $\pi_k = 0.005/(1 - n)$ . If the pressure exponent of the burning rate is 0.5,  $\pi_k$  is then equal to 0.01/K, and the chamber pressure varies 100% for the same temperature range. This large variation of chamber pressure affects the thrust of the rocket motor: the thrust varies more than 100% as shown in Eq. (2), since  $c_F$  increases with  $p_c$ . It is important to note that, when  $n$  is large,  $\pi_k$  becomes large even when  $\sigma_p$  is small. Thus, the required burning rate characteristics for propellants are that  $n$  and  $\sigma_p$  be as small as possible. Changing burning rate by varying the initial temperature alters not only the chamber pressure and thrust but also the burning time of the propellant. Also it varies the flight path of the rocket projectile. However, it should be noted that the initial temperature change never changes the chemical energy contained in the propellant but changes the chemical reaction rate of the propellant burning. Figure 8 shows an example of the calculated results of pressure vs burning rate of a propellant which has the characteristics of  $\sigma_p = 0.005/K$  and  $n = 0.5$ . As shown in Eq. (15), the burning rate increases linearly with pressure in  $\ln p$  vs  $\ln r$  plot, and it shifts parallel with variation in temperature. Figure 9 shows the variation of pressure  $\Delta p_c$  vs pressure exponent relationship when the initial chamber

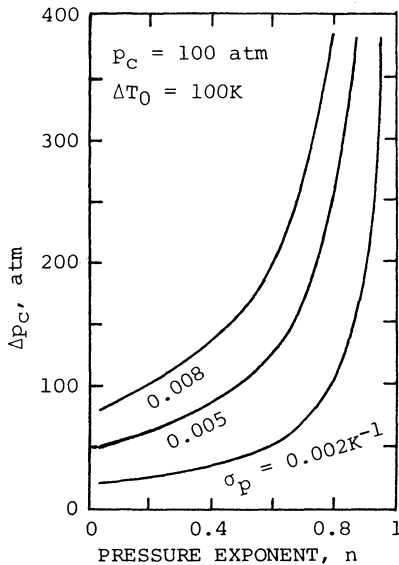


Fig. 9 Pressure increase in a chamber vs pressure exponent of burning rate as a function of temperature sensitivity.

pressure is 100 atm and the variation of temperature  $\Delta T = 100$  K. It is evident that  $\Delta p_c$  becomes large when  $\sigma_p$  and/or  $n$  are large.

### Thermochemical Properties of Propellant Ingredients

Numerous kinds of chemicals have been used in making solid propellants. Different chemical compositions are chosen to obtain optimized combustion characteristics for different purposes. There are two types of propellants which are distinguished by the condition in which their ingredients are connected. As mentioned in the Introduction, one type consists of a substance in which oxidizer and fuel are linked chemically in its structure, and the other type consists of two substances as an oxidizer and a fuel which are physically mixed. The former type is called a homogeneous propellant because the physical structure of the propellant is homogeneous. The latter type is called a heterogeneous propellant because the physical structure of the propellant is heterogeneous.

Nitrocellulose is a typical example of homogeneous propellants. Nitrocellulose is a nitrated cellulose whose chemical structure is represented by  $\text{C}_6\text{H}_7.55\text{O}_5(\text{NO}_2)_{2.45}$  for 12.6% nitrogen content. When nitrocellulose is decomposed thermally, two major fragments are generated. One group of fragments with a C/H and C/H/O structure acts as a fuel with the other fragment of  $\text{NO}_2$  acting as an oxidizer.<sup>6,7</sup> Since

nitrocellulose is a fibrous material, it is difficult to form a specified propellant grain using it. Thus, liquid materials called plasticizers are mixed with the nitrocellulose to gelatinize it and to form a specified shape for the propellant grain. Typical examples of plasticizers include nitroglycerin and trimethylolethane trinitrate. Both of them are also nitrated materials which can individually function also as propellants like nitrocellulose when used as propellants. The C/H and C/H/O from the plasticizers act as fuels, whereas the  $\text{NO}_2$  acts as an oxidizer. Propellants which are composed of nitrocellulose and nitroglycerin or trimethylolethane trinitrate and a small amount of stabilizer are called double-base propellants and are typical homogeneous propellants.<sup>8,9</sup>

Heterogeneous propellants are composed of very fine crystalline particles acting as an oxidizer and an organic plastic binder surrounding each crystalline particle acting as a fuel. Heterogeneous propellants are commonly called composite propellants. Typical crystalline particles used as an oxidizer include ammonium perchlorate, ammonium nitrate, and potassium perchlorate. When these particles are thermally decomposed, the oxidizing fragments leave the surface as a gaseous species. The chemical nature of the gaseous oxidizing fragments generated from the oxidizer is dependent on the chemical structure of the particles. Ideally, the more oxidizing fragments contained in the structure, the better the oxidizer. The fuels used in heterogeneous propellants have a hydrocarbon structure, such as polyurethane and polybutadiene, and act as binders to adhere the oxidizer particles together. Thus, the fuel has a dual function: 1) to produce energy when oxidized and 2) to bind the oxidizer particles together to form a specified propellant grain shape. A typical modern heterogeneous propellant is composed of ammonium perchlorate and polybutadiene.

In general, solid propellants consist of several chemical ingredients such as oxidizer, fuel, binder, plasticizer, stabilizer, curing agent, crosslinking agent, bonding agent, burning rate catalyst, antiaging agent, opacificer, flame suppressant, and combustion instability suppressant. Typical ingredients used for modern types of solid propellants are shown in Table 1. Some combinations of these ingredients will give an optimized thermal performance or burning rate characteristics; some other combinations will make the propellants very dangerous, such as explosives, or give them poor mechanical properties.

Propellant grain shapes are designed to obtain a specified thrust vs burning time relationship. Since propellants

are sometimes required to act at very low or high temperatures, and under high pressure and mechanical impact, propellant grains are required to withstand certain specified thermal and mechanical stresses and to have appropriate mechanical properties such as elongation and tensile strength. Thus, the selection of the ingredients is based

Table 1 List of ingredients used for double-base and composite propellants

---



---

Double-base propellant

plasticizer (fuel and oxidizer)

NG: nitroglycerin

TMETN: trimethylolethane trinitrate

TEGDN: triethylene glycol dinitrate

DEGDN: diethylene glycol dinitrate

plasticizer (fuel)

DEP: diethylphtalate

TA: triacetine

PU: polyurethane

binder (fuel and oxidizer)

NC: nitrocellulose

stabilizer

EC: ethyl centralite

2NDPA: 2-nitrodiphenilamine

burning rate catalyst

PbSa: lead salicylate

PbSt: lead stearate

Pb2EH: lead 2-ethylhexoate

CuSa: copper salicylate

CuSt: copper stearate

LiF: lithium fluoride

high energy additive

RDX: cyclotrimethylene trinitramine

HMX: cyclotetramethylene tetranitramine

NGD: nitroguanidine

coolant

OXM: oxamide

opacificer

C: carbon black

flame suppressant

KNO<sub>3</sub>: potassium nitrate

K<sub>2</sub>SO<sub>4</sub>: potassium sulfate

metal fuel

Al: aluminum

combustion instability suppressant

Al: aluminum

Zr: zirconium

ZrC: zirconium carbide

---

(Table 1 continued on next page.)

on both the optimized combustion characteristics and mechanical properties desired.<sup>10</sup>

The binders, also used as fuels, for composite propellants play a significant role in maintaining propellant grain shape under these stresses. Extensive studies on binder characteristics have been conducted to improve both

Table 1 (cont.) List of ingredients used for double-base and composite propellants

---

Composite propellant

---

oxidizer

AP: ammonium perchlorate  
 AN: ammonium nitrate  
 NP: nitronium perchlorate  
 KP: potassium perchlorate  
 RDX: cyclotrimethylene trinitramine  
 HMX: cyclotetramethylene tetranitramine

binder

PS: polysulfide  
 PVC: polyvinyl chloride  
 PU: polyurethane  
 CTPB: carboxyl terminated polybutadiene  
 HTPB: hydroxyl terminated polybutadiene

curing and/or crosslinking agents

PQD: paraquinone dioxime  
 TDI: toluene-2,4-diisocyanate  
 MAPO: tris[1-(2-methyl) aziridiny] phosphine oxide  
 ERLA-0510: N,N,O-tri (1,2-epoxy propyl)-4-aminophenol  
 IPDI: isophorone diisocyanate

bonding agent

MAPO: tris[1-(2-methyl) aziridiny] phosphine oxide  
 TEA: triethanolamine  
 MT-4: adduct of 2.0 moles MAPO, 0.7 mole azipic acid, and 0.3 mole tararic acid

plasticizer

DOA: dioctyl adipate  
 IDP: isodecyl pelargonete  
 DOP: dioctyl phthalate

burning rate catalyst

Fe<sub>2</sub>O<sub>3</sub>: ferric oxide  
 FeO(OH): hydrated-ferric oxide  
 nBF: n-butyl ferrocene  
 DnBF: di-n-butyl ferrocene  
 LiF: lithium fluoride

metal fuel

Al: aluminum  
 Mg: magnesium  
 Be: beryllium  
 B: boron

combustion instability suppressant

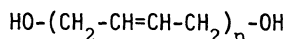
Al: aluminum  
 Zr: zirconium  
 ZrC: zirconium carbide

---

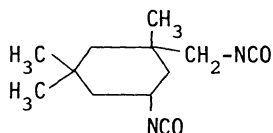
Table 2 Curing process of binder

Hydroxyl terminated polybutadiene

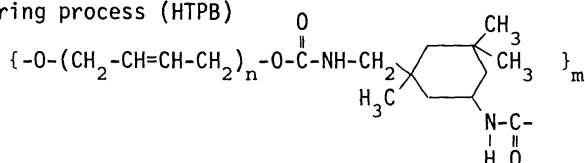
prepolymer (polybd R-45M: ARCO)



curing agent (IPDI)



curing process (HTPB)



thermal performance and mechanical properties of composite propellants. The binders are made of synthetic rubbers whose structures are mainly C-C and C-H bonds. The nature of binders is largely dependent on the kind of polymers used as binders and on the crosslinking and curing processes. A typical polymerization process between a polymer and a curing agent is shown in Table 2. In addition to these processes, the chemistry of the bonding process between polymer and crystalline oxidizers and metal fuels is important in obtaining good mechanical properties of propellants. Detailed chemistry of propellant binders are described elsewhere.<sup>11-13</sup>

The thermochemical properties of propellants are dependent on the nature of each ingredient and are based on thermodynamic calculations.<sup>14-17</sup> Table 3 shows the thermochemical properties of the ingredients used for double-base and composite propellants. It is shown that relatively large amounts of excess oxygen are produced from oxidizers such as AP, NP, and AN whose flame temperatures are low. However, no excess oxygen is produced from near-stoichiometrically balanced ingredients such as RDX, HMX, NG, and NC whose flame temperatures are high.

## Thermochemical Properties of Propellant Combustion Products

The thermal energy contained in solid propellants is represented by the specific impulse which is a function of

Table 3 Thermochemical properties of propellant oxidizers ( $p = 70$  atm)

Oxidizer	Chemical formula	State	$\rho$ (g/cm <sup>3</sup> )	$\Delta H_F$ (298 K) (cal/mole)	Product		
					$T_g$ (K)	$M_w$ (g/mole)	$I_{sp}$ (s)
NC(12.6%N)	$C_6H_{7.55}O_5(NO_2)_{2.45}$	solid	1.66	-160.2	2590	24.7	230
NG	$C_3H_5O_3(NO_2)_3$	liquid	1.60	-9.75	3289	28.9	244
TMETN	$C_5H_9O_3(NO_2)_3$	liquid	1.47	-97.8	2898	23.1	253
TEGDN	$C_6H_{12}O_4(NO_2)_2$	liquid	1.33	-181.6	1376	19.0	183
DEGDN	$C_4H_8O_3(NO_2)_2$	liquid	1.39	-103.5	2513	21.8	241
AP	$NH_4ClO_4$	solid	1.95	-70.73	1405	27.9	157
AN	$NH_4NO_3$	solid	1.73	-78.27	1247	22.9	161
NP	$NO_2ClO_4$	solid	2.22	+8.88	597	36.4	85
RDX	$C_3H_6N_3(NO_2)_3$	solid	1.82	+14.69	3286	24.3	266
HMX	$C_4H_8N_4(NO_2)_4$	solid	1.90	+17.92	3278	24.3	266

Oxidizer	Major combustion products (moles/mole)								
	$O_2$	$H_2O$	CO	$CO_2$	$H_2$	$N_2$	HCl	$Cl_2$	OH
NC(12.6%N)		0.225	0.147	0.128	0.116	0.111			
NG	0.069	0.280	0.107	0.275	0.014	0.181			0.041
TMETN		0.263	0.357	0.096	0.140	0.136			
TEGDN		0.110	0.397	0.063	0.335	0.079			
DEGDN		0.253	0.365	0.079	0.190	0.111			
AP	0.287	0.377				0.119	0.197	0.020	
AN	0.143	0.571				0.286			
NP	0.750					0.125		0.125	
RDX		0.226	0.246	0.082	0.089	0.326			
HMX		0.227	0.246	0.082	0.089	0.326			

flame temperature and the molecular weight of the combustion products. In practice, the mixture ratio of the oxidizer and fuel is selected to shift the equivalence ratio to the stoichiometric as closely as possible. As shown in Fig. 10, the flame temperature  $T_F$  and specific impulse  $I_{sp}$  (assumed equilibrium flow) vary with the mixture ratio of oxidizer and fuel for composite propellants. The maximum  $T_F$  and  $I_{sp}$  occur when an appropriate mixture ratio is selected. It is seen that the  $T_F$  and  $I_{sp}$  exhibit relatively similar behavior in the plots of  $T_F$  vs mixture ratio and  $I_{sp}$  vs mixture ratio. This is because the molecular weight  $M_w$  of the combustion products is relatively independent of the mixture ratio.

The thermochemical properties of RDX and HMX composite propellants are somewhat different from those of other

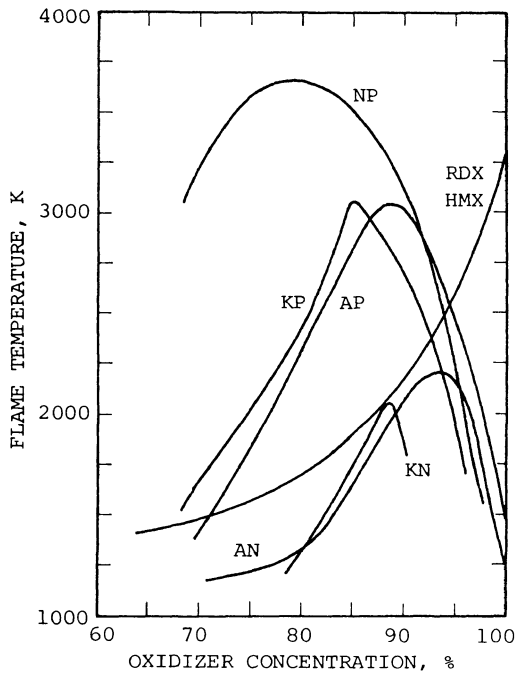


Fig. 10a Flame temperature vs oxidizer concentration of HTPB based composite propellants.

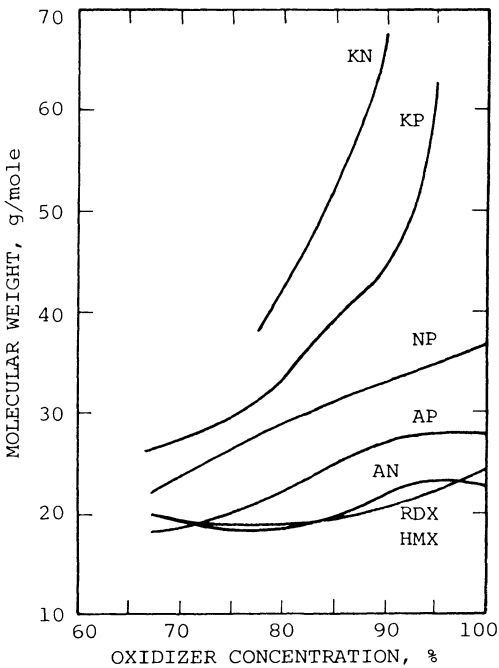


Fig. 10b Molecular weight vs oxidizer concentration of HTPB based composite propellants.



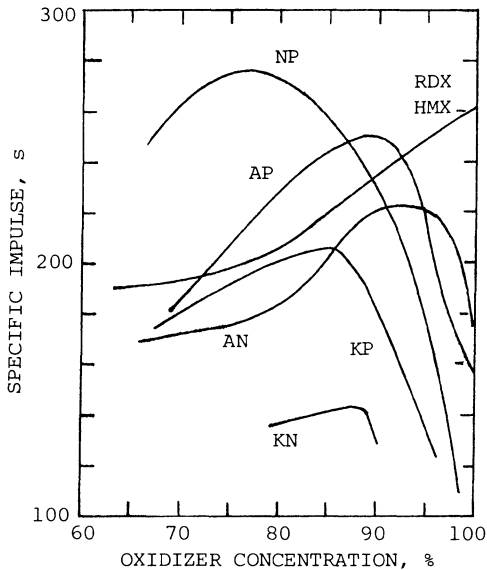


Fig. 10c Specific impulse vs oxidizer concentration of HTPB based composite propellants.

composite propellants. The maximum  $T_f$  and  $I_{sp}$  are obtained when no fuels are added to these oxidizers. Since RDX and HMX are stoichiometrically balanced materials, the addition of fuels reduces the  $T_f$  and  $I_{sp}$ .

The flame temperature and specific impulse of double-base propellants are less dependent on the mixture ratio of nitrocellulose and nitroglycerin, as shown in Fig. 11. Nitrocellulose is slightly fuel-rich, and nitroglycerin is slightly oxidizer-rich, as shown in Table 3. However, since both ingredients contain oxidizer and fuel fragments in their chemical structures, the thermochemical properties of the mixture are similar to those of each ingredient. Thus, the maximum  $T_f$  and  $I_{sp}$  are obtained when the nitrocellulose is 20% and the nitroglycerin is 80%. However, conventional double-base propellants contain about 10% plasticizer and 1% stabilizer, which act as coolants, and the mixture ratio of nitrocellulose and nitroglycerin is limited to use in the range of 4/6 and 6/4. Thus, for conventional double-base propellants, values of  $I_{sp}$  are normally lower than those shown in Fig. 11. However, it is possible to obtain an  $I_{sp} = 220$  s and  $T_f = 2800$  K at 70 atm, when the combustion products are fuel-rich.

The addition of ammonium perchlorate within double-base propellants shifts the equivalence ratio to stoichiometric and increases the flame temperature and the specific impulse. However, since ammonium perchlorate is oxidizer-rich, too

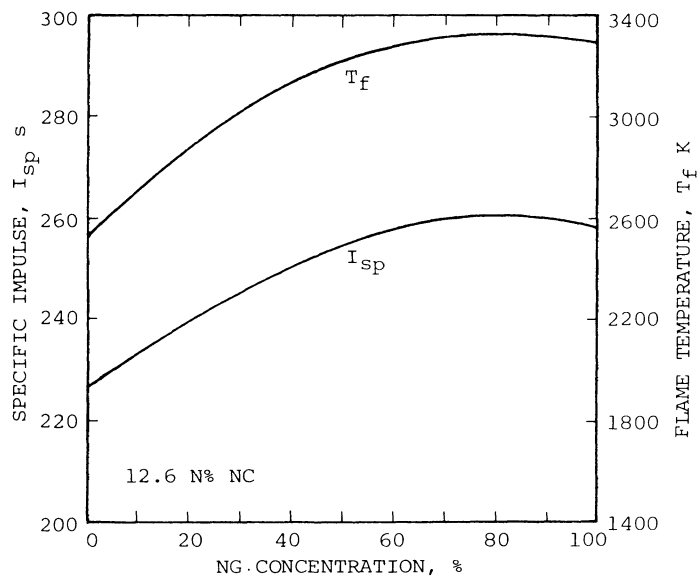


Fig. 11 Specific impulse and flame temperature vs nitroglycerin concentration of double-base propellants.

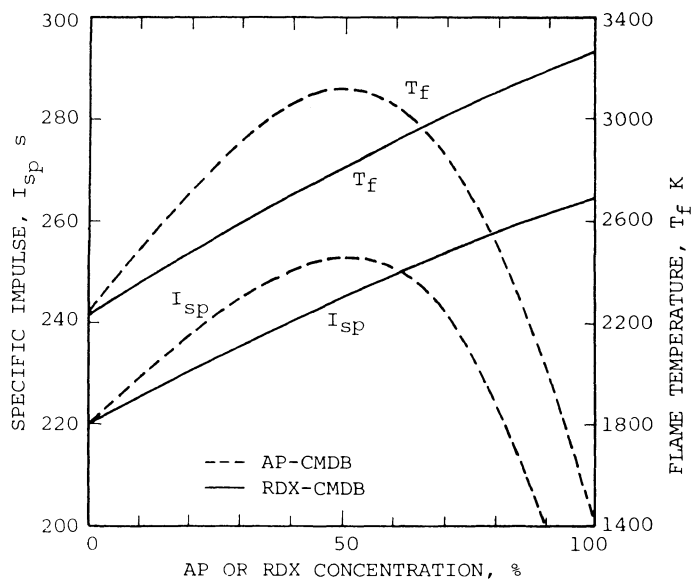


Fig. 12 Specific impulse and flame temperature vs AP or RDX concentration of AP-CMDB and RDX-CMDB propellants.

much addition of ammonium perchlorate can reduce the specific impulse. Thus, the maximum  $T_f$  and  $I_{sp}$  of ammonium perchlorate added double-base propellant, which is called ammonium-perchlorate-based composite modified double-base (AP-CMDB) propellant, are obtained when AP concentration is approximately 50%, as shown in Fig. 12.

The addition of nitramine particles such as RDX and HMX to double-base propellants increases the flame temperature and specific impulse. This type of propellant is called nitramine-based composite modified double-base (RDX-CMDB or HMX-CMDB) propellant. Since no excess oxidizing fragments are contained in the combustion products of these nitramines, no additional oxidizers are available to fuel-rich double-base propellants. However, a large amount of heat is produced from these nitramines, so that the overall heat produced from RDX-CMDB or HMX-CMDB propellants is increased, and thus the specific impulse is increased. A calculated result of the  $T_f$  and  $I_{sp}$  for RDX-CMDB propellants as a function of the concentration of RDX is shown in Fig. 12. The  $T_f$  and  $I_{sp}$  almost increase linearly with the concentration of RDX to maximum  $T_f$  and  $I_{sp}$  at 100% RDX.

Composite propellants consist of crystalline particles and plastic binder to obtain high-temperature combustion gases through the chemical reaction between oxidizer and fuel. However, the mixture of nitramine particles and organic binder forms a new type of solid propellant called nitramine composite propellant and was developed on the basis of a somewhat different idea from ammonium perchlorate composite propellant. The nitramines, such as RDX and HMX, contain fewer oxidizing fragments so that the binder surrounding the nitramine particles cannot be oxidized. Thus, the binder acts as a coolant, and the flame temperature is reduced. However, relatively large amounts of  $H_2$  are produced from the thermal decomposition of the binder which reduces the molecular weight of the combustion products, as shown in Fig. 13. The combustion products of AP composite and RDX composite propellants are compared and plotted as functions of the concentration of AP and RDX. The binder used in the propellants is polyurethane. The major combustion products for an AP propellant are  $CO_2$ ,  $H_2O$ , and  $HCl$  at 85% AP. However, those for the RDX propellant are  $H_2$ ,  $N_2$ , and  $CO$  at the same concentration of RDX as shown in Fig. 13. It is important to note that the flame temperature of RDX propellant is much less than that of an AP propellant at the same  $I_{sp}$  because of the reduced  $M_w$  of RDX propellant, as shown in Fig. 10.

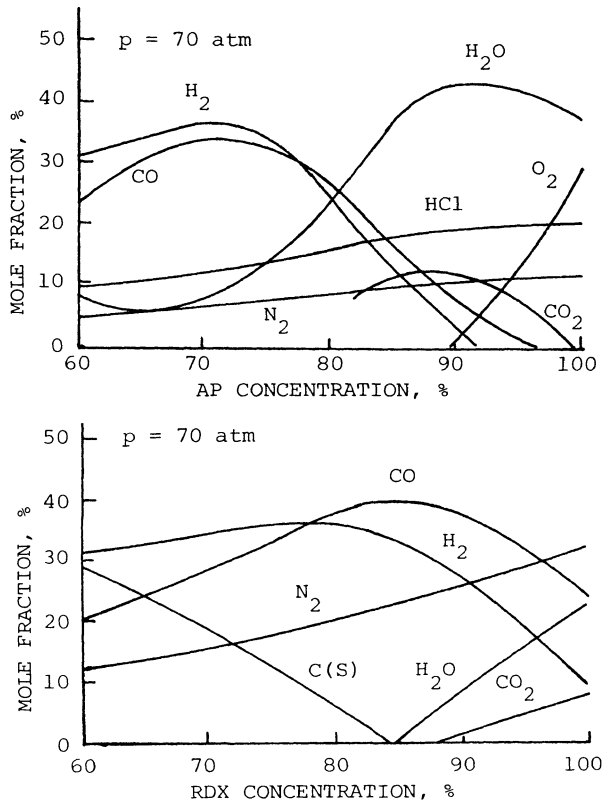


Fig. 13 Combustion products of AP composite and RDX composite propellants.

### Combustion Processes of Various Types of Solid Propellants

Two types of propellants, double-base and composite, have been developed to satisfy the various combustion characteristics described in the previous sections to obtain stable and high-performance combustion in rocket motors. However, the physical and chemical properties of these propellants are entirely different from each other, and the combustion processes are also different. The following paragraphs describe the flame structure and the burning rate characteristics of various types of solid propellants. The propellants are double-base propellants, ammonium-perchlorate-based composite propellants, two types of composite modified double-base propellants, and nitramine composite propellants. Combustion flame photographs of these propellants are shown in Plate 1. The photographs are taken from

## Chapter 2

# Chemistry of Ignition and Combustion of Ammonium-Perchlorate-Based Propellants

Kaushal Kishore\* and Venkatnarayana Gayathri†  
*Indian Institute of Science, Bangalore, India*

### Abstract

In the literature the material on the chemistry of the combustion and ignition of solid composite propellants is scattered. In this chapter the chemical aspects of such propellants are brought together in order to present a comprehensive picture of the combustion mechanism. Ignition is a complex process governed by various factors such as oxidizer and binder characteristics, pressure, oxidizer concentration, pre-ignition reactions, etc. Various models have been proposed; however, because ignition is a complex phenomenon, it cannot be explained by a single theory. Combustion is discussed mainly in terms of condensed-phase and gas-phase reactions. The various processes occurring during combustion are classified as reactions at the surface, below the surface, and in the gas phase. From the concept of bond breakage and vaporization of fragments at the surface, a number called mean fragment size vaporizing has been defined and an attempt has been made to use this to calculate the burning rate. The importance of condensed-phase reactions during combustion has been shown by various studies. The effect of catalysts on combustion has been explained through proton transfer, electron transfer, and by complex formation.

---

Copyright © American Institute of Aeronautics and Astronautics, Inc., 1982. All rights reserved.

\*Associate Professor, Department of Inorganic and Physical Chemistry.

†Research Associate, Department of Inorganic and Physical Chemistry (presently Research Associate, R & D Division, Grindwell-Norton Ltd., Bangalore, India).

## Nomenclature

a	= constant
AK	= intermediate products
AP	= ammonium perchlorate
B	= pre-exponential factor
b	= correlating factor
C	= concentration
c	= specific heat
CC	= copper chromite
CFS	= critical fragment size
CTPB	= carboxy terminated polybutadiene
DTA	= differential thermal analysis
DSC	= differential scanning calorimetry
d	= correlating factor
E	= activation energy
E <sub>ig</sub>	= ignition energy
F	= heat flux
FSV	= fragment size vaporizing
$\Delta H_p$	= heat of polymerization
$\Delta H_v$	= heat of vaporization
$\Delta H_d$	= heat of degradation
$\Delta H_t$	= total heat
HTPB	= hydroxy terminated polybutadiene
K	= thermal conductivity
KP	= potassium perchlorate
k	= rate constant
LPL	= low-pressure limit
MFS	= mean fragment size vaporizing
m	= molecular weight of the fragment vaporizing at the surface
N	= number of bonds
n	= pressure index for burning rate
n'	= pressure index for decomposition
P	= pressure
PB	= polybutadiene
PBAA	= copolymer of butadiene and acrylic acid
PBAN	= terpolymer of butadiene acrylic acid and acrylnitrile
PIB	= polyisobutylene
PMMA	= polymethyl methacrylate
PS	= polysulfide
PST	= polystyrene
PU	= polyurethane
Q	= heat of reaction

$Q_g$	= heat of gasification at the pyrolysis temperature
$R$	= gas constant
$\dot{r}$	= burning rate
$\dot{r}$ No.	= $\dot{r}$ (catalyzed)/ $\dot{r}$ (uncatalyzed)
SEM	= scanning electron microscopy
$T$	= temperature
TD	= thermal decomposition
TD No.	= TD rate (catalyzed)/TD rate (uncatalyzed)
TG	= thermogravimetry
TMO	= transition metal oxides
TPX	= methyl pentene polymer
$t_{ID}$	= ignition delay
$t$	= time
$X$	= distance from the propellant surface
$\alpha$	= thermal diffusivity
$x$	= order of reaction
$\rho$	= density

## I. Chemistry of Ignition

### Sequence of Ignition

The first step in propellant combustion is ignition. This is a transient phenomenon leading to steady-state combustion. Ignition is achieved by a pyrotechnic material and the thermal energy is transferred to the propellant surface by hot gases and hot particles through the processes of conduction, convection and radiation. In an actual rocket motor the ignition process includes the complete ignition of the propellant grain and buildup of the operating pressure level in the motor.<sup>1</sup> This process can be divided into three phases as shown in Fig. 1. During the first phase the propellant is subjected to external heating by a pyrotechnic mixture to achieve the critical conditions required for ignition. During this phase the most important consideration is the time needed to attain propellant combustion after the start of the ignitor. This period is termed ignition delay or  $t_{ID}$ . During the second phase the flame spreads over the unignited surface and during the third phase the combustion products are accumulated in the motor chamber until a steady-state pressure is attained.

From the viewpoint of the chemistry involved,  $t_{ID}$  is an important consideration because it depends upon the chemical characteristics of the propellant. It also depends on the operational and chemical characteristics of the ignition system. The sequence of ignition can be as follows. Due to external heating, depending on the nature of the heating process, the surface temperature of the propellant rises until onset of exothermic chemical reactions at or near the propellant surface. Due to these chemical reactions, the surface temperature rises faster than it would have from external heating alone, represented by the equation,

$$t_{ID} = t_1 + t_2 \quad (1)$$

where  $t_1$  is the time for heating the propellant by an external source and  $t_2$  the time for the heat addition by an exothermic chemical reaction to the point of ignition. According to Barrere<sup>2</sup> the principal parameters affecting the ignition are the level of energy required for inflammation,

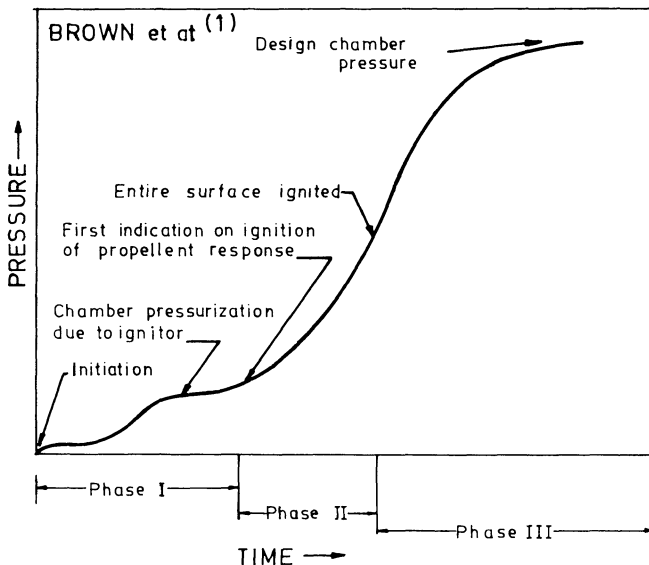


Fig. 1 Chamber pressure transient during ignition.



the nature of the gas surrounding the sample, the gas pressure, the gas velocity near the surface, the temperature of the propellant, and its nature and catalysts. According to Smolensiki et al.<sup>3</sup>  $t_{ID}$  decreases with an increase in the propellant temperature and is inversely proportional to the square of the burning rate. Anderson<sup>4</sup> assumed that the total ignition time is the time for initiation of the adiabatic surface reaction plus the time required to establish self-sustained burning. Under appropriate conditions, either or both of the terms may control the total ignition time.

The study of propellant ignition in the laboratory is compared to motor ignition by various ignition tests where the energy transfer is achieved by conduction from hot gases and hot wires, by convection from hot gases, and by radiation. These aspects are discussed elsewhere.<sup>5</sup>

### Theories of Ignition

Based on theoretical models, there are three main theories for understanding various physico-chemical processes of ignition.

Thermal Ignition Theory. This theory, which was proposed by Hicks,<sup>6</sup> suggests that the exothermic chemical heating occurring in the solid raises the surface temperature to the point of ignition. It is thought that ignition is governed by the temperature rise in the solid below the surface exposed to heat flux.

Gas-Phase Theory. According to this theory the runaway heating conditions are achieved as a result of the gas-phase exothermic chemical reactions between the propellant constituents at a small but finite distance from the surface.

Heterogeneous Theory. This theory states that the primary reactions occur at or below the propellant surface between the gaseous decomposition products of the oxidizer and the solid matrix of the organic binder. These heterogeneous reactions control the ignition process.

### Role of Oxidizer and Binder

It is likely that the degradation behavior of both the oxidizer and binder controls the ignition characteristics of the propellants. However, it is not clearly understood as to which predominates in controlling ignition. According to Shannon<sup>7</sup> both the binder and oxidizer influence the ignition characteristics and the minimum initial pressure depends on the decomposition characteristics of both. Shannon showed that at ambient pressure, ignition is primarily controlled by decomposition of the oxidizer. At lower pressures the binder decomposition characteristics exert an influence on ignition. Variation of the type of oxidizer modifies the surface temperature, the surface structure, the rate of gaseous  $O_2$  generation, and the nature of the gaseous species. This will result in longer or shorter ignition times depending upon the mechanism and the rate of decomposition of the individual oxidizer. The potassium perchlorate (KP) formulations exhibit longer  $t_{ID}$  and higher minimum initial pressure for ignition. Propellants with advanced oxidizers such as hydroxylamine perchlorates and hydrazine diperchlorates are easier to ignite at all pressures and exhibit an extremely low minimum pressure for ignition.

For composite solid propellants containing polysulfide (PS), polyurethane (PU), and carboxy terminated polybutadiene (CTPB) fuel binders it has been observed<sup>8</sup> that the surface decomposition of ammonium perchlorate (AP) is slower than that of the fuel binder at temperatures less than about 650 K.

The surface temperature during ignition is expected to be less than 650 K so the AP decomposition, which is slower than the binder decomposition rate, must be the rate-controlling step in the ignition process. Baer and Ryan<sup>9</sup> have developed a simplified thermal model where the heat conducted into the propellant from the surface has been given as

$$-K\left(\frac{\partial T}{\partial X}\right)_{\text{Surface}} = F + Q_{\text{chem}} \quad (2)$$

where  $K$  is the thermal conductivity of the propellant,  $F$  the ignitor heat flux at the propellant surface,  $Q_{\text{chem}}$  the rate at which heat is liberated due to chemical reactions,  $X$  the distance from the surface of the propellant, and

$$Q_{\text{chem}} = B e^{-E/RT} \quad (3)$$

where  $B$  is the pre-exponential factor,  $E$  the activation energy, and  $R$  the gas constant. The governing heat conduction equation for the temperature distribution in the propellant when the surface is heated by  $F + Q_{\text{chem}}$  and when no significant chemical reactions occur within the solid propellants can be written as,

$$\frac{\partial T}{\partial t} = \left(\frac{-K}{\rho c}\right) \left(\frac{\partial^2 T}{\partial x^2}\right) \quad (4)$$

Baer and Ryan<sup>9</sup> have numerically solved Eq. (4) under the boundary conditions of Eqs. (2) and (3) for ignition delay ( $t_{\text{ID}}$ ) as

$$t_{\text{ID}}^{\frac{1}{2}} = (K\rho c\pi)^{\frac{1}{2}}/2F \left[ (E/R)/(1-1.04 \ln F/B - T_0) \right] \quad (5)$$

Equation (5) can be used to calculate ignition energy ( $E_{\text{ig}}$ ) as follows:

$$t_{\text{ID}} F = E_{\text{ig}} = (K\rho c\pi)/(4F) \left[ (E/R)/(1-1.04 \ln F/B) - T_0 \right] \quad (6)$$

The  $E_{\text{ig}}$  evaluated using Eq. (5), assuming AP decomposition to be the rate-controlling step, tallies well with the  $E_{\text{ig}}$  obtained from radiative and convective experiments, suggesting that the AP decomposition really is the rate-controlling step. This is supported by the results of Baer et al.,<sup>10</sup> where  $E_{\text{ig}}$  and  $E$  for the thermal decomposition (TD) of AP have been shown to be the same, which is equal to 125.5 kJ/mole. Although the  $E$  obtained for the ignition of AP propellants is close to the TD of AP, it can also correspond

to other exothermic processes, for example, oxidation of fuel by  $\text{HClO}_4$  or  $\text{ClO}$ . Thus, the predominant reaction is still not clear.<sup>11</sup>

### Effect of Pressure

The pressure dependence of ignition has been a subject of controversy. Altman and Grant<sup>12</sup> reported that  $t_{ID}$  was insensitive to pressure, whereas Baer et al.<sup>10</sup> have indicated a small pressure dependence. On the other hand, Beyer and Fishman<sup>13</sup> have shown from the arc image furnace data a strong pressure dependence of  $t_{ID}$ . However, different flux ranges were used by these authors. It may be seen from Fig. 2 that the pressure dependence of  $t_{ID}$  is a strong function of the flux employed. The pressure dependence of  $t_{ID}$  can be given by the following empirical equ-

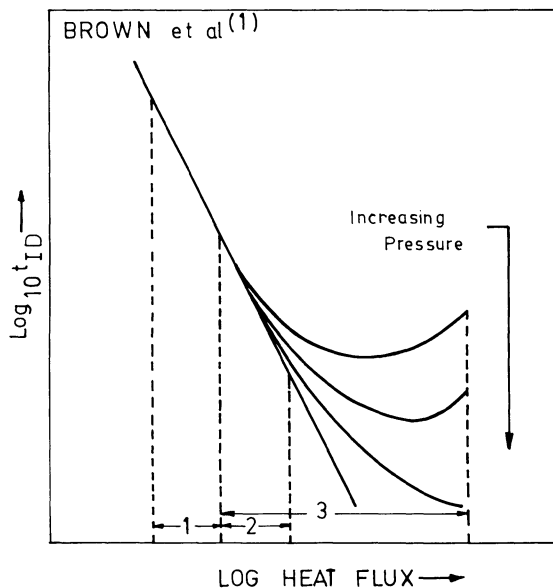


Fig. 2 Plot of  $\log t_{ID}$  vs  $\log$  heat flux showing the effect of pressure by various investigators; 1) Altman and Grant,<sup>12</sup> 2) Baer and Ryan,<sup>9</sup> and 3) Beyer and Fishman.<sup>13</sup>

ation given by Baer and Fishman,<sup>13</sup>

$$t_{ID} = [(d^3/\dot{Q}^6) + (b^3/P^{6.15})]^{1/3} \quad (7)$$

where  $d$  and  $b$  are the correlating factors,  $\dot{Q}$  the rate of heat transfer to the propellant surface, and  $P$  is the pressure. It has been proposed that the inconsistency of pressure dependence on ignition can be qualitatively explained in terms of the heterogeneous theory by including the influence of pressure on the site and magnitude of the surface reaction. Using analog computer Sineau<sup>14</sup> carried out theoretical studies on ignition characteristics of solid propellants. He employed widely useful dimensionless equations to determine the pressure rise in a propellant during burning.

Shannon<sup>7</sup> has studied the effect of pressure on the ignition characteristics of composite solid propellants with different heat fluxes, oxidizer loadings, oxidizers, and binders. He observed that the minimum initial pressure at which ignition can be achieved depends on the characteristics of the binder and the oxidizer, but that the effect of the fuel becomes pronounced at pressures below 0.75 atm. Waldman<sup>15</sup> has found that  $t_{ID}$  is shortened when the pressure of a neutral gas is increased.

The pressure dependence of ignition has also been studied by Kashiwagi et al.<sup>16</sup> At low pressure and with propellants having soft binders, it has been found that the oxidizer gases accumulate near the propellant surface. But at higher pressures and also for propellants having hard binders, it is argued that the ignition is faster because the oxidizer gas liberated at the interface remains confined in the solid as compared to open diffusion and thereby reaches a higher concentration, which facilitates the ignition process.

### Effect of Oxidizing Atmosphere

Studies on the effect of the oxidizing atmosphere on ignition can be divided into two categories: 1) the use of reactive oxidizers such as  $F_2$  and  $ClF_3$  that cause hypergolic ignition after

coming in contact with the propellant surface; and 2) ignition in presence of gaseous oxygen. Reactive oxidizers, when in contact with the surface, generate spontaneous exothermic heterogeneous reactions and raise the surface temperature without any external heat. Anderson and Brown<sup>1</sup> have proposed a theoretical model based on heterogeneous reactions between the reactive oxidizer and the propellant.

The model shows that the  $t_{ID}$  is related to gaseous oxidizer concentration as

$$t_{ID} \propto 1/C^x \quad (8)$$

where  $C$  is the oxidizer concentration and  $x$  the order of the surface reactions.

This equation has been tested for terpolymer of butadiene, acrylic acid, and acrylonitrile (PBAN) propellants and a reasonable agreement between theoretically predicted and experimental values has been obtained assuming a first-order heterogeneous reaction.

Ignition delay has been found to depend on both the partial pressure of  $O_2$  as well as the total pressure. It was found<sup>17,2</sup> that  $t_{ID}$  decreases by increasing the partial pressure of  $O_2$  at a level where the mole fraction of  $O_2$  is higher than 0.6-0.7. It was further suggested that AP decomposition contributes to ignition when the surrounding atmosphere contains less than 50-60%  $O_2$ .

Summerfield et al.<sup>18</sup> found in their shock tube experiments that a surface temperature of 433 K is obtained in propellant ignition. They argued that at such a low surface temperature the TD of AP will not be significant because ignition occurs in a short time ( $\sim 1$  msec) and consequently  $O_2$  has to be supplied externally to support the ignition. It amounts to the fact that in the absence of sufficient oxygen, the AP contained in the propellant has to decompose to provide oxygen and/or oxidizing species to ignite the propellant. In other words, propellant ignition in inert atmospheres is primarily governed by AP decomposition.

### Ignition of Composite Propellant Fuels by $\text{HClO}_4$ Vapor

In case of AP composite propellants, it is well established that the initial products of decomposition are  $\text{NH}_3$  and  $\text{HClO}_4$ . Since  $\text{HClO}_4$  is much more reactive than  $\text{O}_2$ , investigations were made to examine whether  $\text{HClO}_4$  could produce ignition with fuels below 573 K or if ignition could occur only when the  $\text{HClO}_4$  and vaporized fuel diffuse from the propellant surface into a higher temperature reaction.

A series of experiments have been performed by Pearson<sup>19</sup> to elucidate the controlling mechanism in the ignition of composite propellants. Ignition of binders such as polymethyl methacrylate (PMMA), polystyrene (PST), PU, and PS were carried out in  $\text{HClO}_4$  and  $\text{O}_2$  by impinging a stream of either  $\text{O}_2$  or  $\text{HClO}_4$  vapors (72% by weight).  $\text{HClO}_4$  caused much faster ignition at a much lower temperature (473-523 K) than 100%  $\text{O}_2$ . It was shown that  $\text{HClO}_4$  vapor ignites solid fuels by the  $\text{HClO}_4$  reacting either heterogeneously with the fuel surface or homogeneously with the fuel vaporized from the surface.

In the ignition experiments with less volatile fuels such as nylon, terylene, and methyl pentene polymer (TPX), only the first two fuels ignited, supporting the heterogeneous reaction mechanism, but TPX did not ignite. However, TPX ignited in the presence of a catalyst. Ignition may result from either heterogeneous decomposition of  $\text{HClO}_4$  on the fuel surface, yielding reactive  $\text{Cl}_2$  and  $\text{O}_2$ -containing species that then react exothermically with the solid or gaseous fuel, or from homogeneous gas-phase reactions between  $\text{HClO}_4$  and gaseous fuel molecules. However, it is difficult to differentiate between a purely homogeneous (reaction occurring between  $\text{HClO}_4$  vapor and vaporized fuel) and a purely heterogeneous mechanism ( $\text{HClO}_4$  vapor and condensed fuel). The relative importance of each may depend on factors such as heat flux, pressure, and the pyrolysis of the fuel.

In composite propellants it is considered likely that heterogeneous reactions of both  $\text{HClO}_4$  with  $\text{NH}_3$  (occurring at the propellant surface) and  $\text{HClO}_4$  with solid fuel could lead to ignition. High pressure would certainly favor the  $\text{HClO}_4$  and  $\text{NH}_3$  reaction since it would inhibit diffusion of the  $\text{HClO}_4$  to the fuel surface. This is in agreement with the combustion mechanism proposed for AP propellants at higher pressures, which postulates a premixed  $\text{NH}_3/\text{HClO}_4$  flame very close to the surface of the AP crystal.

### Preignition Reactions

Preignition reactions have been studied in depth in liquid and hybrid propellants, but very few studies have been made in composite solid propellants.

Preignition reactions of AP/HTPB propellant have been observed spectrometrically by Law et al.<sup>20</sup> in the temperature range 513-610 K by following the NH absorption at  $3.0\ \mu\text{m}$  and CH absorption at  $3.42\ \mu\text{m}$ . In the absence of AP, the polymer showed a negligible loss of CH at temperatures up to 615 K. The presence of AP accelerates the decomposition of the binder. A single E of 79.5 kJ/mole was obtained for both NH and CH disappearances. Acceleration of AP decomposition by polymer fragments was also observed. E was calculated by using the data taken after the first 10 s at the prescribed reaction temperature and fitted to first-order decomposition kinetics for both CH and NH disappearances. However, Waesche,<sup>21</sup> Inami et al.,<sup>22</sup> and Baer and Ryan<sup>23</sup> have reported a value of 30 cal/mole. The difference in the E values have been attributed to the fact that reaction rates observed for the initial periods cannot be described properly by the first-order kinetics and may also be due to an error in measurement and the small temperature range considered.

Exothermic reactions at the propellant surface preceding ignition were detected by Fishman<sup>24</sup> during arc image furnace experiments on the ignition of AP propellants. As shown in Fig. 3



following initiation of the energy pulse (at the time  $i$ ) the surface temperature rises steadily. At time  $e$  an inflection occurs that can be interpreted only as the onset of exothermic reactions. On termination of the energy pulse at time  $r$ , the temperature continues to rise because of the exothermic reactions. Runaway ignition can be seen after time  $r$ . This exotherm at the surface seems to be associated with the heterogeneous decomposition of  $\text{HClO}_4$  and the heterogeneous oxidation of the fuel.

Osada and Kakinouchi<sup>25</sup> have studied initiation of ignition in solid composite propellants by means of thermogravimetric analysis (TG), differential thermal analysis (DTA), x-ray, gas chromatography, and mass spectrometry. They observed that at 463 K the Thiokol resin undergoes exothermic curing reactions and produces radicals in itself. At 523 K, the bonds S-S and C-S of Thiokol break, producing CS,  $\text{H}_2\text{S}$ , and  $\text{SO}_2$  in the gas phase, followed by the breakage of bonds such as C-S, C-O, and C-H to produce carbonaceous

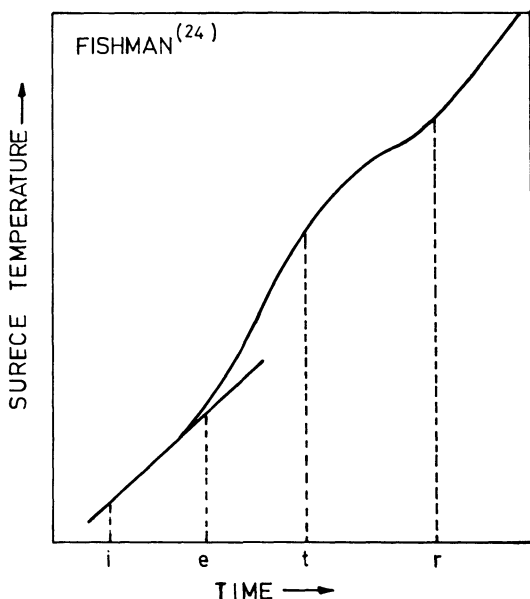


Fig. 3 Plot of surface temperature as a function of time during the preignition period.

gases. Initiation of propellant ignition occurs by the reaction of the Thiokol resin with AP and is affected only by the chemical nature of the resin and not by the reactivity of AP.

### Effect of Catalysts on Ignition

Four possible models of the action of catalysts have been proposed by Pearson<sup>19</sup>: 1) by accelerating fuel decomposition, 2) by accelerating  $\text{HClO}_4$  decomposition, 3) by accelerating the solid-fuel/ $\text{HClO}_4$  reaction on the fuel surface, and 4) by accelerating gaseous fuel (including  $\text{NH}_3$ / $\text{HClO}_4$  reactions in the gas phase. In addition, catalysts may also enhance AP decomposition.

It has been shown<sup>26</sup> that the binder degradation is not affected by the addition of a catalyst; for example, copper chromite (CC) does not change the rate of volatilization of PIB and other fuels. That the catalyst accelerates the decomposition of  $\text{HClO}_4$  has been observed by several workers.<sup>27-30</sup>

Pearson and Sutton<sup>27</sup> showed that fuels which ignite with difficulty in the presence  $\text{HClO}_4$  vapor at 473-523 K will ignite readily in the presence of a catalyst such as copper chromite or chromate. This is confirmed by experiments in which a thermocouple covered with the catalyst was placed in a heated tube. The temperature recorded by the thermocouple was observed to rise sharply (about 40 K) after introduction of the  $\text{HClO}_4$  vapor.

However, this temperature rise may not be the sole factor causing ignition since ignition of TPX did not occur in the presence of  $\text{HClO}_4$  when the TPX temperature was raised by 40 K.<sup>4</sup> Therefore, it has been proposed that a short-lived reactive intermediate might be causing the ignition of TPX in  $\text{HClO}_4$ . It is believed that the reactive intermediate may be a free radical ( $\text{ClO}$ ) since it is probable that  $\text{ClO}$  would have a long enough life to react with the fuel binder. The TPX not ignited in the presence of  $\text{HClO}_4$  was found to achieve ignition in the presence of a catalyst. It was observed that the catalyzed

ignition of TPX occurred faster and at a lower temperature in the presence of  $\text{HClO}_4$  decomposition. Also, it was observed that ignition occurs when the catalyst is in physical contact with the solid fuel and not when catalyst and binder are physically separated. This experiment suggests that the catalyst decomposes  $\text{HClO}_4$  to produce a short-lived reactive intermediate<sup>4</sup> that attacks the binder to cause ignition.

Solymosi et al.<sup>30</sup> suggested that catalysts for  $\text{HClO}_4$  decomposition could be divided into three groups: 1) highly effective oxides ( $\text{Cr}_2\text{O}_3$ ,  $\text{NiO}$ ,  $\text{Al}_2\text{O}_3$ ,  $\text{Fe}_2\text{O}_3$ , and  $\text{CuO}$ ); 2) less reactive oxides ( $\text{TiO}_2$  and  $\text{Cu}_2\text{O}$ ); and 3) inactive oxides ( $\text{CdO}$ ,  $\text{MgO}$ , and  $\text{CaO}$ ). A close correlation was observed between the catalytic effect of the oxides and the relative thermal stability of the corresponding metal perchlorates. On the other hand, the order of reactivity of the catalyst on decomposition and ignition of AP did not correlate with the order of activity of  $\text{HClO}_4$  decomposition.

Solymosi and Borcsok<sup>31</sup> have found that treating AP with  $\text{HClO}_4$  has only a slight effect on the characteristics of ignition, whereas the effect of  $\text{HClO}_4$  on the catalytic ignition of AP is more pronounced.

The relative effectiveness of various catalysts in the ignition process is in general agreement with their effectiveness in promoting the TD of AP. However, the exact order will depend upon surface area, particle size, and quantities of the catalysts used.

Rosser et al.<sup>26</sup> have found in a study of the ignition of an AP/CC mixture that the products of decomposition differ from those of normal AP decomposition in several ways: 1)  $\text{N}_2\text{O}$  and  $\text{HCl}$  are not produced; 2) a short-lived intermediate is formed that is capable of oxidizing  $\text{Cr(III)}$  in copper chromite to  $\text{Cr(VI)}$ ; 3) the gaseous products may be explosive; and 4) the decomposition is not inhibited by  $\text{NH}_3$  and the decrease in catalytic activity associated with item 2 may be prevented. Consequently, an electron-transfer process in the presence of a catalyst has been suggested, followed by the decomposition of the  $\text{NH}_4^+$  and  $\text{ClO}_4^-$  to  $\text{NH}_3$ ,  $\text{N}_2$ ,  $\text{O}_2$ ,  $\text{ClO}_2$ , and  $\text{ClO}_3$ . However,

Pearson and Sutton<sup>27</sup> have invoked the same proton-transfer mechanism for both catalyzed and uncatalyzed decomposition of AP.

Studies on the effect of catalysts on AP decomposition by Inami and Wise<sup>32</sup> have led to the conclusions that CC plays a dual role in a propellant system by acting as an oxidation catalyst for  $\text{NH}_3$  and other organic fuel binder molecules and as a decomposition catalyst for  $\text{HClO}_4$ .

Shannon<sup>7</sup> found that the effects of  $\dot{f}$  catalysts on the ignition mechanism are minimal. The catalysts tend to reduce the  $t_{\text{ID}}$  and the order was the same as their relative order of  $\dot{f}$  effectiveness. A similar observation has also been made by Price et al.<sup>33</sup>;  $\text{LiF}$ , which is a  $\dot{f}$  suppressant, brought about inhibition in ignition. The addition of  $\text{Fe}_2\text{O}_3$ , a known accelerator of the  $\dot{f}$ , reduced  $t_{\text{ID}}$  but<sup>23</sup> did not change the slope of the plot of  $\text{ID} \ln t_{\text{ID}}$  vs  $\ln (\text{O}_2 \text{ content})$ . It was therefore concluded<sup>34</sup> that the catalysts did not change the mechanism, but only increased the rates.

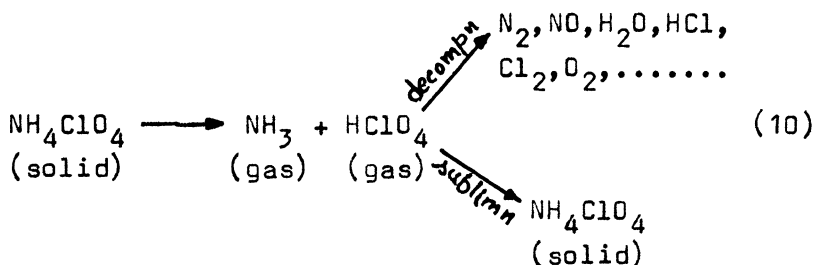
Propellant ignition being an enormously complex process, the various processes occurring cannot be explained in terms of a single rate-determining mechanism. It is likely that one or more types of mechanism models such as gas-phase, condensed-phase, and catalytic reactions contribute energy to the ignition process. For a specific case, the relative importance of any single reaction will depend upon factors such as local concentration, local temperature, interfacial chemical and physical structure, external heating rate, and pressure. There is a need to develop some sort of unified ignition theory taking into account all of the observed factors.

## II. Chemistry of Combustion

### Introduction to Combustion Mechanism

The mechanism of combustion of the propellant is not fully understood. After ignition it is assumed that the solid fuel and oxidizer, which are originally in separate phases, decompose

at the surface to yield adjacent oxidizer and fuel species. The breakdown of the fuel binder in a narrow reaction zone consists of polymer chain scission producing volatile fragments and monomer units consisting primarily of hydrocarbon species. AP gasifies either by endothermic sublimation or exothermic decomposition. These reactions can be represented as



Besides decomposition, sublimation also occurs emitting  $\text{NH}_3$  and  $\text{HClO}_4$ , yielding a premixed flame very close to the AP surface (2  $\mu\text{m}$ ) and producing a large amount of  $\text{O}_2$  and oxidizing species.<sup>35</sup>

For the reaction to take place, the fuel and oxidizer species have to undergo mixing; therefore, the critical process is the diffusional mixing. The characteristic time for the gas-phase reactions decreases with the increase in pressure; therefore, at low pressures (particularly with small AP particle size), one can expect the gases from both the oxidizer and the binder to mix completely before reaction. However, with the increase in pressure or AP particle size, the reaction time becomes short and the mixing step may ultimately become the limiting process.

The exothermic reactions between the oxidizer and binder degradation products in the gas phase establish a flame and produce the final products. The enthalpy of these reactions is transferred back to the solid surface to sustain the decomposition processes. This conductive heat feedback from the flame to the propellant

## Chapter 3

# **The Thermal Behavior of Cyclotrimethylenetrinitramine (RDX) and Cyclotetramethylenetetranitramine (HMX)**

T. L. Boggs\*

*Naval Weapons Center, China Lake, California*

### Abstract

The literature describing the physical properties, sublimation, decomposition, ignition, and self-deflagration of RDX and HMX is surveyed. Discussion of physical properties includes the crystallography of the materials with emphasis on the polymorphs of HMX and the solid-phase transitions of HMX. The energetics and kinetics of HMX sublimation are discussed. The many reported values for energetics, kinetics, and species of thermal decomposition of the solid are presented. Discussion of possible reaction mechanisms is presented. The decomposition--species and energetics--of the liquid is discussed. Data from high heating rate studies are presented and compared with results obtained from the more traditional, controlled tests described. Results from shock tube studies are also presented. The ignition behavior of HMX is presented showing that when the sample is subjected to an energy flux several events occur with time: heating and gasification of the sample, reaction of the pyrolysis products, ignition, and self-deflagration. The dependence of self-deflagration rates as functions of pressure and initial sample temperature are given over the pressure range  $1 \text{ atm} \leq p \leq 50,000 \text{ psi}$  and  $-150 \leq T \leq 150^\circ\text{C}$ . Scanning electron micrographs showing the surface of samples rapidly quenched while self-deflagrating are also shown.

---

This paper is declared a work of the U.S. Government and therefore is in the public domain.

\*Head, Combustion/Detonation Research Branch, Engineering Sciences Division.

## Introduction

The cyclic nitramines cyclotrimethylenetrinitramine ( $C_3H_6N_6O_6$ ), commonly called RDX, and cyclotetramethylene-tetranitramine ( $C_4H_8N_8O_8$ ), commonly called HMX, are important ingredients in propellants used in gun and solid rocket propulsion systems. RDX has also been called 1,3,5-trinitro-1,3,5 triazacyclohexane; 1,3,5-trimethylene trinitramine; hexogen (Soviet literature); and T-4. HMX has also been called 1,3,5,7 tetranitro-octahydro 1,3,5,7 tetrazocine; 1,3,5,7 tetra-nitro 1,3,5,7 tetrazacyclo-octane; octahydro-1,3,5,7 tetranitro-1,3,5,7 tetrazocine; and octogen (Soviet literature). It is widely known that the use of these ingredients offers many advantages. Due to the high energy of these compounds and the large amount of gas produced during the combustion, high values of specific impulse for rocket propellants and impetus for gun propellants can be achieved. In contrast to propellants based on ammonium perchlorate (AP), nitramine propellants do not produce hydrochloric acid (HCl) unless, of course, AP is incorporated into the propellant to serve as a ballistic modifier. Besides being corrosive, HCl in the exhaust provides nucleation sites for moisture droplets to condense upon, thereby producing a visible contrail or secondary smoke.

Although RDX is the cheaper of the two ingredients, HMX has desirable properties when compared to RDX. Beta HMX (the room temperature polymorph of HMX) has a density of  $1.90 \text{ g/cm}^3$  compared to the  $1.806 \text{ g/cm}^3$  of RDX. Beta HMX has an impact sensitivity for a 5 kg weight of approximately 33 cm while RDX has 28 cm (type 12 drop test). The temperature required to cause an explosion in 5 s is  $260^\circ\text{C}$  for RDX compared to  $327^\circ\text{C}$  for HMX. The confined "cook-off" temperature is  $180^\circ\text{C}$  for RDX as compared to  $210^\circ\text{C}$  for HMX.

This paper presents a survey of the literature describing HMX and RDX physical properties, sublimation, decomposition, ignition, and self-deflagration. This is a literature survey, not a literature review. A critical review was intended, but could not be adequately accomplished because of lack of detail in some of the papers. Critical details were often not found in the paper and in many cases, when the author(s) was contacted, it would be found that the details either had not been recorded or could not be remembered. It is hard to make comparisons without knowing such crucial parameters as temperature, pressure, atmospheric gas, degree of containment, and heating rate. In a few cases, proper care in the conduct of an experiment seemed to be lacking. In addition, some

authors presented conflicting or inconsistent results from paper to paper and, in a few cases, within the same paper and made no effort to reconcile the inconsistencies.

Because of these limitations, a survey rather than a review is presented. In several sections, the data from the various investigators are simply presented even though conflict is apparent. It is hoped that investigators describing their work in the future will be more mindful of the need to communicate, not only their results, but the conditions of the experiment(s) and the agreement/disagreement with previous work described in the literature. The conclusion of this survey lists experimental details and protocol that are necessary considerations if a critical review/comparison is to be made. I would encourage investigators to provide this information in future papers.

### Crystallography

RDX is an orthorhombic crystal (Pbca with  $a=13.18$  Å,  $b=11.57$  Å, and  $c=10.71$  Å). There are four polymorphic forms of HMX initially described by McCrone.<sup>1</sup> These are the  $\alpha$ ,  $\beta$ ,  $\gamma$ , and  $\delta$  forms<sup>2</sup> listed in Table 1. The  $\beta$  HMX contains a ring conformation such that the  $\text{NO}_2$  groups adopt a chairlike arrangement, giving the entire molecule a center of symmetry.<sup>3,4</sup> The ring conformations of  $\alpha$ ,  $\gamma$ , and  $\delta$  HMX are such that all of the  $\text{NO}_2$  groups are positioned on one side of the molecule.<sup>3,5,6</sup> The  $\beta$  HMX is the commonly encountered form, but the other polymorphs, especially the  $\delta$ , have relevance to the thermal decomposition of HMX. The stabilities of the four polymorphs at 300 K are  $\beta > \alpha > \gamma > \delta$ . The  $\beta$  form is stable at room temperature. The stability of the other polymorphs is  $\alpha=115$ – $156^\circ\text{C}$ ,  $\gamma$  around  $156^\circ\text{C}$ , and  $\delta=170$ – $279^\circ\text{C}$ . The densities of the polymorphs are:  $\beta=1.903$ ,  $\alpha=1.87$ ,  $\gamma=1.82$ , and  $\delta=1.78$  g/cm<sup>3</sup>.<sup>1</sup>

Each of these polymorphs and the interconversions among the polymorphs have been studied.<sup>6-11</sup> A review of this literature will not be presented here; however, recent work of Brill and co-workers will be presented since it bears on decomposition and self-deflagration of HMX (see, for example, Refs. 12 and 13). Landers and Brill<sup>14</sup> studied the  $\beta \rightarrow \delta$  polymorph transition as a function of pressure and temperature (previous studies of temperature sensitivity had been made). Their work spanned the pressure range 0.1–138 MPa (0–20,000 psig). They found that in this range the  $\beta \rightarrow \delta$  conversion temperature increased from 176 to  $210^\circ\text{C}$ . Their data showed an interesting slope break at 69 MPa (10,000 psi and  $200^\circ\text{C}$ ). The thermodynamic parameters



Table 1 Polymorphic forms of HMX (from Ref. 2)

Polymorph	$\beta$	$\alpha$	$\gamma$	$\delta$
Crystal class	Monoclinic	Orthorhombic	Monoclinic	Hexagonal
Space group	$P2_1/c$	$Fdd2$	$Pc_1$ $P2/c^a$	$P6_122$
Unit cell	$a=6.54$	$a=15.14$	$a=10.95$	$a=7.71$
Dimension	$b=11.05$	$b=23.89$	$b=7.93$	
Å	$c=8.70$	$c=5.91$	$c=14.61$	$c=32.55$
Angles, deg	$\beta=124.3$		$\beta=119.4$	

<sup>a</sup> Old data, new studies indicate neither space group appropriate.

Table 2 Thermodynamic parameters for  $\beta \rightarrow \delta$  HMX transition (from Ref. 14)

Temperature-pressure	$\Delta H$ , kJ/mole <sup>a</sup>	$\Delta S$ , J/°mole <sup>a</sup>
175-200°C, 0.1-69 MPa (0-10,000 psi)	10.1 (2.41 kcal/mole)	23.4
200-212°C, 69-138 MPa (1-2x10 <sup>4</sup> psi)	17.7 (4.22 kcal/mole)	41.1

<sup>a</sup>Calculated for  $T=431$  K.

for the  $\beta \rightarrow \delta$  HMX transition are shown in Table 2. Their data showed the tendency of  $\beta \rightarrow \delta$  transformation to occur at a lower temperature (for a given pressure) in large crystals than in small crystals. Near the transformation,  $\delta$  HMX is the favored form in large crystals while  $\beta$  HMX is the favored form in small crystals, with the data for very fine powder HMX not displaying the slopebreak (in the pressure range studied) displayed by the data for the larger powders.

Hall<sup>15</sup> showed  $\Delta H_{\beta \rightarrow \delta}$  (at  $T=460$  K) to be  $2.35 \pm 0.20$  kcal/mole ( $9.85 \pm 0.84$  kJ/mole) and Selig<sup>16</sup> showed  $\Delta H_{\beta \rightarrow \delta} = 2.25$  kcal/mole, in good agreement with Landers and Brill.<sup>14</sup>

The earlier work by Landers and Brill was extended to higher pressures [138-690 MPa (20,000-100,000 psi)] in another study by Karpowicz and Brill.<sup>17</sup> A very pronounced particle size effect was observed at these higher pressures as shown in Fig. 1. The authors attribute this particle size effect to greater buildup of decomposition products within the crystals of the larger (175  $\mu$ m) particles as compared to the smaller (3  $\mu$ m) particles. In the large particles, trapped decomposition products destabilize  $\beta$  HMX with respect to conversion to  $\delta$  HMX, while the small particles do not retain the decomposition products, thereby yielding a truer  $\beta \rightarrow \delta$  conversion line. The  $\Delta H$  for  $\beta \rightarrow \delta$

conversion of the 3  $\mu\text{m}$  HMX ( $T < 240^\circ\text{C}$ ) was found to be 13 kJ/mole (3.1 kcal/mole). At approximately  $240^\circ\text{C}$  and 207 MPa (30,000 psi) the 3  $\mu\text{m}$  HMX decomposes and the  $\Delta H$  rapidly rises to a limit of 232 kJ/mole (55.4 kcal/mole), which is very similar to the activation energies that others have determined for the decomposition of HMX (see later section on decomposition). As also shown in Fig. 1,  $\delta$  HMX is the stable polymorph above  $248^\circ\text{C}$  regardless of the pressure applied.

Recent studies by Brill and Karpowicz<sup>18</sup> have determined the kinetics for the transitions  $\beta \rightarrow \delta$  [ $E = 204 \pm 14$  kJ/mole (48.7 kcal/mole) and  $\log A = 19.9 \pm 1$ ],  $\alpha \rightarrow \delta$  [ $E = 208 \pm 18$  kJ/mole (49.7 kcal/mole) and  $\log A = 19.9 \pm 2$ ], and  $\gamma \rightarrow \delta$  [ $E = 219 \pm 20$  kJ/mole (52.8 kcal/mole) and  $\log A = 21.8 \pm 2$ ]. From these data, the authors propose a decomposition mechanism significantly different from those proposed by others involving the cleavage of covalent bonds. This new interpretation will be discussed later in the section dealing with decomposition of the solid. In addition, the work by Brill and co-workers<sup>6,10-12,17,18</sup>

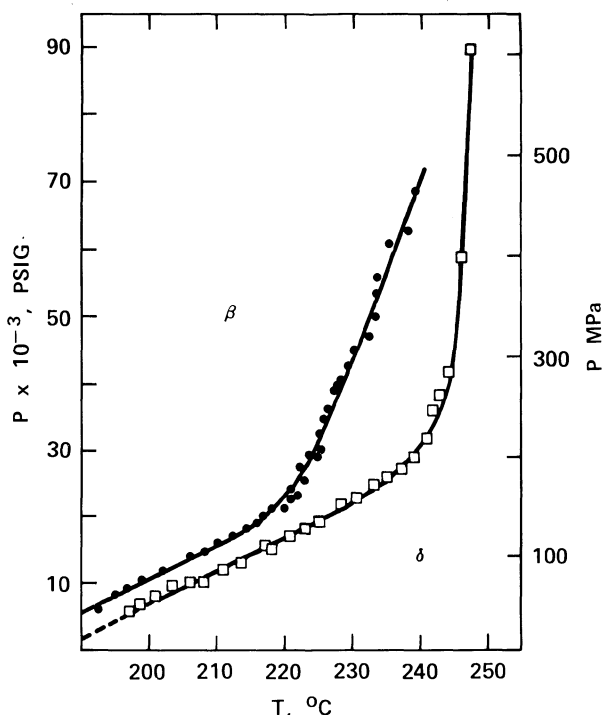


Fig. 1. Transition line of  $\beta \rightleftharpoons \delta$  HMX chosen at the conditions where  $\delta$  HMX can no longer be detected:  $\bullet$  175  $\mu\text{m}$  HMX,  $\square$  3  $\mu\text{m}$  HMX (from Ref. 17).

mirrors the particle size effects seen in the decomposition studies of Goshgarian<sup>12</sup> and may help explain the crystal fracturing that has been a problem in self-deflagration studies.<sup>13,19,20</sup> In addition, modeling of HMX combustion has largely ignored the  $\beta \rightarrow \delta$  phase transition.

Yee, Adicoff, and Dibble<sup>21</sup> have studied the surface properties of  $\beta$  HMX crystals. The critical surface tension  $\gamma_c$ , solid surface energies  $\gamma_s$ , and the polarity  $\gamma^p/\gamma$  of three principal crystal faces were obtained by measuring contact angles with several reference liquids. The values obtained are listed in Table 3, which shows that the three faces have different surface properties. This same conclusion was obtained from the authors' infrared specular reflectance spectra. This work has application to the determination of mechanical properties of propellants as influenced by adhesion of the binder and HMX.

The liquefaction of RDX and HMX has been studied but some controversy exists as to whether this liquefaction is truly melting. The controversy will be presented in the section dealing with liquid-phase processes. At this point, it is sufficient to give the liquefaction temperature to have been measured at 180-205°C for RDX<sup>22,23</sup> and 266-280°C for HMX.<sup>1,8,15,24,25</sup>

### Sublimation of HMX

Several authors have reported results from studies of the sublimation of HMX.<sup>13,26-30</sup>

The works of Rosen and Dickinson,<sup>27</sup> Taylor and Crookes,<sup>28</sup> and Farber and Srivastava<sup>29,30</sup> indicate that HMX can evaporate without appreciable decomposition. The vapor pressures ranged  $10^{-11}$ - $10^{-10}$  atm in the temperature range 98-130°C,<sup>27</sup> and  $10^{-7}$ - $10^{-5}$  atm at 188-213°C,<sup>28</sup> and  $5 \times 10^{-7}$  to  $5 \times 10^{-3}$  atm at 175-275°C.<sup>29</sup>

Several authors have determined the heat of sublimation. Rosen and Dickinson<sup>27</sup> determined the heat of sublimation from vapor pressure measurements over the 97.6-129.3°C temperature range of  $\beta$  HMX to be 41.89

Table 3 Surface properties of crystal faces  
(from Ref. 21)

Crystal face	$\gamma_c$ , dyne/cm	$\gamma_s$ , erg/cm <sup>2</sup>	$\gamma^p/\gamma$
(011)	43	45	0.25
(010)	45	46	0.34
(110)	46	48	0.36

kcal/mole. Meyer<sup>31</sup> approximated the heat of sublimation of  $\delta$  HMX by subtracting the heat of transformation of  $\beta \rightarrow \delta$  HMX from the heat of sublimation of  $\beta$  HMX giving a 39.55 kcal/mole value. Goshgarian<sup>12</sup> reports a heat of sublimation at 150-180°C to be 25.3 kcal/mole, which is in good agreement with the 26.8 kcal/mole calculated by Edwards<sup>26</sup> and a 38 kcal/mole value for the 250-270°C range, again citing agreement with Edwards<sup>26</sup> and with Taylor and Crookes.<sup>28</sup>

The activation energy of the HMX sublimation has been estimated by Kimura and Kubota,<sup>25</sup> subtracting  $RT$  from the heat of sublimation as proposed by Eyring<sup>32</sup> to give a calculated value of 39.45 kcal/mole. Kimura and Kubota<sup>25</sup> report measured activation energies (over  $253 < T < 263$  K) of 38.0 kcal/mole (for weight loss fraction  $\alpha$  of 0.1-0.4) and 22.9 kcal/mole (for  $0.2 < \alpha < 0.55$ ).

#### Decomposition of the Solid

##### RDX

Several experiments have been performed below 203°C to study the decomposition of solid RDX. Batten and Murdie<sup>22</sup> measured total pressure vs time for RDX decomposition in open-ended glass ampules with RDX spread on the bottom of a flask. Tests were run at two temperatures, 196.5 and 180°C. At 196.5°C the RDX sample bubbles at 40% decomposition and is completely liquefied after 60% decomposition (independent of sample geometry). At 180°C more reaction was required before liquefaction occurs. The maximum rate does not correlate with the extent of liquefaction. When the samples were confined in ampules, the induction period and reaction time increased greatly and the curve was more autocatalytic in shape. From these two sets of observations, the authors concluded that the acceleration in rate by progressive melting is of minor importance, but that the rate is greatly influenced by the reaction of active gaseous products with the undecomposed RDX.

In the second part of their presentation, Batten and Murdie<sup>33</sup> determined the activation energy for RDX decomposition in the temperature range of 170-198°C. The values obtained differed for the test conditions: for the spread RDX the activation energy was 63 kcal/mole throughout the course of the reaction, while for the confined samples the activation energies were 49 kcal/mole for the induction period, 43 kcal/mole for the acceleration period, and 63 kcal/mole for the maximum rate. The effect of geometry upon the activation energy was attributed to gaseous products influencing the reaction.

Subsequent work by Batten<sup>23,34</sup> using the spread RDX sample showed that 300 Torr of added  $N_2$ , CO,  $CO_2$ , or  $N_2O$  retards the reaction slightly,  $H_2O$  retards the reaction further, and both  $O_2$  and  $NO_2$  strongly retard the reaction over the entire course of the reaction. With sufficient  $NO_2$  or  $O_2$ , there was no residue at complete reaction and liquefaction of the sample was prevented. Addition of 130 Torr HCHO, while not affecting the shape of the sigmoidal curve, did increase the rate (over added  $N_2$ ) by a factor of 6 at  $170^\circ C$  but by less than 2 at  $197^\circ C$ .<sup>34</sup> With the added HCHO, the activation energy was 44 kcal/mole at all stages. Liquefaction occurs at a lower extent of decomposition when HCHO is added.

Batten<sup>35</sup> also found that the nonvolatile residue greatly increases the rate when in contact with fresh RDX and at  $196^\circ C$  caused initial liquefaction of the sample. Prior ultraviolet irradiation also influenced the liquefaction process as well as enhancing the overall rate and virtually eliminating the induction period.

Cosgrove and Owen<sup>36</sup> decomposed RDX at  $195^\circ C$  with the results shown in Table 4. They also studied the rates of the reaction. They found that at constant reactor volume (150 ml) varying the sample size by a factor of 10 did not affect the decomposition rate, but that the decomposition rate was directly proportional to the volume of the reaction vessel and that the addition of 314 Torr of nitrogen decreased the rate by a factor of 2 during the induction

Table 4 Decomposition products of RDX at  $195^\circ C$ , mole/mole (from Ref. 36)

Product	5% reaction <sup>a</sup>	9% reaction <sup>b</sup>	92% reaction <sup>c</sup>
$N_2$	0.83	0.65	1.26
$N_2O$	1.4	0.92	1.08
NO	0.86	1.30	0.51
$H_2CO$	1.1	1.2	1.04
CO	0.20	0.16	0.36
$CO_2$	0.50	0.30	0.70
HCN	Present	Present	Present
$NH_3$	0.83	0.69	0.34
$HCOOH$	0.93	0.60	0.37
$NO_3$	Present	0.29	0.10
$NO_2$	Present	Present	0.02
$H_2O$	Present	Present	Present
$HOCH_2NHCOH$	Present	Present	Present

Reaction flasks: <sup>a</sup>150 ml; <sup>b</sup>868 ml; <sup>c</sup>150 ml.

period. From these studies, they concluded that in the initial stages the vapor-phase decomposition of RDX is of primary importance.

In a second publication, Cosgrove and Owens<sup>37</sup> presented the effects of added gases on the decomposition of RDX at 195°C. They found that  $N_2$ ,  $N_2O$ ,  $CO_2$ , and  $H_2O$  all inhibit the decomposition. The addition of NO decreased the rate, but not as drastically as the other gases. Formaldehyde addition increased the rate. Added 1,3,5-trinitrobenzene, hydroxymethyl formamide, and methylene diformamide greatly increased the rate. The authors concluded that these additives promote solution-phase decomposition and that initially a vapor-phase reaction occurs that becomes a liquid-phase reaction in the later stages.

### HMX

Several experiments have been performed below 275°C in order to study the decomposition of solid HMX. These studies resulted in information on the energetics, kinetics, gas-phase products, and speculation of the decomposition mechanisms. Unfortunately, there are considerable differences among the investigations. In the following sections of this paper, results from the various investigations will be discussed and generalized summary tables given.

Suryanarayana and Graybush<sup>38</sup> heated HMX (226-260°C) in a constant-volume system connected to a mass spectrometer. After an initial induction period, they found that:

- 1) Rates of formation of  $N_2O$ ,  $N_2$ , CO, and  $CO_2$  were constant with time at 25-95% reacted (zero-order rate).
- 2) NO formation rate was constant with time at 50-100% reacted.

- 3) Rate of HCHO formation was constant at 15-40% HMX decomposition, then decreased and finally became negative (attributed to polymerization).

- 4) The polymerization of HCHO resulted in sigmoidal pressurization curves even though the rate of decomposition was fairly uniform.

- 5) HCHO maximum yield decreased with increasing temperature.

- 6) Gaseous products at the end of the complete reaction (mole/mole HMX) were: 2.6  $N_2O$ , 0.5  $N_2$ , 0.4 NO, 0.4 CO, 0.5  $CO_2$ , and 1.6-0.5  $CH_2O$ . (The remaining C, N, O must have been in solid or as unmeasured products.)

- 7) The gaseous products changed near the melting point. ( $N_2O$  decreased and  $N_2$  and NO increased.)

Table 5 Decomposition of HMX and RDX  $(-\text{CH}_2-\text{N}^{14}-\text{N}^{15}\text{O}_2)_x$ , %<sup>a</sup>  
 (from Ref. 40)

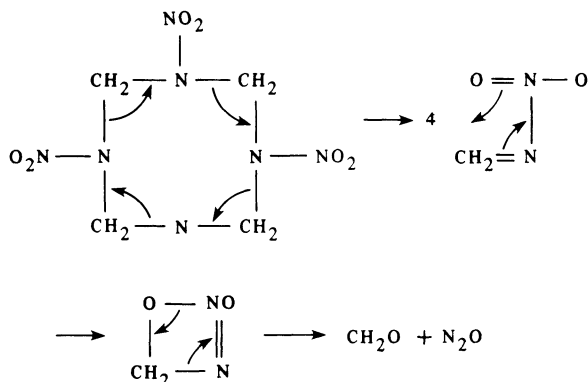
	$\text{N}^{14}\text{N}^{15}\text{O}$	$\text{N}^{14}\text{N}^{15}$	$\text{N}^{15}\text{O}$	$\text{HCN}^{14}$
HMX, 230°C	98	93-100	93-100	100
HMX, 254°C	98	92	95-100	100
HMX, 285°C	98	95	95-100	100
HMX, 190°C	99	99	95-100	100

<sup>a</sup>Test conditions: 50 mg sample, 380 cm<sup>3</sup> reactor, 230-285°C, and 40 Torr argon.

8) Zero-order rate constants for the formation of  $\text{N}_2 + \text{N}_2\text{O} + \text{CO}_2$  were: below 245°C,  $k = 10^{16} \exp(-46,000/\text{RT}) \text{ s}^{-1}$ ; above 245°C,  $k = 10^5 \exp(-18,500/\text{RT}) \text{ s}^{-1}$ .

Suryanarayana, Graybush, and Autera<sup>39</sup> studied the decomposition of  $\text{N}^{15}$  tagged HMX at 230, 254, and 285°C and the product gases were analyzed. They found the following products and percentages: 40%  $\text{N}_2\text{O}$ , 9.9%  $\text{NO}$ , 9.6%  $\text{N}_2$ , 4.5%  $\text{HCN}$ , 22.9%  $\text{HCHO}$ , 8.5%  $\text{CO}_2$ , and 4.1%  $\text{CO}$ . These are the 230°C results which are representative of the studies. A later publication by Suryanarayana et al.<sup>40</sup> presented the decomposition of the labeled HMX and RDX  $(-\text{CH}_2-\text{N}^{14}-\text{N}^{15}\text{O}_2)_x$  as shown in Table 5.

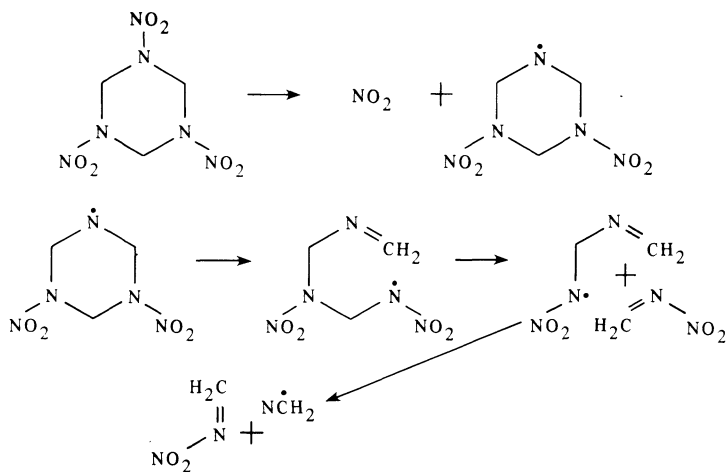
From these studies, the authors concluded that for these temperatures: 1) nearly all of the  $\text{N}_2\text{O}$  and  $\text{N}_2$  form without rupture of the N-N bond, 2)  $\text{NO}$  forms from the  $\text{NO}_2$  group, and 3)  $\text{HCN}$  forms from the ring N. They concluded that fission of the N-N bond occurs to only a minor extent with the C-N bond being more vulnerable. Based on their observations, they proposed a "concerted" mechanism of HMX decomposition, as follows:



In his review,<sup>41</sup> McCarty questioned whether such a mechanism is truly concerted following the principles of orbital symmetry and proposed several alternatives.

Based on their work with tagged nitrogen HMX, Powers et al.<sup>42</sup> disagree with the conclusion that nearly all of the  $N_2O$  and  $N_2$  form without rupture of the N-N bond. They used three sample types:  $N^{15}$  HMX - 99.0% of all nitrogen is  $N^{15}$ ;  $N^{14}$  HMX - 99.0% of all nitrogen is  $N^{14}$ ; and equal mole percent mixtures of  $N^{14}$  and  $N^{15}$ . They used a helium flow reactor with experimental conditions as nearly identical as possible. The interesting features were in the 40-50 m/e range. In all of the  $N^{14}$ -HMX spectra, there was the typical m/e = 44 peak corresponding to  $CO_2 + N_2O$ . There was also a small 46 peak ( $NO_2$ ) and a very small 45 peak. In all of the  $N^{15}$ -HMX spectra there were a 44 peak ( $CO_2$ ) and a 46 peak ( $N^{15} - N^{15} = 0$ ), but not a 45 peak. In the spectra of the 50-50 mole mixture of the materials, there were 44, 46, and 45 peaks. They take existence of the 45 peak as  $N^{14} - N^{15} = 0$  only resulting from the N-N bond cleavage. From the size of the 45 peak in relation to the 46 peak, it appears that there is significant N-N bond cleavage.

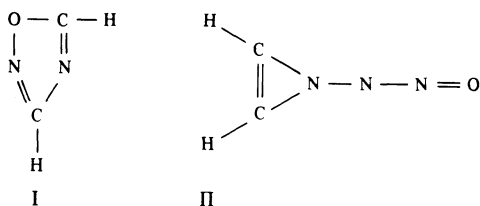
Others<sup>43-45</sup> have suggested that unimolecular N- $NO_2$  cleavage could be followed by concerted (or possible stepwise) breakdown to  $H_2CN$  and two molecules of  $H_2C = NNO_2$ . Schroeder<sup>43</sup> has presented such a stepwise process as:



Goshgarian has studied the decomposition of HMX over a temperature range of 250-284°C using a flowreactor mass spectrometer system.<sup>13</sup> The results of these tests are shown in Figs. 2 and 3. Figure 2 shows two regions of



decomposition in a solid as well as a liquid phase and a deflagration. The activation energies for these processes are also shown in the figure. The results of the product analysis (m/e) are shown in Fig. 3. Of particular interest is the m/e 70 specie which has been identified as a nitrosoamine, occurring prior to HMX liquefaction. Goshgarian postulated two possible structures for the m/e = 70 specie as:



The ring labeled HMX shows this specie to occur at m/e = 72, indicating Goshgarian's mechanism I to be the most reasonable. Goshgarian's differential scanning calorimetric results indicate an exotherm beginning at 274°C and

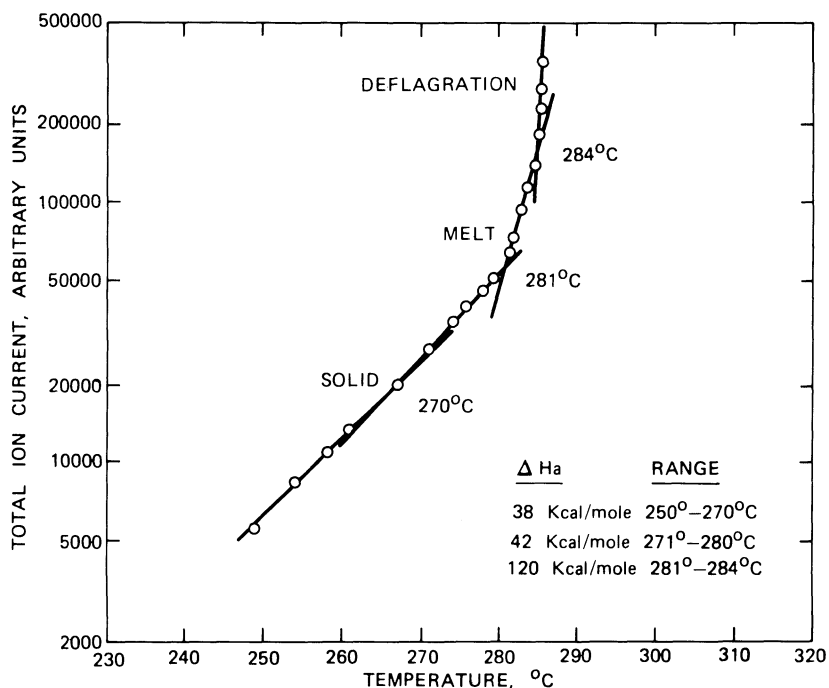


Fig. 2 Changes in slope during HMX decomposition in solid, melt, and deflagration (from Ref. 12).

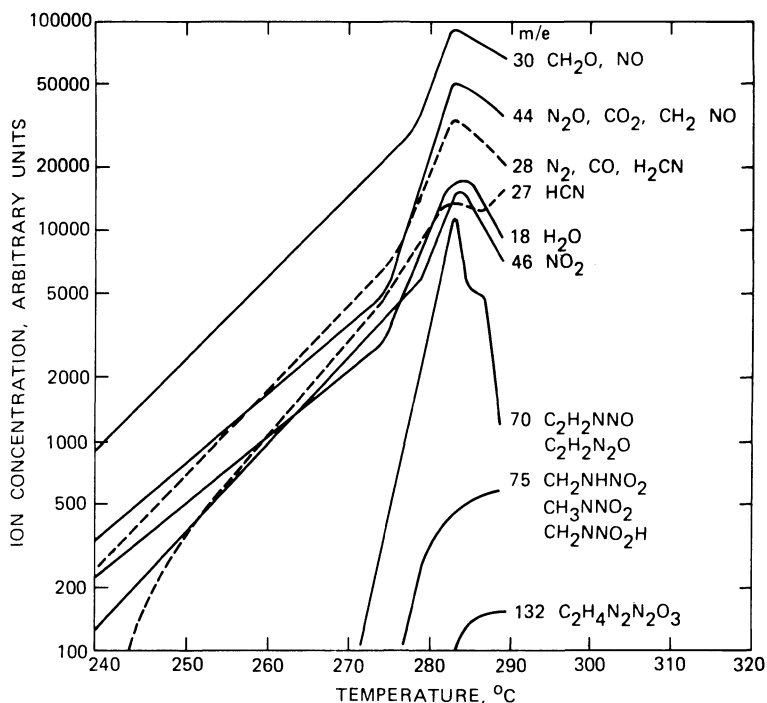


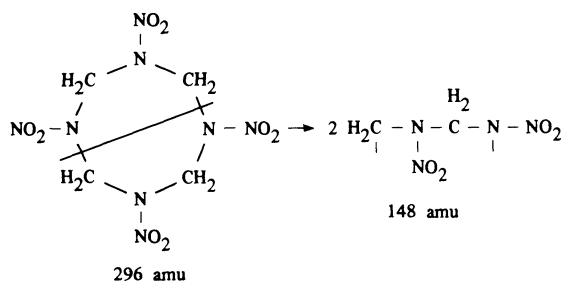
Fig. 3 Change in ion concentration vs temperature for HMX flowreactor tests (from Ref. 12).

continuing to the "melting" point of 282°C, indicating exothermic condensed phase reactions. Schroeder<sup>43</sup> has summarized reports of nitrosoamine formation in the condensed phase and discussed some possible free radical mechanisms.

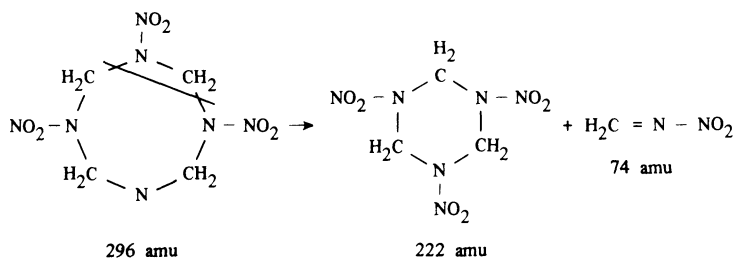
Goshgarian subscribes to the HONO elimination mechanism proposed by McMillen et al.<sup>44</sup> to describe the solid-phase decomposition ( $T < 550$  K). [Shaw and Walker<sup>45</sup> have done an excellent job in presenting eight possible unimolecular steps for HMX decomposition, and Shroeder<sup>46, 47</sup> has done an excellent job in summarizing 13 different reaction schemes (the HONO elimination mechanism included) that may be involved in HMX decomposition.] Obviously, such detailed discussions are beyond the scope of this present work and the reader is referred to Refs. 45-47. Goshgarian<sup>12</sup> also noted a brown solid residue produced during decomposition at 220°C. This residue was found to be C<sub>8</sub>H<sub>4</sub>N<sub>5</sub>O<sub>3</sub>, thus indicating loss of H, N, and O from the HMX molecule.

In addition to studying sublimation, Farber and Srivastava<sup>29, 30</sup> also studied the thermal decomposition at

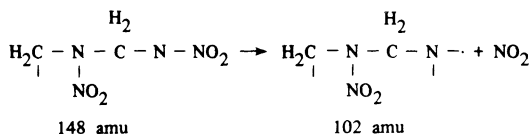
175-275°C using two techniques: Langmuir evaporation or effusion, both coupled to a mass spectrometer. The Langmuir evaporation mass spectroscopy studies showed simultaneous sublimation and thermal decomposition of HMX. The major decomposition reaction product was found to be the  $C_2H_4N_4O_4$  (148 amu) molecule. From these experiments, they proposed that the mechanism for the primary mode of the solid-phase HMX decomposition is a ring cleavage such as



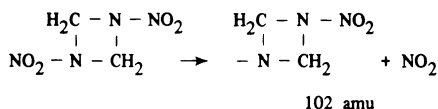
In the effusion cell experiments they did find relatively small amounts of 222 amu and postulated that this relatively small quantity resulted from a decomposition mode of



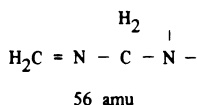
Other peaks found for the effusion cell decomposition include 128, 120, 102, 74, 56, 46, 44, 32, 30, 28, and 18 amu. The authors postulated these to be due to



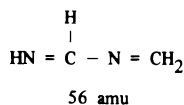
or, from the bond closure molecule,



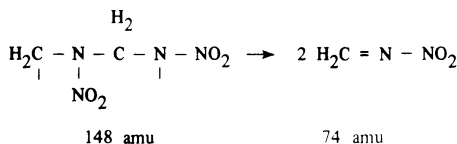
The 102 amu fragment splits off another NO<sub>2</sub> group, yielding



which can rearrange to form a more stable resonating molecule,



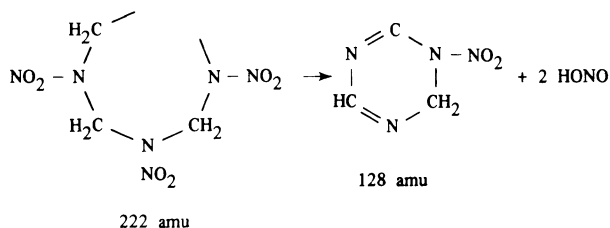
This molecule can split to produce two H<sub>2</sub>C=N radicals. The 148 amu fragment can also split into two equal stable molecules,



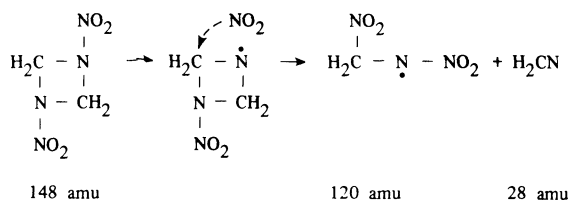
The peaks at 120 amu, CH<sub>2</sub>N<sub>3</sub>O<sub>4</sub>, and at 128 amu, C<sub>3</sub>H<sub>2</sub>N<sub>4</sub>O<sub>2</sub>, are apparently produced in the effusion cell as a result of the reaction of the gaseous products with the condensed phase and with each other.

These peaks have also been observed by Goshgarian,<sup>12</sup> Stals,<sup>48,49</sup> and Suryanarayana et al.<sup>50</sup>

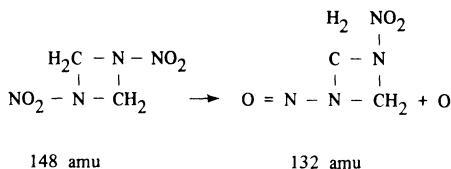
Goshgarian<sup>12</sup> has postulated the formulation of the 128 amu peak as



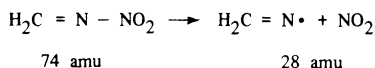
The peak at 120 amu has been postulated by Stals<sup>48,49</sup> as ring migration of the NO<sub>2</sub> group,



Stals<sup>48,49</sup> also indicated that the formation of the 132 amu peak results from the 148 amu molecule losing an O atom,



In ESR studies, Beyer and Morgan<sup>51-54</sup> found a considerable number of free radicals produced from the decomposition of HMX at 260°C. They attributed this free-radical spin resonance to the formation of H<sub>2</sub>CN• at 28 amu. Farber and Srivastava<sup>29,30</sup> showed a mixture of the decomposition products CO, N<sub>2</sub>, and H<sub>2</sub>CN. Beyer postulated that the radical H<sub>2</sub>CN is derived from

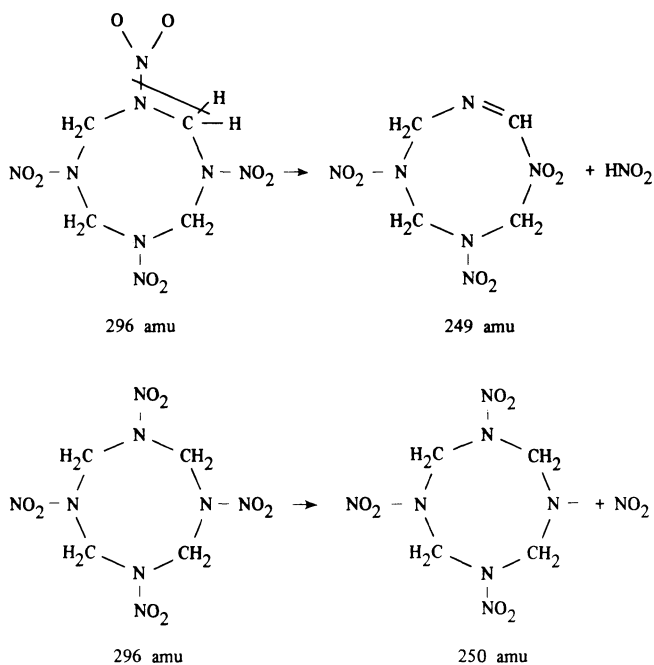


Farber and Srivastava<sup>29,30</sup> found neither 249 nor 250 amu and concluded that the ring migration to form HN(O<sub>2</sub>), one

Table 6 Regions of thermal decomposition (from Ref. 25)

Phase	Temperature, °C	Fraction reacted	Apparent reaction order	Kinetics, s <sup>-1</sup>
I	<255	<0.2	-9	$k=1.2 \times 10^{24} \exp\left(\frac{-66,400}{RT}\right)$
II	253-264	0.2-0.55	0	$k=2.5 \times 10^7 \exp\left(\frac{-22,900}{RT}\right)$
III	264-276	>.55	1	$k=3.8 \times 10^{23} \exp\left(\frac{-61,800}{RT}\right)$

of several mechanisms postulated by Shaw and Walker,<sup>45</sup> was not part of the decomposition mechanism. They also concluded that the N-N bond rupture would not produce NO<sub>2</sub> (a primary mode of decomposition) since it would require the mechanisms,



The results of Farber and Srivastava<sup>30</sup> yielded an activation energy of 42 kcal/mole for the decomposition of HMX to NO<sub>2</sub> groups, which agrees well with that found by Goshgarian<sup>12</sup> for the temperature range 250-280°C (38 kcal/mole for 250-270°C and 42 kcal/mole 271-280°C).

Using differential scanning calorimetry (DSC), Hall<sup>15</sup> found an activation energy for the decomposition between 540-551 K to be 180-210 kcal/mole for runs at a 8 K/min scan rate. The enthalpy of decomposition was obtained using the DSC and scan rates of 0.5 K/min and reported to be -166 kcal/mole.

Using TG-DTG, Kimura and Kubota<sup>25</sup> have shown that the thermal decomposition can be characterized by three regions. Table 6 gives the parameters for the 0.5°C/min heating at 1 atm air. The authors found their results to be a function of the heating rate used and concluded that the weight loss of HMX consists of several independent processes, and that one of the processes becomes the rate-determining step corresponding to the heating rate.

Kraeutle<sup>24,55</sup> also studied the decomposition of HMX using weight loss measurements. When he plotted weight loss as a function of time for different isothermal conditions at 229-269°C, he found that all of the curves had two distinct sections: an acceleratory period that extended to approximately 20% decomposition, followed by a decay period. When Kraeutle excluded the acceleratory portion of the curves, used Erofeev's equation, and assumed a first-order decomposition, he calculated an activation energy of 49 kcal/mole and a pre-exponential factor of  $9.3 \times 10^{16} \text{ s}^{-1}$  for HMX decomposition in air. Kraeutle also found that his results were dependent on sample size. He attributed the effect to the HMX contributing to its own decomposition by the gaseous environment--which would be dependent on HMX concentration.

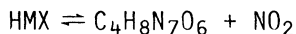
Kraeutle has also studied the decomposition of HMX in oxygen<sup>24,55</sup> and nitrogen<sup>55</sup> atmospheres, finding significant changes due to atmosphere. Weight loss data for the isothermal decomposition of solid HMX were taken over a temperature range of 229-269°C. The weight loss vs time curves show acceleratory (up to approximately 20% decomposition) and deceleratory branches. The acceleratory branches tend to be roughly the same regardless of the atmosphere, but the deceleratory portion of the curves is highly dependent upon the atmosphere. From the weight loss vs time curves, Kraeutle calculated rate constants for a first-order reaction using Erofeev's equation. These were plotted vs  $1/T$  with the results,

$$1) \text{ In oxygen: } k = 1.2 \times 10^{17} \exp(-49,700/RT) \text{ s}^{-1}$$

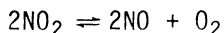
$$2) \text{ In air: } k = 9.3 \times 10^{16} \exp(-49,000/RT) \text{ s}^{-1}$$

$$3) \text{ In nitrogen: } k = 3.2 \times 10^{11} \exp(-35,100/RT) \text{ s}^{-1}$$

From these data, Kraeutle has concluded that oxygen is an inhibitor of the decomposition. He proposes that this is due to a shift of equilibrium of the reactions,



followed by



and cites agreement with the calculations of Shaw and Walker<sup>45</sup> for the N-NO<sub>2</sub> fission [ $k = 10^{16.4} \exp(-46,200/RT)$ ] and McMillen et al.,<sup>44</sup> who require an activation energy of at least 46,000 kcal/mole and a prefactor of  $10^{18} \text{ s}^{-1}$  for N-NO<sub>2</sub> bond scission.

Kraeutle<sup>55</sup> also used nonisothermal differential thermal analysis (DTA) to study HMX decomposition. He determined the following kinetic parameters for the 93 kPa air

tests:

4 mg samples  $k = 7.6 \times 10^{15} \exp (44,700/RT) \text{ s}^{-1}$

5 mg samples  $k = 4.5 \times 10^{15} \exp (44,800/RT) \text{ s}^{-1}$

The differences between the expressions determined using the isothermal weight loss data and the nonisothermal DTA data were attributed to an appreciably smaller particle size of HMX in the DTA tests and the dilution of the sample with inert material in the DTA tests (cited in Ref. 56).

Other DTA tests were made at high-pressure (3.54 MPa) nitrogen atmosphere. The kinetic parameters determined for 2 mg samples,  $k = 2.9 \times 10^8 \exp (-25,900/RT) \text{ s}^{-1}$ , are striking when compared to the parameters determined from the isothermal weight loss measurements at 1 atm. As will be shown later, Flanigan and Stokes<sup>57</sup> observed a similar pressure effect in their studies of liquid-phase decomposition. Additional work needs to be performed to delineate and understand the pressure effects.

The kinetic parameters determined from the several studies are tabulated in Table 7. As is obvious from the table, there are considerable differences between the investigators as to which kinetic parameters describe the decomposition of solid HMX. Obviously, more systematic work is needed in this area. In addition, the mechanism(s) of solid HMX decomposition has not been finally resolved. Several mechanisms have been proposed (see Shaw and Walker<sup>45</sup> and Schroeder<sup>43,46,47</sup>), each with its proponents. Some subscribe to cleavage of the C-N bond and some to HONO elimination, while others say that HONO elimination is not part of the decomposition mechanism. Still others subscribe to fission of the N-N bond to produce  $\text{NO}_2$ . Each group cites its supporting experimental evidence. Unfortunately, agreement between investigators does not seem to exist despite some claims of agreement; several investigators cite only instances of agreement, not disagreement. In addition, a need exists to relate these low-temperature (below the liquefaction of HMX), low-heating-rate results to the results from decomposition of liquid studies, to the high-heating-rate studies, and to the ignition and combustion behavior of HMX.

In the preceding discussions when mechanisms were considered, the assumption was made that the initial chemical event in the thermal decomposition was the breakage of covalent bonds. Brill and Karpowicz<sup>17</sup> question this assumption. Instead, they suggest that the initial rate-controlling step for the decomposition in the condensed



Table 7 Kinetic parameters for decomposition of solids

Investigator	Ref.	A, s <sup>-1</sup>	E, kcal/mole	Order	Temp, °C	Method
RDX						
Batten and Murdie	33		63 <sup>a</sup>		170-198	Pressure vs time
			49 <sup>b</sup>			
			43 <sup>c</sup>			
			63 <sup>d</sup>			
Batten	23,34		44 <sup>e</sup>			
HMX						
Maycock and						
Pai Vernecker	58		62	1 (assumed)	250-265	Isothermal TGA
Suryanarayana and						
Graybush	38	10 <sup>14</sup>	46	0 (assumed)	<245	Mass spec. of
		10 <sup>3</sup>	18.5	0 (assumed)	>245	decomposition
						products
Suryanarayana, Graybush,						
and Autera	39		45	1 (assumed)	226-245	Mass spec. of
			10-15		245-268	decomposition
			52		>268	products
Hondee	59,60		44.2		200-233	Dynamic DTA
			62.3		233-241	
			52.7		>241	
			65.8		232-241	Isothermal DTA
Rogers	67	6.4x10 <sup>18</sup>	51.3		<280	DSC

(Table continued on next page.)

Table 7 (cont.) Kinetic parameters for decomposition of solids

Investigator	Ref.	A, s <sup>-1</sup>	E, kcal/mole	Order	Temp, °C	Method
HMx (cont.)						
Goshgarian	12		29.9 67.4 38 42	1 (assumed)	200-240 240-260 250-270 271-280	Mass spec of decomposition products
Hall	15		180-210		267-278	DSC
Farber and Srivastava	29		42	1 (assumed)	175-275	Mass spec of products
Kimura and Kubota	25	1.2x10 <sup>24</sup> 2.5x10 <sup>7</sup> 3.8x10 <sup>23</sup>	66.4 22.9 61.8	-9 0 1	<255 253-264 264-276	TG-DTG
Kraeutle	55	9.3x10 <sup>16</sup> 1.2x10 <sup>17</sup> 3.2x10 <sup>11</sup> 7.6x10 <sup>15</sup> 4.5x10 <sup>15</sup> 2.9x10 <sup>8</sup>	49 <sup>f</sup> 49.7 <sup>g</sup> 35.1 <sup>h</sup> 44.7 <sup>i</sup> 44.8 <sup>j</sup> 25.9 <sup>k</sup>	1 (assumed)	229-269	Isothermal weight loss  Nonisothermal DTA

<sup>a</sup>Spread sample.<sup>b</sup>Confined sample, induction period.<sup>c</sup>Confined sample, acceleration period.<sup>d</sup>Confined sample, maximum rate.<sup>e</sup>130 Torr of added HCHO.<sup>f</sup>In air, 1 atm.<sup>g</sup>In oxygen, 1 atm.<sup>h</sup>In nitrogen, 1 atm.<sup>i</sup>4 mg sample in 93 KPa air.<sup>j</sup>5 mg sample in 93 KPa air.<sup>k</sup>3.54 MPa nitrogen.

phase (both solid and liquid) involves primarily the disruption of the strong intermolecular electrostatic forces between the HMX molecules (and the HMX molecule and its decomposition products). They base this on a comparison of Arrhenius data for phase transformations to those reported for the condensed phase (solid and liquid) decomposition process. Their paper<sup>17</sup> describes their kinetic study of the solid-solid phase transitions of HMX. Their results reveal why certain polymorph conversions are observed while others are not. The stability and conversion scheme originates in kinetic factors rather than in the enthalpy changes. The activation energies of the phase transitions (presented earlier) reflect the energy needed to disrupt the electrostatic forces in the crystal lattice of HMX.

In their work, the kinetics of two solid-phase transitions were studied using a FT-IR spectrometer with an MCT detector scanning the  $4000\text{--}700\text{ cm}^{-1}$  region with  $4\text{ cm}^{-1}$  resolution. A heating rate of  $2^\circ\text{C}/\text{min}$  was used to reach the temperature range of the phase transition with the temperature then quickly stabilized. Four infrared spectra were recorded as a function of time at each temperature. Loss of absorbance in bands characteristic of the starting polymorph were measured at specific time intervals to determine the rate of change of concentration as a function of time. Plots of  $\ln$  concentration vs time produced straight lines characteristic of first-order reactions. They extend their interpretation to the decomposition as it relates to the mobile liquid layer observed during rapid decomposition of HMX and RDX. They and Kraeutle, as will be discussed in the next section, question whether this liquid is a melt as it commonly has been called. They think of it as the dynamic breakup of the nitramine lattice accompanied by chemical decomposition. The liquefaction results from the mixture of decomposition products and HMX molecules, which is too heterogeneous to remain solid above  $270^\circ\text{C}$ .

### Liquefaction

Although several investigators write of RDX and HMX melting, experimental results indicate that the liquefaction is not a true melting in the sense of a phase change from solid to liquid occurring at a rather precise temperature (and to some extent pressure) as discussed at the end of the previous section. The melting temperatures often quoted ( $205^\circ\text{C}$  for RDX and  $285^\circ\text{C}$  for HMX<sup>2</sup>) are not the temperatures representing equilibrium between the solid and

## THERMAL BEHAVIOR OF RDX AND HMX

143

Table 8 Time to liquefy HMX as a function of temperature  
(average of 5 runs in 93 kPa air) (from Ref. 55)

Temperature, °C	Time, s	Temperature, °C	Time, s
265	No liquefaction	271	146.0
266	824.0	272	102.0
267	502.0	273	82.0
268	343.0	274	41.7
269	294.0	275	33.4
270	181.0		

Table 9 Liquid RDX products of RDX, mole/mole  
(from Ref. 56)

	225°C	267°C		225°C	267°C
NO	0.54	0.75	CO	0.40	0.29
N <sub>2</sub> O	0.98	0.76	CO <sub>2</sub>	0.48	0.44
N <sub>2</sub>	1.16	1.03			

liquid states of the substance in question. As shown earlier, Batten and Murdie<sup>22</sup> observed liquefaction at 180°C for RDX and Batten<sup>23</sup> showed that the nonvolatile residue from RDX decomposition caused initial liquefaction of RDX at 196°C, while the HCHO atmosphere could hasten liquefaction at 196°C.<sup>55</sup>

Kraeutle<sup>55</sup> has studied the liquefaction of HMX. In his study, he placed particles in a preheated microfurnace and measured the time elapsed between the particles reaching the set temperature and the appearance of liquid. The results are presented in Table 8.

In another series of tests, Kraeutle varied the sample weight, particle size (and hence the number of particles), and whether or not the furnace was covered. From these tests he concluded:

1) At constant sample size, liquefaction depends on particle size. Processes occurring within a particle seem to be more important than surface processes.

2) A minimum particle size is necessary for liquefaction at 266°C. Large particles have a lower limiting temperature.

3) There is a minimum sample size (weight) for liquefaction.

4) At constant sample size (weight) large particles liquefy faster than small particles.

5) The importance of the gaseous environment was shown in the covered tests: covered tests yielded liquefaction,

## Chapter 4

### Chemistry of Nitrate Ester and Nitramine Propellants

Robert A. Fifer\*

*U.S. Army Ballistic Research Laboratory  
Aberdeen Proving Ground, Maryland*

#### Abstract

A review is presented of the ignition and combustion chemistry of the nitrate ester nitrocellulose (NC) and the nitramines HMX and RDX. Major topics include 1) decomposition of NC, 2) mechanism of catalysis of nitrate ester propellants, 3) decomposition of HMX and RDX, 4) the search for catalysts for nitramine propellants, and 5) flame reactions. Direct diagnostic techniques have not yet been invented for subsurface (condensed-phase) or heterogeneous (gas-solid) processes during deflagration. Also, sophisticated flame diagnostic techniques have not yet provided species concentration profiles. Consequently, current knowledge of the combustion (and ignition) chemistry of these propellants comes from indirect sources, such as thermal decomposition experiments or isothermal gas-phase kinetic measurements. Even these are difficult to interpret; however reasonable, although generally nonunique, mechanisms can be postulated. Catalysis of nitrate ester propellants by lead compounds begins in the subsurface reaction zone, but also apparently involves acceleration of heterogeneous or gas-phase processes in the "fizz" zone, causing enhanced heat conduction back to the surface. Effective catalysts for nitramine propellants have not yet been found. A new hypothesis is presented which accounts for the phase-dependent decomposition rate constants of propellant molecules.

---

This paper is declared a work of the U.S. Government and therefore is in the public domain.

\*Chemist, Interior Ballistics Division.

## Introduction

Knowledge of the kinetics and mechanisms of the chemical reactions taking place during propellant burning is of more than just academic interest. If the detailed chemical processes were known, likely catalysts could be chosen intelligently rather than by costly and time-consuming trial-and-error techniques. Moreover, burning rate models often make use of global rate constants for the gas- and condensed-phase regions of reactions in order to determine the energy release profiles just above and below the regressing surface; if these are not known from independent experiments, the rate constants become adjustable parameters. The model then loses its "physical significance" and is of little value other than for empirical fitting of experimental burning rate data.

Figure 1 shows the various reaction zones observed with nitrate ester propellants, including "single-base" nitrocellulose (NC) and "double-base" nitrocellulose-nitroglycerin (NC/NG) types. Qualitative information of this type has come from visual and photographic observation.<sup>1</sup> Quantitative information concerning burning surface temperatures has come from imbedded thermocouple and optical techniques. The thermocouple techniques have in addition provided information concerning the variation of temperature with distance in the very thin zones in the condensed and gas phases near the surface (see Kubota et al.<sup>2</sup> for a review, with references, of these techniques).

The reaction begins in the subsurface preheat zone. This is  $\sim 100\text{ }\mu\text{m}$  thick at 1 atm, decreasing to  $\sim 20\text{ }\mu\text{m}$  at 20 atm. Chemical reaction may be confined to only the uppermost 10 or 20% of the thermal wave. At the regressing surface ("foam zone"), a gasification reaction takes place. The surface temperature is typically about  $300^\circ\text{C}$  and increases slowly with increasing pressure (burning rate). A nonluminous "primary flame zone" ("fizz zone") begins at the surface. The fizz zone, like the thermal wave, is quite thin ( $\sim 200\text{ }\mu\text{m}$  at 1 atm,  $\sim 100\text{ }\mu\text{m}$  at 20 atm). At the top of the fizz zone, the temperature is roughly  $800\text{--}1400^\circ\text{C}$ , depending on propellant energy and pressure. An induction zone ("dark zone"), either thermal or kinetic in nature, extends above the fizz zone; in it the temperature, and presumably the concentrations of the major species, remain almost constant. A "secondary," luminous flame finally brings the combustion products to the final temperature, typically  $2500\text{--}3500^\circ\text{C}$ . The standoff of the secondary flame defines the dark zone length, which is about 1 cm at 15 atm. With increasing pressure, the dark zone collapses and the secondary flame approaches the regressing surface. Below about 15 atm

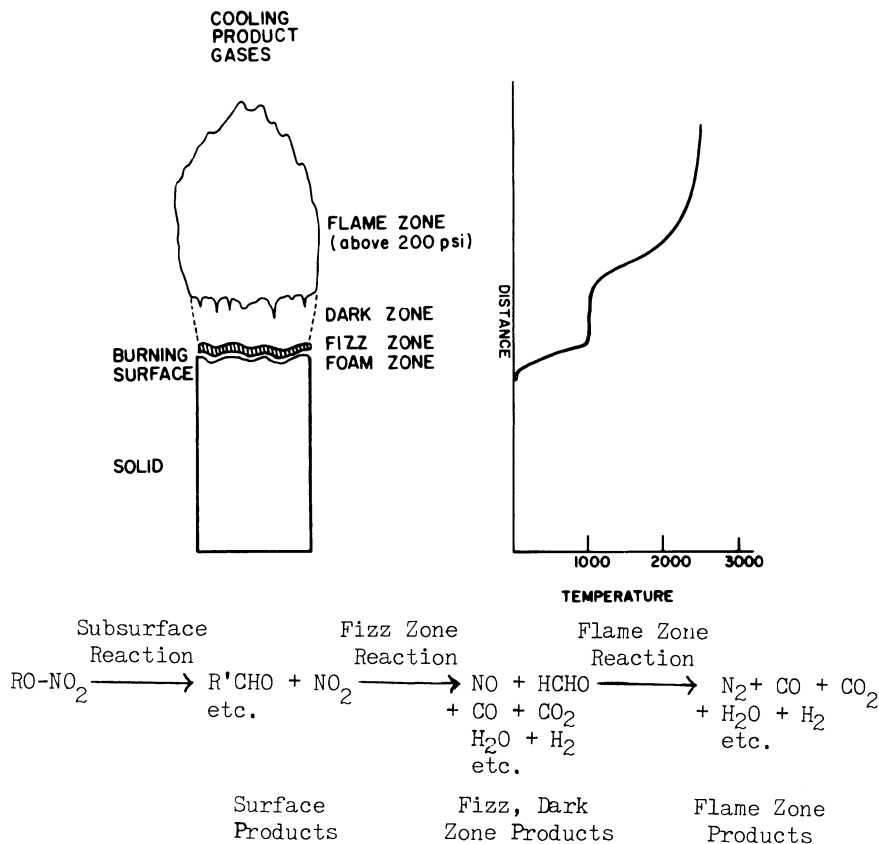


Fig. 1 Reaction zone structure, temperature profile, and probable species distribution for nitrate ester propellant.

many propellants burn without a secondary flame. During such "fizz burning," no flame is visible (the primary flame is present, however) and the combustion products reflect the incomplete burning of the fizz zone.

The following chemical changes take place in each reaction zone. In the subsurface reaction zone, initial endothermic bondbreaking is followed by many secondary reactions, some of which are exothermic. Thermocouple data analysis indicates that approximately 50-100 cal/g are released. Based on thermal decomposition experiments, it is assumed that the surface products consist mainly of NO<sub>2</sub> plus a variety of aldehydes such as formaldehyde (HCHO) and glyoxal (CHOCHO), although it is probable that some of the NO<sub>2</sub> reacts within the solid phase and that significant amounts of CO, CO<sub>2</sub>, H<sub>2</sub>O, etc., are also produced there. In the fizz zone, the NO<sub>2</sub> is

partially reduced (to NO) by reactions with the aldehydes to release another 400 or 500 cal/g and produce significant amounts of final-product-type molecules (CO, CO<sub>2</sub>, H<sub>2</sub>O, H<sub>2</sub>). The fizz zone products have been determined with sampling probes in the dark zone and by final product analysis for fizz burning samples (no secondary flame). In the secondary flame zone, the less reactive NO is reduced to N<sub>2</sub>, with some leftover formaldehyde perhaps playing a role in initiating the reaction. The reaction releases roughly another 500 cal/g of energy and changes the ratios of the final-product-type molecules. The products are highly underoxidized (high CO, H<sub>2</sub>) and, if burning takes place in air, considerably more energy is released in the flame reaction.

For nitramine propellants--those based on cyclotetramethylenetetranitramine (HMX) or cyclotrimethylenetrinitramine (RDX)--the reaction zone structure and temperatures were not known until just recently.<sup>3</sup> Thermocouple measurements recently reported for inert binder nitramine propellants<sup>4</sup> show that the zone structure is qualitatively identical to that for the nitrate esters. (Measurements have not yet been made for the neat nitramines.) The presence of a dark zone suggests that NO may be present, which in turn may indicate that NO<sub>2</sub> is involved in the fizz zone. In thermal decomposition experiments with HMX and RDX at low temperatures, HCHO and N<sub>2</sub>O are frequently observed as the major products; in other experiments significant amounts of HCN and NO<sub>2</sub> are also observed. Thus there are several possible rate-controlling flame reactions. When burned at low pressure,<sup>5</sup> HMX and RDX produce significant amounts of nonequilibrium products (NO, N<sub>2</sub>O, HCN, HCHO, etc.) in addition to N<sub>2</sub> and the water-gas species (CO, CO<sub>2</sub>, H<sub>2</sub>, H<sub>2</sub>O).

The variation in surface temperature ( $T_s$ ) with burning rate ( $r$ ) should indicate the activation energy ( $E_a$ ) for the surface gasification reaction [ $r \propto \exp(-E_a/RT_s)$ ]. If the rate-controlling process at the surface is dissociation of the O-NO<sub>2</sub> or N-NO<sub>2</sub> bond in the nitrate ester or nitramine, respectively, an  $E_a$  of 35-45 kcal/mole would be expected. Such is apparently not the case. Published  $T_s$  vs  $r$  data for double-base<sup>2,6</sup> propellants suggest an  $E_a$  of about 20 kcal/mole or less. For nitramines, the published data<sup>4</sup> suggest a similarly low value (perhaps 10-15 kcal/mole). These low surface activation energies suggest that something other than nitro group separation is rate controlling at the surface. For the nitramines, this may be vaporization. For double-base propellants, vaporization of NG may lead to a low  $E_a$ , or it may be that NC is not present at the surface.

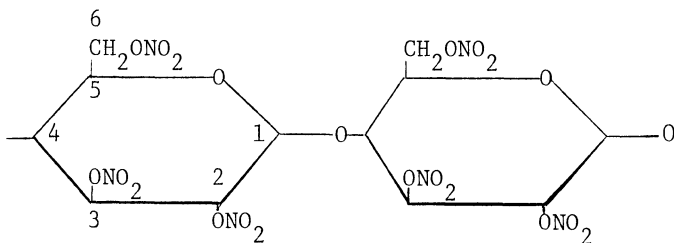
The following review does not cover heterogeneous gas-solid reactions at the propellant surface--a potentially



important effect for which there is, unfortunately, no available experimental data. Binder-nitramine chemical interactions are potentially very important in determining propellant vulnerability,<sup>7</sup> but this area is beyond the scope of this review. Finally, the phenomenon of burning rate "slope breaks" in nitramine propellants will not be discussed, since it appears that the observed burning rate transitions are associated with the composite nature of nitramine propellants (binder-nitramine diffusional flame mixing or nitramine particle ignition delay effects) rather than with specific changes in chemical mechanism with pressure.<sup>3</sup>

### Decomposition of Nitrocellulose

Nitrocellulose is prepared by acid nitration of natural cellulose obtained from either cotton linters or woodpulp. The nitration procedure and, to some extent, the properties of the final product depend on the source of the cellulose. This is because in different celluloses there are differences in impurities, in the relative amounts of amorphous and crystalline regions, and within the crystalline regions in the relative amounts of the two known crystal forms. Typical nitrocelluloses are high-molecular-weight ( $10^5$ - $10^6$  g/mole) polymer chains composed of anhydroglucose units, each containing up to three nitrate groups. Two such units for fully nitrated cellulose are:



Fully nitrated NC is 14.14% nitrogen by weight. For NC containing an average of two nitrate groups per unit, the nitrogen content is about 11.11%. Nitrocelluloses used in propellants commonly are 12-13.2% nitrogen and therefore have a significant number of unnitrated hydroxyl (-OH) groups randomly distributed along the polymer. The preparation and properties of NC are reviewed by Urbanski,<sup>8</sup> who also gives references to a number of the older thermal decomposition studies that cannot be included in this review.

Table 1 Kinetic parameters for nitrate esters

System	Temp. Range, °C	Method	$\log_{10} A$ , $s^{-1}$	$E_a$ kcal/mole	$k$ at 177°C, $s^{-1}$	Ref.
NC	~ 135	Flowing CO <sub>2</sub>	19.30	46.2	$7.3 \cdot 10^{-4}$	9
NC	84-162	Flowing N <sub>2</sub>		46.7		10
NC (in sol)	165-200	Gas evolution	18.0	43.0	$1.3 \cdot 10^{-3}$	11
NC	140-190	I.r. thin film	18.36	44.3	$7.0 \cdot 10^{-4}$	12
NC	140-190	TGA, vac.	17.92 <sup>a</sup>	43.7	$5.0 \cdot 10^{-4}$	12
NC	100-170	Mass Spec, vac.		38.0		13
NC	140-165	DTA	19.0	47.0	$1.5 \cdot 10^{-4}$	14
NC	140-165	DTA	12.0	31.0	$8.8 \cdot 10^{-4}$	14
NC	90-140	Taliani, air		30.7		15
NC	90-140	Taliani, N <sub>2</sub>		37.6		15
NC	180-290	DTA, thin film		41.2		16
NC + NG	~ 170	TGA, air	18.88	45.3	$7.6 \cdot 10^{-4}$	17
NC + NG	~ 212	DTA, air	14.30	35.6	$1.0 \cdot 10^{-3}$	17
NG (gas)	150-160	I.r.	15.51	36.0	$1.0 \cdot 10^{-2}$	18
NG (liq)	150-160	I.r.	20.20	46.9	$2.7 \cdot 10^{-3}$	18
CH <sub>3</sub> ONO <sub>2</sub> (gas)	210-240		15.5	39.8	$1.5 \cdot 10^{-4}$	19
CH <sub>3</sub> CH <sub>2</sub> ONO <sub>2</sub> (gas)	160-210		16.5	39.4	$2.3 \cdot 10^{-3}$	19

<sup>a</sup>Calculated from published data; value quoted (18.95) not consistent with results

### Kinetics of Nitrocellulose Decomposition

Some kinetic parameters for NC are shown in Table 1, together with some results for methyl and ethyl nitrate and nitroglycerin. Activation energies for NC range from 31-47 kcal/mole, but generally fall in the 44-47 kcal/mole range when care is taken to avoid product acceleration ("auto-catalysis"). A thorough study was conducted by Phillips, Orlich, and Steinberger.<sup>12</sup> They decomposed thin (~ 3  $\mu$ m) films of NC (11.01-13.96% N) in a vacuum and measured the rate constant both from weight loss and from the disappearance and appearance of infrared (i.r.) bands.

The effects of film thickness, pressure, and stabilizers were also investigated. The rate constants for almost fully

nitrate (13.96% N) NC (Table 1) were almost two times larger than those for a partially nitrated (11.01% N) sample, and exhibited a short period of somewhat slower decomposition early in the degradation. The turn-of-the-century results of Will<sup>9</sup> are in excellent agreement with those of Phillips, as are also the TGA results of Eisenreich<sup>17</sup> for a double-base propellant after NG evaporation.

The published  $E_a$  and pre-exponential factors ( $A$ ) for nitrocellulose are somewhat higher than expected, and no satisfactory explanation for this has been put forward in the literature. Gaseous methyl and ethyl nitrate (Table 1) exhibit "normal" kinetic parameters: the observed activation energies (39-40 kcal/mole) are quite close to the O-NO<sub>2</sub> bond dissociation energies, and  $\log_{10}A$  (15.5-16.5) is in the normal range for a unimolecular dissociation. For NC,  $E_a$  should be even lower than for the gaseous nitrates, since the stability of a nitrate group is decreased if there is another nitrate group in the vicinal position. An  $E_a$  of perhaps 35-38 kcal/mole would therefore seem reasonable rather than the observed 43-47 kcal/mole. This, plus the low NO<sub>2</sub> yields observed in many studies, has led some investigators<sup>20,21</sup> to conclude that some process other than O-NO<sub>2</sub> bond breaking must be involved in the primary dissociation step.

An "autocatalytic" (product acceleration) process would not explain these results, since "autocatalytic" effects generally tend to give low rather than high  $A$  and  $E_a$ . For example, Manelis et al.<sup>14</sup> report  $E_a = 31$ ,  $\log_{10}A = 12$  for NC under autocatalytic conditions. A chain reaction initiated by O-NO<sub>2</sub> bond breaking might produce a large  $A$  factor if the chain length were long, but probably would not produce an overall  $E_a$  larger than that of the rate-determining step in the sequence.

A simple explanation for the unusual kinetic parameters of NC appears to have been overlooked and is proposed here. This is that the condensed-phase reaction is inhibited by NO<sub>2</sub> with the inhibition decreasing with increasing temperature. Mobility is severely limited for the newly formed NO<sub>2</sub> molecule in the solid; most of the time it will recombine to regenerate the nitrate group. (This apparently must occur in a time scale short compared to the lifetime of the radical produced in the initial dissociation.) The result is that the measured reaction rate is slower than the rate at which dissociation is occurring. With increasing temperature, the inhibiting effect of the recombination reaction diminishes, due to increased mobility with increasing temperature and/or the expected tendency with increasing temperature for the NO<sub>2</sub> to undergo an oxidation-reduction

reaction rather than a recombination reaction.<sup>22</sup> (Recombination reactions have lower  $E_a$  than other types of reaction; in the gas phase they frequently have negative  $E_a$ .) The net result is that the reaction has a large apparent activation energy, which in turn necessitates a high-frequency factor to account for the experimentally measured rate. Waring and Krastins<sup>18</sup> suggested such an autoinhibition mechanism to explain their results for nitroglycerin, which they found decomposed more slowly in the liquid phase than in the gas phase, with liquid-phase apparent  $E_a$  and  $A$  much higher than for the gas-phase decomposition (see Table 1).

The proposed effect is equivalent to what is known as the "cage effect" and has been observed for many reactions in solution. Koenig and Fischer<sup>23</sup> have reviewed the experimental evidence for, and theoretical treatment of, "cage effects." As will be shown below, this hypothesis also explains the phase-dependent (solid/liquid/solution/gas) rate constants of the nitramines HMX and RDX.

The explanation proposed above for the unusual kinetic parameters for NC explains as well the solution-phase results of Smith<sup>11</sup> for decomposition of a 1% solution of NC in 1-chloro-2,4-dinitrobenzene (Table 1). At 177°C (450K), the rate measured by Smith is twice as high as calculated from the expressions of Will<sup>9</sup> and Phillips et al.<sup>12</sup> for solid NC. Also the  $E_a$  (43) and  $\log_{10}A$  (18) in solution are somewhat lower than for the solid. This is as would be expected for the proposed mechanism, since mobility is higher in solution than in the solid phase and the  $NO_2$  formed by dissociation is less likely to undergo recombination.

The practical implications of the proposed mechanism are quite important: the rate expressions determined at ~160°C for NC may seriously overestimate the rate of reaction if extrapolated to propellant burning surface temperatures (e.g., 320-400°C). For example, for nitroglycerin at 377°C (650K), the rate constant predicted for the liquid ( $2.7 \times 10^4 \text{ s}^{-1}$ ) is more than an order of magnitude higher than for the gas ( $2.5 \times 10^3 \text{ s}^{-1}$ ). In fact, however, inhibition would be expected to cease at some intermediate temperature and the high-temperature liquid decomposition would then have a low  $A$  and  $E_a$  like those for the gas phase. Since there are no data available for gaseous NC, the rate constant for the high-temperature uninhibited reaction must be considered to be unknown.

### Products and Mechanism of Nitrocellulose Decomposition

Most attempts to determine the decomposition pathway of NC have involved determination of the gaseous products formed

during decomposition. Very little has been learned in this way. Apparently, many condensed-phase reactions occur between the initial dissociation reaction and the appearance of gaseous species. Thus, for example, even when thin films (e.g., 5  $\mu\text{m}$ ) of NC are decomposed slowly in a vacuum, the observed gaseous products consist mostly of final-product-type molecules: CO, CO<sub>2</sub>, and H<sub>2</sub>O plus smaller amounts of H<sub>2</sub> and N<sub>2</sub>. In addition, large amounts of nitric oxide (NO) are usually observed, along with lesser amounts of N<sub>2</sub>O, HCN, HCHO, (CHO)<sub>2</sub>, plus trace amounts of various hydrocarbon and CHO species. A few investigators observe NO<sub>2</sub>.

The nitrate esters are generally assumed to dissociate by rupture of one of the O-NO<sub>2</sub> bonds to form NO<sub>2</sub> and an alkoxy radical. The failure of some investigators to observe NO<sub>2</sub> has led them to question this assumption. For example, Dauerman and Tajima<sup>20</sup> and Tranchant<sup>21</sup> observed no NO<sub>2</sub> during vacuum decomposition of NC. Juhasz and Rocchio<sup>24</sup> observed no NO<sub>2</sub> during studies of the pyrolysis of NC at high heating rates (10<sup>4</sup> deg/s), but did not expect NO<sub>2</sub> to survive the chromatographic column used to separate the gases prior to mass spectrometric identification. In other studies, no analysis for NO<sub>2</sub> is reported.

Taken as a whole, however, the literature indicates that considerable amounts of NO<sub>2</sub> can be observed during NC decomposition under the right experimental conditions. Unlike Dauerman,<sup>20</sup> both Mal'chevskii et al.<sup>13</sup> and Farber and Strivastava<sup>25</sup> have observed large amounts of NO<sub>2</sub> using time-of-flight mass spectrometric analysis for NC decomposed in a vacuum. Rideal and Robertson<sup>26</sup> obtained 10.1% NO<sub>2</sub> (plus 37.2% NO, 9.9% N<sub>2</sub>, and 5.4% N<sub>2</sub>O) in the gaseous products for NC (only 10.3% N) decomposed in a vacuum at 160°C. Lengellé et al.<sup>27</sup> found 28.3% NO<sub>2</sub> (plus 10.3% NO) for a double-base propellant decomposed rapidly in a vacuum by being pressed against a metal plate electrically heated to 300°C, simulating a burning surface temperature. By using highly nitrated (14.0% N) NC and very small extents of weight losses (~4%), Gelernter et al.<sup>28</sup> were able to observe NO<sub>2</sub>/NO ratios as high as 2 for decomposition of NC at about 150°C in a current of cold inert gas. Bent and Crawford<sup>29</sup> also obtained evidence for NO<sub>2</sub> formation for NC decomposed in potassium halide pressed disks.

Actually, the experimental conditions necessary to prevent the disappearance of NO<sub>2</sub> in secondary reactions were elucidated long ago by Robertson and Napper.<sup>30</sup> Using relatively large (2 g) samples of NC (13.1% N) at 135°C, approximately 40% of the nitrogen was obtained as NO<sub>2</sub> when the gaseous products were removed in a stream of CO<sub>2</sub>. Experiments

were also carried out in a stationary atmosphere of  $\text{CO}_2$  and in a vacuum, giving values of about 15 and 25%, respectively. Flowing  $\text{CO}_2$  was considered to be more effective than a vacuum because it minimized diffusion of the  $\text{NO}_2$  back into the heated NC (it would also minimize contact of the decomposition gases with the heated wall surfaces near the sample). Robertson also showed that traces of liquid (but not gaseous) water dramatically decreased the amount of  $\text{NO}_2$  observed.

Thus, there appears to be little question that  $\text{NO}_2$  is produced in large amounts during decomposition of nitrocellulose, but the amount observed is very sensitive to experimental conditions. Decomposition in a stream of cold inert gas seems to be more effective than vacuum techniques in preventing secondary reactions. It is not clear whether the reactions which remove  $\text{NO}_2$  are gas-phase reactions or heterogeneous reactions between gaseous products and nitrocellulose. Small sample size, low decomposition temperature, and small extent of reaction all promote a high  $\text{NO}_2$  yield.

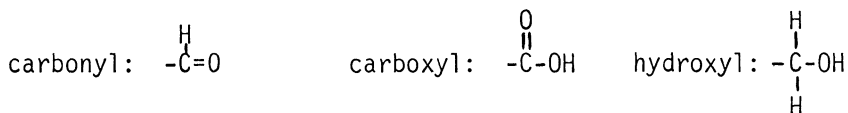
Although the observed gaseous decomposition products do not provide much insight concerning the reactions that follow the initial rupture of the O- $\text{NO}_2$  bond, there is considerable evidence that the secondary reactions in the condensed phase do not lead immediately to degradation of the glucose ring into gaseous species. For example, for small extent of reaction of highly nitrated samples, Gelernter et al.<sup>28</sup> found that the  $\text{NO}_2$  (plus NO) liberated accounted for almost all of the observed weight loss, i.e., very little CO,  $\text{CO}_2$ , and other volatiles were liberated. This indicates that the alkoxy radical produced in the initial dissociation reacts or rearranges in such a way that a stable solid species remains. Similarly, Manelis et al.<sup>14</sup> found that at the lower temperatures the rate constant deduced from heat liberation was higher than that derived from weight loss, indicating that exothermic reactions unaccompanied by weight loss (gas evolution) take place early in the decomposition.

Much more can be learned by residue analysis for partially decomposed samples and by experiments with isotopically tagged nitrocellulose. From infrared spectra, both Phillips et al.<sup>12</sup> and Gelernter et al.<sup>28</sup> found that one carbonyl group forms in the solid for each nitrate group lost. This is consistent with the generally accepted view that aldehydes and ketones result from O- $\text{NO}_2$  bond fission. Gelernter, however, also observed some hydroxyl, suggesting some abstraction by the intermediate alkoxy radical. Gelernter et al. performed experiments with partially nitrated NC tagged with  $^{15}\text{N}$  on the sixth carbon atom of the glucoside unit. The amount of  $^{15}\text{N}$  in the gaseous decomposition products was lower

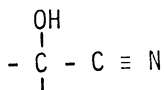
than in the starting material and increased with time, indicating that the nitrate groups on carbon atoms 2 and 3 are less stable than the one on carbon 6 and therefore dissociate earlier in the decomposition sequence.

Wolfrom et al. have published a series of papers<sup>31</sup> describing extensive studies of the products formed during burning of nitrocellulose at reduced pressure (2-300 Torr). These experiments involved analysis of solid and liquid decomposition residues, as well as analysis of volatile products from samples isotopically labeled with <sup>14</sup>C at different carbon atoms in the glucoside ring. Only a few of the findings of these experiments can be detailed here.

When ignited at 2-3 Torr,<sup>31a</sup> the nitrocellulose (12.6% N) produced an amorphous solid residue in good yield (~50%). This was identified as a fragmented oxycellulose nitrate (~9% N) consisting of still-intact glucose rings as well as glucose units apparently broken between C2 and C3 by sequential elimination of two NO<sub>2</sub> molecules, the resulting radical sites being stabilized by formation of carbonyl (i.e., aldehyde) groups. The residue also contained carboxyl and hydroxyl

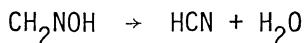


groups, suggesting some alkoxy radical stabilization by H-atom transfer. At somewhat higher pressures<sup>31b,c</sup> a liquid mixture formed, being produced in greatest amounts at ~30 Torr. The main components of this liquid were water, formic acid (HCOOH), formaldehyde, and glyoxal (CHOCHO),<sup>31b</sup> plus minor amounts of other carbonyl and carboxyl compounds including acetone, acetaldehyde, acrolein, ethyl acetate, and others.<sup>31g</sup> A triose (phenylosazone) and glyceraldehyde were also detected. The gases produced under these conditions consisted of CO, CO<sub>2</sub>, NO, N<sub>2</sub>O, NO<sub>2</sub>, and HCN.<sup>31c</sup> Nitrogen was observed in the condensable products only in the form of α-hydroxynitriles



and dissolve cyanide (-C≡N). The nitriles apparently resulted from reactions of CN with carbonyl compounds, possibly in the gas phase. The total yield of triple-bound carbon-nitrogen was independent of pressure (2-300 Torr), suggesting that the cyano group forms early in the ignition process and is stable once formed. Its formation is difficult to explain. Wolfrom suggested<sup>31c</sup> that it might result from dissociation of for-

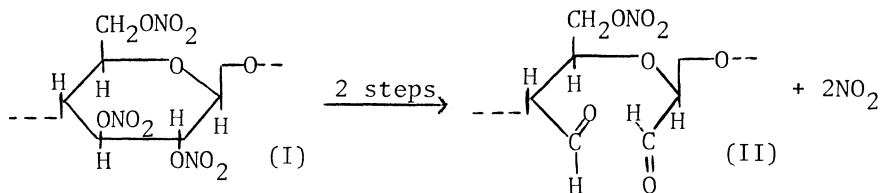
maldehyde oximine



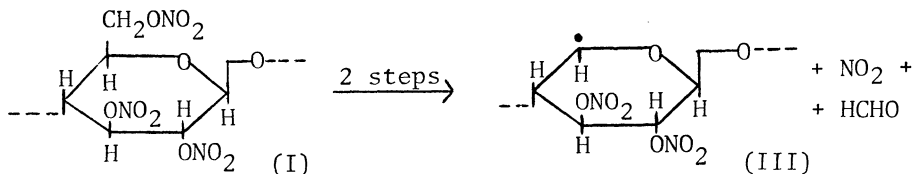
In other experiments,<sup>31d,e</sup> Wolfrom et al. analyzed the radioactive content of the volatile ignition products of nitrocellulose labeled with  $^{14}\text{C}$  at either the C1 and C6<sup>31d</sup> or the C2 and C5<sup>31e</sup> positions. These experiments indicated that formaldehyde is produced mainly from C6, glyoxal mainly from C2 and one of its neighbors (largely C1), and carbon dioxide and formic acid mainly from C1 and to a lesser extent from C2-C5.

Other potentially valuable experiments with labeled NC can be proposed. For example, since the oxygen of the alcohol groups is not eliminated during nitration of cellulose,<sup>32</sup> samples of NC prepared from an  $^{18}\text{O}$ -enriched sulfuric acid-nitric acid-water mixture will have nitrate groups in which only two of the three nitrate oxygens are  $^{18}\text{O}$  enriched. Thermal decomposition studies using samples tagged in this way would undoubtedly provide additional information about the decomposition mechanism--for example, which products contain oxygen derived from  $\text{NO}_2$  oxidation-reduction reactions.

Unfortunately, the sequence of reactions is probably so complex that it is unlikely that the total mechanism leading to gaseous products will ever be completely understood. Different glucose units in the NC polymer may break down by different pathways, both because initial bond breaking can occur at any of three sites and because the resulting alkoxy radical can be stabilized in a number of different and possibly competing ways. There is good evidence that the breaking of one of the  $\text{O}-\text{NO}_2$  bonds is the first step and that this may be followed by elimination of the adjacent  $\text{NO}_2$  and breaking of the C2-C3 bond, e.g.,

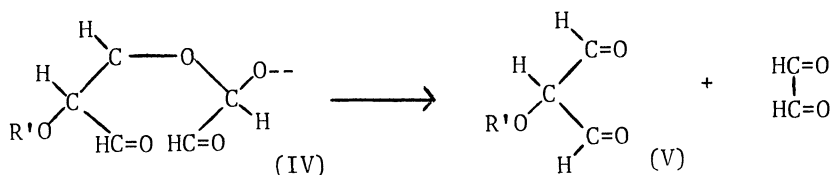


Alternatively, or subsequently, cleavage of the  $\text{O}-\text{NO}_2$  bond at C6 could occur, followed by elimination of formaldehyde, e.g.,





If both processes were to occur in the same glucose unit, a radical would result that could rearrange with chain cleavage to give glyoxal, e.g.,



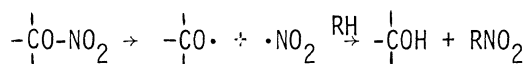
However, any of the three alkoxy radical sites in this scheme could also form a hydroxyl group and/or the radical site in IV could also be stabilized by H-atom addition to C5, changing the subsequent course of the decomposition. If an H-atom were to be removed from C1, chain breaking could occur with formation of a carboxyl group at C1. (All these and other possible reactions are discussed by Wolfrom.<sup>31a,b</sup>) Furthermore it is not known which of the larger condensed-phase fragments might be attacked by NO<sub>2</sub>. The number of possible schemes that can be written is almost unlimited, and any proposed mechanism involving reactions beyond the first step or two is little more than speculation. This situation is unlikely to improve unless rapid diagnostic techniques can be devised to monitor condensed-phase reactions as they occur.

#### Plasticizers and Stabilizers in Nitrocellulose Decomposition

Double-base propellants contain, in addition to NC, nitroglycerin (NG) plasticizer and various stabilizers, and it is important to determine what effect these have on the thermal decomposition of NC. Korobeinichev and Khlevnoi<sup>33</sup> have decomposed a double-base propellant in the ion source ( $P = 10^{-5}$  Torr) of a time-of flight mass spectrometer. At 170–200°C the mass peaks observed corresponded to those due to electron fragmentation of NG, and only at higher temperatures were NC decomposition products observed along with the NG. This suggests that the primary process in the propellant is not dissociation of the NC, but evaporation of the plasticizer. (Phillips<sup>34</sup> had already suggested that the large 46/30 peak ratio reported by Dauerman et al.<sup>35</sup> was not, as claimed by Dauerman, evidence of NO<sub>3</sub> formation, but rather due to vaporization of NG from the propellant.) Using pulsed heating thermogravimetric techniques, Aleksandrov and Khlevnoi<sup>36</sup> measured the evaporation rate of volatiles from a double-base propellant as a function of sample thickness. Half times as short as 0.1 s were measured for the thinnest samples ( $\sim 1 \mu\text{m}$ ) at the highest temperatures (200–210°C) where

NC decomposition did not affect the measurements. A rate law for the diffusion controlled evaporation was derived with an "activation energy" of 13.6 kcal/mole. [Eisenreich and Pfeil<sup>17</sup> have recently reported a similar value (13.8 kcal/mole)]. Aleksandrov and Khlevnoi concluded that there must be a very thin layer (thinner than the thermal wave) of NG-free NC at the surface of the propellant, enabling the surface temperature (>300°C) to be much higher than the boiling temperature of the volatiles (~200-230°C). These ideas differ from those of Koval'skii et al.,<sup>37</sup> who suggested that, although the burning rate at low pressure is controlled by condensed-phase reactions, the surface temperature is determined by the boiling point of the volatiles. This was based on their observation that 1)  $T_s$  was largely independent of initial propellant temperature, and 2) a plot of  $\log P$  vs  $1/T_s$  gave a slope corresponding to a heat of vaporization of 26 kcal/mole, only a few kcal/mole higher than expected for NG evaporation.

Thus, nitroglycerin seems to vaporize from NC before decomposition (at least in most thermal decomposition experiments if not during burning) and there is no information available concerning what effect, if any, NG might have on the kinetics or mechanism of nitrocellulose decomposition. Such is not the case with the stabilizers commonly added to NC-based propellants to improve storage life. Stabilizers are believed to react with the small amounts of  $\text{NO}_2$  liberated from NC, and by so doing prevent further degradation of the polymer via oxidation by the free  $\text{NO}_2$  ("autocatalysis"). For example, Frey<sup>38</sup> found that after storage some of the diphenylamine stabilizer in a propellant is converted into N-nitrosodiphenylamine, as well as the mono-, di-, and trinitrodiphenylamines. Aleksandrov and Bufetov<sup>39</sup> report a twofold increase in the heat release rate (180-280°C) for a propellant containing centralite stabilizer, with no increase in the apparent activation energy. Stabilizers that form nitro compounds would in general release a hydrogen atom in the process. This hydrogen atom might then stabilize the radical produced by converting it to a hydroxyl group, e.g.,



Sollott and Einberg<sup>40</sup> have performed extensive tests to determine the types of molecules that make the best stabilizers.

## Chapter 5

### Solid-Propellant Ignition Theories and Experiments

Clarke E. Hermance\*

*University of Waterloo, Ontario, Canada*

#### Abstract

The experimental and theoretical literature pertaining to the ignition of solid propellants over the period 1966-1980 is reviewed. The purpose is to present a cohesive description and evaluation of the research in solid-propellant ignition to date. Experimental research papers are reviewed first, then the theoretical papers are introduced; finally a summary is presented. As a result it seems clear that, while previously detailed experimental work was required, it now appears that further theory is necessary. It is finally evident, however, that the establishment of a sustained exothermic reaction in the gas phase is a necessary condition for the ignition of both homogeneous and composite propellants. Finally, needed experimental and theoretical research is indicated.

#### Nomenclature

A	= nondimensional heat release parameter
a	= $(\rho\lambda/c)$ or $\rho^{2D}$
B	= nondimensional heat absorption (endothermicity) parameter
b	= constant
C	= concentration, $\text{kg/m}^3$

---

Copyright © American Institute of Aeronautics and Astronautics, Inc. 1982. All rights reserved.

\*Professor, Department of Mechanical Engineering (presently with University of Vermont, Burlington).

$c, c'$	= specific heat, J/kg·K
$D$	= mass diffusivity, m <sup>2</sup> /s
$E$	= activation energy, J/kg·mole·K
$E', E''$	= dimensionless activation energies; $E/RT_0$ , $E_g/RT_0$
$F$	= operator, $\partial/\partial\tau - \partial^2/\partial\tau$
$G$	= operator, $\partial/\partial\tau - V\partial/\partial\xi - \partial^2/\partial\xi^2$
$H$	= operator, $\partial/\partial\tau - V\partial/\partial\xi - \partial^2/\partial\xi^2$
$h$	= enthalpy, J/kg
$I'$	= radiant flux, J/m <sup>2</sup> ·s
$I$	= radiant flux parameter, m
$L, L^*$	= ignition criterion indicator
$n$	= reaction order or stoichiometry coefficient
$P$	= pressure, Pa
$Q$	= heat of reaction, absolute value, J/kg or dimensionless equivalent
$q$	= heat flux (external), J/m <sup>2</sup> ·s
$R$	= universal gas constant
$r$	= solid phase regression rate, m/s
$T$	= temperature, K
$t$	= time, often dimensionless
$U$	= nondimensional velocity, + X direction
$v$	= dimensionless similarity parameter
$W$	= nondimensional Arrhenius rate function
$X$	= mole fraction
$x$	= distance, dimensionless
$Y$	= mass fraction
$Z$	= Arrhenius pre-exponential factor, appropriate units
$\alpha$	= dimensionless parameter, defined in text, p
$\alpha'$	= thermal diffusivity, m <sup>2</sup> /s
$\Gamma$	= thermal responsivity, $(\lambda\rho c)^{1/2}$ , ratio: gas to solid
$\gamma$	= dimensionless parameter, defined in text, p
$\Delta$	= dimensionless parameter
$\delta$	= $\theta c/E'$ , dimensionless parameter
$\epsilon$	= fraction reacted, dimensionless ratio
$\eta$	= dimensionless length variable; or space/time similarity variable
$\theta$	= dimensionless temperature, $T/T_0$ or $(T-T_0)/T_0$
$\lambda$	= thermal conductivity, J/m·s·K
$\mu$	= dimensionless extinction coefficient
$\xi$	= dimensionless space variable, $\xi = qx/\lambda T_0$
$\rho$	= density
$\sigma$	= dimensionless time
$\tau$	= dimensionless time, $= t'q/\lambda\rho cT_0^2$
$\phi$	= dimensionless temperature difference, or $RT/E$
$\psi$	= dimensionless temperature difference
$\omega$	= symbol for $\exp(-x)$
$\Omega$	= dimensionless heat flux

Subscripts

c	=	critical
e	=	external, applied
exp	=	experimental
f	=	fuel
g	=	gaseous
i	=	specie or substance
j	=	jump value
o	=	initial, input
s	=	solid
os	=	on the surface
ox	=	oxidizer
ss	=	steady state
$\tau, \xi$	=	partial derivative taken with respect to

Superscripts

'	=	a dimensional, real, quantity
*	=	ignition, when some specified criterion satisfied
$\wedge$	=	stretched coordinate

## Introduction

Solid propellants are complicated systems in any aspect of combustion that may be of interest, as a casual thumbing through the contents of this volume easily reveals. Quite naturally, there is a tendency for the investigator of some aspect of solid-propellant combustion to simplify the characterization of the process or the propellant in some manner that retains the essential characteristics of interest and homogenizes the rest. The applicability of the results of this selective characterization depends to a large extent on the ability of the modeler--whether experimentalist or theoretician--to make the appropriate selection of essential characteristics. Solid-propellant ignition theories and experiments are rife with such selection processes. This paper attempts a cohesive description and evaluation of the selections made by various investigators.

Ignition of solid propellants is the process occurring between the initial application of some energetic stimulus to a quiescent chunk of propellant and the full-scale combustion of the propellant. The term "ignition" is used commonly in two ways: 1) the process of achieving full-scale combustion, and 2) the point in time at which sufficiently full-scale combustion is deemed to occur. Ignition of the propellant is thus a transient process with a definite point of initiation

but an endpoint that depends completely upon the definition of that endpoint. Intrinsic to ignition is an energetic stimulus that may be chemical, thermal, or even photochemical. But whatever the form of the stimulus, transient thermal processes involving net exothermic chemical reactions, together with transient diffusional and chemical changes in reactant concentration, are inherent in the ignition process and are necessary for ignition to be achieved. The total ignition process of propellants therefore involves a transition from a nonreactive to reactive state via some thermochemical "runaway" (on a time scale), followed by an essentially equally rapid transition to full-scale combustion. Virtually all studies of solid-propellant ignition are concerned with the time required for the thermal "runaway" to occur and the mechanism (or sequence of them) responsible.

Interpretive difficulties are possible, therefore, between what "ignition" means among practical systems and most of the theoretical models and experiments to be described. These difficulties are recognized, but whether they are resolved in the various theories and experiments in a manner satisfactory to practical situations frequently depends on the intent of the investigator and the degree of involvement with practical engineering. In the practical sense, ignition means that full-scale combustion was achieved and the time required as a function of igniter type is of interest and is determined experimentally in the practical configuration. Usually the ignition stimulus is not very uniform or known precisely from point to point. If the results are not satisfactory, changes are attempted on the basis of what is known or imagined about the solid-propellant ignition process. It is here that theories and experiments on the ignition of solid propellants under as controlled conditions as possible are supposed to help.

The theories attempt definition of the correct (controlling) set of physicochemical processes responsible for thermal runaway under some defined stimulus, calculation of the time required for runaway to occur, and dependence of this time upon macroscopic system parameters such as pressure, gas velocity, temperature, etc. Thermal runaway is usually defined in terms of some temporal temperature behavior. The experiments, on the other hand, usually determine some aspect of "did ignition--implying complete burn-out of the sample--occur or not" (i.e., some sort of "go/no-go" criterion) under controlled conditions of macroscopic parameters such as propellant composition, pressure, heat flux, flow velocity, flow temperature, and environmental chemical and physical composition. The experiment may also simultaneously measure some observable aspect of the development of thermal runaway. Due to time scale requirements and (often) small sample sizes, it is

usually optical aspects that are observed by recording a light emission vs time history via photocells and/or high-speed cinephotography. Ignition is often said to have occurred when some optically gathered information is of sufficient magnitude as interpreted by the experimenter, a logical enough procedure in most cases. But there is no unambiguous link between temporal light generation, temporal temperature behavior, and the actual state of combustion! Therefore interpretations are required in both experiment and theory. The situation may be less ambiguous when surfaces are examined for i.r. emission during an experiment. Although such an experiment may be "contaminated" by i.r. emission from gases within the optical path, a close link between temporal i.r. emission and temporal surface temperature behavior is possible, although the actual measured temperature value may be in error due to uncertainties in surface emissivity. Further possible interpretative difficulties are generated between the scientific theory/experiment package and the practical case because the practical case may depend upon phenomena not considered in the theory/experiment. Possibilities are propellant cracks or roughness, local regions of high igniter gas shear flow, igniter generated particles, and the combination of "spotty" ignition sites and their joining by flame-spreading processes.

In view of the complexity of the propellant and the interpretive problems mentioned above, a rather remarkable amount of understanding has been developed concerning solid-propellant ignition at the present time. This is due to a number of detailed, ingenious experiments and measurements, some careful theoretical modeling covering a wide variety of thermal runaway sites and mechanisms, computers, and some inspired mathematical analysis.

Historically, openly published theories of solid-propellant ignition appear to start in 1950 with Frazier and Hicks.<sup>1</sup> Altman and Grant<sup>2</sup> reported in 1953 on composite-propellant samples ignited by a hot wire through the sample and a correlation based on an ignition temperature assuming the propellant acted like heated inert material. B.L. Hicks<sup>3</sup> reported in 1954 on numerical solutions where the propellant was treated as a homogeneous reactive solid subjected to surface heating. Double-base propellants were thus viewed as igniting due to solid-phase exothermic reactions. Composite propellants, constructed from ammonium perchlorate oxidizer crystals imbedded in a matrix of a rubber or other polymer, seemed unlikely candidates for an ignition concept entirely based on exothermic condensed-phase reactions. Thus, investigations were directed toward models supporting a pressure sensitivity and exothermic gas-phase reactions.

By 1960, McAlevy, Cowan, and Summerfield<sup>4</sup> reported on ignition experiments involving composite propellants igniting after exposure to stagnant reflected shock conditions in a shock tube, and presented the seminal ignition model of propellants governed by gas-phase processes. Shortly afterward similar experimental results were reported by McAlevy and Summerfield<sup>5</sup> for double-base propellants. Thereafter, a sequence of studies at Princeton University was reported<sup>6,7</sup> that described a numerical solution of equations describing a "gas-phase" ignition model of a solid fuel which decomposed upon sudden contact with a hot stagnant atmosphere containing an oxidizer. The solid fuel represented the fuel binder used in composite propellants; the fuel and oxidizer vapors were mixed by counter-diffusion with simultaneous second-order chemical reaction occurring. Eventually there was sufficient exothermic reaction to produce a marked local maximum temperature in the gas phase and ignition was defined in terms of the maximum temperature reaching a specified value. The model suffered notable deficiencies. Only a fuel was treated, not a propellant, and the solid/gas interface was assumed to have a constant temperature.

During the period 1962 to 1964 a third body of theory and experiments was developed at the United Technology Center and reported,<sup>8-12</sup> evolving from studies in which the ignition stimulus was provided by a chemical attack/exothermic reaction on the propellant surface by powerful oxidizing gases such as fluorine. This "hypergolic" model took the usual one-dimensional form of the "solid-phase" and "gas-phase" theories and considered transient gas-phase diffusion of chemical reactants and products with simultaneous heat conduction in the gas and solid phases. Exothermic chemical reaction was present only at the solid/gas interface. No externally added heat flux was considered, or at least presented in any detail.

Both the "gas-phase" and "hypergolic" theories demonstrated a decreased ignition delay with increased oxidizer concentration in the gas phase, and strong effects of pressure ( $t^* \approx P^{-1.7}$  typically). At that time the hypergolic model predicted oxidizer mole fraction effects at constant pressure more closely resembling experimental data ( $t^* \exp \approx (Y_{Ox})^{-2.2}$  typically), providing a first-order surface reaction was assumed in the theory, than did the gas-phase theory, but there was considerable debate whether gaseous oxygen could react with polymeric-type solid fuels in a hypergolic surface reaction and have such fuels still behave as they do under ambient Earth environments. In addition, neither theory explained the ignition of composite propellants in chemically inert atmospheres. Thus, both theories remained alive and kicking despite their deficiencies, and quite natur-



ally, a "heterogeneous" theory arose from the hypergolic theory<sup>4,11</sup> on a heuristic basis. In this theory it was argued that under inert atmosphere conditions the heating of the ammonium perchlorate oxidizer caused it to decompose, producing anhydrous perchloric acid which then attacked the surrounding fuel in a hypergolic manner. No detailed analytical representation of this theory was presented, however.

Further experiments in solid-propellant ignition proceeded apace while theorists argued. Experimental studies on ignition by convective fluxes<sup>13-15</sup> were reported, indicating heat flux and pressure effects on the ignition delay of both composite and double-base propellants. Experimental studies using radiant energy were also reported<sup>16-18</sup> showing similar effects.

An outstanding discussion of the state-of-the-art in solid-propellant ignition theories as of 1965/6 and their relationship to each other and to experiments was given by Price et al. in Ref. 19. Price and his colleagues examined each theory in detail, pointing out strengths, weaknesses, and properties, and presented an extensive compilation of work done on the solid-phase ignition theory for a solid propellant treated as a homogeneous reactive solid. Further background in thermal ignition theory in general can be found in the review by Merzhanov and Averson<sup>20</sup> which contains comprehensive compilation and discussion of work done in thermal ignition analysis, utilizing numerical and classical methods of analysis based on the pioneering work of Frank-Kamenetskii.<sup>21</sup>

Our present goal is to review the experimental and theoretical work done in solid-propellant ignition since circa 1966, a formidable task in view of the excellence and complexity of the work done, and the standards set by the reviews of Price et al. and Merzhanov and Averson. The work after that discussed by Price et al. shall be termed "recent" for the purposes of this paper.

It is worthwhile to summarize several comments by Price et al. regarding theoretical and experimental work in solid-propellant ignition required in their future, and to keep them in mind as we review the work of the last fifteen years. There were pleas for: 1) development of the gas-phase theory to include the case when all gas-phase reactants originate from the decomposition of a single ingredient and determine the effect of external gas-phase pressure and composition on the ignition delay, and of ignition stimulated by an externally applied heat flux, i.e., a radiant heat input; 2) general development of all theories using consistent representations of initiating stimuli and the development of experiments consistent with these stimuli and the models; 3) development

of all theories with the same external environmental temperature, pressure, and heating mode--particularly an imposed, controlled, constant heating mode as approximated by arc-image experiments of the time; 4) theoretical treatment, model-by-model, for the case when the external heating is of some duration less than the observed ignition delay; and 5) the development and use in all cases of consistent ignition criteria, preferably one bearing some clear relationship to experimentally determinable events or characteristics. Price et al. succinctly gave the reason for these pleas: "so that a combination of theory and matching laboratory experiments will, in the future, permit identification of the controlling steps in ignition of real propellants; show how these steps change as a function of propellant, environment, and ignition stimulus; and how these changes should be allowed for in ignition system design."

### Radiant Energy Ignition Sources

By far the greatest amount of recent work in solid-propellant ignition both in quantity and in internal detail has used radiant energy as the stimulus for ignition. The basic reason is the ability to select the heat flux applied to the propellant independently of all other environmental parameters: namely pressure, initial temperature, and chemical composition of the gas phase surrounding the propellant surface being heated. In view of the cacaphony generated by proponents of various ignition theories, this property of radiant ignition experiments gave promise of allowing the experimentalists to conduct the diagnostic experiments that were greatly needed. To a reasonable degree the promise has been realized.

Consider for a moment the other alternatives for heating. In the shock reflection, stagnant heating case,<sup>4-7</sup> the jump temperature of the solid/gas interface is pressure dependent and the test pressure and gas temperature are not independently variable. Thus, the conductive heat input cannot be selected independently of other gas-phase parameters. If a shock tunnel<sup>13-15</sup> is used instead, aerodynamic factors immediately arise in addition to those problems just mentioned. These introduce problems in test sample geometry to insure "nice" laminar (or turbulent) flow, remove the boon of one-dimensionality for any modeling that may be done, and cause the heat flux to be nonuniform in the flow direction. These are formidable problems. If one goes to more practically aligned or "igniter" types of stimuli, control of gas composition is lost in addition to the problems induced by flow, and other effects such as hot particles and time unsteadiness may arise. And finally, other configurations, such as hot plates and

muffle furnaces, remove the possibility of the desired rapid (small) ignition time scale required for any pretense of the research having anything to do with practical rocket ignition systems.

By removing most of the above problems, the radiant energy input experiment is attractive even though new problems are introduced and have to be dealt with. The two major ones, making radiant stimuli greatly different from most practical ignition situations are: 1) the absence of a hot gas adjacent to the igniting propellant surfaces; and 2) the general introduction of interior, as well as surface, heating of the propellant sample due to the nonopaque nature of the majority of solid propellants. A third problem, of a possibly more minor character, is the relative slowness of the rate of surface temperature rise compared to practical and shock tube ignition stimuli.

There was early recognition and evaluation of the problems associated with radiant ignition studies, see Ohlemiller and Summerfield.<sup>25</sup> Furnace<sup>16</sup> and arc-image experiments<sup>17</sup> on composite propellant ignition were already published and this method became well established indeed. The desired diagnostic experiments began to flow increasingly.

Rosser, Fishman, and Wise<sup>26</sup> ignited pressed pellets of ammonium perchlorate (AP), with and without catalysts, and polyethylene pellets, over a range of pressures and heat flux in  $N_2$  and He atmospheres. Results were reported in terms of required exposure time (a go/no-go criteria) as a function of pressure, or peak calculated (inert heating<sup>+</sup>) surface temperature vs flux, parametrically with atmosphere composition in both cases. In subsidiary experiments, the authors investigated the possibility of extensive solid-phase decomposition of the AP prior to their observed ignition, using subsurface thermocouples. From these data, kinetic arguments, and their main test results regarding the effect of the external atmosphere compositions, it was concluded that catastrophic solid-phase decomposition does not precede their observed ignition, which was dominated by gas-phase processes.

In a subsequent study, Fishman<sup>29</sup> studied a model AP/PBAN/carbon black propellant in an  $N_2$  atmosphere with an arc-image furnace using go/no-go methods. He observed that up

---

<sup>+</sup>"Inert heating" means the heating of a nonreactive solid by the applied flux with or without in-depth absorption of energy accounted for, assuming a constant energy input and heat conduction in the solid. For this model, surface temperatures can be calculated as a function of time (see Ref. 27 for the case without in-depth absorption, and Ref. 28 including absorption in-depth).

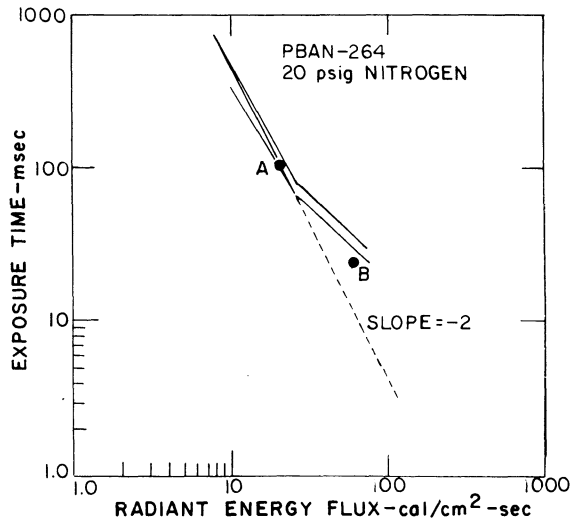


Fig: 1 Radiant ignition characteristic for PBAN-264 AP composite propellant: Exposure time required for ignition vs flux (from Ref. 29, Fig. 1).

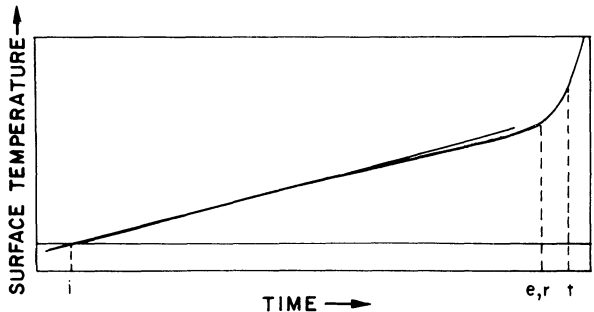


Fig 2a Trace form thermocouple touching propellant surface exposed to radiant flux: Pressure independent regime of inert surface temperature (from Ref. 29, Fig. 2).

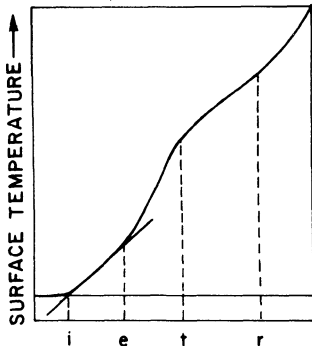


Fig. 2b Same as Fig. 2a except pressure-dependent regime of surface temperature (from Ref. 29, Fig. 3).

to a critical flux level and pressures above some atmospheres absolute,  $t^* \approx 1/q^2$  in accordance with inert heating to a constant ignition temperature. No surface exotherms were found in this case. But at flux levels greater than the critical level he found that: 1)  $\ln(t^*)$  vs  $\ln(q)$  plots had slopes more positive than  $(-2)$ ; 2) a pressure dependence of  $t^*$  was found; and 3) that preignition (near surface) exotherms were found from embedded thermocouple traces, see Figs. 1 and 2. He concluded that (near) surface exotherms in the solid phase may be an important part of the ignition process of composite propellants, but that the "why and when" they are important is not yet determinable and deserves research.

Subsequently, Pantoflíček and Lébr<sup>30</sup> argued that the effects observed by Fishman<sup>29</sup> are explainable, assuming that a critical energy that must be supplied for ignition is a constant equal to  $(q_c t_c^*) = Q_c$  where  $t_c^*$  is the ignition delay at the critical flux  $q_c$ . If  $q > q_c$  then  $t^* = Q_c/q$  to give a slope of  $(-1)$  on a  $\ln t^*$  plot, as observed by Fishman. Since the steady burning rate of a propellant increases with pressure, the temperature gradient at the surface also increases, causing the value of  $q_c$  to increase. Therefore, the shift in slope of  $\ln(t^*)$  vs  $\ln(q)$  plots from  $(\approx -2)$  to  $(\approx -1)$  occurs at larger  $q_c$  values as the pressure is increased, see lines (a) and (b) of Fig. 3, respectively. This argument is reasonable provided a critical ignition energy,  $Q_c$ , exists; unfortunately there is no inarguable evidence that it does.

In 1970 Shannon<sup>31</sup> reported an extensive set of arc-image ignition results for different AP composite propellants using polybutadiene-acrylic acid--acrylonitril (PBAN), polyurethane (PU), carboxy-terminated-polybutadiene (CTPB), or polyisobutylene (PIB) as binders, and a nitrate-ester plasticized polyester (PEP) propellant. Ignition data were obtained on a go/no-go basis for a pressure range of 0.1-4 atm (10-400 kPa) generally, and heat fluxes of 10-100 cal/cm<sup>2</sup>s (0.42-4.2 MJ/m<sup>2</sup>s). Potassium perchlorate (KP), hydroxylamine perchlorate (HAP),

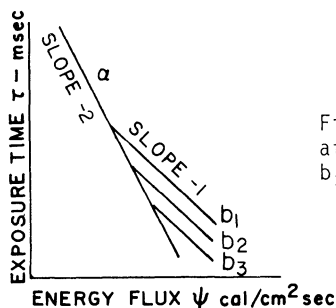


Fig. 3 Predicted ignition delay vs flux at different pressure levels,  $b_i$ , for  $b_3 > b_2 > b_1$  (from Ref. 30, Fig. 3).

and hydrozine diperchlorate (HDP) oxidizers were also used in some diagnostic tests. Finally, in rather nice experiments, tests were made on CTPB/AP propellants in which 1) the AP was coated with 1.5% by weight Kel-F, unchanged binder, and 2) 1.5% Kel-F added to binder alone. The tests showed large effects of flux level at fixed pressures greater than the minimum ignition pressure, see Fig. 4, together with rather modest AP particle size effects at any flux or pressure level used. Large effects of pressure on  $t^*$  at fixed flux levels greater than some value like  $40 \text{ cal/cm}^2\text{s}$  ( $1.7 \text{ MJ/m}^2\text{s}$ ), see Fig. 5, and large effects of fuel binder on minimum ignition pressure, see Fig. 6 were reported. Of particular interest are the effects of the Kel-F addition to the propellant, see

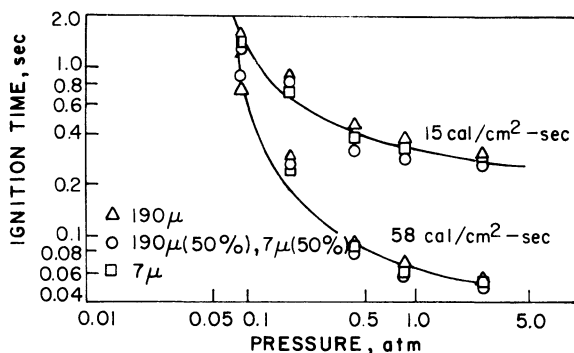


Fig. 4 Measured effect of particle size on radiant ignition delay as a function of pressure at two input flux levels for PBAN/AP composite propellant (from Ref. 31, Fig. 6).

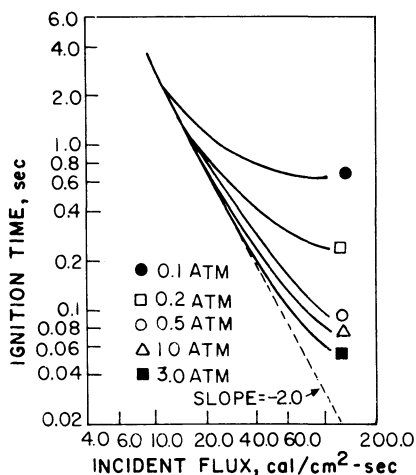


Fig. 5 Measured effect of flux at different pressure levels on radiant ignition delay for PBAN/AP composite propellant (from Ref. 31, Fig. 2).

Fig. 7. In a thorough and tightly reasoned discussion Shannon related his observations to the current solid-phase, heterogeneous/hypergolic, and gas-phase theories.

A bold summary of his discussion is possible. Observe via Fig. 4 that an increase of about 25X of the binder/oxidizer interface area per unit volume of propellant occurred in changing from 190  $\mu\text{m}$  particles to 7  $\mu\text{m}$  AP particles, and that the effect of this change was rather small at low pressures and fluxes, and smaller yet at high fluxes and maximum tested pressures. If interfacial oxidation were an important factor in heat generation in any solid phase exothermicity, then a significant particle size effect should have been seen at short heat-up times (large flux) and highest sample compression (highest pressure), and it was not. Then observe from Fig. 7 that the presence of Kel-F had the same effect whether in the binder or between the oxidizer/binder interface. Therefore interfacial heterogeneous/hypergolic binder oxidizer reactions are not an important factor in composite propellant ignition; however condensed-phase, particle diameter independent, exothermic reactions may still be important as would be thought on the basis of their importance in steady-state burning theories. From Fig. 7 it may be observed that binder material is important in ignition if  $P < 0.75$  atm but not at greater pressures. If differences in binder susceptibility to oxidative reaction by heterogeneous reactions were important, any subsequent heat release should still be important in the

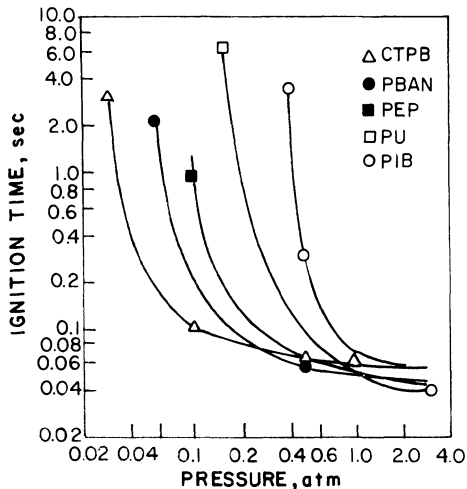


Fig. 6 Measured effect of binder changes on ignition delay of AP composite propellants as a function of pressure at constant flux, 58 cal/cm<sup>2</sup>s and 2.43 MJ/m<sup>2</sup>s (from Ref. 31, Fig. 8).

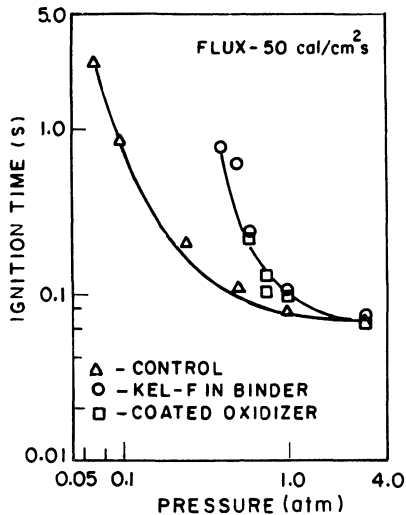


Fig. 7 Measured effect of incorporating Kel-F in binder, or as a coating around oxidizer crystals, on radiant ignition delay as a function of pressure at constant flux of  $2.09 \text{ MJ/m}^2\text{s}$  ( $50 \text{ cal/cm}^2\text{s}$ ) (from Ref. 31, Fig. 7).

$0.75 < P < 3 \text{ atm}$  pressure range. But negligible relative differences in  $t^*$  were found in this range. Finally, consider the obvious differences in minimum ignition pressure with binder material at constant heating and oxidizer properties, combined with the Kel-F effects. These results imply gas-phase compositional and pyrolysis differences more than they do solid-phase reaction (pressure independent) or surface (heterogeneous/hypergolic) reaction differences, since presumably reaction order and pre-exponential are independent of pressure. Thus Shannon concluded that gas-phase reaction establishment is an important process in composite propellant ignition by radiant energy, possibly together with solid-phase reactions.

In order to develop a complete understanding of radiant energy ignition of solid propellants, and to develop further information regarding the ignition process, Summerfield and his associates<sup>32-38</sup> undertook extensive studies of ignition of composite propellants and their components, and double-base (DB) propellants, exposed to a radiant heat flux. The majority of results are discussed in Ref. 33, which deals with ignition delay of fuels as a function of total pressure and oxygen partial pressure at constant flux, see Fig. 8, and as a function of flux level at several constant pressures and 100%  $\text{O}_2$ , see Fig. 9. At fixed total pressure, the termination of ignition as oxygen partial pressure decreased is characteristic. It



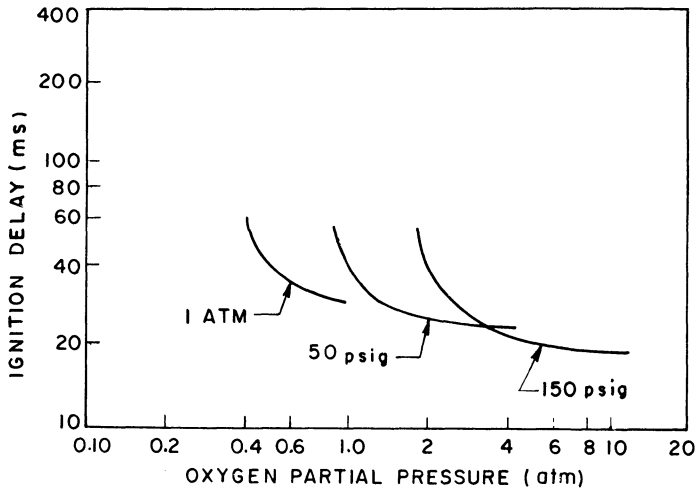


Fig. 8 Measured effect of oxygen partial pressure, at different total pressure levels, on radiant ignition delay of cured epoxy fuel binder at constant flux of  $3.85 \text{ MJ/m}^2\text{s}$  ( $92 \text{ cal/cm}^2\text{s}$ ) (from Ref. 33, Fig.1).

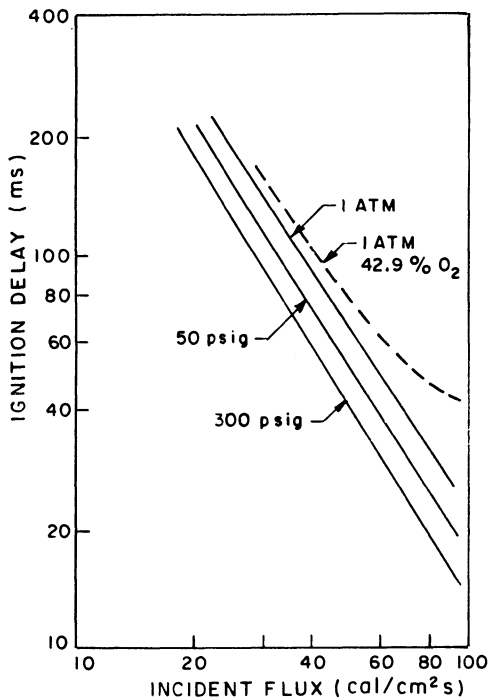


Fig. 9 Measured radiant ignition delay as a function of input flux at several pressure levels for cured epoxy fuel binder in 100% O<sub>2</sub> environment (from Ref. 33, Fig. 2).

was ascribed to insufficient oxygen diffusion into the incipient reaction zone, with the shift to lower oxygen partial pressures as the total pressure was decreased being due to an increased diffusion coefficient. In each case, as the limit is reached, reactive consumption of oxygen finally exceeds the rate at which diffusion can supply oxygen to maintain the reaction. This situation is made even more detrimental to ignition because of the thickening of the preflame reaction zone, and its movement away from the propellant surface, which increases the rate of heat loss to the gas phase. The tendency of the ignition delay toward independence of oxygen partial pressure as the latter becomes the dominant gas-phase component is essentially the converse situation. In this instance there is ample oxygen for all previsible-flame reactions (no photocell output), reaction develops close to the fuel surface (feeding back energy for further vaporization) and any tendency to consume the oxygen is easily countered by diffusion. The absolute pressure level effect at large oxygen mole fractions is small but noticeable, and seems to be explainable in terms of tendency of high oxygen partial pressures to increase fuel binder decomposition rates as observed by Pearson<sup>39</sup> and as reported in a particularly detailed studies of radiative polymer kinetic degradation studies reported by Bouck et al.<sup>40</sup> and Ryan.<sup>41</sup>

Pearson<sup>39</sup> observed moderately high-temperature oxygen could ignite polymeric fuels in a 1 atm experiment where 100% O<sub>2</sub> was passed over pulverized fuel samples, if a burning rate antalyist was added in an admixture, and that 90% HClO<sub>4</sub> vapor ignited the samples more readily, without any catalyst added. In a particularly detailed set of experiments Bouck et al.<sup>40</sup> and Ryan<sup>41</sup> investigated the radiant decomposition products of thin polymeric films and films with an admixture of fine AP up to 30% by weight in the presence of various inert gases and oxygen. Ryan reports (Ref. 41, pp. 171-172) that with PBAA fuels an endotherm exists prior to the start of vigorous gasification, that both processes are pressure dependent, and that the presence of oxygen influences the decomposition process. The latter effect is more fully described in the body of the report. At the same time, Ryan found that with propellant levels of AP in the films, no oxygen affect was observed. But, these tests were at low total pressure (0.85 atm). In Ref. 40 it is indicated that the presence of oxygen can lower the bulk and preignition exotherms as much as 200 K below the ignition temperature, while producing negligible mass loss, in a number of polymers. Clearly there is a probable link between these findings and Ohlemiller's results shown in Fig. 8 from Ref. 33.

Figure 9 indicates the effect of flux level at constant pressure of 100%  $O_2$  on the radiant ignition of epoxy polymer for the pure epoxy and for epoxy plus 1% C-black at the highest pressure of 300 psig (2.17 MPa). The basic slopes of the high-pressure ( $P > 0.45$  MPa) data tend to look like a dominance of "inert" heat-up time but have a lesser slope than would be the case if that were completely true. Possibly this indicates the shading effect of gas-phase diffusion/reaction development, but it also can be due to solid-phase reactions as will be seen later. At the highest pressure, the pure fuel and the blackened fuel have virtually the same ignition characteristics, indicating that in-depth absorption was indeed as small an effect as the measured extinction coefficient of  $340 \text{ cm}^{-1}$  would indicate. Of much more interest was the observation<sup>33</sup> that the high-pressure data on ignition delay corresponded to the first observation of gasification during ignition tests at the same flux level but lower pressures.

The observation of real, measurable delays between first gasification and achievement of self-sustaining ignition was valuable and exciting, and its further investigation was pursued strongly by Summerfield and his associates in a series of papers, Refs. 34-38. Schematically their results are illustrated in Fig. 10 which is self-explanatory on knowing that  $L_{1a}$  through  $L_{1d}$  are criteria describing the time of various physical events, as shown in the figure. Reference 35 presents film strip prints of the gasification to visible

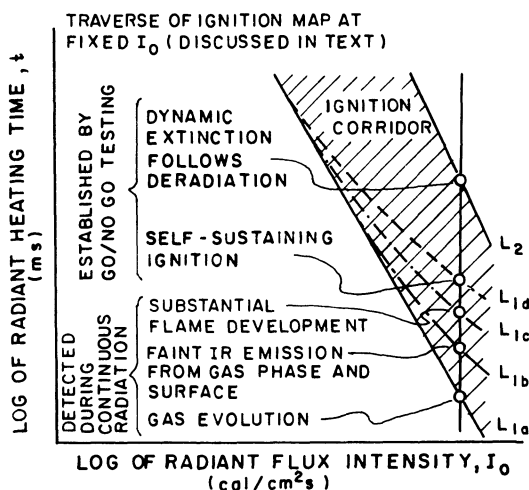


Fig. 10 Generalized ignition map showing event limits or signals that occur during radiant ignition of solid propellants; the  $L_i$  are ignition criteria corresponding to labelled event/signal (from Ref. 37, Fig. 2).

flame process, continuing through to a dynamic extinction limit. Very detailed sets of experiments are described in Refs. 35-38, with Refs. 37 and 38 probably the best for overall summaries and discussion, of which we can only hit the high points herein. Figure 11 illustrates that 1) composite propellants are immune from the  $L_{1a} - L_{1d}$  delay; 2) the  $10.6 \mu\text{m}$   $\text{CO}_2$  laser radiation is absorbed in the same way by the composite propellants which were AP/hydrocarbon binder (no binder composition referenced) with propellant 1 = 75% AP, 0% C; 2 = 75% AP, 1% C; 3 = 80% AP, bimodal; 4 = 24% AP, 51% B (metallized); 3) 1% C does 'not opacity make' for arc radiation; and 4) even 51% B did not make the propellant have an infinite extinction coefficient, though almost. Figure 12a, for a catalyzed DB propellant illustrates the  $L_{1a} - L_{1d}$  difference clearly. The  $L_{1a}$  limit is always the basic, lower most line for each propellant and also indicates that the actual data on pressure sensitivity is dependent upon the

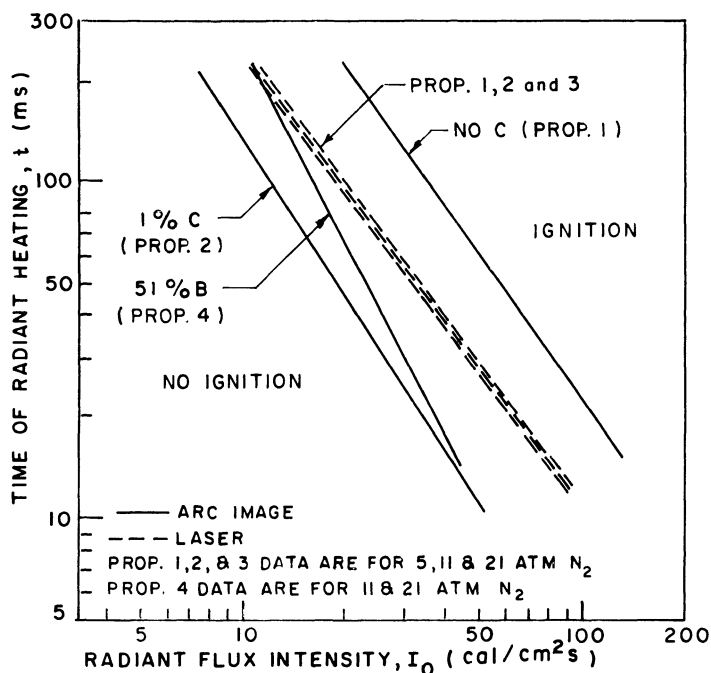


Fig. 11 Radiant ignition of composite propellants demonstrating independence of pressure. Propellants 1-4 are, respectively: 1) 75%/45  $\mu\text{m}$  AP, 0% C; 2) No. 1 plus 1% C; 3) 80%, 30% 15  $\mu\text{m}$ , 70% 180  $\mu\text{m}$ , 0% C; 4) metallized, 24% AP, 51% B. Shows dependence on source and extinction coefficient (from Ref. 33, Fig. 5 and Table 1 of Ref. 37).

nature of DB propellants. The degree to which gas-phase reactions can be coupled to solid phase/surface events is seen in Fig. 12b for HMX composites. Other data found in Ref. 38 indicated that in composite propellants, the close coupling of the gas-phase AP decomposition processes performed the same function as did air in the DB ignition tests, removing the  $L_{1a}$ - $L_{1d}$  spread.

Summarizing, it is clear that composite and DB propellants can be ignited by radiant energy fluxes over a wide range of flux levels and pressures, and environmental atmospheric composition. Environmental gaseous composition has a small effect on the magnitude of the ignition delay for both propellant types but in DB propellants a gaseous oxidizer accelerates the second stage (gas-phase development) of a two-stage ignition process.<sup>38</sup> The experimental results in total indicate a coupling exists between solid-phase exothermic decomposition in a very narrow region of the solid adjacent to the surface and the development of the final-stage gas-phase reaction. The size of the first-stage, solid-phase reaction zone is governed by the transmissivity of the solid phase and therefore the presence and importance of this stage may be magnified by ignition with radiant energy sources. The presence of burning rate catalysts are found to accelerate both fuel and oxidizer decomposition and thus to speed up ignition, but the mechanism of their interaction still seems obscure in

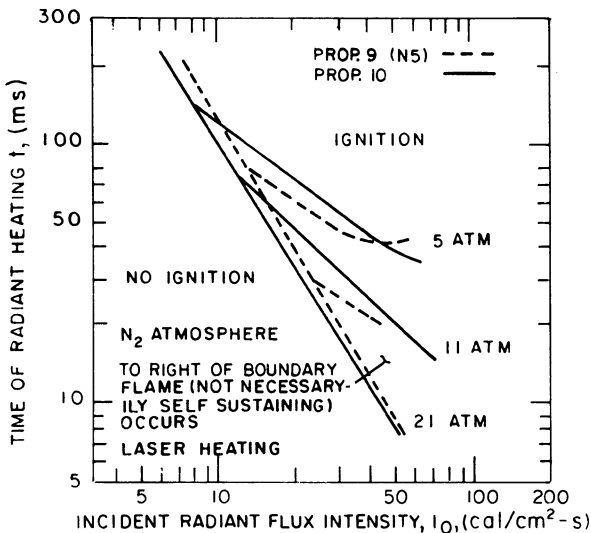


Fig. 12a Radiant ignition delay vs flux as a function of pressure level, showing that ignition processes depend on details of propellant chemistry (from Ref. 38, Fig. 1b).

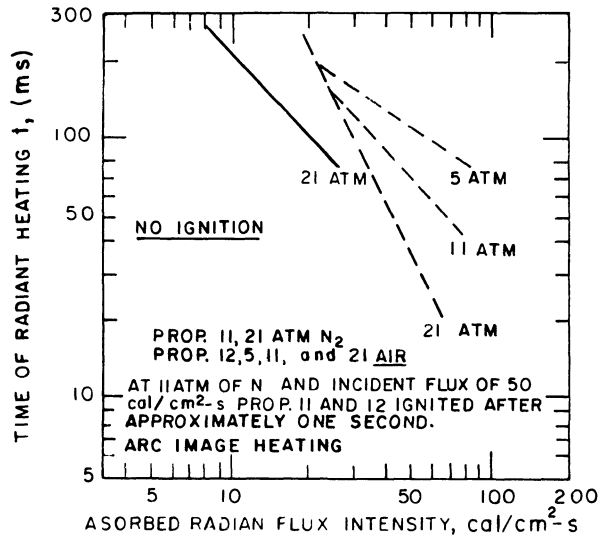


Fig. 12b Radiant ignition delay of HMX composite propellants vs flux as a function of pressure (from Ref. 37, Fig. 6b).

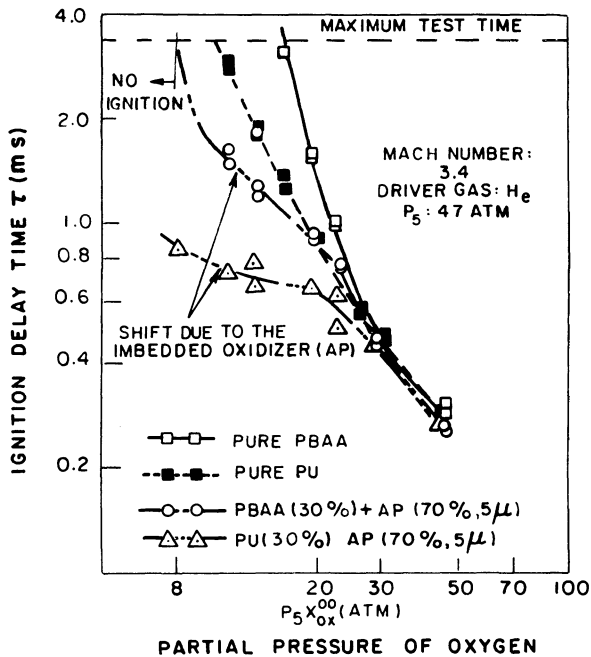


Fig. 13 End wall shock tube study of ignition of pure fuels and AP augmented fuels as a function of oxygen partial pressure at constant total pressure (from Ref. 45).

## Chapter 6

# Flame Spreading and Overall Ignition Transient

Mridul Kumar\* and Kenneth K. Kuo†  
*The Pennsylvania State University,  
University Park, Pennsylvania*

### Abstract

A review of the literature on the overall ignition transient in rocket motors and flame spreading over solid propellants and in propellant cracks or flaws is presented to establish the state-of-the-art. Even though previous studies have been helpful in interpreting many fundamental processes, at the present time, the understanding of flame spreading and ignition transient is still incomplete. For the ignition transient, both lumped parameter  $[p(t)]$  and one dimensional  $[p(x,t)]$  models exist. The former should be limited to trend analysis only and must not be used for design calculations for rocket motors with high volumetric loading density. Transient one-dimensional flame-spreading models seem to do a reasonable job of predicting flame-spreading rates over solid propellants and in propellant cracks where convective heating dominates, and for propellants whose flame standoff distances are small. Most of the models employ the simple "critical surface temperature" ignition criterion, even though now it is generally agreed that ignition takes place in the gas phase. This simple criterion may not work for rapid ignition and flame spreading over nitramine propellants. Future models should consider detailed gas-phase reactions and multidimensionality of the flowfield and solid propellant grain configurations. More fundamental studies are needed to explain the appearance of secondary/tertiary ignition (downstream of the flame front) during the flame-

---

Copyright © American Institute of Aeronautics and Astronautics, Inc., 1983. All rights reserved.

\*Assistant Professor, Department of Mechanical Engineering, presently working as Research Engineer at Gulf Research and Development Company, Houston, Texas.

†Professor, Department of Mechanical Engineering.

spreading process. Measurements of the empirical constants (such as convective heat-transfer coefficient, friction coefficient, etc.) under transient rocket-motor-like conditions are needed for more precise predictions. Also, accurate physical and chemical parameters associated with propellants and gas-phase reactions are desirable.

### Nomenclature

$A$	= cross-sectional area of crack or port
$A_t^p$	= motor nozzle throat area
$a$	= pre-exponential factor in the nonerosive-burning-rate law $r_b = aP^n$
$B$	= body force
$b^x$	= covolume
$c$	= speed of sound
$c_f$	= friction coefficient = $2\tau_w/\rho u^2$
$c_p$	= specific heat at constant pressure
$d_h$	= hydraulic diameter of crack
$E$	= total stored energy (internal and kinetic)
$G_1$	= relaxation modulus
$\bar{h}_c$	= local convective heat-transfer coefficient
$\bar{h}_{cp}$	= local convective heat-transfer coefficient over propellant surface
$\bar{h}_{cw}$	= local convective heat-transfer coefficient over non-propellant port wall
$k$	= erosive burning constant
$K$	= bulk modulus
$L$	= length of crack
$L^*$	= characteristic length
$\dot{m}_{ig}$	= igniter mass flow rate
$M_w^{ig}$	= molecular weight
$n$	= pressure exponent in nonerosive-burning-rate law
$P$	= pressure or perimeter
$Pr$	= Prandtl number
$q_1$	= rate of heat transfer
$R$	= specific gas constant for combustion gases
$Re$	= Reynolds number
$r_b$	= burning rate of solid propellant, including erosive-burning contribution
$T$	= temperature (without subscript, static gas temperature)
$T_{af}$	= average film gas temperature = $(T + T_{ps})/2$
$T_f$	= adiabatic flame temperature of solid propellant
$T_{pi}$	= initial propellant temperature
$T_{ps}$	= propellant surface temperature



$T_{ws}$	= nonpropellant wall surface temperature
$t$	= time
$u$	= gas velocity
$V$	= volume
$v_{gf}$	= velocity of propellant gas at burning surface
$W$	= molecular weight of the combustion gases
$x$	= axial coordinate
$x_E$	= position at the entrance to the motor nozzle
$x_L$	= position at the end of crack
$x_p$	= position at the entrance to the propellant section (propellant slab edge)
$x_r$	= distance from the point of impingement of the igniter jet
$y$	= transverse coordinate, measured from propellant surface into solid
$\alpha$	= thermal diffusivity
$\beta$	= erosive-burning exponent
$\gamma$	= ratio of specific heats
$\delta$	= gap width of crack
$\epsilon$	= strain tensor
$\epsilon_s$	= surface roughness
$\lambda$	= thermal conductivity
$\sigma$	= stress tensor
$\mu$	= gas viscosity
$\rho$	= density (without subscript, gas density)
$p_b$	= burning perimeter
$p_w$	= wetted perimeter of the port
$\tau_w$	= shear stress on port wall
$\tau_{xx}$	= normal viscous stress
$\theta_w$	= angle measured, in a counterclockwise direction, at lower side of propellant

### Subscripts

$c$	= chamber conditions
$E$	= entrance to motor nozzle (motor chamber aft end)
$eff$	= effective
$es$	= entrance section
$g$	= gas
$i$	= initial value
$ign$	= ignition condition
$n$	= nozzle
$pr$	= propellant
$ps$	= propellant surface
$t$	= nozzle throat

## I. Introduction

In the recent past, there has been a continued trend toward the use of larger and more sophisticated solid propellant rocket motors. These motors require greater accuracy in the prediction and control of the thrust and ignition transients (i.e., more precise prediction of the pressure-time history of the motor). This is also because a detailed knowledge of thrust during the ignition transient may be required for critical guidance and control, especially during the initial phase of motor operation. In addition, since the solid propellant grain and many of the motor components are viscoelastic in nature, both the chamber pressure and the rate of pressurization are of prime concern to rocket motor designers.

The ignition transient is usually defined as the time interval between the application of the ignition signal and the instant at which the rocket motor attains its equilibrium or designed operating conditions. The ignition transient can be generally considered to consist of three intervals: 1) the induction period for first local ignition, 2) the period for flame spreading over the exposed surface of the propellant grain, and 3) the chamber-filling period. The first ignition and flame-spreading periods are preceded by the heating of the propellant grain by igniter products.

Both the ignition delay (which is defined either as the induction period for local ignition or, more commonly, as the time interval between the application of the ignition signal and the attainment of 10% or 50% of the maximum or steady-state chamber pressure) and the flame-spreading rates depend very strongly upon the heat-transfer process, the grain configuration, the chamber conditions, and the physicochemical properties of the propellant. A detailed understanding of ignition and flame-spreading mechanism is essential for accurate prediction of the ignition transient and, consequently, for the design and development of solid rocket motors. Processes that influence the ignition delay, and detailed mechanisms of ignition are reviewed by Hermance in another chapter of this volume entitled "Solid Propellant Ignition Theories and Experiments."

The flame-spreading process, perhaps, most significantly influences the initial portion of the thrust or pressure transient. Since the flame-spreading rate determines the instantaneous ignited fraction of the total surface area available for combustion, the gas generation rate or chamber pressure are strongly dependent upon it. Understanding the flame-spreading process is also important

for deflagration-to-detonation transition (DDT) studies in solid propellants, because convective flame propagation into cracks and flaws is believed to be a precondition for subsequent transition to detonation.

In the past, numerous experimental and theoretical studies have been conducted on flame spreading, ignition transient, and associated processes. This research can be subdivided into the following major subgroups:

1) research into the nature of ignition transient as a whole, 2) fundamental studies on the mechanism of flame spreading over solid propellants, and 3) flame spreading in propellant cracks. Accordingly, these topics are treated separately in the following subsections. In addition to the above-mentioned subject areas, a considerable amount of research has also been conducted on igniter and ignition systems, and on other fundamental processes related to the ignition transient and flame spreading, such as heat transfer, chemical reactions, erosive burning, etc. Even though many of the purely experimental studies have assisted in providing considerable physical insight into this complex problem, the major thrust of the research has been toward development of predictive models in order to reduce the cost associated with experimental trial and error design technique. Moreover, because of the radical differences in size and the design of new rocket motors, extrapolation from previous empirical data is unreliable. Experimental investigations, however, are necessary to establish the data base for model validations, etc.

## II. Ignition and Thrust Transients in Solid Propellant Rocket Motors

### A. Ignition Devices or Igniters

This section presents a very brief discussion of ignition devices or igniters. A typical solid propellant rocket motor with a head-end igniter is shown in Fig. 1. Because igniters provide the external stimulus needed to ignite solid propellant rocket motors, the overall ignition transient is strongly influenced by the composition, location, and mass flow rate of the igniter. Igniters are generally categorized as 1) pyrotechnic igniters, 2) pyrogen igniters, and 3) hypergolic igniters.<sup>1,2</sup>

Pyrotechnic and pyrogen igniters are made of solid propellant or materials with propellant-like chemical formulations,<sup>1</sup> and are also referred to as solid propellant igniters.<sup>2</sup> All solid propellant igniters not categorized as pyrogen igniters are considered to be pyrotechnic

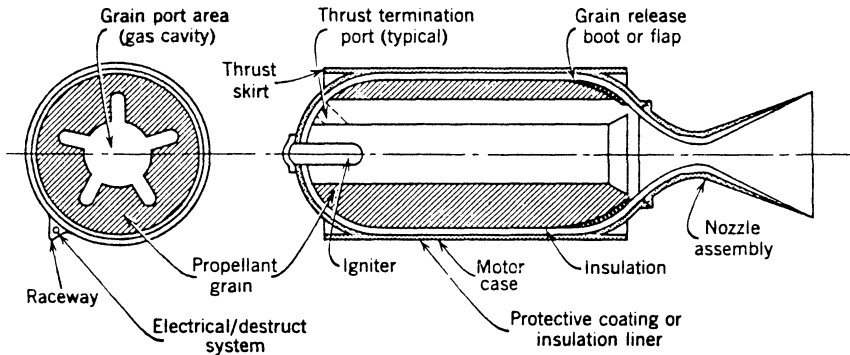


Fig. 1 Typical solid propellant rocket motor with head-end igniter (adopted from Ref. 1, Fig. 10-1).

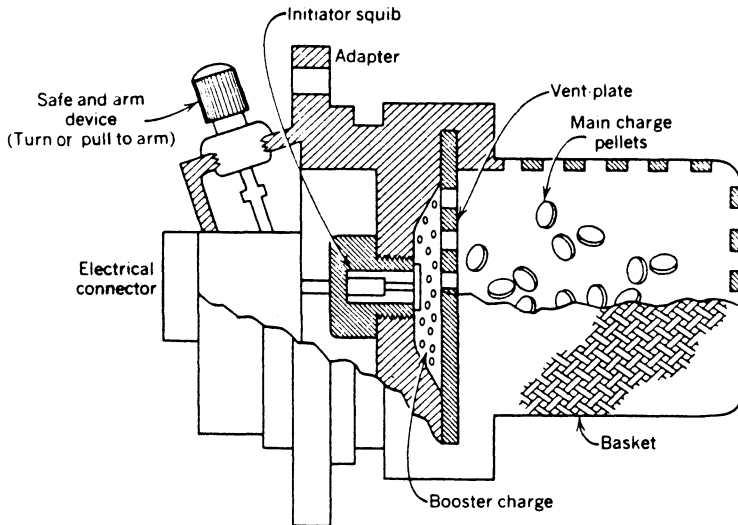


Fig. 2 Simplified typical pyrotechnic igniter (adopted from Ref. 1, Fig. 12-3).

igniters. Pyrotechnic igniters include some easily ignitable high-energy charge in the shape of pellets. This charge is generally made up of black powder or boron and potassium nitrate, and a binder. Hot wire or electric squib is often used as the initiator for the ignition of the pellets. The product of a burning pyrotechnic igniter is hot gases and, frequently, hot particles which ignite the propellant grain in the motor by conduction, convection, and radiation heat transfer. A typical pyrotechnic igniter is shown in Fig. 2. The pyrotechnic

igniter may be placed at the head or aft end of the rocket motor or in a distributed form in the grain perforation.

A pyrogen igniter (see Fig. 3), on the other hand, can be considered to be a small, easily ignitable rocket motor. Besides the obvious differences in the size of the pyrogen and pyrotechnic igniter, another major difference is the composition of the product of the two systems. Unlike the pyrotechnic igniter, the pyrogen igniter produces mainly hot gases, and therefore convection is the primary heat-transfer mechanism for the ignition of propellant grain in the motor. A monograph published by NASA<sup>3</sup> on solid propellant rocket igniters summarizes a considerable amount of information that can be used in igniter design. Detailed data on the performance characteristics of typical igniter systems and design criteria were also compiled by Falkner and Miller.<sup>4</sup>

Pyrogen igniters can be located either at the head end or the aft end of the rocket motor. For aft-end igniters, the igniter exhaust gas penetrates axially through the motor nozzle toward the head end. Obviously, the characteristics of aft-end-mounted igniters will be quite different than those of head-end igniters, since the pattern of jet impingement and flow characteristics are dissimilar. Aft-end igniters can be mounted either external or internal to the rocket motor. The inherent advantage of externally mounted aft-end igniters is that the igniter becomes a piece of ground support equipment. This results in a reduction of the total weight of the motor and allows a more conservative design of the igniter.

Hypergolic igniters employ a pressurized hypergolic reagent, e.g., liquid chlorine trifluoride, which is injected over the propellant surface. Propellant ignition is caused by heterogeneous reaction at the surface. Since

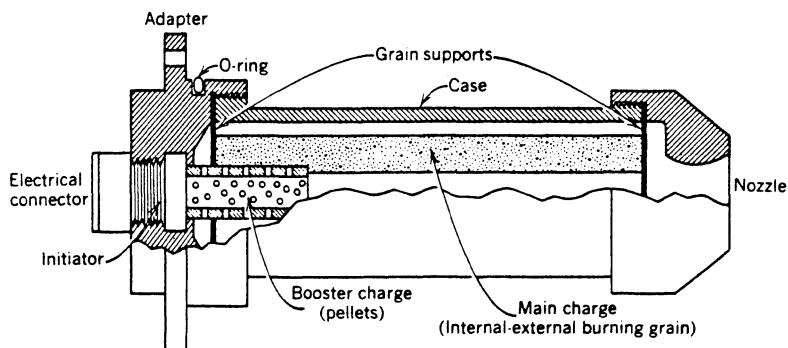


Fig. 3 Typical pyrogen igniter (adopted from Ref. 1, Fig. 12-4).

ignition in this case is dependent upon the contact between the hypergolic reagent and the propellant, injection of large drops is preferred in some cases to fine atomization. References 5 and 6 contain more details of such igniters. Because hypergolic igniters are less commonly used, they will not be discussed in this chapter.

### B. Physical Processes During Ignition Transient

The ignition transient comprises a complex series of interrelated events/processes such as 1) initiation of igniter discharge signal, 2) heat generation caused by chemical reaction between igniter species, 3) conductive, convective, and radiative heat transfer from igniter products to the propellant surface, 4) flame spreading over the entire propellant surface, 5) development of the flowfield in the chamber, and 6) increase of chamber pressure to the quasisteady operating condition. These processes are sometimes accompanied by many abnormalities, such as overpressures, hang-fires (delayed ignition), damaging shock waves (detonation), combustion oscillations, chuffing, and extinguishment.

The actual sequence of events that occur during an ignition transient strongly depends upon the type of igniter used and its location in the rocket motor (i.e., head-end, aft-end, or distributed igniter). Pyrogen-type igniters located at the head end of a rocket motor have been most extensively studied. For such an igniter, the physical processes that take place during the ignition transient are as follows: The hot product gases from the igniter flow over the propellant grain and transfer energy

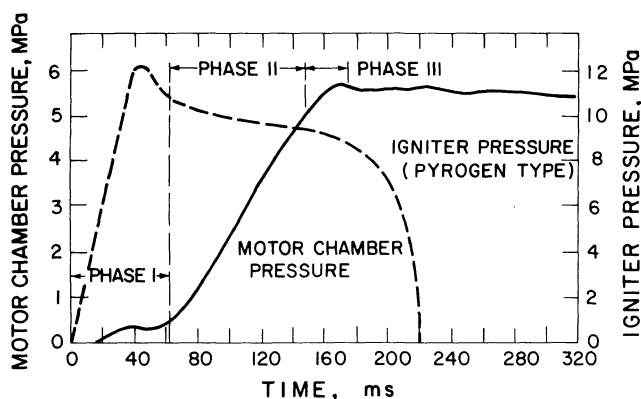


Fig. 4 Typical pressure-time traces of rocket motor and pyrogen igniter (adopted from Ref. 1, Fig. 12-1).

to the propellant surface. This causes the propellant grain near the igniter, where the heat-transfer rate is the highest, to ignite. As the igniter gases continue to flow over the propellant, and part of the grain begins to burn, the region downstream also ignites. The flame spreads over the entire grain; the chamber pressure rises and eventually reaches the equilibrium operating condition. A typical pressure-time trace for a rocket motor and a pyrogen igniter is shown in Fig. 4. In terms of the most conveniently measured ballistic parameter, chamber pressure, the ignition transient represents the time period required to attain the equilibrium (quasisteady) pressure.

For ease of discussion, the ignition transient can be subdivided into three separate intervals: 1) ignition time lag or induction interval, 2) flame-spreading interval, and 3) chamber-filling interval. These intervals are qualitatively represented as phases I, II, and III, respectively, in Fig. 4. This subdivision of ignition transient is quite appropriate for head-end igniters and facilitates the discussion and analysis by confining some of the complex physical processes to one or the other of the intervals.

The ignition time lag or induction interval is generally defined as the interval between the initiation of the igniter and the appearance of first ignition on the propellant surface. This includes delays associated with the ignition and ballistics of the igniter, and the delay associated with the ignition process of the rocket grain itself. In most analyses, the time delay associated with the igniter is assumed to be a known input (empirically or otherwise). Because the ignition delay associated with the propellant is quite complex (see ignition chapter of Hermance), several practical simplifying assumptions are often made for ease of modeling.

The flame-spreading interval is defined as the time interval between first ignition of the propellant surface and ignition of the entire propellant grain. The mechanism of propagation of ignition front or flame spreading depends upon the igniter gas flowfield and the rate of heat transfer to the propellant surface, as well as igniter and propellant compositions. For igniters located at the head end of rocket motors, the assumption of successive ignition of adjacent propellant elements (proposed by Summerfield in 1964) has been successfully used to describe the flame propagation event, especially when the heat-transfer mechanism is strongly convective. In some models, the flame-spreading rate is considered as an empirical input.

The time interval between the end of flame spreading and attainment of equilibrium chamber conditions is called

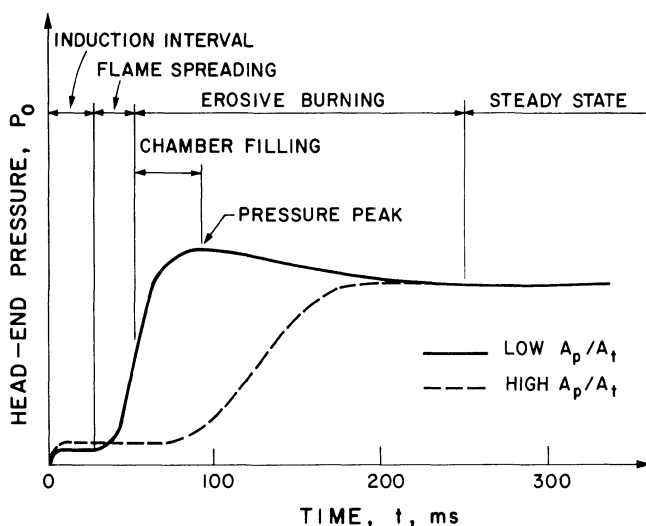


Fig. 5 Typical starting transients of HVT motors (low  $A_p/A_t$ ) compared with that of motors having high ( $A_p/A_t$ ) (adopted from Ref. 26, Fig. 1).

the chamber-filling interval. During the chamber-filling interval, the high rate of increase of chamber pressure may result in coupling of the pressurization rate and burning rate (known as the dynamic burning effect). Also, the high cross-flow velocity of the product gases may result in enhanced burning of the propellant grain (called the erosive burning effect). The net result of the two enhanced burning effects is a pressure overshoot observed during the chamber-filling interval. These effects are much more important in the case of solid propellant motors with high volumetric loading density, large length-to-diameter ratio, or small port-to-throat area ratio. Such motors are sometimes referred to as high-velocity transient (HVT) motors. Figure 5 shows a schematic of a typical starting transient for HVT motors compared to that of motors with high port-to-throat area ratio.

The sequence of events that takes place with the use of an aft-end pyrogen igniter is somewhat different. The igniter jet, which enters from the exit nozzle and penetrates the rocket motor, expands and then reverses the flow direction. Usually, a stagnant region of compressed colder gas is created near the head end of the motor. Within this zone, the dominant mode of energy transfer to the propellant surface is radiation and conduction from hot gases/particles. The heat-transfer process in the region



downstream of the stagnant zone is mainly convective. Because of the complex flow structure and associated heat-transfer rate, the propellant ignites near the aft end and sometimes near the middle of perforation. Unlike the head-end igniter, the flame spreads both upstream and downstream from this point, with the downstream flame propagation rate being faster. Location of the first-ignition point and the entire ignition transient for a rocket motor with aft-end igniter is strongly influenced by the degree of igniter jet penetration. Complete ignition is often observed to occur at the same time that equilibrium pressure is attained.

### C. Ignition Transient Models and Experiments

Models for the prediction of the overall ignition transient can be subdivided into three major categories: 1) lumped chamber parameters, or  $p(t)$  models; 2) quasisteady one-dimensional flow, or  $p(x)$  models; and 3) temporal and spatial flowfield, or  $p(x,t)$  models. Almost all theoretical modeling effort has been concentrated on head-end igniters; no detailed model is available in the open literature for predicting the overall ignition transient of rocket motors with aft-end igniters.

Lumped parameter models do not allow for any spatial changes in chamber variables. This assumption is questionable, especially for motors with high volumetric loading density or large length-to-diameter ratios, because significant spatial variations in chamber parameters do exist during the ignition transient. Lumped parameter models can be further categorized as isothermal or dynamic temperature analysis. Isothermal lumped models, which are limited further because of the assumption of constant gas temperature in the chamber, consider only the gas-phase mass conservation equation in the chamber:

$$\frac{dm_c}{dt} = \dot{m}_{ig} + \dot{m}_b - \dot{m}_n \quad (1)$$

For gasless igniters, the rate of mass addition due to the igniter  $\dot{m}_{ig}$  is zero. The mass flow rate out through the nozzle  $\dot{m}_n$  is generally obtained using the condition of choked nozzle flow. The mass addition due to propellant burning depends on the instantaneous burning surface area, which, in turn, is linked to the ignition interval and the flame-spreading rate. The major difference between the isothermal models is the manner in which they treat the injection and flame-spreading intervals.

Most of the earlier analyses of ignition transient have dealt with the chamber-filling interval only, perhaps because it is the least complex of the three intervals. In these analyses, ignition and flame spreading were either assumed to be instantaneous or treated empirically. The earliest analysis of the overall ignition transient was conducted by von Kármán and Malina in 1940.<sup>7</sup> Since several oversimplifying assumptions were made in the first attempt to model the complex ignition transients, the model is of limited practical utility today.

In the mid-60's, research work in this area was conducted by several scientists. DeSoto and Friedman<sup>8</sup> were the first to report the treatment of entire pressure transient, including the flame-spreading process. Their model<sup>8</sup> assumes isothermal one-dimensional gas flow in the chamber, spatially uniform pressure  $p(t)$ , mass addition in the chamber due to grain burning only, and choked nozzle flow. The initial conditions include instantaneous ignition of a part of the grain near the head end, uniform gas pressure and temperature, uniformly distributed pressure and temperature in the unignited part of the grain, and an axially varying velocity distribution. Two-dimensional transient heat conduction in the propellant grain was considered. Flame spreading was described by the successive ignition hypothesis of Summerfield,<sup>9</sup> and a constant propellant surface temperature ignition criterion was employed. No comparisons were made with experimental data.

Sharn et al.<sup>10</sup> conducted an experimental and analytical study of the ignition transient. The ignition time was calculated using a critical surface temperature and a critical temperature profile criteria. An isothermal analysis, combined with instantaneous flame spreading, was used for the calculation of pressure transient. A single comparison with an experimental pressure-time history for a pyrogen igniter showed good agreement during the initial portion of the transient.

Adams<sup>11</sup> presented another isothermal analysis and some comparison with measured pressure histories. The analysis assumes known ignition delay times, flame-spreading rates (usually a linear function of time), and igniter mass flow rates. Approximate expressions were used to take into account effects of erosive burning and pressurization rates on the propellant burning rate. Reasonable agreement between calculated and experimentally measured pressure-time histories were reported. It was also claimed that ignition spikes are primarily caused by erosive burning, since inclusion of the erosive burning effect in the

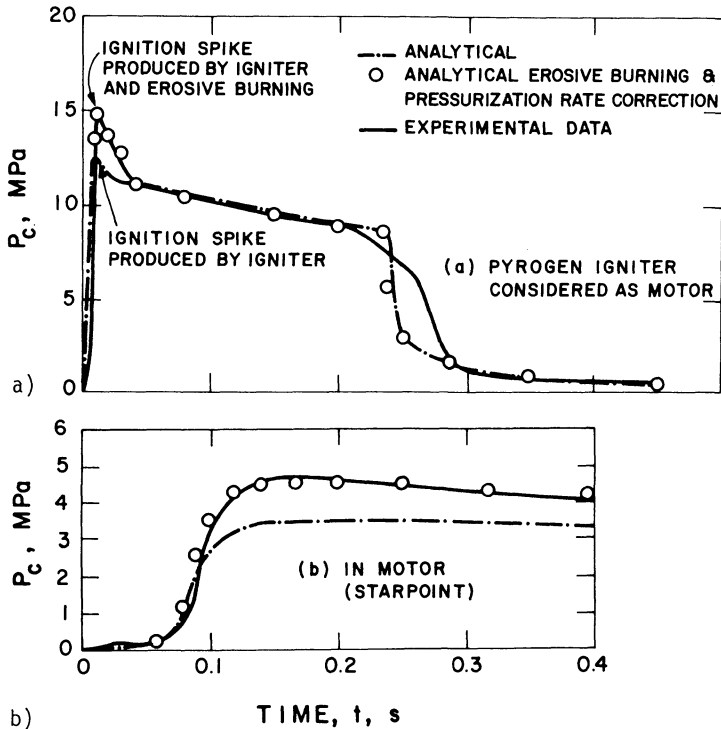


Fig. 6 Effect of erosive burning on predicted ignition transient for a rocket motor (adopted from Ref. 11, Fig. 6).

analysis produced better comparisons with experimental pressure transients (see Figs. 6 and 7).

A further development of the lumped chamber parameter model was the use of temporal variation of the chamber temperature (dynamic temperature analysis). That is, in addition to the mass conservation equation, Eq. (1), considered in the isothermal analysis, the energy conservation equation for the chamber gas was also included. The gas-phase energy conservation equation is usually of the form:

$$\frac{d}{dt} (m_c c_v T_c) = \dot{m}_{ig} h_{ig} + \dot{m}_b h_b - \dot{m}_n c_p T_n \quad (2)$$

where  $h_{ig}$  and  $h_b$  are the enthalpies of the combustion products from the igniter and burning propellant, respectively.

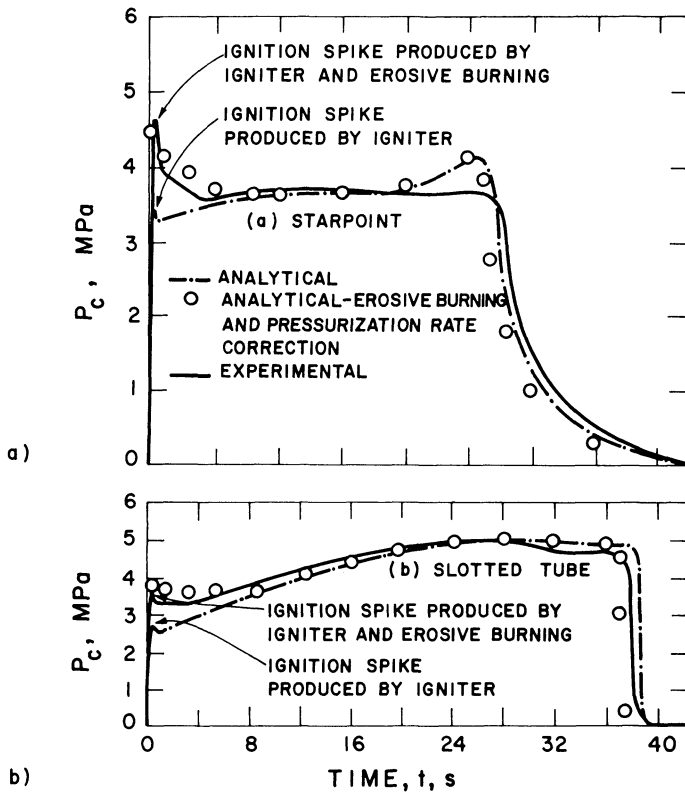


Fig. 7 Effect of erosive burning on predicted pressure transients in a star-point and slotted-tube motor and comparisons with measurements (adopted from Ref. 11, Fig. 7).

Baker<sup>12</sup> first used such an analysis. Experimentally obtained time-to-first-ignition and flame-spreading rates, or a specified burning surface area as a function of time, were employed in his analysis. Both choked and unchoked nozzle condition were considered. The analysis could also be used to compute flame-spreading rates from a given chamber pressure transient. Baker reported good agreement between predicted results and experimental data for a slotted grain motor.

Bradley<sup>13</sup> presented another theoretical analysis for dynamic temperature conditions assuming a homogeneous (no spatial dependence) adiabatic system. This was the first analysis to qualitatively predict effects of various parameters, such as  $L^*$  of the motor, ratio of igniter weight to motor free volume, igniter and propellant burning rate pressure exponents and flame temperatures, initial

pressure and temperature in the motor, etc. A general igniter form function was used to show the effect of igniter mass flow rate on the transient. The mechanism of flame spread was not considered; however, the importance of flame spreading on the pressurization process was demonstrated by assuming a linear relationship between the flame-spreading rate and burning rate.

Bradley<sup>13</sup> also found that the ignition transient was relatively insensitive to the initial temperature, and that the pressure exponent in the burning rate law has a more pronounced effect on peak pressure and time-to-peak pressure. Igniter with higher flame temperatures resulted in a higher and earlier peak pressure. Bradley concluded that "the igniter volumetric fraction is by far the most influential in determining the pressure-time transient."

Lovine and Fong<sup>14</sup> employed a dynamic temperature analysis for the chamber-filling period only. They used expressions for unsteady burning rate<sup>15</sup> and unsteady nozzle flow. The induction interval was obtained by evaluating average values of heat flux from the igniter and pressurization rate and experimentally measured pressure-time and heat-flux data for ignition. The flame-spreading interval was not considered.

Detailed experimental and theoretical analysis of the ignition transient was conducted by Summerfield and his co-workers at Princeton University.<sup>9,16-20</sup> Their theoretical analysis was based on the dynamic temperature and well-stirred reactor (spatially uniform pressure and temperature). Ignition was defined as the attainment of a critical propellant surface temperature. Flame spreading was postulated to result from successive ignitions of adjacent elements of the propellant surface, and ignition front propagation was attributed entirely to convective heat transfer from hot combustion gases. The model established by Parker et al.<sup>10,16,17</sup> assumes a gasless igniter and initial burning surface area. Most et al.<sup>18-20</sup> extended the analysis to include igniter operation preceding an early stage of flame spreading. The flame-spreading rate was calculated by solving the solid-phase energy equation coupled to the gasdynamic equations. Because the convective heat-transfer coefficient used varies with the axial coordinates, the heat flux to the propellant surface is a function of both time and distance from the head end. The driving temperature difference, however, is assumed to be constant in both time and space.

Summerfield and co-workers<sup>9,16-20</sup> also measured the flame propagation as well as the pressure transient in a windowed experimental rocket motor with slab-type propellant grain. Figure 8 shows a blowup of the

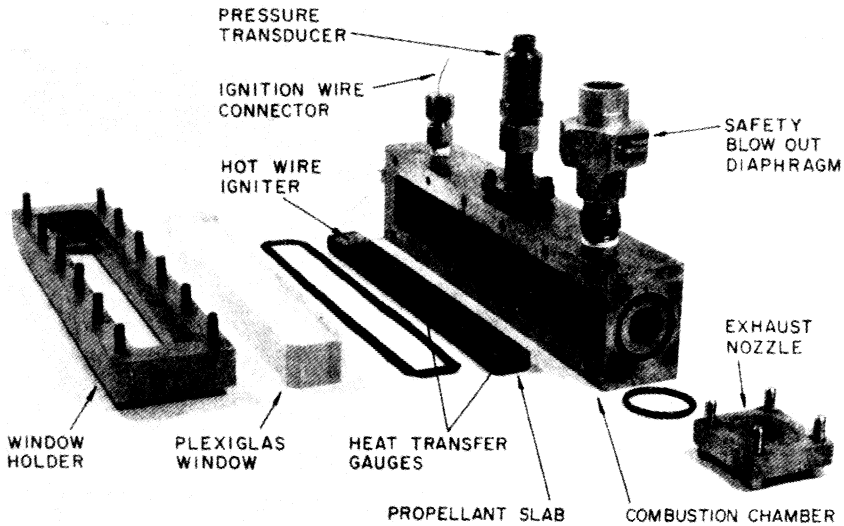


Fig. 8 Experimental rocket motor (adopted from Ref. 17, Fig. 3).

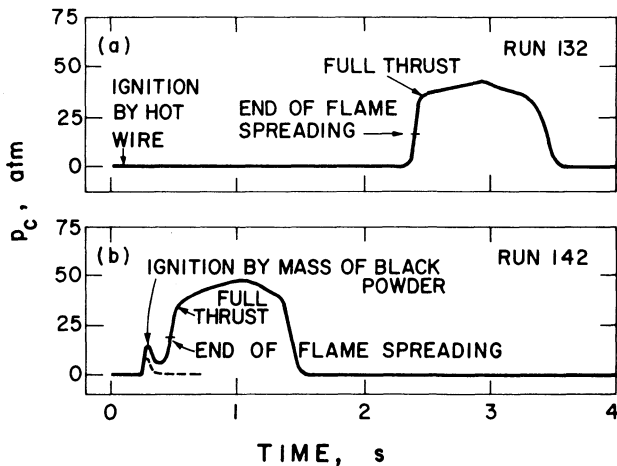


Fig. 9 Effect of ignition by hot wire and black powder on pressure traces of experimental rocket motor (adopted from Ref. 17, Fig. 7).

experimental rocket motor. They also observed that the ignition by a hot wire (simulating a gasless igniter) resulted in a much longer ignition and flame-spreading interval than that with black powder (see Fig. 9). A comparison of measured and computed nondimensional pressure and burning area obtained with a hot wire igniter by Parker et al. is shown in Fig. 10.

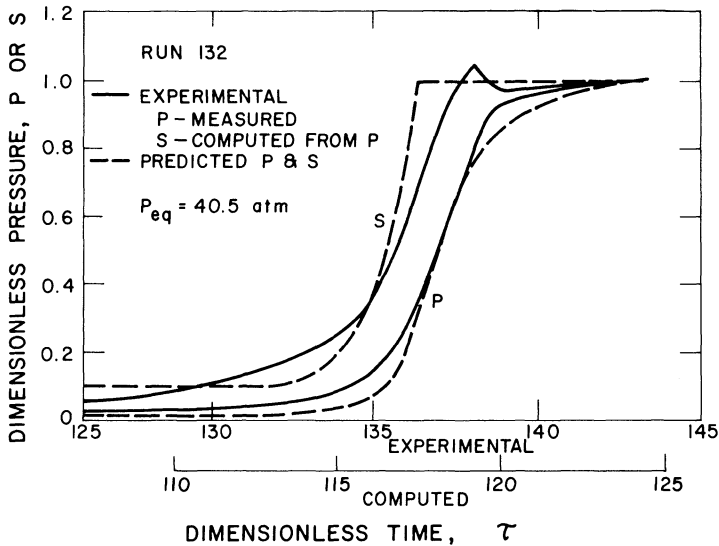


Fig. 10 Comparison of predicted and measured dimensionless pressure (P) and burning area (S) (adopted from Ref. 17, Fig. 12).

Most et al.<sup>18-20</sup> observed experimentally the effects of igniter mass and mass flow rate and the effect of the addition of aluminum to the propellant. Figure 11 shows the effect of variation in the igniter mass flow rate when the total igniter mass remained constant. A gas torch (methane/oxygen) igniter was used in the experiments. It was observed that when the igniter mass flow rate was reduced, a hang-fire developed due to longer preheating of the propellant grain (C-4 in Fig. 11). It was also noted that the model did not do a good job in predicting marginal ignition (hang-fire) situations. Addition of aluminum to the propellant did not affect flame-spreading behavior; however, it did change the pressure transient due to the influence of aluminum on the propellant burning rate.

Sforzini and Fellows<sup>21</sup> also presented a simplified dynamic temperature analysis. The flame-spreading rate was treated as a phenomenological constant, the value of which was deduced by comparison of theoretical and experimental results. Empirical induction intervals were required to predict pressure transients of three different motors.

One-dimensional, quasisteady  $p(x)$  models have been used to analyze solid propellant rocket motors with high volumetric loading density and low port-to-throat area ratios.<sup>22</sup> In these models,<sup>23-25</sup> the motor was divided into a number of consecutive control volumes along the axis, and

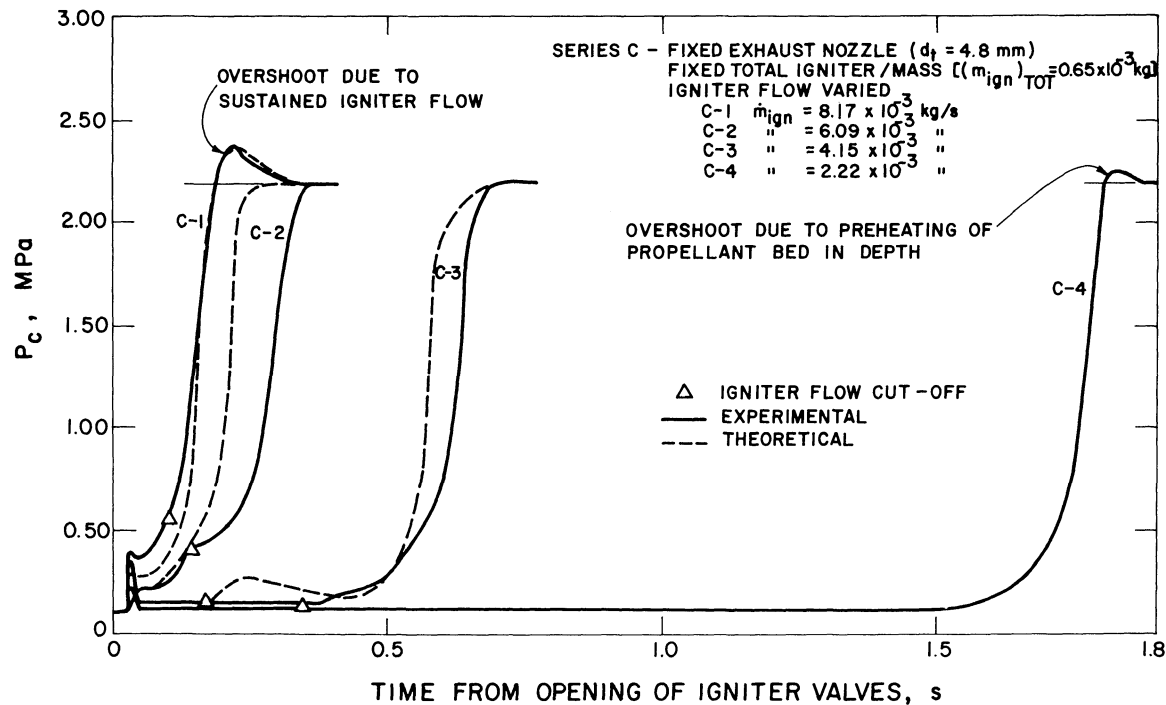


Fig. 11 Effect of igniter flow rate on ignition transient (adopted from Ref. 19, Fig. 11).



one-dimensional, steady-state gas-flow equations were written for the elements. These models allow for variation in flow and burning surface area, and in burning rate along the motor axis. However, the flame-spreading rate is required as a prescribed input to the model, and the induction interval is usually not taken into account. Due to the nature of the models, pressure peaks observed during the ignition transient are attributed only to erosive burning and friction losses along the motor.

The general calculation procedure employed in the quasisteady models is as follows: The head-end pressure is approximated to establish the gas generation rate at that location; steady-state equations for each increment are successively solved until the nozzle-entrance pressure is obtained; predicted stagnation pressure at the nozzle entrance is compared with that necessary for passage of the calculated total mass flow rate through the given nozzle throat area; an iterative procedure is used until the two values of nozzle pressure converge. This procedure is repeated for each step in the transient.

Both the lumped chamber parameter  $p(t)$  and quasisteady  $p(x)$  models are inadequate to describe the ignition transient of rocket motors with high volumetric loading density and small port-to-throat area ratio frequently combined with large length-to-diameter ratios. For such motors, the chamber parameters cannot be considered uniform throughout the motor, nor can they be treated in a quasisteady manner if the entire ignition transient is to be predicted. Peretz et al.<sup>26,27</sup> conducted an experimental and theoretical study of starting transients in high-velocity transient (HVT) motors. The model was successfully used by Caveny et al.<sup>28,29</sup> to predict thrust transients of large solid rocket motors. This appears to be the most complete model proposed to date. A discussion of this model is given below.

The basic assumptions used in the analytical model of Peretz et al.<sup>26,27</sup> are as follows:

- 1) All chemical reactions occur on the propellant surface in a thin planar zone.
- 2) Flow in the chamber is one dimensional.
- 3) Rate processes at the propellant surface are quasisteady; i.e., their characteristic times are short compared to that of the pressure transient.
- 4) Propellant combustion products and pyrogen igniter gases have the same specific heats and molecular weight.
- 5) Gases obey the perfect gas law.

It should also be noted that the solid phase is treated as a nonreactive material prior to ignition. Local ignition

is defined as attainment of a critical temperature at the propellant surface, and flame spreading is defined as the successive ignition of propellant surface elements.

The mathematical formulation of the model, which was compatible with their experimental setup, consists of the following:

1) mass, momentum, and energy conservation equations in unsteady, one-dimensional form for the gas phase;

2) equation of state for the gas flowing in the motor;

3) proper initial conditions at the start of the transient (onset of igniter flow);

4) two boundary conditions at the fore end of the propellant section (obtained from a pair of ordinary differential equations) which describe the rate of change of pressure and temperature in the entrance section;

5) a third boundary condition, which describes gas velocity at the entrance to the motor nozzle for either choked or unchoked flow;

6) semiempirical correlations for the convective heat-transfer and friction coefficients for the highly turbulent flow in the port;

7) burning rate law for the solid propellant, including effects of initial temperature, pressure, and velocity (erosive burning);

8) a solid-phase heatup equation for determining propellant surface temperature during the induction interval, coupled to an ignition criterion for the solid propellant.

The governing gas-phase equations under the assumptions discussed are conservation of mass:

$$\frac{\partial \rho}{\partial t} + \frac{\partial (\rho u)}{\partial x} + \frac{\rho u}{A_p} \frac{\partial A_p}{\partial x} = \frac{r \dot{P}_b}{A_p} \rho_{pr} \quad (3)$$

conservation of momentum:

$$\frac{\partial (\rho u)}{\partial t} + \frac{\partial (\rho u^2)}{\partial x} + \frac{\rho u^2}{A_p} \frac{\partial A_p}{\partial x} + \frac{P_b}{A_p} \rho u = - \frac{\partial p}{\partial x} - \frac{\tau_w P_w}{A_p} \quad (4)$$

conservation of energy:

$$\frac{\partial (\rho A_p E)}{\partial t} + \frac{\partial (\rho A_p u E)}{\partial x} = - \frac{\partial (A_p p u)}{\partial x} - q_{\ell} P_w + \rho_{pr} r \dot{P}_b h_f \quad (5)$$

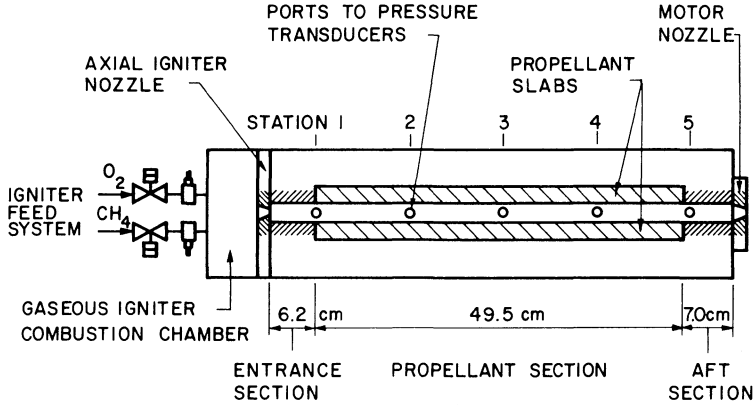


Fig. 12 Experimental rocket motor for starting transients (adopted from Ref. 26, Fig. 2).

where  $q_l$  is the rate of (convective) heat loss to propellant and nonpropellant port walls.

The above conservation equations do not include the following terms, which were found to be negligible in an order of magnitude analysis: rate of mass accumulation in the free volume created by the propellant surface regression (as compared to the rate of mass addition due to burning); axial viscous stress; and axial heat conduction. The wall friction at any axial location is neglected after onset of ignition.

Initial conditions for the gas-phase equation are

$$u(0,x) = u_i, \quad T(0,x) = T_i, \quad p(0,x) = p_i \quad (6)$$

The two physical boundary conditions at the head end of the motor are obtained by writing continuity and energy equations for the entrance section (see Fig. 12). They describe the rate of change of pressure and temperature in the entrance section:

$$\begin{aligned} \frac{dp_{es}(t)}{dt} = \frac{1}{V_{es}} & \left( \gamma R T_{ig} \dot{m}_{ig}(t) - \gamma A_{p,es} p_{es}(t) u_{es}(t) \right. \\ & \left. - \frac{(\gamma-1) A_{p,es} p_{es}(t) u_{es}(t)^3}{2 R T_{es}(t)} \right) \end{aligned} \quad (7)$$

$$\frac{dT_{es}(t)}{dt} = \frac{1}{V_{es}} \left[ \frac{RT_{es}(t)\dot{m}_{ig}(t)}{p_{es}(t)} [\gamma T_{ig} - T_{es}(t)] - (\gamma-1)A_{p,es}u_{es}(t) \left( T_{es}(t) + \frac{u_{es}(t)^2}{2R} \right) \right] \quad (8)$$

The igniter mass flow rate  $\dot{m}_{ig}$  is assumed to be a prescribed input determined from experiments. Simultaneous integration of Eqs. (7) and (8) determines two boundary conditions at the head end. The boundary conditions at the aft end of the motor are obtained by assuming isentropic flow through the exit nozzle, and is given by

$$u_E(t)^2 = \frac{\frac{2}{\gamma-1} RT_E(t)}{\left[ \left( \frac{A_p}{A_t} \right)^2 \left( \frac{p_t(t)}{p_E(t)} \right)^{-\frac{2}{\gamma}} - 1 \right]} \left[ 1 - \left( \frac{p_t(t)}{p_E(t)} \right)^{\frac{\gamma-1}{\gamma}} \right] \quad (9)$$

When the flow through the nozzle is unchoked, the pressure at the nozzle throat equals the ambient pressure. When the nozzle is choked, Eq. (9) has the following implicit form:

$$u_E(t)^2 = \frac{\gamma RT_E(t)}{(A_p/A_t)^2} \left( \frac{2}{\gamma+1} + \frac{\gamma-1}{\gamma+1} \frac{u_E(t)^2}{\gamma RT_E(t)} \right)^{(\gamma+1)/(\gamma-1)} \quad (10)$$

Empirical correlations must be used for the friction coefficient, convective heat-transfer coefficient, and burning rate law. Peretz et al.<sup>26,27</sup> used a modified Dittus-Boelter equation for the convective heat-transfer coefficient, and a modified Colebrook's expression<sup>30,31</sup> for the friction coefficient. The burning rate law takes into account the effect of the erosive burning rate by using a modified Lenoir-Robillard<sup>32</sup> expression.

The propellant surface temperature before the onset of ignition is obtained by considering the heat equation for the solid phase and employing an integral solution method. The resulting ordinary differential equation, which describes the variation of propellant surface temperature

## Chapter 7

### Steady-State Burning of Homogeneous Propellants

G. Lengellé,\* A. Bizot,\* J. Duterque,\* and J. F. Trubert\*  
*Office National d'Etudes et de Recherches Aéronautiques (ONERA)*  
*Châtillon, France*

#### Abstract

Homogeneous (or double-base) propellants are still often used in small- to medium-sized rockets because of their smokeless qualities and the possibilities they offer of particular shapes and small burning thicknesses through rolling and extruding processes. Although their ingredients are premixed, their flame structure is very complex, since the flame is the stage of many chemical reactions. Much detailed work has been carried out on the processes of the condensed phase, revealing that they are essentially untouched by the super-rate and plateau-producing lead additives. The interaction of these additives is to be found in the primary flame zone, which is enhanced. Although much is known about the combustion of double-base propellants, a true understanding of the various burning rate laws observed is still far from realization.

#### Nomenclature

(The values used for representative computations are indicated.)

- $B_c$  = pre-exponential factor in the condensed-phase propellant degradation kinetics,  $s^{-1}$   
 $B_{g,c}$  = pre-exponential factor in the condensed-phase  $NO_2$  recombination kinetics,  $s^{-1}$   
 $B_{g1}$  = pre-exponential factor in the primary flame kinetics,  $s^{-1}$

$B_{g2}$	= pre-exponential factor in the secondary flame kinetics, $\text{cm}^3/\text{mole.s}$
$c_p$	= specific heat capacity of propellant, assumed constant ( $0.35 \text{ cal/g.}^\circ\text{C}$ )
$c_g$	= specific heat capacity of gases, $\text{cal/g.}^\circ\text{C}$ , (average value $0.35 \text{ cal/g.}^\circ\text{C}$ )
$d_p$	= propellant thermal diffusivity, $\lambda_p/\rho_p c_p$ , assumed constant ( $1.3 \times 10^{-3} \text{ cm}^2/\text{s}$ )
$D_g$	= coefficient of gaseous diffusion, $\text{cm}^2/\text{s}$
$E_c$	= activation energy for the propellant degradation ( $40 \text{ kcal/mole}$ )
$E_{g,c}$	= activation energy for the condensed-phase $\text{NO}_2$ recombination (unknown)
$E_{g1}$	= activation energy for the primary flame overall reaction ( $\approx 5 \text{ kcal/mole}$ , from Zenin <sup>20</sup> and ONERA)
$E_{g2}$	= activation energy for the secondary flame overall reaction ( $\approx 50 \text{ kcal/mole}$ , from Zenin <sup>20</sup> )
$\mathcal{E}_c$	= $E_c / R T_s$
$\mathcal{E}_{g2}$	= $E_{g2} / R T_{f2}$
$h^\circ$	= specific enthalpy of formation at 0 K, $\text{cal/g}$
$m_1, m_2$	= overall reaction order in primary and secondary flames (1 and 2)
$M$	= average gas molar mass, $\text{g/mole}$
$\dot{m}$	= mass flux through the combustion wave, $\text{g/cm}^2.\text{s}$
$n$	= pressure exponent in burning rate law
$p$	= pressure
$q(0)$	= heat flux density from the gas phase at the surface, $\text{cal/cm}^2.\text{s}$
$Q_c$	= heat evolved per gram of propellant initially degrading in the condensed phase, $< 0$ (unknown)
$\Delta Q_c$	= $c_g T_s - c_p T_0 - Q_s$
$Q_{g,c}$	= heat evolved per gram of $\text{NO}_2$ reacting in the condensed phase, $> 0$ (unknown)
$Q_{g1}$	= heat evolved in the primary flame or total
$Q_{g2}$	(primary plus secondary) flame at high pressure, based on enthalpies of formation
$Q_s$	= heat evolved in the superficial degradation layer (from 60 to $\approx 120 \text{ cal/g}$ , Fig. 12)
$R$	= universal gas constant, $\text{cal/mole.}^\circ\text{C}$
$T$	= temperature, $T_0$ initial, $T_s$ at surface, $T_{f1}$ at end of primary flame, $T_{f2}$ at end of secondary flame
$v_b$	= burning rate, $\text{cm/s}$
$x$	= coordinate normal to the surface, $> 0$ into the gas phase
$Y$	= mass fraction

- $Y_{NO_2,0}$  = mass fraction of  $NO_2$  potentially available in the propellant  
 $\lambda_p$  = propellant conductivity, assumed constant ( $7.5 \times 10^{-4}$  cal/cm.s. $^{\circ}C$ )  
 $\lambda_g$  = gas conductivity, cal/cm.s. $^{\circ}C$ , average value  
 $\lambda_{g,s}$  = at surface (values from Zenin,<sup>21</sup> at 650 K for example,  $1.63 \times 10^{-4}$ )  
 $\rho_p$  = propellant specific mass ( $1.64$  g/cm<sup>3</sup>)

## I. Introduction

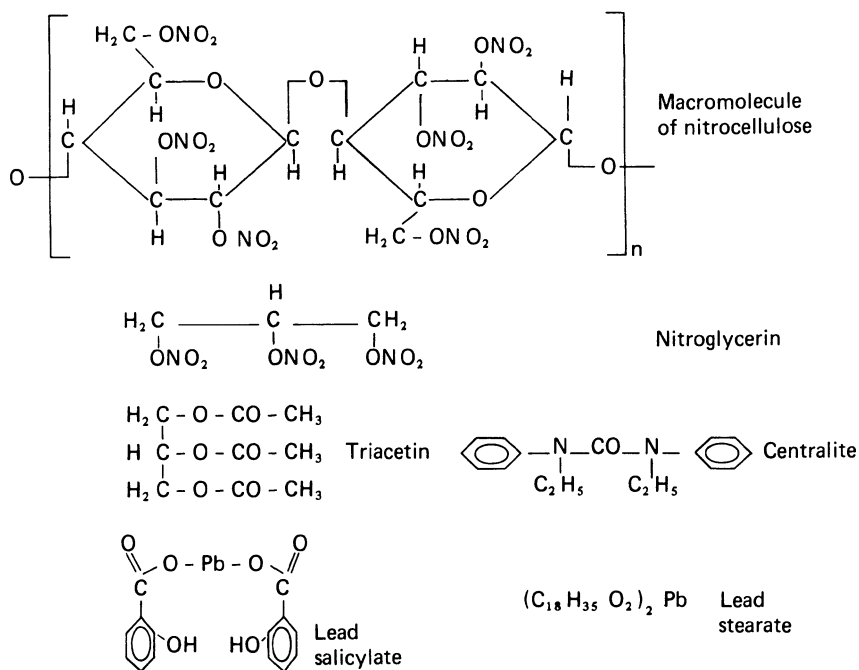
Homogeneous propellants have been used in guns since the last decades of the 19th century and in rocket motors since the years before World War II. These propellants, based on nitrocellulose and nitroglycerin, are still very much in use in small- to medium-sized rocket motors. Compared to composite propellants based on ammonium perchlorate, aluminum and a polymeric binder, their specific impulse is lower, but they are "smokeless," they do not generate hydrogen chloride, which condenses rather easily in the presence of the water vapor in the plume of the rocket motor. When used in small motors, they are rolled or extruded in various shapes and very small burning thicknesses not possible in other propellants. In medium-sized motors they are put into use through processes close to casting. In this latter case, the tendency is to increase their specific impulse with the addition of oxidizers such as cyclotetramethylene-tetranitramine (HMX), while at the same time retaining their smokeless quality. It has been shown in many references that the combustion behavior of such composite-modified double-base propellants is very much dominated by the energetic binder. On the other hand, when the double-base binder is associated with an oxidizer such as ammonium perchlorate, the combustion behavior of the resulting propellant is closer to that of a composite propellant.

From the viewpoint of a detailed investigation of the combustion, double-base homogeneous propellants seem attractive, since their components are premixed; their flames are controlled by one-dimensional chemical processes, rather than by complex three-dimensional diffusion processes as is the case for composite propellants; and the flames should be more amenable to analysis, both theoretical and experimental. However, as will be seen, the flames of double-base propellants involve many chemical reactions and a true understanding of their structure has not yet been acquired.

Double-base propellants are made in a number of ways. When they are rolled or extruded, the components are

nitrocellulose and nitroglycerin, to which some stabilizers such as centralite and plasticizers are added, see Fig. 1. When they are cast, a casting powder (made of nitrocellulose, some nitroglycerin, and the various additives) is swelled within the mold by a liquid mixture of nitroglycerin and triacetin. The grain thus obtained is then inhibited and used free standing in the motor. The propellant ingredients can also be stirred, cast, cross linked, and the grain case bonded.

Depending on the relative amounts of nitrocellulose and nitroglycerin, the energetic level of the propellant can be increased or, in the usual terminology, its "heat of explosion" or "calorimetric value," that is, the heat evolved in a calorimetric bomb by combustion under an inert atmosphere. One can then talk about "cool" and "hot" compositions.



Hot propellant used at ONERA (extruded)

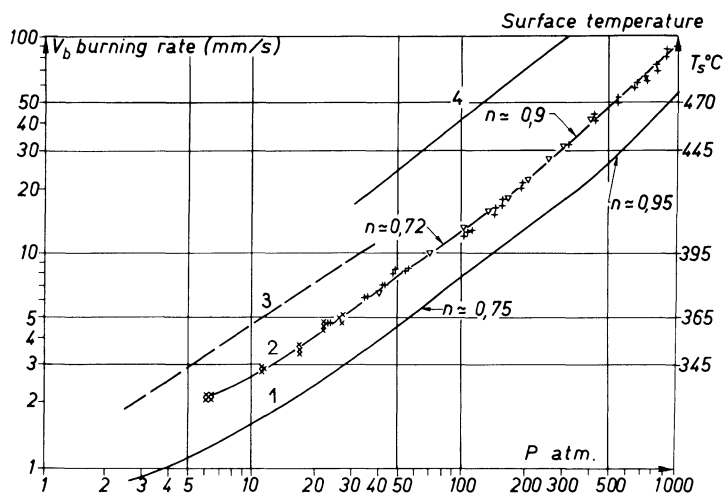
52.25 % nitrocellulose	- 42.75 % nitroglycerin
- 3 % centralite	- 2 % plasticizer

1100 cal./g heat of explosion

Fig. 1 Double-base propellant components.



Double-base propellants are used in small- and medium-sized rockets and are thus exposed to varying ambient temperatures. The sensitivity of the motor operation to temperature depends upon the propellant burning rate sensitivity to both the temperature and the pressure. As can be seen on Fig. 2, the pressure exponent, in the usual empirical law  $v_b \sim p^n$ , is around 0.7 and increases to nearly 1 at high pressure. Super-rate effects (Fig. 3) are created by the use of additives, most often lead salts, some examples of which are shown in Fig. 1. At the end of the super-rate zone, the burning rate falls back to that of the control propellant, with the occurrence of a nearly zero pressure exponent zone, a "plateau" effect, or a negative pressure exponent zone, a "mesa" effect. These terms are used by analogy with topographical features. It is only in these reduced pressure exponent zones that the propellant is used to minimize the motor operation sensitivity to ambient temperature. Due to this fact, the study of the combustion



- 1 "Cool" propellant, 820 cal./g
- 2 + x "Hot" propellant, 1100 cal./g
- ▼ "Hot" propellant, 1100 cal./g, Ref. 30
- 3 "Hot" propellant, 1320 cal./g, Ref. 12
- 4 Pure nitroglycerin 1770 cal./g.

Figures for the surface temperature are obtained from the average curve of Fig. 11a.

Fig. 2 Burning rate laws of control double-base propellants.

of propellants without additives should be conceived only as a first step leading to an understanding of modified (that is, with additives) propellants.

The first mention of the effect of lead additives upon the burning rate of double-base propellants is attributed to Avery, Preckel, and Camp.<sup>1-3</sup> References 4 and 5 are the first widely circulated publications on this subject. References 6-29 are of a general nature and many results will be drawn from them in this paper. They will be discussed briefly in this section. The following references are more specialized and will be introduced in the course of the paper.

As early as 1950,<sup>6-12</sup> basic studies gave a good understanding of the combustion of unmodified double-base propellants, most notably those of Heller and Gordon<sup>12</sup> of the U.S. Naval Ordnance Test Station (now the Naval Weapons Center), which examined the temperature and chemical composition in detail. For modified propellants in general, Refs. 13-19 are representative of the work carried out in the United States; Refs. 20-23 report work performed in the Soviet Union on reference and modified propellants.

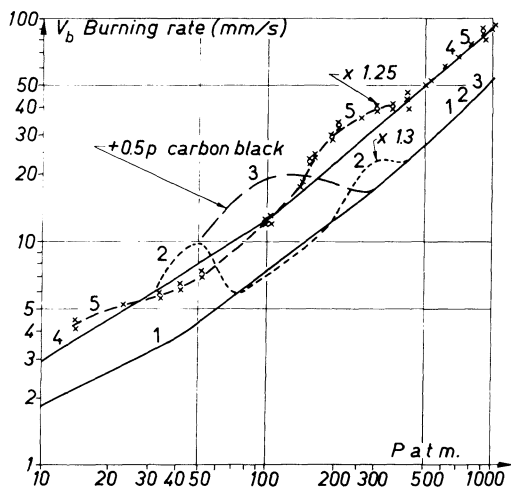


Fig. 3 Super-rate effects.

- 1 Control cool propellant, 820 cal./g
- 2 Cool propellant + 2p.\* lead salt
- 3 Cool propellant + 2p. lead salt + 0.5p carbon black
- 4 Control hot propellant, 1100 cal./g
- 5 Hot propellant + 2p. lead salt.

\*Meaning 2 parts of additive per 100 parts of propellant.

Zenin<sup>20-22</sup> of the Institute of Chemical Physics, USSR Academy of Sciences, made some excellent explorations of combustion wave temperatures, the results of which will be cited repeatedly herein. Hewkin and his colleagues,<sup>24,25</sup> of the British Explosives Research and Development Establishment, conducted an extensive experimental program on modified propellants and developed several ideas to explain the action of the additives. The work of Kubota<sup>26-28,60</sup> at Princeton University and the Technical Research and Development Institute, Japan Defense Institute, is very extensive and its results will be cited frequently in the following sections. Finally, the work of ONERA was summarized in Ref. 29.

This paper draws from these references. Many of the statements herein should be viewed as propositions only, since the various suggested mechanisms are not in fact truly established facts. A double-base propellant combustion wave structure is rapidly described in Sec. II and the observed burning rate laws in the presence of additives in Sec. III. The condensed- and gas-phase processes are covered in the next two sections. Section VI describes the mechanisms thought to occur in the super-rate and plateau ranges.

## II. General Behavior and Flame Structure of Homogeneous Propellants

From the works mentioned previously it is possible to describe the combustion wave structure of double-base propellants, in particular its chemical processes, see Figs. 4-6. The various data will be discussed and justified later.

The propellant components (Fig. 1) pass unaffected through a preheated zone of a few tens of micrometers in a few milliseconds and reach a superficial degradation zone (or "foam" zone in the early literature) where the temperature becomes high enough for the molecular degradation to take place, initiated by the rupture of the C-O-NO<sub>2</sub> bond. Simultaneous recombination occurs so that a mixture of NO<sub>2</sub>, aldehydes, but also NO emerges from the surface and the net energy balance of the degradation is exothermic. At pressures under about 100 atm, a clearly separated primary flame ("fizz" zone) and a secondary flame ("luminous" flame) are observed, the first involving NO<sub>2</sub>-aldehydes reactions and the second NO-CO and NO-H<sub>2</sub> reactions. In this pressure range the secondary flame is too far away to have any effect on the surface or even to induce a temperature gradient into the primary flame. The

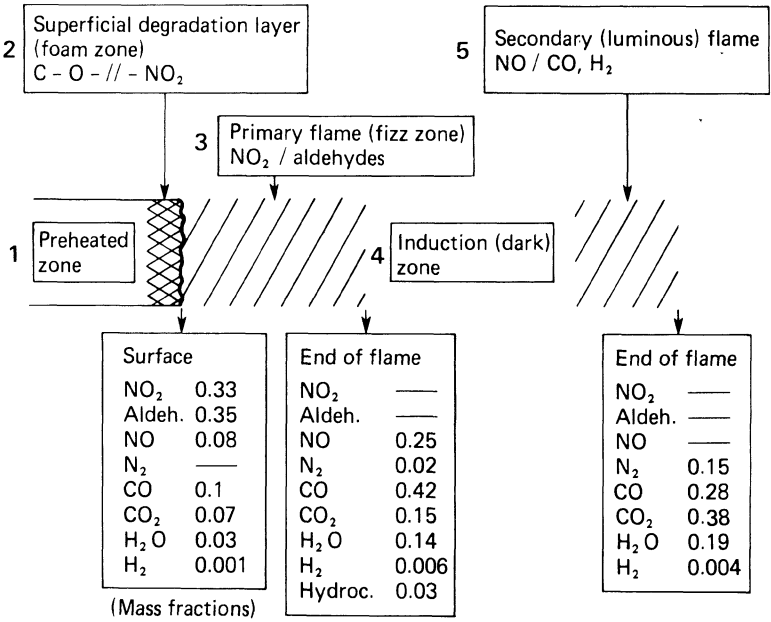


Fig. 4 Various zones in the combustion of a double-base propellant.

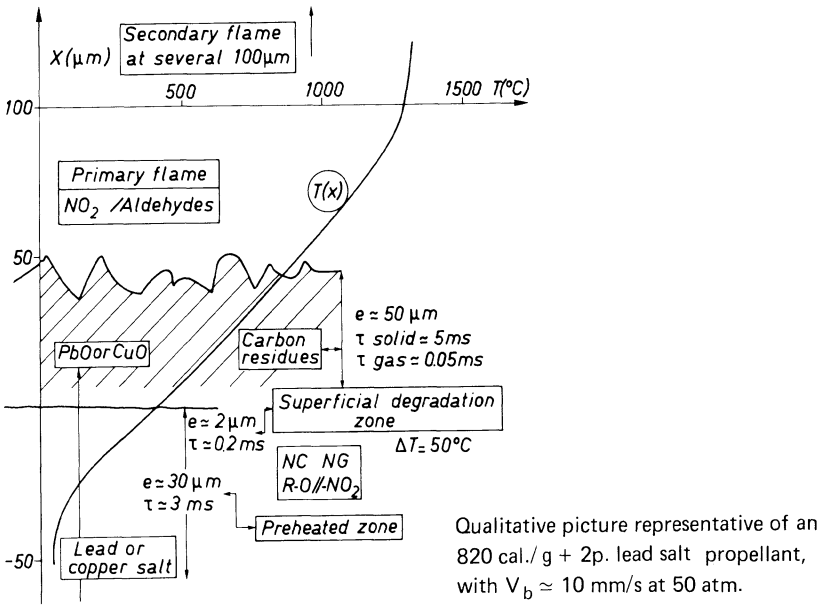
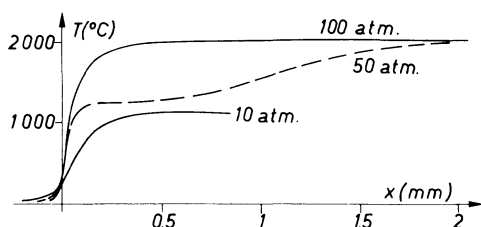


Fig. 5 Zones of the combustion.



Pressure atm.	10	50	100
$V_b$ mm/s	1.9	6.7	10.6
$T_s$ , °C	330	380	400
Preheated zone, $\mu\text{m}$ (measured/computed)	140/155	50/45	45/28
Residence time in preheated zone, ms	80	7	3
Superficial degradation zone $\mu\text{m}$	9	3	2
Residence time in superficial zone, ms	5	0.4	0.15
Flame thickness, $\mu\text{m}$ (measured)	200	75	110 (secondary flame)

Measured results from Zenin, Ref. 21

Fig. 6 Characteristics of the combustion zones.

burning rate is then entirely under the influence of the latter. This corresponds to a burning rate/pressure law with a 0.7 pressure exponent (Fig. 2). As the pressure increases, the secondary flame perturbs and then merges into the primary flame and a transition is observed to a zone with a pressure exponent close to 1. When the secondary flame is fully developed, even at pressures for which it does not yet influence the burning rate, the final products ( $\text{N}_2$ ,  $\text{CO}$ ,  $\text{CO}_2$ ,  $\text{H}_2\text{O}$ , and  $\text{H}_2$ ) and the final temperature (2100–2900 K, depending on the heat of explosion) are realized.

The data of Figs. 5 and 6 show clearly that the combustion zone thicknesses are very small, rendering detailed investigations very difficult and making it necessary to

use thermocouples with sizes down to a few micrometers.<sup>20,21,26</sup> The residence times are of the order of milliseconds in the condensed phase and of tens of microseconds in the gas phase. A number of studies have been carried out at lower temperatures and at times on the scale of tens of minutes by techniques such as thermogravimetry, differential thermal analysis, etc. The question must always be raised about how to extrapolate the results to the higher temperatures and much shorter times involved in the actual combustion of the propellant.

The consideration of a few relations that characterize the combustion process will help to explain the different ways an additive can be thought a priori to act. The burning rate will result from physicochemical processes that are summarized by the following relations, which will be fully established in subsequent sections. The burning rate and surface temperature are related by a pyrolysis law,

$$v_b \sim \exp(-E_c / 2 R T_s) \quad (1)$$

The regression of the surface is related to the heat flux from the gas phase via the conservation of energy at the surface

$$q(0) = \lambda_{g,s}(dT/dx)_{g,s} = \rho_p v_b (c_g T_s - c_p T_0 - Q_s) \quad (2)$$

The heat flux results from the heat evolved in the gas flame, following the kinetics of that flame, and is expressed as

$$q(0) = f(T_{f1}, T_s, Q_{g1} \dots) p^{m1/2} B_{g1} \exp(-E_{g1} / 2 R T_{f1}) \quad (3)$$

Finally, an energy balance between the propellant at the initial temperature and the end of the primary flame is expressed as

$$c_g T_{f1} = c_p T_0 + Q_s + Q_{g1} \quad (4)$$

the same applying with the values relative to the end of the secondary flame.

The set of Eqs. (1-4) determines the four unknowns,  $T_s$ ,  $T_{f1}$  (or  $T_{f2}$ ),  $q(0)$  and  $v_b$ . As will be seen later, Eq. (1) shows that  $T_s$  varies moderately with  $v_b$  due to the high activation energy  $E_c$ . The heat flux is modified [Eq. (3)] by any change in the flame temperature or kinetics. The flame temperature is changed by any modification of the gas

composition [Eq. (4)]. Finally, the burning rate [Eq. (2)] follows changes in  $q(0)$  and  $Q_s$ , the impact of  $T_s$  being moderate since it varies little. As an example from the results of Zenin<sup>21</sup> at 50 atm,  $q(0)$  is measured to be  $\approx 24.5$  cal/cm<sup>2</sup>.s; see Fig. 6. The ratio of the heat flux from the gas flame to that from the condensed-phase reaction is then

$$q(0) / \rho_p v_b Q_s \approx 0.21$$

Any change brought about by the additive in the condensed-phase processes could then have a large impact on the burning rate. From the measured flame temperatures of Fig. 6 and Eq. (4), one can evaluate the heat evolved in the primary flame  $Q_{g1}$  (e.g., at 50 atm) and  $Q_{g2}$ , the total heat evolved in the gas phase when the final temperature is reached,

$$Q_{g1} \approx 320 \text{ cal/g}, \quad Q_{g2} \approx 600 \text{ cal/g}$$

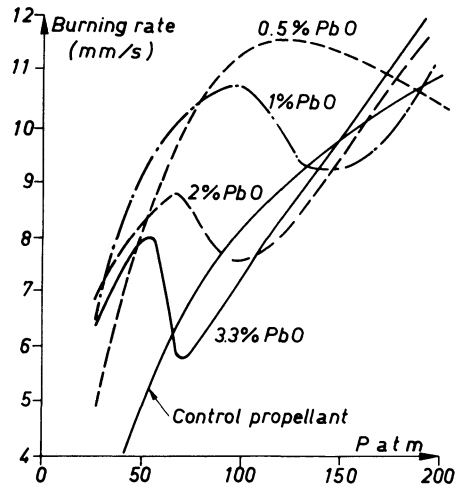
Any modification that brings some of the energy available in the secondary flame closer to the surface will then have a large influence on the burning rate.

### III. Burning Rate Laws: Influence of Additives

The burning rate of a double-base propellant is, at a given pressure, related primarily to its heat of explosion. Figure 2 shows this trend from a "cool" propellant to pure nitroglycerin. As the pressure increases, a shift in the pressure exponent from  $\approx 0.7$  to  $\approx 1$  is observed, the change in slope occurring at a lower pressure as the heat of explosion increases.

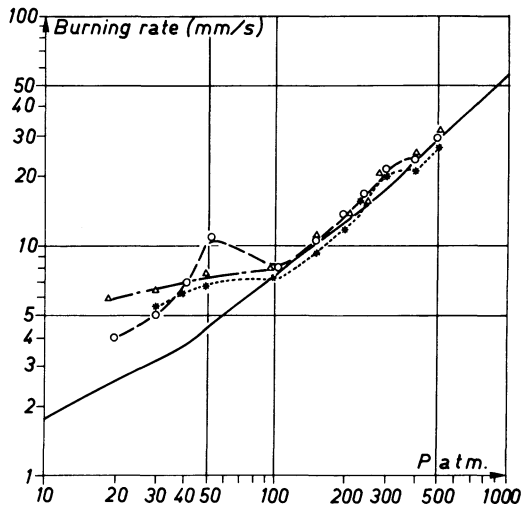
In the presence of lead salts, cool propellants give rise to strong super-rate and mesa effects, as shown in Fig. 3. Hot propellants have lower super rates located at lower pressures. The magnitude of the super rate might depend on the details of the fabrication.<sup>31</sup> This has also been observed at ONERA and it seems to be primarily a problem of thorough additive distribution in the propellant. The super-rate range can be extended to higher pressures by the addition of small quantities of carbon black (Fig. 3), if its size is small enough (under a few tenths of a micrometer).<sup>4,5</sup>

The results presented here and in most of the literature cited were obtained on strands burning in pressurized vessels. It can be shown that within experimental error they are representative of the burning in motors, provided that they operate under nonerosive conditions.



Results of Hewkin, Ref. 24.

Fig. 7a Effect of lead compound concentration.



- △ Cool propellant, 820 cal./g, + 0.73 p. PbO
- Cool propellant, 820 cal./g, + 1.57 p. lead salicylate  
(→ 0.73 PbO)
- \* Cool propellant, 820 cal./g, + 2.52 p. lead stearate  
(→ 0.73 PbO).

Fig. 7b Super rates with various lead compounds.



A second super-rate effect is observed in Fig. 3 for both cool and hot compositions with a comparable magnitude and pressure range. A careful review of the literature shows that either control propellants are studied in a large pressure domain or modified propellants are usually investigated in a limited pressure range. This is the case for the work of Kubota,<sup>26-28</sup> Hewkin,<sup>24,25</sup> Denisjuk.<sup>23</sup> Any detailed work found in the literature on the effects of additives is for the first super rate. A few comments relative to the second super rate will be presented in Sec. VI.

A number of observations has been made with respect to the first super rate. It has been found that the effect of the lead (or copper) salt particle size is moderate,<sup>26</sup> while an increase in the amount of lead compounds shifts the super-rate range to lower pressures; see Fig. 7a (from Hewkin<sup>24</sup>) and also Preckel.<sup>4</sup> It seems that, when compared on the criterion of the amount of PbO residue they can give after decomposition, lead compounds have a fairly similar effect, particularly with regards to the pressure range (Fig. 7b). No dramatic differences, comparable, for example, to the effect of small amounts of carbon black, as shown on Fig. 3, are observed between aliphatic and aromatic salts, or simply PbO. This contradicts somewhat the conclusions of Preckel.<sup>5</sup> Other lead oxides such as PbO<sub>2</sub> and Pb<sub>3</sub>O<sub>4</sub> have also been found to be effective in creating super-rate effects.<sup>25</sup>

The results of Fig. 8a show that carbon black by itself is slightly effective in creating a super rate, a result also found by Kubota.<sup>26</sup> A copper compound by itself, CuO in this case, has little effect, which is also observed by Denisjuk<sup>23</sup> and Kubota<sup>26</sup> (for copper salicylate). However, Eisenreich<sup>53</sup> finds copper salicylate to give slight super-rate and plateau effects. It is when copper compounds are associated with lead compounds that very important super rates are obtained. Reference 30 shows how an extensive empirical research of copper and lead salts can produce plateau effects with high burning rates of important practical interest, see Fig. 8a.

It is seen in Fig. 8b that a metallic oxide, Fe<sub>2</sub>O<sub>3</sub>, which is often used in composite propellants based on ammonium perchlorate, has no effect on the burning rate of a double-base propellant when introduced with a particle size comparable to that of the lead compounds used in the propellants of the previous figures. However, when Fe<sub>2</sub>O<sub>3</sub> with a large particle size is introduced, a more or less constant super rate is observed. This has also been observed by Hewkin<sup>24</sup> for a size  $\approx 140 \mu m$  and for a variety of metallic oxides. It seems that in the case of large

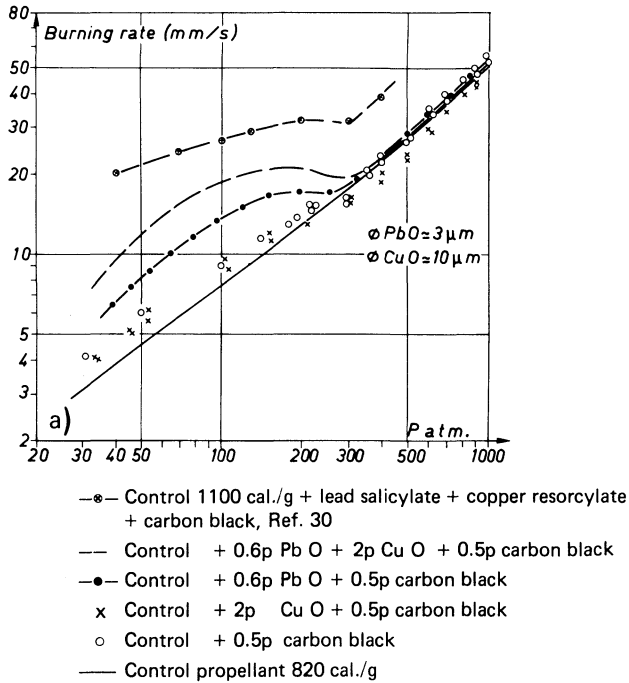


Fig. 8a Activity of copper and lead compounds.

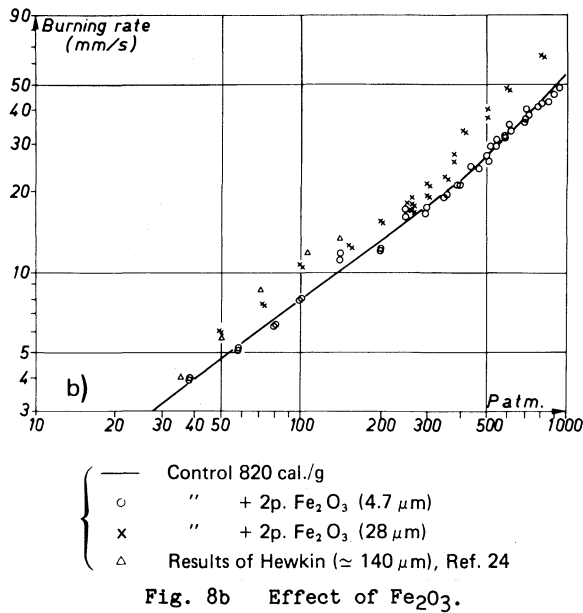


Fig. 8b Effect of  $Fe_2O_3$ .

particles a flame holder effect results that is similar to what is thought to occur when metallic oxides increase the burning rate of composite propellants, in which the flame attaches to the particles protruding from the surface and increases the heat flux to the surface. Such an effect therefore seems different from what occurs when small-size particles of lead compounds are used, for which the effect is probably a chemical interaction.

Many of the results presented in this section cannot be truly explained by the detailed consideration of the combustion mechanisms presented in the following sections. At most, ideas can be presented and trends rationalized. Any search for specific results, such as the precise burning rate levels in a plateau in a given pressure range, will have to be empirical.

#### IV. Detailed Study of the Combustion Mechanisms in the Condensed Phase

As was said in Sec. II, in the condensed phase the propellant components undergo a preheated zone through which they remain essentially intact and a superficial zone in which they are degraded into gases (Figs. 4-6). In this degradation process, it is likely that the initial step is the  $\text{CO} \leftrightarrow \text{NO}_2$  bond breaking. Simultaneously, recombination reactions involving  $\text{NO}_2$  occur, so that the amount of this species coming off the surface is less than what is contained in the initial molecules and the net energy evolved in the degradation is exothermic. The kinetics and energetics of this degradation, the nature of the gases, and the behavior of the additive in the condensed phase will be considered.

#### Degradation of the Propellant

The consideration of the characteristic equations of the processes will lead to estimates of the quantities involved. The conservation of energy, assuming average constant thermal properties, outside of the superficial zone and in a coordinate system tied to the regressing surface with  $x$  positive into the gas phase, is expressed as

$$\rho_p v_b c_p (dT/dx) = d(\lambda_p dT/dx)/dx \quad (5)$$

so that the temperature profile is

$$[T(x) - T_0] / [T_s - T_0] = \exp(x v_b / d_p) \quad (6)$$

The thickness of the preheated zone can be conventionally defined from

$$T(e_{\text{preh}}) - T_0 = (1/10) (T_S - T_0)$$

that is

$$e_{\text{preh}} = (\ln 10) (d_p / v_b) \quad (7)$$

The superficial degradation zone thickness can be defined from the temperature at which the degradation rate has dropped to one-tenth of its value at the surface; the temperature drop  $\Delta T_{\text{react}}$  is then

$$\exp [-E_c / R (T_S - \Delta T_{\text{react}})] = (1/10) \exp [-E_c / R T_S]$$

$$\Delta T_{\text{react}} / T_S = 1 / (1 + E_c / \ln 10) \approx (\ln 10) / E_c \quad (8)$$

This temperature drop introduced into Eq. (6) gives a rough estimate of the degradation zone thickness

$$\begin{aligned} e_{\text{react}} &= -(d_p / v_b) \ln [1 - \Delta T_{\text{react}} / (T_S - T_0)] \\ &\approx (d_p / v_b) (\ln 10) (1 / E_c) T_S / (T_S - T_0) \end{aligned} \quad (9)$$

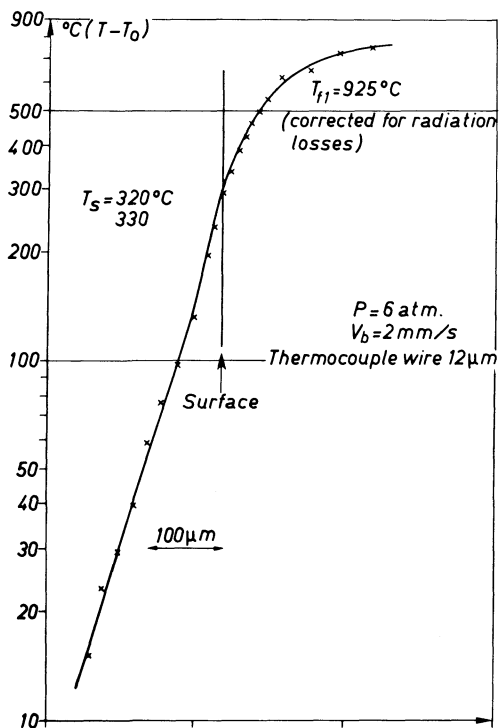


Fig. 9 Temperature profile in the condensed phase.

The numbers given on Figs. 5 and 6 for the zone thicknesses are extracted from the above equations. It is seen that the superficial degradation zone is of the order of  $1/\mathcal{E}_c$  that of the preheated zone, with  $\mathcal{E}_c \approx 30$ .

An example of a temperature profile, obtained by inserting a small thermocouple in a propellant strand, is shown in Fig. 9. Kubota<sup>26</sup> and Zenin<sup>20,21</sup> have made many such experiments with thermocouples down to a few micrometers in size. It is seen that the profile expressed by Eq. (6) is fairly well satisfied; its slope gives an estimate of a constant average thermal diffusivity  $d_p \approx 1.3 \cdot 10^{-3} \text{ cm}^2/\text{s}$ , which is in agreement with direct measurements at low temperatures.

The degradation of the components of double-base propellants, of compounds similar to these components, and of complete propellants has been studied by a number of authors. The results concerning the kinetics of the degradation are given in Table 1. It is seen that an activation energy between 35 and 40 kcal/mole and a reaction order of 0 (with respect to the specific mass of the compound remaining to be degraded) are found. Also, from the results of Aoki and Kubota,<sup>60</sup> there seems to be a given kinetics, independent of the propellant composition, meaning that the kinetics of nitrocellulose and

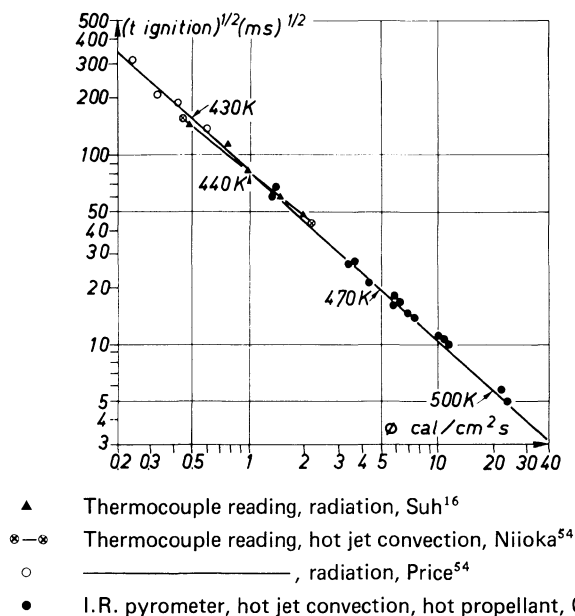


Fig. 10 Ignition of double-base propellants.

Table 1 Degradation characteristics of propellants components

Origin	Compound	Method	Activation energy kcal./mole
BAKHMAN <sup>32</sup>	CH <sub>3</sub> O-NO <sub>2</sub>	Thermal decomposition < 210 - 240° C	39.5
HICKS <sup>33</sup>	C <sub>2</sub> H <sub>5</sub> O - NO <sub>2</sub>	Combustion	38
HARTMAN <sup>34</sup>	Nitroglycerin	Thermal decomposition 90 to 160° C	34.4 ± 1.5
ALEKSANDROV <sup>35</sup>	Nitroglycerin	—————	$k = 4 \cdot 10^{13} \exp (-35 \cdot 10^3 / R \cdot T) \text{ s}^{-1}$ 0 order reaction
BAKHMAN <sup>32</sup>	Nitroglycerin	Thermal decomposition 75 to 150° C	40 - 45
PHILLIPS <sup>36</sup>	Nitrocellulose	Vacuum thermogravimetry on films, < 190° C	≈ 40
ALEKSANDROV <sup>37</sup>	Nitrocellulose	Vacuum thermogravimetry + literature results	$k = 10^{16.9} \exp (-42 \cdot 10^3 / R \cdot T) \text{ s}^{-1}$ T 70 - 300° C, 0 order reaction
ALEKSANDROV <sup>38</sup>	N powder	"Pulsed" thermogravimetry	41
AOKI/KUBOTA <sup>60</sup>	Propellants 700 to 1090 cal./g	Differential thermal analysis up to ≈ 220° C	≈ 34
SUH <sup>16</sup>	M2 propellant	Ignition studies, radiation (T <sub>s</sub> /ign. ≈ 200° C)	$k = 10^{17} \exp (-40 \cdot 10^3 / R \cdot T) \text{ s}^{-1}$ 0 order reaction
NIIOKA <sup>54</sup>	750 cal./g propellant	Ignition studies, hot jet	$k = 0.6 \cdot 10^{17} \exp (-40 \cdot 10^3 / R \cdot T) \text{ s}^{-1}$
NIIOKA/PRICE <sup>54</sup>	JPN propellant	Ignition studies, radiation	$k = 1.1 \cdot 10^{17} \exp (-40 \cdot 10^3 / R \cdot T) \text{ s}^{-1}$

nitroglycerin are probably fairly close. It is also possible to extract data on the degradation kinetics from ignition experiments. It can be shown<sup>16,39</sup> that the evolution of the time required to reach ignition with the heat flux imparted to the surface is determined by this kinetics; in particular, the value of  $E_c$  can be extracted from the slope of a representation such as that of Fig. 10. A fairly reliable (due to the large range of heat fluxes utilized) value of 40 kcal/mole is obtained. Suh,<sup>16</sup> who matched the results of a numerical approach to experiments, also gives this value. The results of Nioka,<sup>56</sup> who uses an approximate approach (previously found to be very close to a more rigorous numerical one) matched to experiments, have been recomputed to take into account  $E_c = 40$  kcal/mole; they are then very close to those of Suh.

These results on the degradation kinetics are obtained at temperatures below  $\approx 220^\circ\text{C}$ . One does not know a priori if they will apply to the combustion regime in which temperatures higher by  $100\text{--}200^\circ\text{C}$  are thought to occur at the surface (Fig. 2).

One can consider the equations representing the conservation of the nondegraded propellant with a zero-order reaction,

$$v_b d(\rho_p Y_p)/dx = - \rho_p B_c \exp(-E_c / R T) \quad (10)$$

the conservation of  $\text{NO}_2$ , with an assumed first-order recombination reaction,

$$\begin{aligned} v_b d(\rho_p Y_{\text{NO}_2})/dx = & + Y_{\text{NO}_2,0} \rho_p B_c \exp(-E_c / R T) \\ & - (\rho_p Y_{\text{NO}_2}) B_{g,c} \exp(-E_{g,c} / R T) \end{aligned} \quad (11)$$

and finally the conservation of energy,

$$\begin{aligned} \rho_p v_b c_p dT/dx = & d(\lambda_p dT/dx)/dx + Q_c \rho_p B_c \exp(-E_c / R T) \\ & + Q_{g,c} (\rho_p Y_{\text{NO}_2}) B_{g,c} \exp(-E_{g,c} / R T) \end{aligned} \quad (12)$$

Summation of Eq. (10) from the initial propellant to the surface, with  $Y_{p,0} = 1$  and  $Y_{p,s} = 0$ , results in

$$\rho_p v_b = \int_{\infty}^0 \rho_p B_c \exp(-E_c / R T) dx \quad (13a)$$

meaning that the surface regression is the result of the in-depth (although on a very small thickness) transformation of the propellant into gases. From Eq. (11)

it is obtained

$$Y_{NO_2,s} = Y_{NO_2,0} - (1/\rho_p v_b) \int_{-\infty}^0 (\rho_p Y_{NO_2}) B_{g,c} \exp(-E_{g,c} / R T) dx \quad (13b)$$

which expresses that the amount of  $NO_2$  coming off the surface is that potentially available in the initial propellant,  $Y_{NO_2,0}$ , minus that amount which has reacted in the condensed phase. Since the kinetics of the condensed-phase reaction of  $NO_2$ , which takes place simultaneously with the initial degradation, is totally unknown, there is no way to estimate the extent of this reaction. Experimental determinations of the gas composition evolving from the surface will be presented later. Finally, the summation of the energy equation (12) gives

$$\lambda_{g,s} (dT/dx)_{g,s} = \rho_p v_b [c_g T_s - c_p T_0 - Q_c - Q_{g,c} (Y_{NO_2,0} - Y_{NO_2,s})] \quad (14)$$

This equation was used as Eq. (2) in Sec. II; it shows that the heat evolved in the transformation propellant/gases  $Q_s$  (positive if exothermic) is

$$Q_s = Q_c + Q_{g,c} (Y_{NO_2,0} - Y_{NO_2,s}) \quad (15)$$

and depends upon the amount of  $NO_2$  that has reacted in the condensed phase. In view of the above considerations it is impossible to evaluate it a priori and the computation recently presented by Cohen<sup>62</sup> is probably oversimplified. Values of  $Q_s$  will be extracted later from the experimental data.

Returning to Eq. (13) and taking into account the fact that the degradation zone thickness is given by Eq. (9), it is found that

$$\rho_p v_b \sim \rho_p B_c \exp(-E_c / R T_s) d_p / \mathcal{E}_c v_b$$

This relationship has been established more rigorously in Ref. 40 (see also Ref. 41) to be

$$v_b = \exp(-E_c / 2 R T_s) \left\{ B_c d_p / \mathcal{E}_c [1 - (T_0 / T_s) - (Q_s / 2 c_p T_s)] \right\}^{1/2} \quad (16)$$

This equation essentially relates the burning rate and the surface temperature; it is Eq. (1), the pyrolysis law.



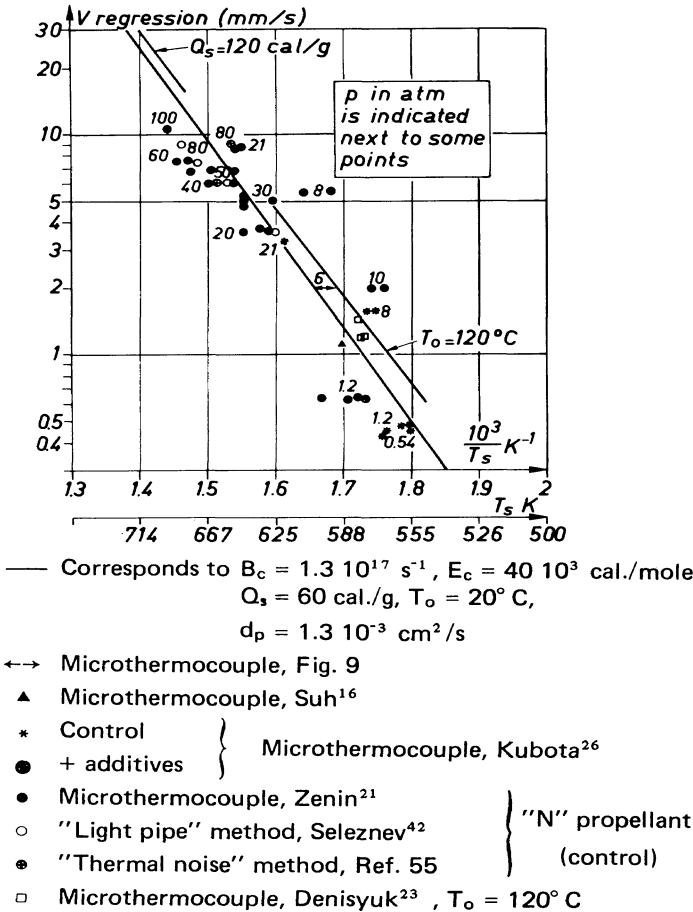
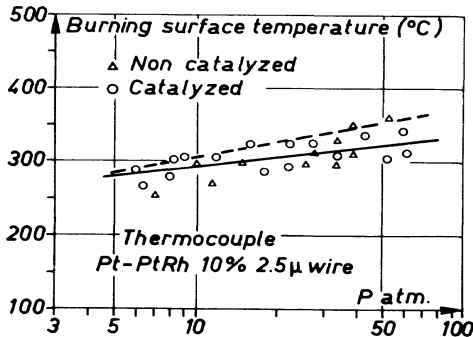


Fig. 11a Burning rate/surface temperature law.



Results of Kubota<sup>27</sup> (Double base matrix with 23 % HMX)

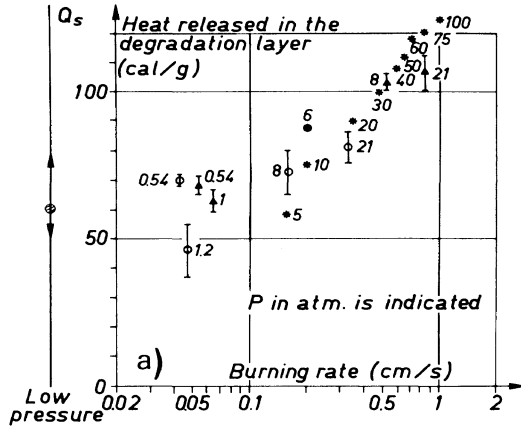
----- Average curve, for the control propellant, from Fig. 11a.

Fig. 11b Surface temperature.

Many measurements of surface temperatures have been made. The results are collected on Fig. 11a. In view of the very small thicknesses and high-temperature gradients involved, some important scatter should be expected. With this in mind, the results of Fig. 11a are coherent. If one draws an average curve through these results, the values indicated for the kinetic factors are obtained by matching Eq. (16). It would be worthwhile to confirm the results of Table 1 regarding ignition, but so far there is a good agreement between the degradation observed at ignition and during combustion.

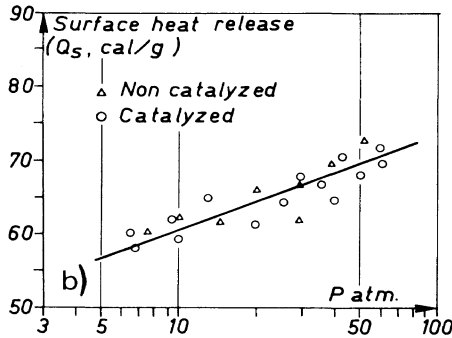
From the results of Fig. 11a, the conclusion can be drawn that the condensed-phase degradation is a thermal phenomenon. It seems that both nitrocellulose and nitroglycerin degradations are taking place. No evaporation of the latter is involved and pressure does not enter into the  $(v_b - T_s)$  relationship; this is also concluded by Zenin and Novozhilov.<sup>22</sup> No influence of the additive on the  $(v_b - T_s)$  law and, consequently, on the degradation kinetics is detected, the comparison being made for two sets of results due to Kubota<sup>26,27</sup> in Fig. 11. Such a conclusion renders improbable Suh's hypothesis<sup>18</sup> of an interaction (a "chelatisation") between the lead salt and propellant components that would weaken the CO-NO<sub>2</sub> bond, modify the degradation kinetics, and expedite the decomposition when additives are present. Furthermore, such an interaction would be possible only for lead salts; however, it has been observed that PbO is effective in creating super-rate effects (Figs. 7 and 8a).

The use of Eq. (14) for the energy balance at the surface and the knowledge of the temperature gradients obtained from small thermocouple traverses allow one to produce estimates of the net heat generated in the condensed phase,  $Q_s$ . The results are shown in Fig. 12. Again, considering the very high temperature gradients, a large uncertainty should be expected. The results are coherent. The net heat  $Q_s$  is exothermic, meaning that the heat evolved in the reaction of NO<sub>2</sub> overcomes that absorbed in the degradation [see Eq. (15)]. It is found to increase with pressure or burning rate. As long as the kinetics of the condensed-phase NO<sub>2</sub> reaction is not known, it is impossible to estimate how much the amount of NO<sub>2</sub> coming off the surface  $Y_{NO_2,s}$  decreases [Eq. (13b)] or how much consequently  $Q_s$  increases [Eq. (15)]. Another important conclusion is that  $Q_s$  is not affected significantly by the presence of additives, as also pointed out by Kubota.<sup>27</sup>



- From Fig. (9)
  - $\circ$  Control propellant
  - $\triangle$  Control + lead and copper salicylate
  - \* Control propellant "N"
  - $\odot$  Ignition studies
  - $\dagger$  Combustion at 10 to 600 mm Hg
- } Kubota<sup>26</sup>  
Zenin<sup>21</sup>  
Suh<sup>16</sup>  
Zenin<sup>56</sup>

Fig. 12a Heat released in the condensed phase.



Results of Kubota<sup>27</sup>  
(Double base matrix with 23% HMX)

Fig. 12b Heat released in the condensed phase.

Condensed-Phase Degradation Gases

The nature of the gases resulting from the degradation (and the unavoidable simultaneous reaction of  $\text{NO}_2$ ) of components similar to the propellants or of the propellants themselves has been the object of a number of investigations, summarized on Table 2. It can be seen that quite frequently the production of  $\text{NO}_2$  and aldehydes is assumed rather than truly detected and that no complete quantitative results can be found.

Experiments have been carried out at ONERA<sup>29</sup> in which a propellant sample is pressed against an electrically heated plate or exposed to a radiation beam under a vacuum, so

Table 2 Degradation products of nitric esters

Reference	Compound	Decomposition scheme and products
ADAMS <sup>43</sup>	Methylnitrate $\text{CH}_3 - \text{ONO}_2$	$\longrightarrow \text{CH}_2\text{O} + 1/2 \text{H}_2 + \text{NO}_2$ Assumed
ADAMS <sup>43</sup>	Ethylene glycol dinitrate $\begin{array}{c} \text{C H}_2 - \text{ONO}_2 \\ \text{C H}_2 - \text{ONO}_2 \end{array}$	$\longrightarrow 2 \text{CH}_2\text{O} + 2 \text{NO}_2$ Assumed
POWLING <sup>44</sup> see also Fig. 16	$\begin{array}{c} \text{ONO}_2 \\   \\ \text{CH}_3 - \text{CH} - \text{CH} - \text{CH}_3 \\   \\ \text{ONO}_2 \end{array}$ $\begin{array}{c} \text{ONO}_2 \\   \\ \text{CH}_2 - \text{CH}_2 - \text{CH}_2 - \text{CH}_2 \\   \\ \text{ONO}_2 \end{array}$ Combustion	$\longrightarrow 2 \text{CH}_3\text{CHO} + 2 \text{NO}_2$  $\longrightarrow 2 \text{CH}_2\text{O} + 2 \text{NO}_2 + \text{C}_2\text{H}_4$  $\approx 30\% \text{NO}_2$ experimentally observed
MALTSEV <sup>45</sup> BENT <sup>46</sup>	Nitroglycerin and propellants	$\longrightarrow \text{CH}_2\text{O}, \begin{array}{c} \text{H} \quad \text{O} \\   \quad    \\ \text{C} - \text{C} \dots \\    \quad   \\ \text{O} \quad \text{H} \end{array}$ $\text{NO}_2$ assumed in Ref. 45 $\text{NO}_2$ seemingly observed in Ref. 46
RIDEAL <sup>47</sup>	Nitrocellulose $\approx 160^\circ \text{C}$ Decomposition under vacuum	$\longrightarrow 37\% \text{NO} \ 10\% \text{N}_2 \ 14\% \text{CO} \ 20\% \text{CO}_2$ $10\% \text{NO}_2$ by difference
DAUERMAN <sup>48</sup>	Propellant under ignition	Results not clearly usable. $\text{NO}_3$ is "detected", disputed by a number of authors.
FARBER <sup>49</sup>	Propellant $> 150^\circ \text{C}$ Decomposition under vacuum	$\longrightarrow \text{CO}_2 \ \text{NO} \ \text{CO} \ \text{H}_2 \dots$ $\text{NO}_2$ observed in mass spectrometry

that no primary flame can occur (Fig. 13). In this way, the regression rate is close to 1 mm/s, the heated zone and residence time in the condensed phase are simulated, but the gases sampled and analyzed by mass spectrometry are those evolving from the condensed-phase degradation. The peaks obtained are used to identify the various species (Fig. 13) and, with the knowledge of the response of the mass spectrometer to each species taken individually (Table 3), the gas composition is found. It can be corrected to take into account the defect in carbon with respect to the original elemental composition, observed to be due to residues on the surface. Large amounts of aldehydes and  $\text{NO}_2$  are indeed found, in quantities inferior to that

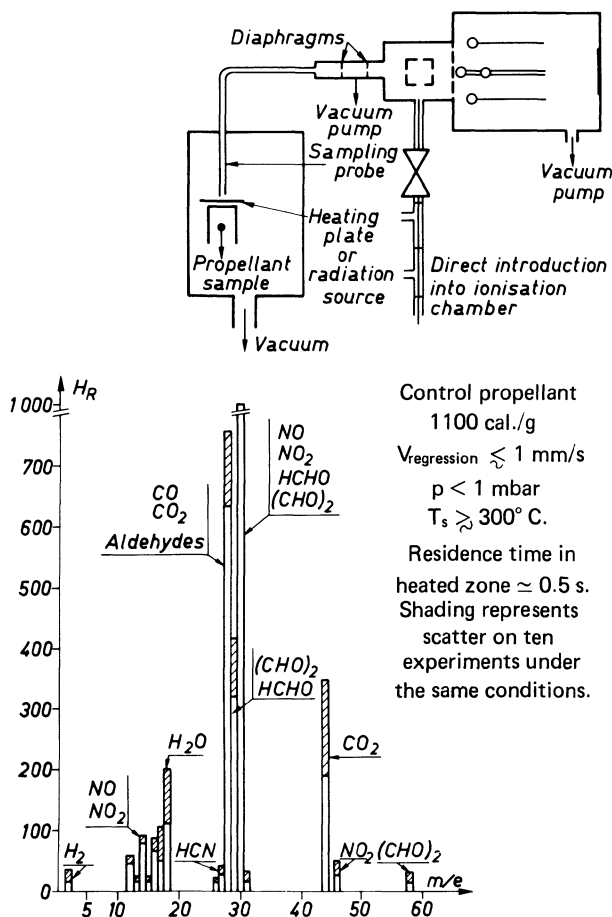


Fig. 13 Gases produced in the condensed phase.

Table 3 Gases from the condensed phase

Gas	NO 30	NO <sub>2</sub> 30	CO 28	CO <sub>2</sub> 44	H <sub>2</sub> O 18	H <sub>2</sub> 2	HCHO 29	(CHO) <sub>2</sub> 29
Main peak height (mm)	19.4	22.5	26.8	12.3	5.4	1.5	12.1	5.9
Sensitivity factor (mm/mb)	355	163	400	410	185	147	105	105
Partial pressure (mb) Total = 0.5 mb	0.055	0.14	0.067	0.03	0.029	0.01	0.116	0.056
Molar fraction %	10.9	27.5	13.4	6	5.8	2.1	23.1	11.2
Mass fraction %	8.9	34.4	10.2	7.2	2.8	0.1	18.8	17.6

Mass fractions of the elements %

	Gases (after correction)		Propellant
C	21.1	(24.6)	24.6
H	2.3	( 2.2)	2.8
O	62	(59 )	58
N	14.6	(14 )	14.5

Mass fractions after correction for carbon

%	Carbon	NO	NO <sub>2</sub>	CO	CO <sub>2</sub>	H <sub>2</sub> O	H <sub>2</sub>	HCHO	(CHO) <sub>2</sub>
	4.4	8.5	32.9	9.7	6.9	2.7	0.1	18	16.8

Potential NO<sub>2</sub> in the propellant  $\approx$  46.7 %. Hot propellant.

potentially contained in the initial propellant, after reactions to give NO.

### Condensed-Phase Behavior of the Additive

Thermogravimetric analyses of lead salts have been run in which samples of a few milligrams are exposed to rising temperatures and continuously weighed (Fig. 14a). It is found that even at temperatures of 300°C, not much below those occurring at the surface of burning propellants (see Fig. 11a), it takes minutes for the salt to decompose. Under the same conditions nitrocellulose will decompose at  $\approx 200^\circ\text{C}$ . The activation energy of the decomposition of nitrocellulose being 40 kcal/mole and that of lead stearate  $\approx 30$  kcal/mole, there is no way that the latter's degradation can catch up at higher temperatures. From the characteristics, for example of lead stearate, obtained from Fig. 14a, it can be evaluated that, for a typical residence time in a burning propellant combustion wave of 10 ms, the salt will have to rise to  $\approx 700^\circ\text{C}$  to decompose; this will occur well above the surface. The results of Morrow<sup>50</sup> and de Schor<sup>51</sup> in Fig. 14b show that the thermal degradation of nitrocellulose or propellants is not affected by additives.

These results suggest that the active part of the lead salt, the PbO residue, will be obtained only above the surface once it is trapped in the carbon residues (see Fig. 5) that are formed even in the case of nonmodified propellants. The kinetics and energetics of the propellant degradation are not affected and, although no true comparisons have yet been made with leaded propellants in the experiment shown in Fig. 13, it seems plausible that the gas composition emerging from the surface is unaffected by the presence of the salt.

The action of the super-rate-producing lead additives does not seem to take place in the condensed phase; a more likely site is the gas flame, which will be covered in the following section.

### V. Detailed Study of the Combustion Mechanisms in the Gas Phase

It was mentioned in Sec. II that the gas phase of a burning double-base propellant comprises two separate flames, at least at pressures below 100 atm (see Fig. 4). From detailed measurements of temperature profiles and by considering the equation representing the conservation of energy (this will be seen later), Zenin<sup>20</sup> has extracted

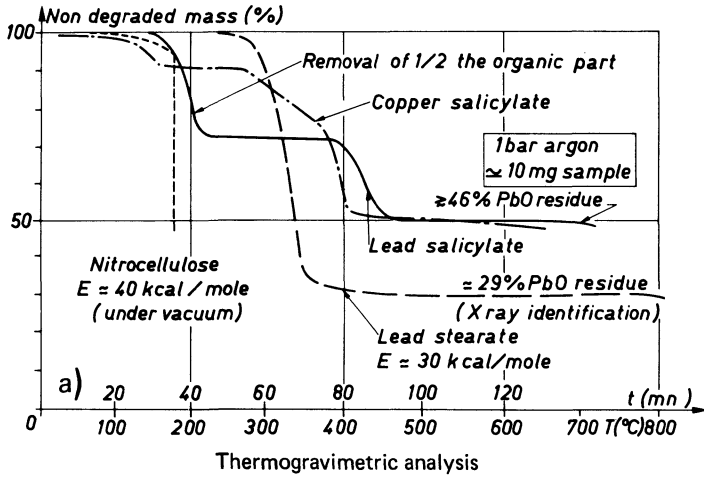
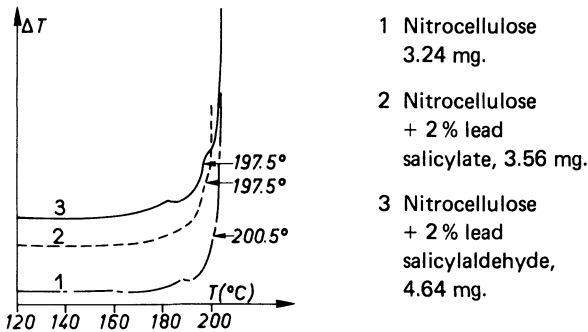
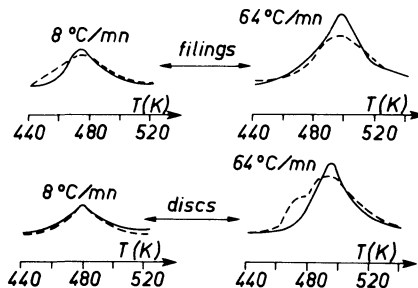


Fig. 14a Additive thermal degradation.



Differential scanning calorimetry of catalyzed vs. pure 12.6 % N Nitrocellulose films. Results of Morrow<sup>50</sup>.



Differential scanning calorimetry.

— Control propellant

- - - Catalyzed propellant

Results of Bañá de Schor<sup>51</sup>

Fig. 14b Additive thermal degradation.



## Chapter 8

### Steady-State Burning of Composite Propellants under Zero Cross-Flow Situation

Kumar N. R. Ramohalli\*  
*University of Arizona, Tucson, Arizona*

#### Abstract

An attempt is made to review a variety of the analytical modeling studies available on this subject. Presentation of a thorough historical survey is not an objective of this chapter. Since the intent is to use a textbook philosophy, certain basic aspects related to solids loading, particle size and shape, binder type, processing influences, and the vapor phase mechanics are briefly mentioned in an effort to develop a feeling for the composite propellant system. Typical burn-rate influences of ingredient and processing variations are mentioned. The majority of the discussion focuses on the most widely used type of composite propellant, Ammonium perchlorate (AP) as oxidizer with inert hydrocarbon binder systems. The thorough analysis of AP combustion by Giurao and Williams, the granular diffusion flame model of Summerfield, the Hermance model, the Beckstead-Derr-Price model and the petite ensemble model are described from the literature. More recent statistical analyses of polydisperse heterogeneous system are referenced. Some related, but often overlooked, work in nonpropellant heterogeneous composites are mentioned as are papers on unconventional ingredients for specially tailored burn-rate performance and diagnostic tools for better understanding and modeling.

#### Nomenclature

A = Arrhenius pre-exponential (frequency) factor

---

Copyright © American Institute of Aeronautics and Astronautics, Inc., 1983. All rights reserved.

\*Associate Professor, Department of Aerospace and Mechanical Engineering.

$A_F$	= Arrhenius pre-exponential (frequency) factor for fuel pyrolysis in the Hermance model and in the PEM
$A_{fh}$	= Ratio of peak diffusional distance to the effective heat transfer distance in diffusion flame in BDP model
$A_{ox}$	= Arrhenius pre-exponential for oxidizer pyrolysis
$A_{PF}$	= Arrhenius frequency factor for the primary flame
$a$	= Constant in the GDF correlation
$B$	= Mass of fuel vapor produced by oxidizer decomposition
$(B)$	= Mass concentration of $B$
$b$	= Burner radius from the Burke-Schumann analysis
$b$	= Also, the characteristic surface dimension (BDP model)
$b$	= Also, constant in the GDF correlation
$C$	= Mass of oxidant vapor produced by oxidizer decomposition, $HClO_4$ when oxidizer is AP (Hermance model)
$(C)$	= Mass concentration of $C$
$C_p, C_s$	= Specific heat of the solid propellant
$C_p$	= Specific heat of the propellant vapors
$C_{ign}$	= Constant in the equation for the oxidizer ignition delay (PEM)
$D_1, D_2$	= Mass of reduced oxidizer vapors produced by surface and gas phase reactions (Hermance model)
$D, D_1$	= Diameter of oxidizer particles (Hermance model)
$D_c$	= Characteristic diameter of decomposing oxidizer particle
$D_0$	= Diameter of oxidizer particle before combustion (Hermance model BDP and PEM)
$D^1$	= Mean intersection diameter of an oxidizer particle with the fuel plane (PEM)
$D$	= Binary diffusion coefficient for vapors
$D_0$	= $D$ at reference conditions (BDP model)
$d$	= Typical dimension of a vapor pocket (GDF model)
$d$	= Characteristic diffusion dimension (BDP model)
$d_f$	= Distance of the fuel regression (PEM)
$d_{ox}$	= Distance of the oxidizer regression (PEM)
$E$	= Activation energy for chemical reactions

$E_f, E_{sr}, E$	=	E for fuel pyrolysis, surface reaction, and gas phase reaction, respectively (Hermance model)
$E_{ox}$	=	Half the activation energy of the oxidizer decomposition in the Hermance model, activation energy for oxidizer pyrolysis in the PEM
$E_{PF}$	=	E for the primary flame (PEM)
$F_{k,j}$	=	Oxidizer particle size distribution function for particles in mode j (PEM)
$\Delta H_p$	=	Endothermic heat of pyrolysis (Hermance model)
$h$	=	Distance oxidizer crystal protrudes above, or is recessed below, the mean propellant surface (BDP)
$K_O$	=	Oxidizer ignition delay parameter (Hermance)
$K_{AP}$	=	AP flame rate constant
$K_{PF}$	=	Primary flame rate constant
$k$	=	Thermal conductivity of combustion gases
$k$	=	Rate constant, $A \exp(-E/RT)$ , in BDP model
$k_f, k_{ox}$	=	Mass flow rates from fuel pyrolysis and oxidizer decomposition (Hermance model)
$k_{sr}, k'_{sr}$	=	Rate constants associated with surface reactions (Hermance model)
$M_g, M_C$	=	Molecular weight of combustion gases and C, respectively (Hermance model)
$M_i, m_i$	=	Mass flow rate and mass flux associated with propellant component as designated by subscript, respectively (Hermance model)
$M_k$	=	The number of distribution modes of oxidizer species k (PEM)
$m$	=	Diameter exponent in particle ignition term (Hermance)
$m$	=	Mass flux associated with propellant components (BDP)
$\dot{m}_T$	=	Total mass flux from propellant
$\dot{m}$	=	Mass flux from an oxidizer fuel pair in propellant (PEM)
$\dot{m}$	=	Mass flux from propellant (GDF); same as $\dot{m}_T$ in BDP
$\dot{m}_f$	=	Mass flux from the fuel surface
$\dot{m}_{ox}$	=	Mass flux from the oxidizer surface
$\dot{m}_t$	=	Total mass flux from propellant burning surface in PEM; same as $\dot{m}_T$ in BDP

$\bar{m}_t$	= Average mass flux per unit planar burning surface area (PEM)
$m''$	= Mass flux as any point on the burning surface (PEM)
$m_{d,k}''$	= Mass flux per unit burning surface area from the subarea containing oxidizer particles of size between $D_0$ and $D_0 + dD_0$ and oxidizer species $k$ (PEM)
$\overline{m_{d,k}''}$	= Average of $m_{d,k}''$ (PEM)
$\overline{m_{p,d,k}''}$	= Average mass flux per unit planar surface area from a subsurface containing oxidizer crystals of size between $D_0$ and $D_0 + dD_0$ and oxidizer species $k$ (PEM)
$m_{o,k,j}$	= Total mass of oxidizer in mode $j$ and oxidizer species $k$ (PEM)
$dm_{o,d,k}$	= The elemental mass of oxidizer with diameter between $D_0$ and $D_0 + dD_0$ and oxidizer species $k$ (PEM)
$dm_{o,d,k,j}$	= The elemental mass of oxidizer with diameter between $D_0$ and $D_0 + dD_0$ in distribution mode $j$ and oxidizer species $k$ (PEM)
$N$	= Total number of particles at the burning surface (PEM)
$n$	= Pressure exponent in the burning rate law
$n$	= Pressure exponent in the particle ignition term (Hermance)
$\Delta N_{p,d,k}$	= Number of particles at the burning surface of size between $D_0$ and $D_0 + dD_0$ and species $k$ , per unit of planar burning surface area (PEM)
$dN_{o,d}$	= Number of oxidizer crystals per unit volume with diameters between $D_0$ and $D_0 + dD_0$ (PEM)
$dN_{p,d,k}$	= Number of particles at the burning surface of size between $D_0$ and $D_0 + dD_0$ and species $k$ per unit of planar burning surface area (PEM)
$P$	= Pressure
$P_C$	= Partial pressure of oxidant $C$ (Hermance)
$P_1, P_2$	= Mass of inert products, or oxidized fuel vapors produced by gas phase reactions
$Q$	= Heat release associated with combustion steps
$Q_f, Q_{fuel}$	= Heat of pyrolysis of fuel binder (BDP, PEM)
$Q_f$	= Heat released in gas phase flame of propellant (Hermance)
$Q_L$	= Heat of gasification of oxidizer (latent heat)

$Q_{gp}$	= Gas phase heat release of oxidizer decomposition (Hermance)
$Q_{sr}$	= Heat released by surface reaction (Hermance)
$Q_r$	= Heat of combustion of propellant (GDF)
$Q_s$	= Net heat release for gasification of propellant (GDF)
$Q_{surf}^{PF}$	= Heat flux at the surface from primary flame (PEM)
$R$	= Universal gas constant
$r$	= Propellant linear burn (regression) rate
$\bar{r}$	= Time-averaged propellant burn rate (PEM)
$\bar{r}_{d,k}$	= Burning rate of pseudopropellant (PEM)
$S$	= Surface area
$S_b$	= Burning surface area (PEM)
$S_f$	= Surface area of pyrolysis fuel (Hermance, PEM)
$S_o$	= Total planar, cross-sectional area of burning surface of propellant
$S_{ox}$	= Oxidizer surface area (planar in Hermance)
$S_{sr}$	= Surface area available for surface reaction (Hermance)
$S_f^P$	= Planar fuel surface area
$S_{ox}^P$	= Planar oxidizer surface area
$S_T^P$	= Planar total burning surface area
$S_{o,d,k}^*$	= The exposed surface area of oxidizer in a pseudopropellant with oxidizer particles of size between $D_0$ and $D_0 + dD_0$ and oxidizer species $k$
$S_{p,f,k}^*$	= Planar surface area of a pseudopropellant containing oxidizer particles of size between $D_0$ and $D_0 + dD_0$ and oxidizer species $k$
$s$	= Number of oxidizer types (PEM)
$\Delta S_{b,d,k}$	= Burning surface area of a pseudopropellant containing oxidizer particles of size between $D_0$ and $D_0 + dD_0$ and oxidizer species $k$
$\Delta S_{p,d,k}$	= Planar surface area of a pseudopropellant containing oxidizer particles of size between $D_0$ and $D_0 + dD_0$ and oxidizer species $k$
$T$	= Temperature
$T_f$	= Adiabatic flame temperature of propellant
$T_0, T_p$	= Initial (conditioning) temperature of propellant

$T_s$	= Surface temperature
$T_{AP}$	= Adiabatic AP flame temperature
$T_{FF}$	= Adiabatic final flame temperature
$T(x_{AP})$	= Temperature at the location of the AP flame
$t$	= Time
$t_b$	= Burn time
$t_c$	= Characteristic time of exposure of oxidizer crystal at propellant surface
$t_{ign}$	= Ignition delay time of oxidizer crystals
$U$	= Diameter exponent in the equation for the oxidizer ignition delay
$V$	= Linear burning rate constant of oxidizer crystal (Hermance)
$v$	= Gas (vapor) velocity normal to the burning surface
$\bar{v}$	= Time-averaged $v$
$v_b$	= Linear burning rate of an oxidizer crystal (Hermance)
$v'$	= Fluctuating velocity normal to the burning surface
$W$	= Pressure exponent in the equation for the oxidizer ignition delay
$w$	= Molecular weight (BDP)
$X, x$	= Distance coordinates
$x_{AP}$	= Location of the AP flame heat release
$x_{FF}$	= Location of the final flame heat release
$x_{AP}^*$	= AP flame standoff distance
$x_{FF}^*$	= Final flame standoff distance
$x_{PD}^*$	= Primary flame diffusion distance
$x_{DF}^*$	= Primary flame kinetics distance
$\bar{x}^*$	= Effective heat transfer distance (BDP) = $x^*/A_{fh}$
$Z$	= Pre-exponential factor of gas reaction rate (Hermance)
$\alpha$	= Oxidizer mass (weight) fraction
$\beta$	= A constant in Hermance model
$\beta$	= Species concentration term in the diffusion flame analysis (PEM)
$\beta_f$	= Fraction of reactants involved in the primary diffusion flame (BDP)
$\delta$	= Reaction order (BDP)
$\delta$	= Pressure exponent oxidizer burn rate (Hermance)
$\delta$	= Distance between the inner and outer annulus of the "Bunsen Burner" configuration
$\zeta$	= Volume fraction of oxidizer in propellant
$\zeta_{d,k}$	= Volume fraction of pseudopropellant containing oxidizer particles of size be-

	tween $D_0$ and $D_0 + dD_0$ and species $k$
$d\xi_d$	= Volume fraction of oxidizer particles with diameter between $D_0$ and $D_0 + dD_0$
$\lambda$	= Coefficient of thermal conductivity
$\lambda_p, \lambda_g$	= $\lambda$ for (solid) propellant and gas, respectively
$\eta'$	= Stoichiometry-related coefficient (BDP)
$\eta_{d,k}$	= Fraction of particles in the propellant with diameter between $D_0$ and $D_0 + dD_0$ and oxidizer species $k$
$\xi, \xi^*$	= Nondimensional flame standoff distance (PEM, BDP)
$\xi$	= Nondimensional length (Hermance)
$\xi_{AP}^*, \xi_{PF}^*, \xi_T^*$	= $\xi$ for AP flame, primary flame and final flame, respectively (PEM)
$\nu$	= Stoichiometry-related variable (PEM)
$\rho$	= Density
$\tau$	= Characteristic time (e.g., for oxidizer particle in PEM)
$\sigma$	= Fraction of oxidizer having particle size spread $D_0$ (Hermance)
$\sigma^*$	= Standard deviation of oxidizer particle size in the log normal distribution (PEM)
$\theta$	= Dimensionless temperature or the activation temperature parameter $\equiv (RT/E)$
$\varepsilon$	= Depth of fissure surrounding oxidizer crystals (Hermance)

### Introduction

Composite propellants, in their simplest form, consist of a dispersion of particulate oxidizers within a matrix of the fuel. Even if all the particles were the same size and shape (e.g., spherical) and even if the dispersion of the oxidizer in the fuel was uniform, the combustion of the propellant would involve a multitude of subprocesses. Thus any attempt at understanding their combustion behavior must identify the key processors that control the burning. Some of these are heating of the condensed phase, degradation (decomposition) of the oxidizer and the fuel, possible melting, vaporization, mixing in the vapor phase, and gas-phase combustion. In a practical propellant, the oxidizer particles are not all the same size or shape. In fact, it is an easy exercise in solid geometry to see that multimodal particles are indeed necessary to achieve the solids loading that make sense energetically. In addition, a practical propellant consists of many additives that serve

Table 1 Typical state-of-the-art propellant  
(note that the actual numbers seemingly exceed a 100% by weight)

Propellant EB-248			
Ingredient	Lot No.	Percent	Weight, g
Butarez HT	4760	4.1452	658.050
R45M		7.6395	1212.771
Alrosperser		0.2180	34.6075
Iso Stearyl Alcohol		0.5473	86.8839
AO-2246		0.1400	22.2250
IPDI		1.3100	207.963
MT-4		0.200	31.7500
Al 1230		18.00	2857.50
AP, unground 5272		47.60	7556.50
AP, grind 8		20.40	3238.50
Total:		100.200	

various important functions. Examples are plasticizers, cure catalysts, burning-rate catalysts, bonding agents for improved mechanical properties, and antiaging chemicals to assure long life. At the combustion conferences, papers describing special ingredients to achieve special effects are a routine feature. A typical simple (metallized) propellant has the composition shown in Table 1.

From the time of the first formulation of a composite propellant at the Jet Propulsion Laboratory in the 1940's (using potassium perchlorate and asphalt), burning-rate tailoring, if not prediction, appears to have been understandably a "black art" until a major step was taken by Summerfield and co-workers<sup>1,2</sup> to actually model the very complex combustion processes in these very nonhomogeneous materials. It may be easy to fault that study, called the granular diffusion flame (GDF) model, for its various shortcomings, but it would be unfair to forget that practically all of the more modern models<sup>3-10</sup> that claim improved predictions owe their origins, at least in principle, to the GDF model. A study of the GDF model enables one to understand the manner in which future complex problems may be handled: perhaps an entirely new form of propellant formulation involving not just chemical variations on in-



gredients. Basically all modeling efforts attempt to isolate the signal from the noise, and the GDF model is a classic example of how one sets about this task when few previous studies are available. Inasmuch as this book is meant as a textbook, too, it is instructive to devote some space to the GDF model.

All models attempt to explain experimentally observed facts (and predict trends), so long as the experimental results are themselves reproducible and show some orderly trends. With this basic premise, some of the mainstream of experimental data pertaining to the time-independent combustion of nonmetallized AP/composite propellants in the absence of cross flow are discussed in the course of the presentation. The combustion characteristics of AP as a monopropellant are presented. The most comprehensive attempt at understanding AP combustion behavior appears to be that of Guirao and Williams, and this model is discussed in the subsequent section. The low-pressure extinction limit of single crystals of AP at approximately 215 psia at 25°C initial crystal temperature, the burning-rate pressure index value of approximately 0.77, and the initial temperature sensitivity are the principal experimental features addressed by the model. The introduction of a liquid layer on the surface of a deflagrating AP crystal is the central aspect of this model. The exothermic reactions in this liquid layer sustain the deflagration. The disappearance of this liquid layer at the low pressure (<215 psia) results in the low-pressure extinction limit observed experimentally. The detailed reaction schemes used by Guirao and Williams are presented and some comments are made on the rate calculations they made.

Considering that composite propellants, by definition, consist of a heterogeneous dispersion of oxidizer particles in a fuel matrix, it may be tempting to model the propellant as oxidizers surrounded by a rubbery, continuous matrix and to analyze the evolution of vapors from such a "two source" system. A second look at the propellant in a quantitative manner, however, would indicate that such descriptions (of oxidizer vapors in an annulus of fuel vapors) may not be necessary. Typical composite propellants, even of the nonmetallized variety, consist of 80-85% solids (oxidizer). It is easily seen (Fig. 1b) that such loadings invariably imply that the evolution of vapors is largely dominated by the AP. This is not to say that the binder is unimportant. Even in its small proportion, the binder has been known to profoundly influence the time-independent<sup>11</sup> and the oscillatory<sup>12</sup> combustion. The author feels that, for the purposes of modeling, the descriptions

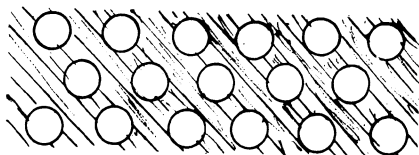


Fig. 1a Highly popular "picture" invoked of the "typical" AP/composite propellant for purposes of combustion modeling. The binder and AP are treated in detail.

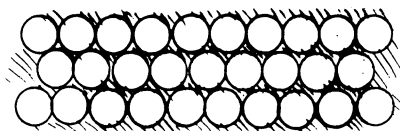


Fig. 1b More realistic representation recognizing the state-of-the-art loadings of 80-90% AP. It is seen that the binder geometry ought to be quite insignificant compared to that of AP. Nonmonomodal particles are needed to get  $\sim 80\%$  solids.

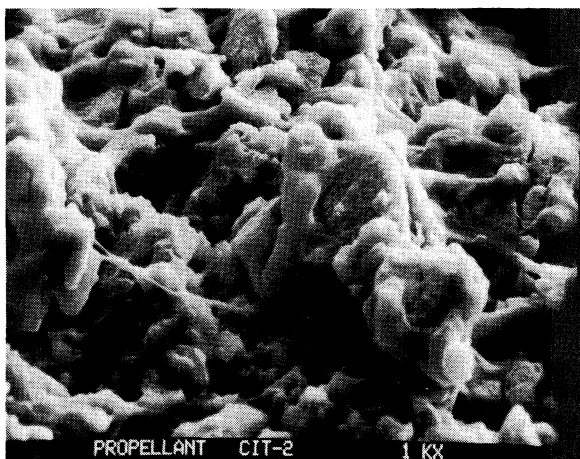


Fig. 1c SEM picture (1000X) of a typical nonmetallized (CIT-2) propellant (see Fig. 10).

of vapors from AP surrounded by a corridor of vapors from the fuel (binder) do not appear to be consistent with the state-of-the-art oxidizer loading.

The combustion of composite propellants is characterized as time dependent when oscillations, chuffing, and ignition/extinction phenomena are seen. Even under "steady combustion" conditions the processes are not really steady

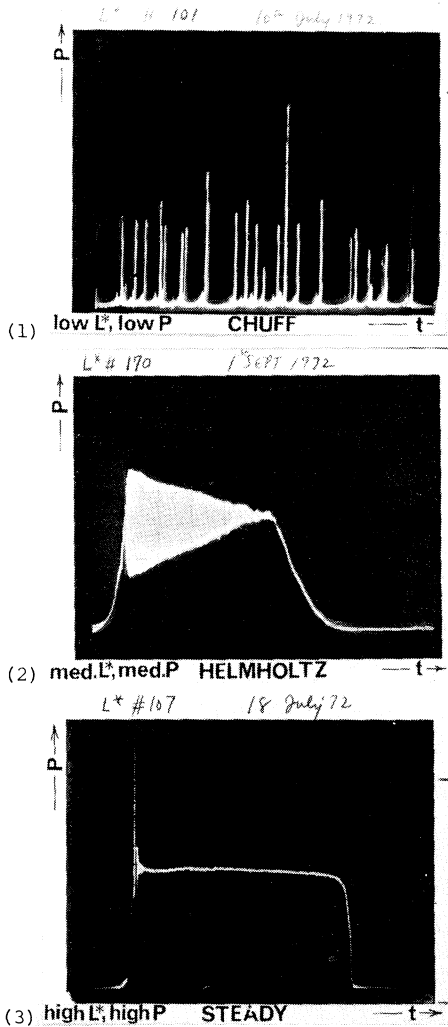


Fig. 1d Chuff (intermittent) (1); oscillatory (2); "steady" combustion of propellants (3).

in the sense of total absence of fluctuations. (These fluctuations are not to be confused with the molecular fluctuations which, averaged over many thousand events, lead to the continuum concept.) Fluctuations arise because of the nonidentical events originating from the heterogeneity and the nonidentical nature of the heterogeneity. Typical pressure-time traces are shown in Fig. 1d for a nonmetallized monomodal AP/PBAN propellant. While the trace Fig. 1d(3) is unmistakably the steady combustion case, contrasted with the other traces in Fig. 1d, fluctuations are clearly seen. For these reasons, many investiga-

tors prefer the description "time independent" to "steady state."

The following sections contain a description each of the Guirao-Williams model<sup>13</sup> for AP deflagration, the GDF<sup>1,2</sup> model for AP/composites, the Hermance model<sup>3</sup>, the BDP model<sup>4</sup> and the petite ensemble<sup>7</sup> model (PEM). Repeated attempts by the author to learn of the more recent studies by our colleagues in the USSR resulted in a communication (dated April 13, 1983) referring us to 53, 54, and 55. The interested reader is also referred to the earlier summaries by Bakhman and Balyaev<sup>14</sup> (which is a book) and Novikov et al.<sup>15</sup> In addition, it should also be mentioned that solid-propellant combustion has been discussed in the books by Williams et al.,<sup>14</sup> Barrere et al.,<sup>42</sup> and Penner.<sup>43</sup> The material<sup>44</sup> has also been the subject of a review by Kishore.<sup>44</sup>

Incidentally, the selection of these descriptions is based upon what is felt to be major steps toward a sound model. Several other attempts are also mentioned in one section.

The reader may find it useful at this stage to briefly review the material (at least the figures and tables) in Chap. 1.

### The Guirao-Williams Model for AP Combustion

Since AP concentrations in propellants range upward of 70% by weight, and since it is the main "energy ingredient," it is natural to study the AP combustion in some detail as a prelude to the consideration of propellant combustion. Ammonium perchlorate, as a salt crystal and as a chemical, has been extensively studied.<sup>16-20</sup> Specifically, graphic studies of its behavior in degradation and combustion appear to have begun at the Naval Weapons Center.<sup>21</sup>

High-quality color motion pictures of AP deflagration at several pressures were obtained at the Naval Weapons Center. Surface irregularities (departures from a planar surface) were visible. Quenched samples of deflagrating AP were examined under a scanning electron microscope. It was inferred from these pictures that a layer of molten material existed on the deflagrating surface. The thickness was estimated to be between  $2\mu$  and  $5\mu$  in the pressure range of 20-50 atm. In the range of 50-150 atm, the surface was observed to be covered with ridges and valleys, with increased activity at the bottoms of the valleys. At pressures in the range of 150-170 atm, the surface appeared to consist of closely packed "needles." Those needles were

Table 2 Chain reaction mechanism

---



---

$\text{HClO}_4 + \text{NH}_3 \rightarrow \text{ClO}_3 + \text{NH}_2 + \underline{\text{H}_2\text{O}},$	
$\Delta H = 31.5 \text{ kcal/mole}$	(1)
$\text{ClO}_3 \rightarrow \text{ClO} + \underline{\text{O}_2}, \Delta H = -12.8 \text{ kcal/mole}$	(2)
$\text{NH}_3 + \text{ClO} \rightarrow \text{NH}_2 + \text{ClOH}, \Delta H = 5.1 \text{ kcal/mole}$	(3)
$\text{NH}_2 + \underline{\text{O}_2} \rightarrow \text{HNO} + \text{OH}, \Delta H = -6.2 \text{ kcal/mole}$	(4)
$\text{HClO}_4 + \text{HNO} \rightarrow \text{ClO}_3 + \underline{\text{NO}} + \underline{\text{H}_2\text{O}},$	
$\Delta H = -11.79 \text{ kcal/mole}$	(5)
$\text{ClOH} + \text{OH} \rightarrow \text{ClO} + \underline{\text{H}_2\text{O}}, \Delta H = -21.6 \text{ kcal/mole}$	(6)
$\text{ClO} + \text{ClO} \rightarrow 2\text{Cl} + \underline{\text{O}_2}, \Delta H = 9.72 \text{ kcal/mole}$	(7)
$\text{Cl} + \text{ClOH} \rightarrow \underline{\text{HCl}} + \text{ClO}, \Delta H = -4.8 \text{ kcal/mole}$	(8)
$\text{Cl} + \text{Cl} + \text{M} \rightarrow \underline{\text{Cl}_2} + \text{M}, \Delta H = -58.0 \text{ kcal/mole}$	(9)
$\text{ClO} + \text{OH} \rightarrow \underline{\text{HCl}} + \underline{\text{O}_2}, \Delta H = -55.7 \text{ kcal/mole}$	(10)

---



---

typically 100  $\mu$  in length. The basic suggestions were also made that the energy needed to sustain deflagration came variously from exothermic reactions in the condensed phase and heat feedback from the vapor phase in different proportions in different regimes of pressure.

Guirao and Williams systematically analyzed the liquid layer on the surface and a scheme of chemical reactions believed to be important in describing the transformation of AP to various products. In addition to the reaction pattern (or the chain steps), they also inferred the key rates and the overall activation energy for the gas-phase reaction. A principal feature of their model is the introduction of a fraction (G) of the AP that reacts in the gas phase and a fraction (1-G) that forms final reaction products instantaneously at the surface (interface between the vapor phase and the condensed phase). G, incidentally, is the only adjustable parameter in the system. A value of 0.3 was chosen to fit the experimental deflagration rate curve. It is important to realize that after an examination of various theoretical and experimental data, ten equations (Table 2) are used to represent the kinetic mechanism for the gas-phase reaction. Products that have been positively identified experimentally in the reaction of AP are shown underscored.

Although a detailed mechanism was proposed, the actual values of activation energies and pre-exponential factors were not available for all steps. This deficiency forced the authors to resort to reasonable (but nevertheless unproven) approximations of zero activation energy E for exothermic chain-carrying steps and  $E = \Delta H$  for endothermic chain-carrying steps; B was calculated from collision reaction rate theory with steric factors of unity and collision diameters of 4, 3.5, 4, and 10 Å respectively, for  $\text{ClO}_3$ ,

$\text{ClO}$ ,  $\text{HHO}$ , and  $\text{HClO}_4$ . It should be remembered that the ultimate aim of this work is the prediction of the time-independent one-dimensional deflagration rate of the AP. To this end, an overall activation energy and an overall pre-exponential factor would suffice. In order to arrive at these values of  $B$  and  $E$ , kinetic calculations for isothermal isobaric systems were performed to represent the vapor phase. Typical results are shown in Fig. 2 here.

It is seen from the steep gradients that there exists a sharp boundary between high and low concentrations of reactants. The effective reaction time is thus defined without much ambiguity. These concentration profiles computed by Guirao and Williams can actually be helpful in

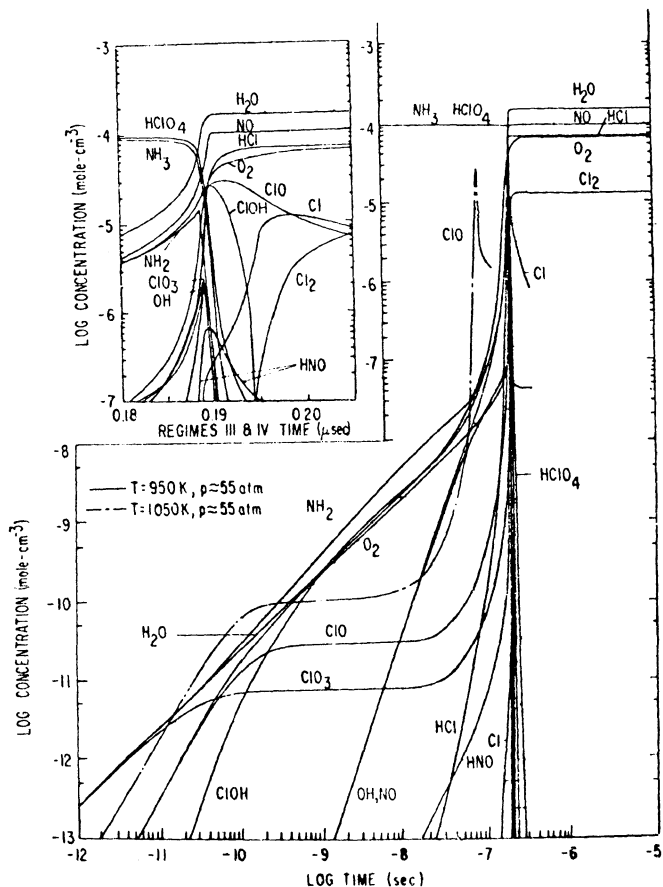


Fig. 2 Species concentration profiles for the gas-phase reaction of AP decomposition.

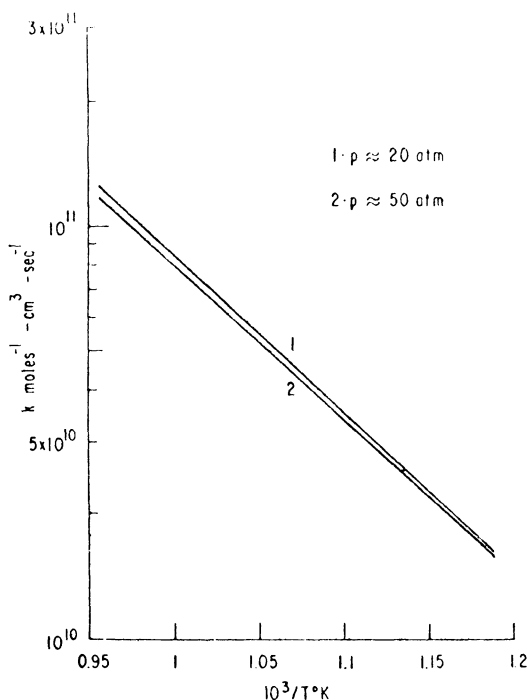


Fig. 3 Arrhenius plot for the overall rate of the main reaction for AP decomposition.

research involving modern concepts of free radicals generation, injection, and control.

The overall kinetic equation,

$$\frac{d}{dt} [\text{HClO}_4] = -k [\text{HClO}_4] [\text{NH}_3]$$

is shown in Fig. 3. It is seen that, over the pressure range of 20-50 atm, there is very little variation.

Assuming an equilibrium dissociative sublimation at the surface of AP and using the earlier analysis of Johnson and Nachbar<sup>22</sup>, upper and lower bounds,<sup>†</sup> were found for the eigenvalues  $\Lambda^+$  and  $\Lambda^-$ , and the mean eigenvalue is  $\Lambda$  and is defined by  $\Lambda^{1/2} = (\Lambda^+)^{1/2} + (\Lambda^-)^{1/2}$ . It was found in this study that the flame temperature is only a weak function of the surface temperature, which is itself a fairly strong function of the pressure. This indicates the existence of near equilibrium in the vapor-phase reactions at least in

<sup>†</sup>The eigenvalue  $\Lambda$  is the nondimensional burning rate where  $\Lambda \propto 1/\text{m}^2$ .

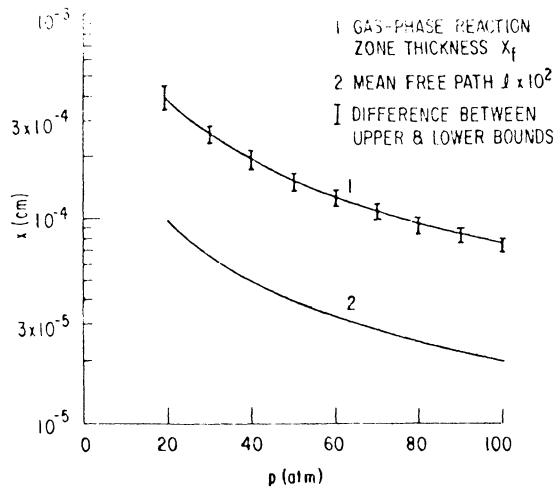


Fig. 4 Dependence of AP flame thickness and mean free path on pressure, from Ref. 13.

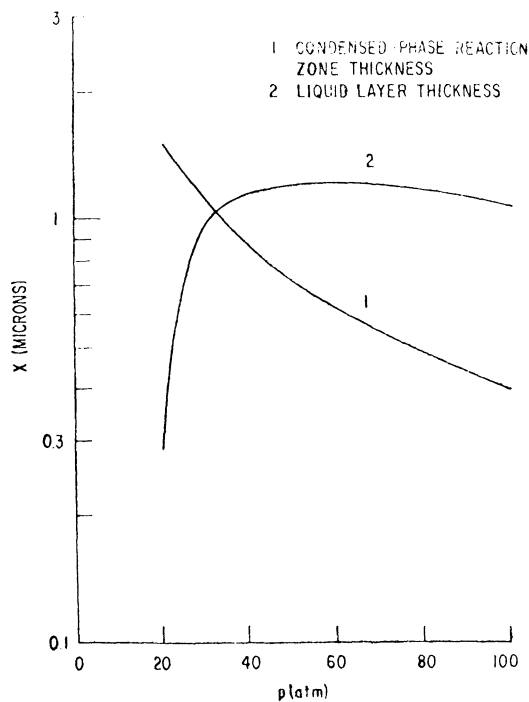


Fig. 5 Dependence of condensed-phase reaction zone thickness and liquid layer thickness on pressure for AP decomposition (Ref. 13).



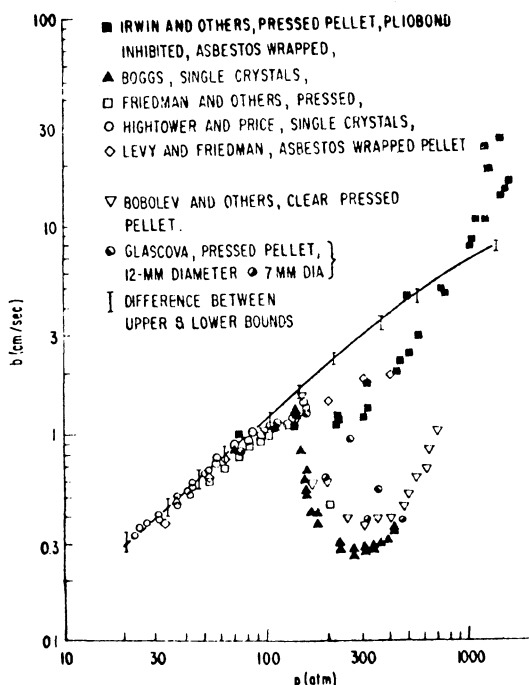


Fig. 6 Pressure dependence of AP deflagration rate.

the pressure range of 20–100 atm. The low-pressure deflagration limit occurred when the surface temperature fell just below the melting point of AP (560 C). The vapor phase was analyzed in some more detail and it was shown that the flame thickness, while very small ( $\sim 1 \mu$ ), was still quite large compared to the mean free path. This lends credence to the continuum analyses (Fig. 4). The calculated condensed-phase reaction zone thickness and the liquid layer thickness on the surface are shown in Fig. 5.

A useful table of AP properties is presented in Table 3 for any future studies. A compilation of AP deflagration rate data is presented in Fig. 6.

Some points are worth mentioning here. The model of Guirao and Williams addresses specifically the single crystal combustion behavior of AP. The initial temperature sensitivity of single crystal AP deflagration is shown in Fig. 7 (from Boggs and Zurn). This initial temperature sensitivity appears to be a simple energy consequence and probably not related to any details of chemistry, as shown in Ref. 23.

Now, we are in a position to consider the more complex case of actual composite propellant combustion. Before

Table 3 Table of physical constants<sup>a</sup>

Isobaric specific heat of AP orthorhombic phase $c_{\pi_1}$	0.309 cal/g-°K
Isobaric specific heat of AP cubic phase $c_{\pi_2}$	0.365 cal/g-°K
Isobaric specific heat of AP liquid phase $c_l$	0.328 cal/g-°K
Mean isobaric specific heat of gaseous mixture $c_g$	0.3 cal/g-°K
Heat of phase transition $\Delta h_{tr}$	2.5 kcal/mole
Heat of fusion $\Delta h_m$	7 kcal/mole
Heat of vaporization	58 ± 2 kcal/mole
Heat absorbed by gas-phase reactions $\Delta h_g$	-772 cal/g
Melting point temperature $T_m$	560 ± 20°C
Transition temperature $T_{tr}$	240°C
Effective liquid temperature at $x = -\infty, T_\infty$	0°K
Dissociation pressure of AP	$\log_{10} p_d$ (Torr) = 10.56 + $\frac{6238.7}{T_8}$
Molecular weight of AP $W_\pi$	117.5 g/mole
Orthorhombic phase density $\rho, \pi$	1.95 g/cm <sup>3</sup>
Liquid phase density $\rho_l$	1.71 g/cm
Thermal conductivity of the gaseous mixture $T_{fa}$	10 <sup>-4</sup> cal/cm-sec-°K
Thermal conductivity of the liquid phase $T_l$	9 x 10 <sup>-4</sup> cal/cm-sec-°K
Total hemispherical emissivity of the condensed-phase surface $\epsilon_3$	1
Adiabatic flame temperature	1205°K
Mean molecular weight of gaseous products $\bar{W}_p$	28.4 g/mole

<sup>a</sup>From Guirao & Williams.

considering that aspect, it would be useful to remind ourselves that the binder (matrix) physics and chemistry, especially as related to combustion, have been studied in great detail over the years. Polymer degradation in vacuum, inert, and active (oxidative) atmospheres have been studied at various temperatures and heating rates. While the utility of that data to composite propellant combustion has frequently been questioned on grounds of relevant regimes of heating rates, mixing with oxidizers and dispersion, the relevance seems to be in little doubt. Also, since pure polymers are easier substances to analyze (homogeneous), theories have been developed<sup>24,25</sup> to predict the regression rate as a function of surface temperature and the condensed-phase details. In addition, the topic of

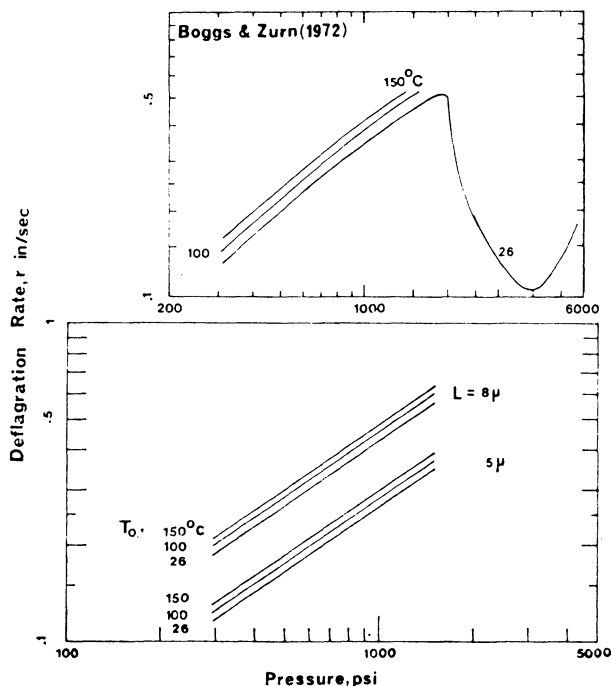


Fig. 7 Linear regression rate of self-deflagration flame-heated AP, and predictions from Ref. 23.

polymer combustion is of great importance to various fields and is being studied extensively (see, for example, Ref. 26). Data on fire-safety aspects of polymer combustion are discussed in Ref. 47. The data on polymer combustion appear to be empirical. Nevertheless, the data on such quantities as activation energy, pre-exponential factors, and melting points should be of some help in understanding propellant combustion behavior. In this connection, the reader may find it useful to consult Madorsky's monograph<sup>27</sup> for basic details of the degradation of polymers.

### The Granular Diffusion Flame Model

Based on enlarged pictures of the burning zone of simple (AP/polystyrene) composite propellants, Summerfield and co-workers<sup>1,2</sup> set out to theoretically predict the effects of pressure, oxidizer particle size, and fuel-oxidizer ratio upon the mean burning rate. The pictures clearly indicated inescapable heterogeneity both near the surface and in the vapor phase. Instead of the popular procedures of attempting to "average" the heterogeneity in the vapor

phase, the investigators considered the heterogeneity as a principal feature. Herein lies the remarkable advance made in our understanding of composite propellant combustion.

Photographic evidence obtained with quenched samples, Schlieren and silhouette techniques revealed that the surface of the propellant during combustion was unmolten, or at least free of large thickness melt layers; the vapor zone was nonturbulent at least in key heat-transfer region up to 1 mm from the surface. [In contrast to these photographs, potassium perchlorate propellants clearly indicate deep melting (through bubbles) on the surface during combustion.] It is now important to locate the actual vapor-phase zone of action or the "flame." While the luminosity may be high far away from the surface, nearly adiabatic flame temperatures were measured within a distance of only 50  $\mu$  from the surface. Such temperature measurements were made with the sodium-D line reversal technique. In addition, fine bead (12 $\mu$ ) thermocouples imbedded in the propellants indicated, upon emerging into the vapor phase, that the gaseous reaction zone is less than 100  $\mu$  from the surface at pressures above 200 psi (16+ atm). Based on all of these experimental evidences, the bases of the theoretical work is established as 1) the AP propellant surface is "practically dry" (at least with polystyrene type binders); 2) the gaseous reaction zone is nonturbulent; and 3) most of the heat release in the gaseous zone occurs at very small distances ( $\sim 100$   $\mu$ ) from the surface.

Fuel and oxidizer vapors were believed to be released in the form of pockets of a certain mass content, and these pockets proceeded to burn in the surrounding medium of complementary reactants. The heterogeneity represented by the pocket size was implicitly taken as related to the condensed-phase heterogeneity--namely, the oxidizer particle size. The vapor-phase pockets were gradually consumed through mixing, diffusion, and reaction. Heat was released at a corresponding rate. The heat generated was transferred to the surface (and subsurface) mainly through conduction. Radiation was ignored. Flow, or mass evolution, was considered only in the direction normal to the burning surface. It is clearly mentioned that the flat surface is an approximation only. Incidentally, the flat surface is as (un)realistic as the "flame sheet"; in analyses, the former is as useful as the latter.

The condensed-phase analysis is based upon the one-dimensional heat conduction equation involving moving material to keep the surface stationary:

$$\dot{m} c_s (T_s - T_0) - \lambda_{gs} \left( \frac{dT}{dx} \right) + \dot{m} (Q_r - Q_s) = \dot{m} Q_r \quad (1)$$

The burning rate of the solid, purely from the condensed-phase considerations, can be expressed as

$$r_i = B_i \exp(-E/RT_{is}) \quad (2)$$

where the subscript  $i$  can refer to fuel or oxidizer. Experiments have indicated that, at least for pure components, such an Arrhenius representation may be valid.

Up to this point the development is straightforward. Now the concept of a flame thickness or reaction distance (or flame standoff distance)  $L$  is implicitly introduced through the vapor-phase energy equation with averaged properties and a suitably defined average final temperature. The averaging used here should not be regarded as inconsistent with the general approach, which considered the gas-phase heterogeneity in the pockets. The averaging used here is used only on the property values while retaining the physical heterogeneity through the diffusion:

$$\dot{m} [c_s (T_s - T_0) - Q] = \lambda_{gs} [(T_f - T_s)/L] \quad (3)$$

Some order-of-magnitude estimates may be helpful in recognizing the role of diffusion in the vapor phase. Let us loosely define a flame standoff distance  $L$  as that distance above the surface where the adiabatic flame temperature is attained. Using a typical value of the effective heat of vaporization for the propellant as 200 cal/g, at equilibrium the conduction heat flux from the combustion zone to the surface is  $\lambda_{gs} \Delta T/L$ , which is equated to  $\rho \dot{m}$ . If the density of the propellant ( $\rho$ ) is 2 g/cm<sup>3</sup>, and the  $\Delta T$  is 2000 C, the  $L$  is seen to have values of 10  $\mu$  at  $r = 1$  cm/s and 100  $\mu$  at  $r = 0.1$  cm/s. Such burning rates may be taken to correspond approximately to 100 and 1 atm pressure respectively. It is also seen that the characteristic time scale ( $\tau_f$ ) in the vapor phase is given by the ratio of the flame standoff distance ( $L$ ) to the mean flow velocity of the vapors; thus  $\tau_f \sim 2 \times 10^{-5}$  s at 200 atm and at 1 atm. The numbers are close mainly because of the direct dependence of the vapor density on the mean pressure.

As it travels through the vapor, a "pocket" diffuses laterally by a distance of the order of  $(D\tau_f)^{1/2}$ , where  $D$ , the laminar diffusivity, is inversely proportional to the mean pressure and, at a mean temperature of 2000 K, has values of the order of 5 cm<sup>2</sup>/s at 1 atm and 0.05 cm<sup>2</sup>/s at 100 atm. Hence the lateral diffusion distance will be 10  $\mu$  at 100 atm and 100  $\mu$  at 1 atm. If the "pocket" dimension is of the order of the condensed-phase heterogeneity (par-

ticle size), as it would seem logical, it is apparent that diffusional transport must be extremely important at high pressures, since the diffusional distance is of the same order as the pocket (particle) size for typical (100-150  $\mu$ ) AP particle sizes. At the lower pressures (1 atm), the diffusion is sufficiently fast to give essentially premixing over the required 100- $\mu$  distance. Thus chemical kinetic rates should control the overall rate of the lower pressures. Thus different pressure regimes need different treatments to arrive at this important parameter L.

Low Pressures. The "premixed" flame is governed by a single second-order reaction, with  $\epsilon$  being the product concentration. Thus

$$L_f \approx \frac{\dot{m}}{\rho_g} \frac{1}{\frac{d\epsilon}{dt}_{av}} = \frac{\dot{m}}{\rho_g} (1 - \epsilon)^2 \rho_g A \exp\left(\frac{-E}{RT_g}\right) \quad (4)$$

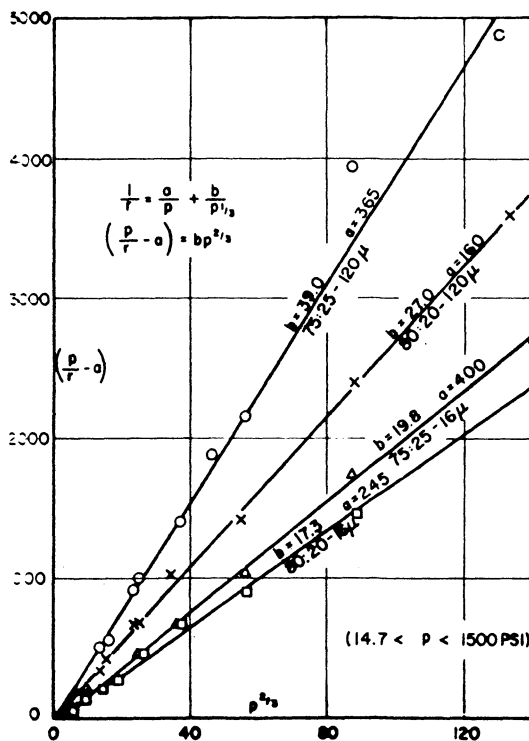


Fig. 8 Comparison of Sutherland's burning rate data with Summerfield's theory. (Theoretical equation appears as straight line on this type of plot.)

## Chapter 9

# Combustion of Metalized Propellants

E. W. Price\*

*Georgia Institute of Technology, Atlanta, Georgia*

### Abstract

Metal powders are of interest as fuel ingredients because of their high density and high heat of reaction. However, their combustion behavior is quite varied and unlike the other more volatile ingredients of propellants. This combustion behavior typically consists of an accumulation of the metal on the burning surface, leading to formation of aggregates that coalesce into relatively large, slow burning agglomerates that burn after leaving the burning surface. Details are highly dependent on the metal, propellant formulation, ingredient particle size distributions, and flow conditions in the combustion environment. In turn, the detailed behavior determines the effect of the metal on the propellant burning rate, combustion stability and combustion efficiency. The details are described for the most commonly used metal--aluminum.

### I. Metals as Fuel Ingredients in Propellants

Metals are used in solid propellants for a variety of reasons, but primarily to increase motor specific impulse and propellant density. Some metals react with very high flame temperatures, the primary cause of the increased specific impulse and primary reason for their use in propellants. However, the metals burn in a very different manner than other propellant ingredients, and sometimes in the process they modify the burning characteristics of the

---

Copyright © 1983 by E. W. Price. Published by the American Institute of Aeronautics and Astronautics with permission.

\*Professor, School of Aerospace Engineering.

propellant. The particular effects depend on the metal used and the nature of the propellant.

Metals that have been used or considered include aluminum, magnesium, boron, zirconium, and beryllium. In most cases, a powdered form is appropriate and is incorporated in the composite propellant in the same way as other granular ingredients (randomly mixed). Particle sizes in the range of 5-200  $\mu\text{m}$  are used, with the range 10-40  $\mu\text{m}$  being most common. Of the metals noted above, only aluminum has been used extensively and is used in mass fractions of 12-22%. Occasionally, low concentrations of aluminum are used to suppress oscillatory combustion. Metals have also been used in wire, foil, and screen forms as means of controlling the burning rate or mechanically reinforcing the charge, but such use is so limited it will not be reviewed here.

The unique combustion behavior of metals is due in large measure to the physical properties of the metals and their oxides. Most do not vaporize at the temperatures of propellant burning surfaces, and hence can reside on the burning surface for a time after emerging there. Even after leaving the burning surface, the metal particles may burn relatively slowly because of low volatility. Given this property, it should be no surprise that metal particles tend to accumulate on the burning surface and then burn in the combustor cavity where the other ingredients have already reacted to the equilibrium gaseous products. The slowness of some metals to burn is aggravated by their resistance to ignition, due to the formation of protective oxide "skins" on the particles. In the case of aluminum, combustion is prolonged even more by the coalescence of large numbers of particles into large "agglomerates" on the propellant burning surface. Such large droplets (typically 50-200  $\mu\text{m}$ ) require a time of 10-100 ms to complete burning. Combustion of the metal does not usually contribute much to the burning rate of the propellant itself, because most of the heat release occurs far from the propellant surface. However, as with most generalizations about metal behavior, this one is violated by some propellant compositions (e.g., in oxidation of the metal accumulation on the burning surface by fluorine-containing oxidizers).

Metals (particularly aluminum) have been used routinely in many service propellants and pose no serious problems in those applications. Some accommodation must be made in motor design to tolerate the high heat transfer associated with high flame temperature and condensed phase reaction



products. A significant deficit in thrust results from the two-phase flow losses in the nozzle, causing a smoky exhaust plume. What we have come to expect of the metal fuel is based on the performance in successful applications which have used 12-22% aluminum. The full potential of metal fuels is difficult to approach in many situations and performance deficits are difficult to predict because of the complex combustion behavior. Some of the problem areas are suggested by the following:

- 1) The optimum content of metals based on thermochemical equilibrium calculations is substantially higher than the contents used in practice, but the ideal performance is not approached with the high-aluminum-content propellants because of low combustion efficiency and the two-phase flow loss in the nozzle.

- 2) The high energy of metalized propellants is particularly important in upper stage and space motors, but combustion efficiency tends to be particularly poor at the low pressures used in such motors.

- 3) The details of the metal combustion and size distribution of the condensed phase products are important to combustor stability, but those details remain substantially undetermined, unpredictable, and unmeasurable to date.

- 4) In some applications involving high accelerations and/or high metal content, the condensed phase material (metal and oxide) "puddles" and flows, with anomalous burning and heat-transfer effects and retention of the material in the motor after burnout.

Problems such as those listed under items 1-4 above represent opportunities for fuller exploitation of the potential of metals as propellant ingredients and have been the basis for continuing research on metal combustion, in both idealized laboratory conditions and propellant experiments. In this chapter, the details of metal combustion will be discussed briefly and experimental observations of propellants summarized and interpreted.

## II. Metal and Oxide Properties

In order to understand and anticipate metal behavior in propellant combustion, it is helpful to examine some critical properties such as the melting and boiling points of the metals, and how these temperatures compare with those at various locations in the propellant combustion zone. To illustrate, if a metal is molten at temperatures present on the burning surface of the propellant, a possibility exists that the particles will coalesce to form large droplets (which may have a long burning time). Alternately, if the

surface oxide skin has a high melting temperature, it may be difficult to ignite the particles. Some of the properties of importance are:

1) The ratio of molar volume of solid oxide to constituent solid metal. Values less than one lead to surface oxide layers on particles that are permeable, while values greater than one tend to yield impermeable surface oxide skins that limit oxidation at temperatures present on the propellant burning surface.<sup>1-4</sup> The degree of inhibition by the oxide skin is reported to be affected also by plastic flow behavior of the oxide and metal during surface oxidation.<sup>5</sup>

2) Ratio of coefficients of thermal expansion of the solid metal and oxide. Values greater than one lead to stressing of the oxide skin during heating. Positive values of the expansion of the metal during melting tend to fracture oxide skins.<sup>2,4,6,7</sup>

3) Melting point of the metal. When the value is in the temperature range present on the burning surface of the propellant, particle coalescence becomes possible, see Table 1. Concurrent fracture of the oxide skins and flow of the metal during coalescence usually results in an increased oxidation rate and possible ignition.<sup>2,3,6-8</sup>

4) Melting point of the oxide. Wherever this temperature is reached, the role of the oxide skin changes, giving rise to different effects with different metals, see Table 1. When  $T_{MOx} > T_{MM}$ , the melting oxide may dissolve in the molten metal (Zr), or alternately may retract from the surface (Al); if the oxide melting temperature is attained at the propellant burning surface, the oxide may cause the particles to stick together there (B).<sup>1,2,8-11</sup>

5) Solubility of the molten oxide in the molten metal. With high solubility (Zr and Ti), burning may proceed by diffusion of the metal to the surface through an oxide layer.<sup>11</sup> With low solubility, high oxide surface tension and low interfacial surface tension between the oxide and the metal (Al), the oxide tends to accumulate on the surface, and retract and expose the metal.<sup>2,4,5,7</sup> With low solubility and high interfacial surface tension, an oxide surface layer impedes reaction.<sup>12,13</sup>

6) Boiling point of the metal. When this temperature is approached, the oxide skin, if still present, is destroyed and burning initiates and proceeds by a flame envelope around the droplet, yielding vapor or a condensed

Table 1 Physical properties of some candidate metals for solid-propellant fuels

Metal	Metal melting temperature <sup>a</sup> ( $T_{MM}$ ), °K	Oxide melting temperature <sup>b</sup> ( $T_{MOx}$ ), °K	Metal boiling temperature <sup>c</sup> ( $T_{BM}$ ), °K at 1 atm	Oxide boiling or dissociation temperature <sup>d</sup> ( $T_{BOx}$ ), °K at 1 atm	Porosity of oxide skin <sup>e</sup>	Ratio of thermal expansion coeff. of metal and oxide <sup>f</sup> ( $\Delta V_M / \Delta V_{Ox}$ )	Expansion of metal upon melting, % <sup>g</sup>
<b>Volatile metals</b>							
K	336		1035	1154 D	0.45	-----	-----
Mg	923	3080	1385	3533-3853	0.81	-----	-----
<b>Nonvolatile metals, nonsoluble oxides</b>							
Al	933	2320	~2750	3253 D	1.45	>1.0	6
Be	1557	2830	2757-3243	4060-4533	1.68	-----	-----
Si	1687	1990	2953-3514	2503	-----	-----	-----
<b>Nonvolatile metals, soluble oxides</b>							
Ti	1945	2125	3560	-----	1.73	-----	-----
Zr	2127	2988	4700	-----	1.45	-----	-----
<b>Nonvolatile metals, volatile oxides</b>							
B	~2400	728	3940	2133-2316	-----	-----	-----
W	3680	1750	5273-5936	1997 D	-----	-----	-----

Physical consequences of tabulated properties: <sup>a</sup>Can lead to disruption or solution of oxide skin, with increasing reaction rate of particle adhesion. <sup>b</sup>Can lead to retraction or solution of oxide skin, much increased reaction rates. <sup>c</sup>Can lead to rupture, dispersal of oxide, onset of detached flame, high reaction rate, smoke formation, and high luminosity. <sup>d</sup>Leads to complete re-

moval of surface oxide, possibly vapor-phase product oxide. <sup>e</sup>Values < 1 correspond to porous oxide skin, slow but continued oxidation even at room temperatures. <sup>f</sup>Values > 1 mean that the oxide skin is stressed, and possibly cracked during temperature rise, exposing aluminum. <sup>g</sup>Solid oxide skins are stressed during metal melting due to expansion.

"smoke" oxide (Mg, Al, possibly Be). In the case of magnesium the metal boiling temperature is low enough to assure ignition on or near the propellant burning surface. When the metal boiling point is very high (Ti, Zr, B, W) it may not be approached at all, in which case the droplet must burn primarily by a surface reaction with the oxide properties governing the mode of behavior as in item 5, such as,

Al: oxide melt retracts, resulting in a flame envelope and oxide smoke.

Ti and Zr: oxide dissolves, resulting in surface reaction and large oxide product particles.

B: oxide may evaporate, resulting in surface reaction or flame envelope.

W: oxide decomposes and the particle burns on the surface to lower oxide vapors.

7) Boiling point of the oxide (or dissociation). When this temperature is approached, the droplet surface clears and combustion proceeds rapidly by the surface reaction or flame envelope. This is important in the case of boron and tungsten. Note that the boiling points are pressure dependent.

The foregoing enumeration of typical effects of the physical properties of the metals and oxides illustrate the diversity of ignition and combustion behavior possible with the various metals at different droplet temperatures and dependence on thermophysical properties. The modes of behavior noted are verified experimentally, but are dependent on details of the oxidizing atmosphere (pressure, temperature, composition).<sup>11-17</sup> In a propellant combustion environment the environmental composition is complex and the composition and temperature are progressive (i.e., change with time during ignition and burning of the droplets) and it is not practical or currently possible to describe the complete range of combustion behavior for all metals. Because of the wide use of aluminum in propellants, the balance of this chapter will be concerned primarily with its behavior in controlled experiments and propellant combustion.

### III. Results of Controlled Experiments with Aluminum

Motivated by observations of aluminum behavior in propellant studies, laboratory experiments have been developed to study such aspects of the behavior as 1) mode of, and conditions for, breakdown of the oxide skin, believed to be critical to coalescence of particles and to

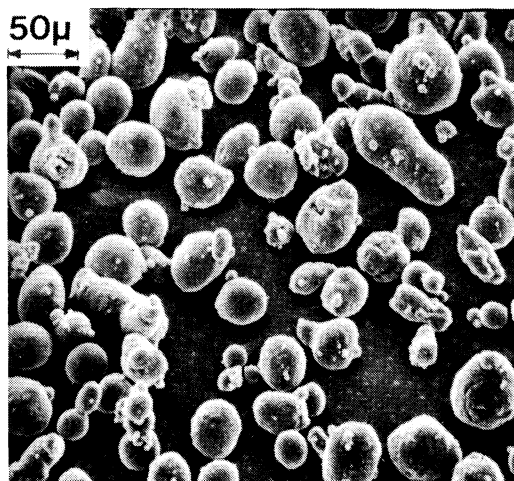


Fig. 1 Aluminum particles typical of propellant ingredients.

ignition<sup>2,6-8,10,18,19</sup>; 2) nature and control of the initial oxide skin<sup>6-8,18,20</sup>; 3) coalescence of particles in powders, dependence on temperature, atmosphere, and powder characteristics<sup>2,6,8,18,19</sup>; 4) single particle and fine wire combustion in controlled atmospheres (with ambient temperature and pressure atmospheres and in gas burner flames)<sup>9-11,13-17,21-26</sup>; and 5) combustion in pressed powder mixtures (simpler than propellants, e.g., aluminum-ammonium perchlorate mixtures).<sup>2,17-19,27-30</sup>

Experimental observations include microscopic studies of partially burned or heated samples, visual and photographic observation of the burning, spectroscopic observations of the flame, and collection and observation of the reaction products (i.e., oxides).

Aluminum particles typical of propellant ingredients are shown in Fig. 1. When such particles are heated in a hot stage microscope, their response is only marginally visible until the aluminum melting point is reached. At that temperature, the thermal expansion is evident. When heating is continued in inert atmospheres, the oxide skin seems to have broken down enough so that the aluminum can drain out under the influence of surface tension.<sup>2,3,6-8,10,18,19</sup> (See Fig. 2.) In an oxidizing atmosphere this behavior is impeded until a higher temperature is reached. The mechanisms are

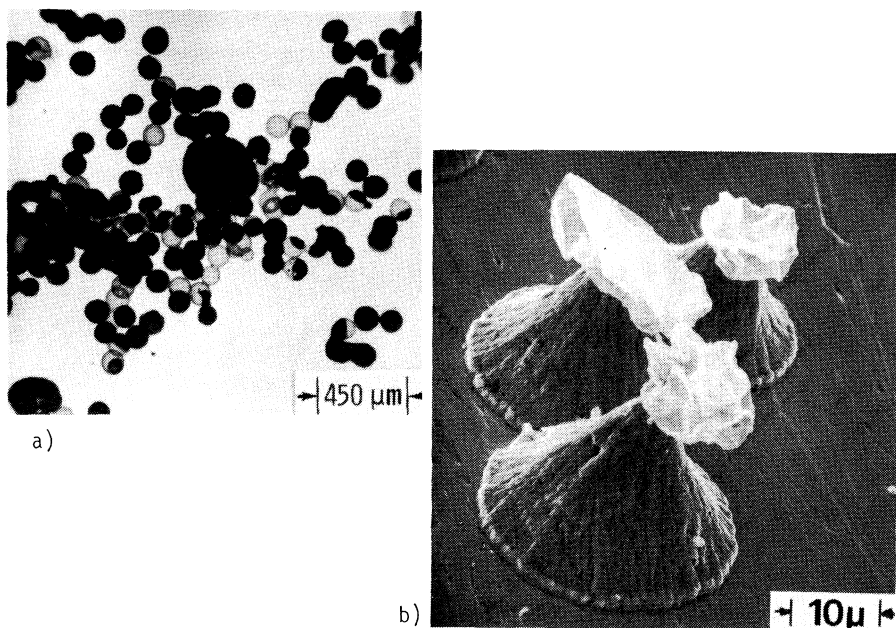


Fig. 2 Drainage of aluminum from oxide "skins" above the metal melting point: a) on a sapphire surface, showing particles in various stages of drainage (optical microscope picture) (photo by K. Kraeutle, U. S. Naval Weapons Center); b) on a platinum wire, where the interfacial forces with platinum draw the metal out and leave collapsed oxide skins (scanning electron microscope picture).

suggested by observations of particles rapidly heated by dropping them on a preheated plate (Fig. 3). Recovered particles show expansion crack patterns in the oxide, "healed up" by oxidation of emerging metal.<sup>6,7,10,19</sup> Under other conditions, "warts" are formed on particles by expansion of molten aluminum through the oxide skin at local sites<sup>8,18</sup> (Fig. 4). Modifications of the oxide skin are observed to change both this detailed behavior (Fig. 5) and the propellant combustion behavior.<sup>2,6,18-20</sup>

When collections of contacting particles are heated in inert atmospheres, molten aluminum is observed to withdraw from the oxide skins and coalesce into larger "agglomerates" (Fig. 6).<sup>2,6-8,18,19</sup> In oxidizing atmospheres, the particles sinter together instead (Fig. 3) and agglomerate only moderately. When lightly packed powders are heated, similar behavior occurs; measurements of electrical conductivity show a transition from low conductivity to metallic conductivity in the vicinity of the metal melting point,

## ALUMINUM PARTICLE AGGLOMERATION

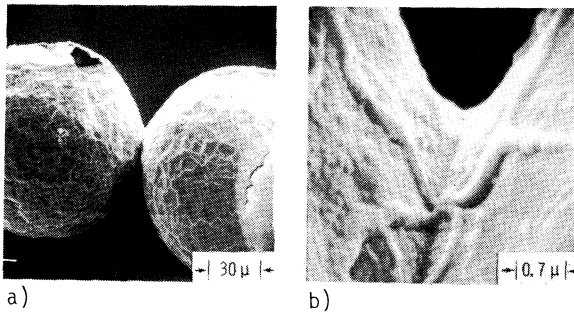


Fig. 3 Cooled particles that have been heated to  $1400^{\circ}\text{C}$  on a sapphire plate in an oxygen-containing atmosphere: a) cracked oxide shells evident; b) oxidation healing of cracks, including contact point between particles. (Photos by K. Kraeutle, U. S. Naval Weapons Center.)

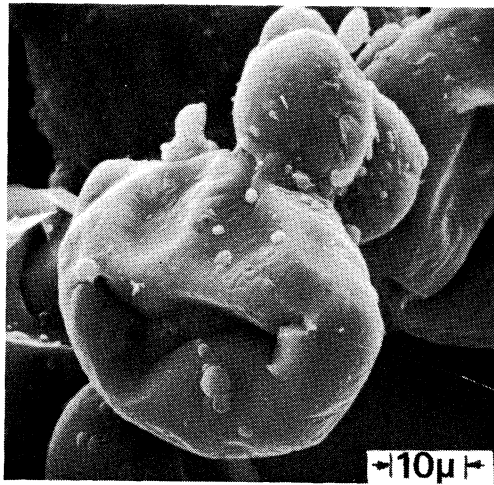
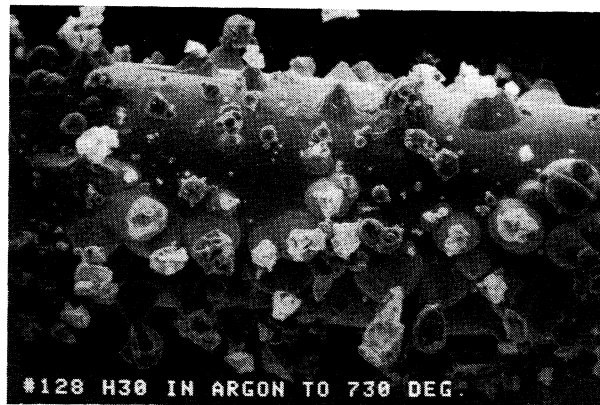
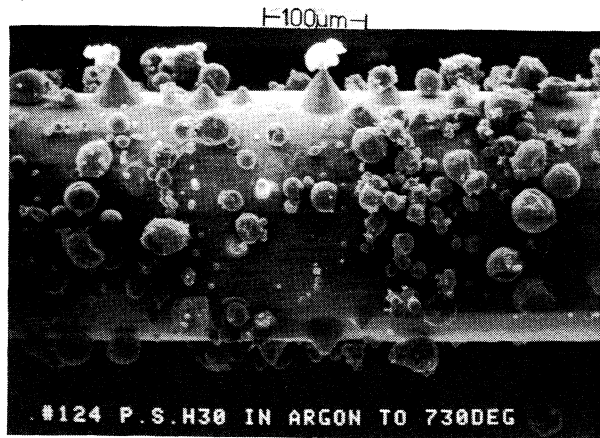


Fig. 4 Exudation of aluminum is sometimes localized, resulting in a wart-like protrusion, and collapse of the original oxide skin during the subsequent cooling in laboratory heating tests.

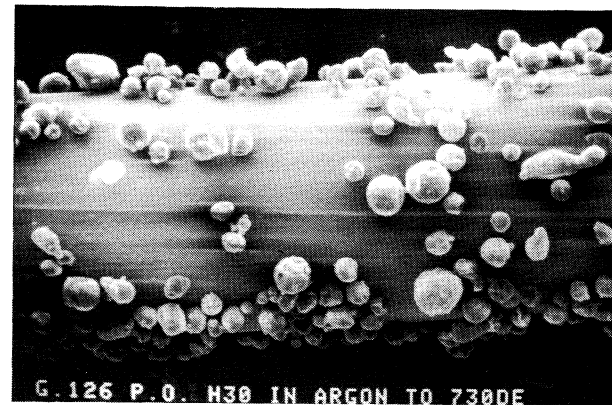
indicating metal bridging between particles (Fig. 7).<sup>6,7,19</sup> The temperature for this transition is sharply dependent on the quality of the oxide skin on the particles (compare with curves in Fig. 7), indicating once more that the breakdown of the skin due to droplet expansion can be decisive in the occurrence of agglomeration. Because the temperatures involved in these experiments are typical of propellant surface temperatures, it is no surprise that the agglomeration of aluminum particles occurs during propellant



a)



c)



b)

Fig. 5 Comparison of tendency for aluminum to leak from the oxide skin during heating to  $730^{\circ}\text{C}$  in argon; a platinum wire surface was used to enhance effects. Valley Met H-30 aluminum a) as received; b) enhanced oxide skin; c) prestretched oxide skin cones indicate breakdown of the oxide and withdrawal of aluminum. (See Fig. 2.)



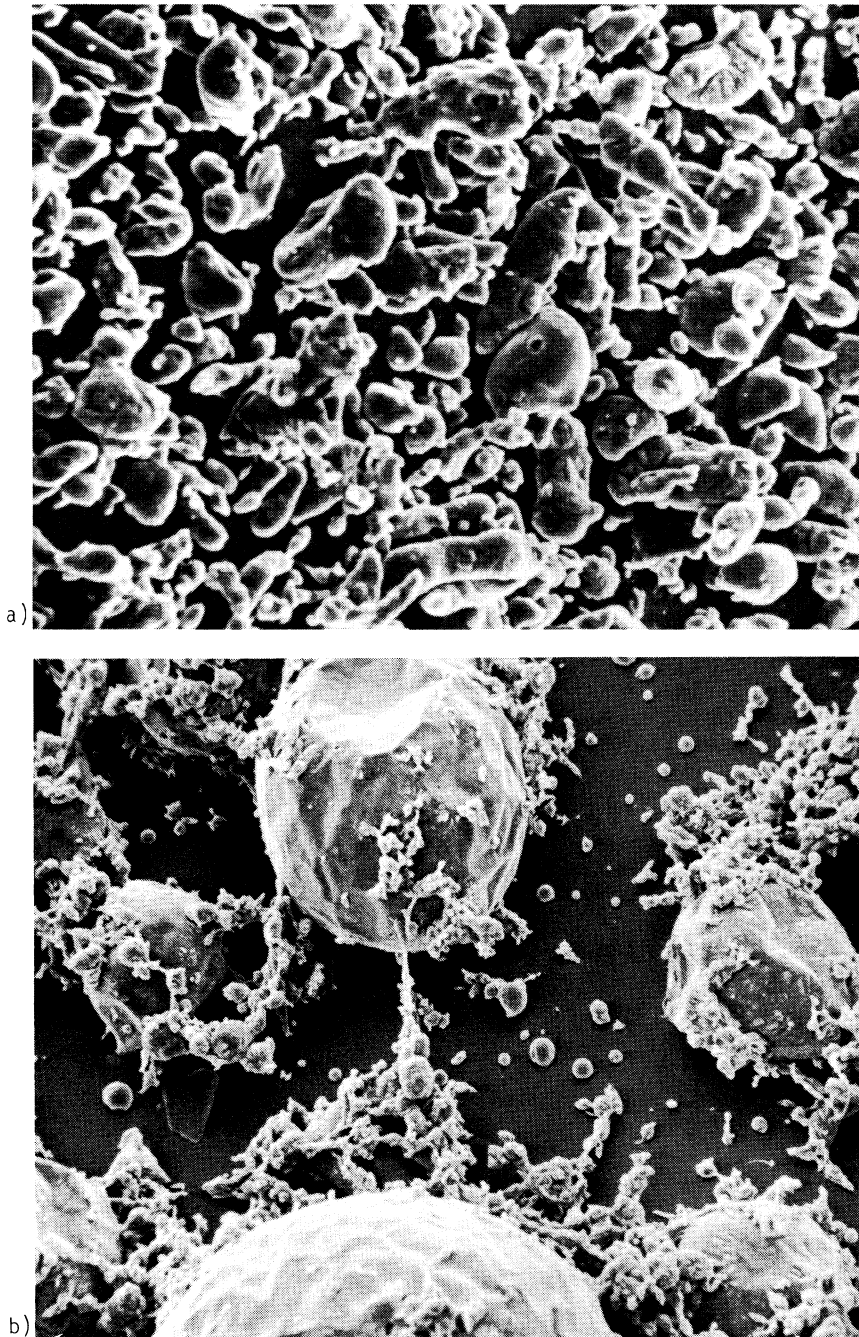


Fig. 6 Comparison of response of aluminum powder to heating (Alcoa 123): a) no heating; b) heated to 1300 K in argon.

## Chapter 10

### Erosive Burning of Solid Propellants

Mohan K. Razdan\* and Kenneth K. Kuo†  
*The Pennsylvania State University,  
University Park, Pennsylvania*

#### Abstract

Erosive burning usually refers to the increase in the propellant burning rate caused by high-velocity combustion gases flowing over the propellant surface. It may seriously affect the performance of solid-propellant rocket motors. This article reviews both theoretical and experimental studies of erosive burning. Theoretical models are classified into four major groups: 1) phenomenological heat-transfer theories, 2) integral boundary-layer analysis, 3) modification of the propellant combustion mechanism, and 4) chemically reacting turbulent boundary-layer analysis. Experimental methods and observed effects of various physical parameters on erosive burning are discussed and reviewed. The erosive burning mechanism is believed to be caused by the increase in gas-to-solid heat feedback introduced by the increase in transport coefficients, and by the turbulence-enhanced mixing and reaction of the oxidizer- and fuel-rich gases pyrolyzed from composite propellants. Both theoretical and experimental studies are summarized in tabular form to facilitate comparison between various approaches. Areas of future studies are also recommended.

---

Copyright © American Institute of Aeronautics and Astronautics, Inc., 1983. All rights reserved.

\*Assistant Professor, Department of Mechanical Engineering (presently Staff Engineer at Exxon Research and Engineering Company, Clinton, N.J.).

†Professor, Department of Mechanical Engineering.

## Nomenclature

$a$	= pre-exponent in normal burning rate law, $(\text{m/s})/(\text{MPa})^n$
$A$	= cross-section flow area, $\text{m}^2$
$A_1, A_2, A_3$	= empirical constants relating $r_o$ to $p$ in Eq. (44)
$A_g$	= Arrhenius frequency factor in gaseous reactions, $(\text{m}^3)^{n-1} \text{s}^{-1} (\text{kmole})^{1-n}$
$A_s$	= Arrhenius frequency factor in propellant surface decomposition, $\text{m/s}$
$A^+$	= damping constant in van Driest's hypothesis
$b$	= correlation parameter in granular diffusion flame model
$B$	= $(\rho_s r_p)/(\rho U)_\infty$ , nondimensional mass blowing rate
$C_1, C_4, C_\mu, C_\omega$	= constants in turbulence models
$C_p$	= average heat capacity of reacting gases, $\text{kcal/kg}\cdot\text{K}$
$C_s$	= heat capacity of solid propellant, $\text{kcal/kg}\cdot\text{K}$
$d_{AP}$	= average diameter of ammonium perchlorate particles, $\text{m}$
$D$	= port diameter of rocket motor, $\text{m}$
$\mathcal{D}$	= diffusion coefficient in Fick's law, $\text{m}^2/\text{s}$
$\mathcal{D}$	= damping coefficient defined in Eq. (30)
$E_{ag}, E_{as}$	= activation energies in gas-phase reaction and propellant surface decomposition, $\text{kcal/mole}$
$g_F$	$\equiv \overline{Y_F'^2}$ , mean square of fuel mass fraction fluctuations
$G$	= mass velocity of combustion gas, $\text{kg/m}^2\cdot\text{s}$
$h$	= static enthalpy of gases, $\text{kcal/kg}$
$H$	= stagnation enthalpy of gases, $\text{kcal/kg}$
$I$	$\equiv G\sqrt{C_f}/r_o\rho_s$ , nondimensional erosive burning parameter
$k$	= von Kármán's constant
$K$	$\equiv \overline{u_i' u_i'}/2$ , turbulent kinetic energy, $\text{m}^2/\text{s}^2$

$K_e, K_e', K_e'', K_e'''$	= empirical constants for erosive burning correlation
$L$	= port length, m
$Le$	= Lewis number based upon molecular properties of gases
$L_f$	= flame height, m
$Le_t$	= turbulent Lewis number
$\dot{m}_b$	= mass burning rate, $\text{kg/m}^2 \cdot \text{s}$
$M$	= Mach number or mass
$n$	= exponent in normal burning rate law or order of reaction
$p$	= pressure, Pa
$p_o$	= stagnation pressure, Pa
$Pr$	= Prandtl number based upon molecular properties of gases
$Pr_t$	= Prandtl number for turbulent flow
$\dot{q}_w$	= gas-to-wall heat flux, $\text{kcal/m}^2 \cdot \text{s}$
$Q_\ell$	= heat of sublimation, $\text{kcal/kg}$
$\dot{Q}_r$	= rate of heat generation in gas phase, $\text{kcal/m}^3 \cdot \text{s}$
$\overline{Q}_s$	= heat of reaction at a reference temperature, $\overline{T}_s$ , $\text{kcal/m}$
$Q_v$	= heat of vaporization, $\text{kcal/kg}$
$r$	= coordinate in radial direction, m
$r_b$	= total burning rate of a solid propellant, m/s
$r_e$	= erosive burning rate component of $r_b$ , m/s
$r_o$	= normal (nonerosive) burning rate component of $r_b$ , m/s
$R$	= port radius of a rocket motor, m
$Re_x$	= Reynolds number based on $x$ defined as $\rho_\infty U_\infty x / \mu$
$R_h$	= roughness height, m
$R_u$	= universal gas constant, $\text{N.m/kmole.K}$
$Sc$	= Schmidt number based upon molecular properties of gases
$Sc_t$	= Schmidt number for turbulent flow
$St$	= Stanton number under blowing conditions
$St_o$	= Stanton number under no-blowing conditions
$t$	= time, s

$T$	= gas temperature, K
$T_f$	= flame temperature, K
$T_o$	= stagnation temperature, K
$T_p$	= temperature within solid propellant, K
$T_s$	= temperature at propellant surface, K
$u$	= gas velocity in x direction, m/s
$u_*$	= friction velocity defined as $\sqrt{\tau_s/\rho_\infty}$ , m/s
$u^+$	= nondimensional friction velocity defined as $u_*/u$
$U$	= axial gas velocity outside boundary layer, m/s
$v$	= gas velocity in y or r direction, m/s
$v_w$	= transpiration gas velocity at propellant surface, m/s
$w$	= gas velocity in z direction, m/s
$W$	= molecular weight of gases, kg/kmole
$x$	= coordinate in axial direction, m
$y$	= coordinate normal to propellant surface, m
$y_w$	= vertical coordinate with its origin on propellant surface, $y_w \equiv R-y$ , m
$Y_k$	= mass fraction of kth species
$y^+$	= nondimensional distance, $y^+ \equiv \rho u_* y/\mu$
$(\bar{\quad})$	= time-averaged quantity in ( )
$(\quad)'$	= fluctuating quantity in ( )
$\alpha, \beta$	= constants in erosive burning rate equation
$\alpha_g$	= thermal diffusivity of gas, $m^2/s$
$\gamma$	= ratio of constant-pressure to constant-volume specific heats
$\epsilon$	= turbulent dissipation rate, $m^2/s^3$
$\epsilon_b$	= erosive burning augmentation ratio, $\epsilon_b \equiv r_b/r_o$
$\theta$	= flow angle (see Fig. 3)
$\lambda, \lambda_p$	= thermal conductivities of gases and propellant, kcal/m·s·K
$\lambda_A, \lambda_B$	= thermal conductivities of gas with lumped-in area ratio term for each flame, kcal/m·s·K
$\lambda_t$	= thermal conductivity for turbulent flow, kcal/m·s·K

$\mu$	= gas viscosity, kg/m•s
$\mu_{eff}$	= effective viscosity, $\mu_{eff} \equiv \mu + \mu_t$ , kg/m•s
$\mu_t$	= turbulent viscosity defined in Eq. (14), kg/m•s
$(\mu/Pr)_{eff}$	= $(\mu/Pr) + (\mu_t/Pr_t)$ , kg/m•s
$(\mu/Sc)_{eff}$	= $(\mu/Sc) + (\mu_t/Sc_t)$ , kg/m•s
$v_k$	= number of kmoles of the kth species
$v_t$	= turbulent diffusivity, m <sup>2</sup> /s
$\rho, \rho_s$	= densities of gas and propellant, kg/m <sup>3</sup>
$\tau, \tau_s$	= shear stress in gas phase and at propellant surface, N/m <sup>2</sup>
$\phi$	= angle of divergence of port radius
$\sigma_p$	= temperature sensitive, K <sup>-1</sup>

### Subscripts

b	= bulk flow conditions
c	= centerline conditions
fu	= solid fuel in propellant
i	= initial condition and indices for coordinate directions
k	= species index representing fuel gas (F), oxidizer gas (O), and product gas (P)
ox	= solid oxidizer in propellant
th	= threshold value
$\infty$	= freestream condition

### Introduction

The burning mechanism of a solid propellant involves many chemical and physical processes, including change of phase, energy transfer, and mass transfer. The transfer of heat from the flame zone to the propellant surface causes the propellant to pyrolyze and the pyrolyzed gases to react close to the propellant surface. The burning rate of a solid propellant depends on a number of parameters such as the pressure under which it burns, initial propellant temperature, propellant type, fuel-to-oxidizer ratio, and oxidizer particle size in the case of composite propellants. The burning process becomes more complicated as the propellant burns in the presence of a cross flow of combustion gases in the port of a rocket motor grain.

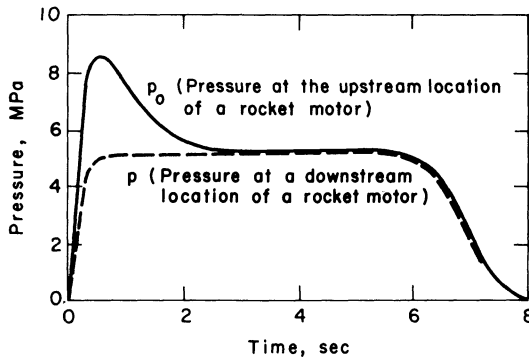


Fig. 1 Typical pressure-time curve of a rocket motor having low port-to-throat area ratio.

Normally, the burning rate of the propellant increases as the cross flow gas velocity increases. The velocity-dependent contribution to the burning rate of a solid propellant is called "erosive burning."

Knowledge about the burning behavior of a solid propellant is of prime importance in the design of a rocket motor because both the thrust level and the burning time depend on the burning rate. High-performance rockets require high-thrust, short-burning solid-propellant grains. To improve rocket motor performance, high volumetric loading fractions (ratio of propellant weight to combustion chamber volume) are required. High loading fractions result in low port-to-throat area ratios of propellant grains; however, this leads to serious erosive burning problems. A typical pressure-time curve of a rocket motor having a low port-to-throat area ratio is shown in Fig. 1. At the beginning of the thrust transient, the pressure at the fore end ( $p_0$ ) differs significantly from that at the aft end ( $p$ ). Therefore, gases accelerate toward the nozzle end of the rocket motor, thereby increasing the burning rate due to erosive burning effect. This can result in unequal propellant-web burnout and early exposure of part of the rocket motor casing to the hot combustion products. If the erosive burning effect is not properly accounted for in the design, rocket chamber failure may occur due to overpressurization immediately following ignition.

Nozzleless rocket motors have recently attracted considerable interest because they offer significant economic advantage and simplicity over conventional motors. However, gases in nozzleless rocket motors choke somewhere within the port and the gas velocity reaches sonic and

supersonic speeds over some portions of the propellant surfaces, leading to high erosive burning rates. It is important, therefore, to be able to predict the erosive burning rate of a solid propellant. An understanding and accurate prediction of the erosive burning characteristics of a solid propellant can lead to the elimination of the aforementioned problems through proper modification in the motor and/or grain design. The erosive burning characteristics of the propellant can also be used to improve the thrust performance of a motor.

According to von Braun,<sup>1</sup> erosive burning studies of solid propellants, date back as early as 1889 in Germany, Japan, Britain, and The Soviet Union. The erosive burning effect was observed in experiments by Mansel<sup>2</sup> on Cordite (a modified double-base propellant), which indicated a sharp pressure rise in a rocket motor and its dependence on the geometrical configuration of the propellant grain. Muraour<sup>3</sup> was probably the first investigator to describe the erosion effect explicitly. The first systematic studies of erosive burning were apparently initiated in the United Kingdom and the United States, using colloidal, double-base propellants. Erosive burning problems have subsequently been the subject of numerous studies for both double-base and composite propellant formulations.

Literature reviews on erosive burning problems have been reported by Williams et al.,<sup>4</sup> Kuo and Razdan,<sup>5</sup> and King.<sup>6</sup> In the last several years, however, a renewed interest has developed in understanding the erosive burning phenomenon in solid-propellant rocket motors, and a number of publications on the subject have appeared in literature.

In the following sections, theoretical studies are grouped under four major categories, according to the physical basis of each theoretical model. Three recent theoretical models are described in some detail. Various experimental methods used in erosive burning studies are discussed subsequently, and two recent experimental studies are also described. For an easy comparison between the various studies, theoretical and experimental studies reported in literature are presented in tabular form. Observed effects of various parameters on erosive burning and the physical mechanism of erosive burning phenomenon are also discussed in detail. Finally, recommendations for future work and conclusions are presented.

### Theoretical Approaches to Erosive Burning

#### Classification of Erosive Burning Theories

Without consideration of the type of propellants (i.e., homogeneous or heterogeneous), existing theories on



erosive burning may be divided into four major groups, depending upon whether models are based on phenomenological heat transfer theories,<sup>7-12</sup> an integral boundary-layer analysis,<sup>17-27</sup> a modification of the propellant combustion mechanism,<sup>28-33</sup> or a chemically reacting boundary-layer analysis.<sup>35-42,83,84</sup> It should be noted, however, that some of the theoretical models have a combination of the aforementioned physical bases. In these cases, models were classified according to the major physical basis used. Some theoretical work could not be included in any of the groups and are classified as other models.<sup>43-45</sup>

Models Based on Phenomenological Heat-Transfer Theories. Lenoir and Robillard<sup>7</sup> (L-R) were the first to develop a model based on the heat-transfer theory. Two mechanisms of gas-to-solid heat transfer were proposed: 1) from the primary burning zone, which is independent of core gas velocity and is a function only of pressure; and 2) from the core of hot combustion gases, which depends on gas velocity. Using this approach, total burning rate is expressed as

$$r_b = r_o + r_e \quad (1)$$

where  $r_o$  is the pressure-dependent normal burning component and  $r_e$  the erosive burning component. The erosive burning rate was postulated to be proportional to the convective heat-transfer coefficient under conditions of transpiration. The Chilton-Colburn heat-transfer correlation, with a correction for transpiration, was used to obtain the following equation for the total burning rate:

$$r_b = ap^n + \alpha G^{0.8} \exp(-\beta r_b \rho_s / G) / L^{0.2} \quad (2)$$

where  $\alpha$  and  $\beta$  are empirical constants for a particular propellant. Results of studies on similar types of propellants showed that  $\beta$  is apparently independent of propellant identity and has a value around 53. An expression for  $\alpha$  was derived by Lenoir and Robillard<sup>7</sup> by considering the energy balance between the heat transfer from the flame to the propellant surface and the heat required to raise the propellant temperature from its initial temperature  $T_{pi}$  to its final surface temperature  $T_s$ . The expression derived was

$$\alpha = \frac{0.0288 C_p \mu^{0.2} Pr^{-2/3}}{\rho_s C_s} \left( \frac{T_f - T_s}{T_s - T_{pi}} \right) \quad (3)$$

Because of its simplicity, the L-R correlation [Eq. (2)] has been widely used in rocket motor performance calculation. However, there has been some criticism<sup>11,13-15</sup> as well as some support<sup>21</sup> for the additive assumption of the burning rates represented by Eq. (1). The validity of the additive assumption of burning rates is still unresolved in the literature, even though it does not appear to have any physical basis. Since its development, several authors<sup>8-12</sup> have modified the L-R correlation in one form or another. One common modification has been to use the heat-transfer correlation as a function of Reynolds number, which is based on the port diameter of a rocket motor rather than its length. It has been observed<sup>15,42</sup> that the L-R theory overpredicts erosive burning in full-scale motors for values of  $\alpha$  and  $\beta$  obtained from correlations using subscale motor data.

Marklund<sup>8</sup> modified the L-R correlation by considering only the mass addition due to oxidizer in a composite propellant. By doing this, some of the physicochemical properties of the propellant (e.g.,  $Y_{fu}$ ,  $Q_{v_{ox}}$ ,  $T_{f_{ox}}$ ,  $T_{s_{ox}}$ ) were introduced into the final form of the correlation. However, agreement with the data was achieved by adjusting two constants. Zucrow et al.<sup>9</sup> extended the work of Marklund<sup>8</sup> by incorporating more physicochemical properties of the propellant into the final form of the erosive burning correlation. In their analysis, Burick and Osborn<sup>10</sup> included the mechanical erosion effect, in addition to the erosion effect due to heat transfer. According to these authors, mechanical erosion plays an important part in the erosive burning phenomena, a conclusion not supported by other studies reported in literature. King<sup>11</sup> developed a correlation by assuming the total gas-to-solid heat flux to be the sum of heat fluxes by conduction from the flame zone and core gases and by using the concepts of the granular diffusion flame (GDF) theory.<sup>16</sup> Thus, King<sup>11</sup> argues that the additive assumption of the L-R theory is removed. King's approach has been criticized,<sup>13,14</sup> however, because of his assumption of additive heat fluxes. Another modification of the L-R theory is that of Jojić and Blagojević<sup>12</sup> who added a component of the burning rate due to the plateau effect in their modified L-R correlation. Both negative and threshold effects are predicted by the modified correlation if the "proper" parameters and constants are chosen.

Models Based on Integral Boundary-Layer Analysis.  
Erosive burning models in this group are based on the increased heat transfer to the propellant surface, due to

the enhancement of transport properties in the boundary layer caused by turbulent flow. Integral boundary-layer analysis is generally used to obtain expressions for transport coefficients. Corner<sup>17</sup> was the first to use this concept in developing an erosive burning theory. His analysis was based on the assumption that the erosive burning component is proportional to the effective thermal conductivity. He used the Prandtl-Kármán boundary-layer theory to relate effective thermal conductivity to the freestream gas velocity. However, Corner's work gave no consideration to the effect of mass injection into the boundary layer. Geckler<sup>18</sup> developed his model along lines similar to those of Corner,<sup>17</sup> postulating that the erosive burning augmentation ratio  $\varepsilon_b$  was proportional to the product of the eddy diffusivity and the freestream mass velocity of the gas. In the analysis of Erokhin et

al.,<sup>19</sup> burning rate was taken to be proportional to the turbulent heat flux from the flame zone to the propellant surface. Temperature distribution was obtained by integrating the energy equation into the heating zone (with no heat release) and the reaction zone (with heat release). Erokhin et al.<sup>19</sup> used Prandtl's mixing length hypothesis to obtain an expression for eddy thermal conductivity. Zel'dovich<sup>20</sup> developed a theory of erosive burning based on the concepts of Corner<sup>17</sup> and Erokhin et al.<sup>19</sup> The final expression for the erosive burning rate obtained by Zel'dovich<sup>20</sup> is similar to that obtained by Corner.<sup>17</sup> Perhaps one of the better models using integral boundary-layer analysis is that developed by Lengellé.<sup>21</sup>

Lengellé<sup>21</sup> developed the erosive burning model for a composite solid propellant using the granular diffusion flame theory.<sup>16</sup> The burning rate is related to the flame thickness through the relation

$$\dot{m}_b Q_v \approx \lambda (T_f - T_s) / L_f \quad (4)$$

where  $Q_v$  is the energy required to raise the propellant from its initial temperature  $T_{pi}$  to the surface temperature  $T_s$  and to transform it into gases. Following the granular diffusion flame theory,<sup>16</sup> the flame thickness is expressed as

$$L_f \sim \dot{m}_b M_p^{2/3} / \rho^{2/3} / (\rho D) \quad (5)$$

where the characteristic mass of the gaseous fuel pocket is  $M_p$  (determined by the ammonium perchlorate (AP) content and its mean particle size). Lengellé argued that, in a

normal, nonerosive combustion regime, the transport coefficients  $\lambda$  and  $D$  in Eqs. (4) and (5) are the laminar ones. Under erosive conditions, these coefficients are modified by turbulent components that depend on the nature of the flow. Assuming that the turbulent Lewis and Schmidt numbers are close to unity and that the flame thickness is not affected by the turbulent flow, the burning mass flow rate, from Eqs. (4) and (5), is then expressed as

$$\dot{m}_b \approx \left[ \frac{C_p (T_f - T_s)}{Q_v} \right]^{1/2} \left( \frac{\rho}{M_p} \right)^{1/3} (\mu + \rho v_t) \quad (6)$$

Using Couette flow and Prandtl's mixing length approximations, Lengellé integrated the boundary-layer equations (momentum and continuity) to obtain an expression for the velocity profile and turbulent momentum diffusivity  $v_t$ . Average values of the turbulent diffusivity in the flame zone were used by Lengellé in Eq. (6). Lengellé's approach has a good physical basis but it represents an oversimplification of the problem in an attempt to obtain a simple final expression for the burning rate. The assumption that the flame thickness is not affected by the presence of the flow is in direct conflict with the basis of King's model.<sup>31</sup> However, Lengellé, obtained favorable comparison of his prediction with experimental data.

Joulain et al.<sup>22,23</sup> have formulated the problem of the combustion of solid fuel (or solid oxidizer) in the presence of a turbulent flow of gaseous oxidizer (or gaseous fuel). They considered conservation equations for mass, momentum, species mass fraction, and energy. The Couette flow assumption was used to integrate the governing equations within the boundary layer. In solving the energy equations, a thin flame sheet approximation was also employed. Joulain et al.<sup>22,23</sup> performed numerical solutions of their model that compared favorably with their experimental data. Mukunda<sup>24</sup> also formulated the erosive burning problem of double-base solid propellants based on the Couette flow approximation of turbulent boundary-layer equations. He obtained numerical solutions of the eigenvalue problem, but compared them with experimental data of composite solid propellants due to the lack of data on double-base propellants. In both of the aforementioned models, the use of the Couette flow approximation for the entire boundary layer thickness is incorrect. This assumption precludes any possible turbulent correlations

between velocity and temperature. Such relationships have been found<sup>38-42</sup> to make important contributions to heat-transfer processes within the boundary layer.

In their recent work, Parkinson and Penny<sup>25,26</sup> have associated the erosive burning phenomena with the reattachment of a blown boundary layer in a rocket motor. They used the momentum integral theory to predict the boundary-layer reattachment point. Along with a modified Lenoir-Robillard<sup>7</sup> correlation, the resultant theory was used to predict the pressure-time history of a rocket motor. Parkinson and Penny conclude that the erosive burning effect (represented by maximum-to-minimum pressure ratio in a rocket motor) strongly correlates with  $B Re_x^{0.2}$ , and erosive burning reaches serious proportions when  $B Re_x^{0.2}$  is less than 0.3. The assumption that erosive burning is caused by reattachment of the boundary layer may require direct experimental evidence. In a follow-up work of Parkinson,<sup>27</sup> erosive burning effect was associated with enhancement of the thermal conductivity by turbulent mixing. This approach is quite similar to that of Erokhin et al.<sup>19</sup> and Zel'dovich.<sup>20</sup>

Models Based on a Modification of the Propellant Combustion Mechanism. Models for erosive burning rate in this group are based upon the flame structure and the mechanism of solid-propellant burning. Vandenkerckhove<sup>28</sup> developed an erosive burning model by considering the flame zone structure of a double-based solid propellant. He assumed that the fizz zone thickness is decreased by the cross flow of gases, resulting in an increase in heat transfer to the propellant surface and, therefore, an increase in surface temperature. Consequently, the increase in  $T_s$  results in a higher burning rate from the Arrhenius law<sup>s</sup> of surface pyrolysis. The height of the fizz zone was assumed to be equal to the laminar sublayer thickness. Vandenkerckhove explained the threshold velocity effect as representing the moment when the turbulence reaches the boundary of the fizz zone. This approach, however, is limited to double-base solid propellants. Moreover, the effect of mass injection on the laminar sublayer height was not considered. Miller<sup>29</sup> based his model on the assumption that the time required for the propellant to be consumed is a linear sum of chemical reaction time and the time required for turbulent transport of heat to reach the propellant surface. This assumption does not appear to have any physical basis. The final correlation for the burning rate somewhat resembles the Lenoir-Robillard correlation.<sup>7</sup>

Saderholm et al.<sup>30</sup> modeled the erosive burning problem of fuel-rich AP composite propellants by the direct extension of the granular diffusion flame theory.<sup>16</sup> The laminar diffusivity was replaced by turbulent diffusivity obtained through Prandtl's mixing length theory. In this way, the model predicts a reduction in diffusion flame offset distance that results in an increased heat-transfer rate to the propellant surface and, therefore, increases the burning rate. However, Saderholm et al.<sup>30</sup> conceded that the model is valid only for low port gas velocity ( $M \sim 0.01$ ). King<sup>31-33</sup> has developed a model for the erosive burning of composite propellants based on the assumption that the cross flow of gases bends the diffusion flame, thus bringing the heat release zone closer to the propellant surface. The basic assumption of this model is that the flame is located within the laminar sublayer of a turbulent boundary layer where turbulence is negligible. In a follow-up work, King<sup>32</sup> extended his model on the basis of the modified composite propellant combustion model of Beckstead, Derr, and Price (BDP).<sup>34</sup> A detailed description of King's work is given in the section of this chapter entitled Recent Theoretical Approaches.

Models Based on a Chemically Reacting Boundary-Layer Analysis. Models in this category are based on an aerothermochemical analysis of the erosive burning problem, which considers heat, mass, and momentum transfer in a chemically reacting boundary layer. Earlier attempts of Tsuji,<sup>35</sup> Schuyler and Torda,<sup>36</sup> and Razdan<sup>37</sup> were limited to laminar boundary layers. Tsuji<sup>35</sup> was the first investigator to formulate the problem for a double-base propellant in terms of mass, momentum, species mass fraction, and energy conservation equations for a laminar two-dimensional chemically reacting boundary layer flow over a propellant surface. The burning rate was expressed as a function of surface temperature by the Arrhenius law of surface pyrolysis. Following a number of simplifying assumptions, analytical solutions were obtained for momentum and species mass fraction equations and the energy equation was solved numerically. The solutions were limited to linear streamwise variation of freestream velocity and the propellant surface temperature was assumed constant. Schuyler and Torda<sup>36</sup> used a computer program to solve the boundary-layer equations simultaneously. In their formulation, they also included conservation equations for mass, momentum, and energy in the inviscid core region of a grain. Razdan<sup>37</sup> formulated the boundary-layer problem for double-base solid propellants, and

conducted a parametric study for the effect of various physicochemical parameters on erosive burning. In all the aforementioned laminar boundary-layer studies on erosive burning problems, no comparison was presented of theoretical predictions with experimental results. In a typical erosive burning situation, the boundary layer is turbulent over most of the propellant surface;<sup>24,40</sup> therefore, the assumption of laminar flow is not realistic.

A comprehensive turbulent boundary-layer modeling of the erosive burning problem was initiated recently by Beddini<sup>38,39,42</sup> and Razdan and Kuo.<sup>40-41</sup> A detailed description of these recent models is given in the next subsection.

Other Models. Theoretical work grouped here does not fit any of the previously mentioned categories. For the most part, these models were developed for overall rocket motor performance calculations, and no new erosive burning theory was developed. By considering mass and momentum balances for one-dimensional adiabatic flow inside a grain, Blatz<sup>43</sup> obtained an expression for an erosion constant in terms of the port-to-throat area ratio of a rocket motor. This erosion constant can be used in a correlation in which erosive burning augmentation ratio is assumed proportional to freestream velocity. The analysis of Blatz<sup>43</sup> does not account for any effects of heat transfer on erosive burning. Stone<sup>44</sup> discussed a method for compensating for the initial pressure peak caused by erosive burning. This method requires the reduction of the initial burning surface, i.e., a theoretical burning surface variation with a progressivity ratio greater than unity. In Stone's experiments on a slotted tube grain design, the progressivity ratio was tailored, through experimental motor firings, to match the initial overpressure with the final erosion free-burning pressure.

A one-dimensional combustion model was developed by Rout et al.<sup>45</sup> by considering conservation equations for mass, momentum, and energy. Solutions of the model were obtained numerically to investigate the effects of erosive burning on the variation of pressure with respect to time in a solid-propellant rocket motor. Although this study does not develop an erosive burning theory, it shows an interesting implication of erosive burning on rocket motor performance. The results show that higher values of threshold velocity lead to higher pressure peaks and that cylindrical grains have greater erosion effects than rectangular configurations.

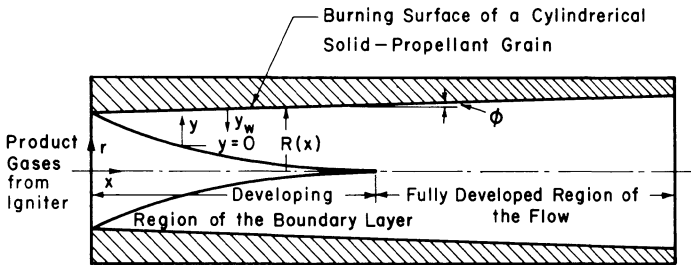


Fig. 2 Physical model considered in the theoretical formulation of Razdan and Kuo.<sup>41</sup>

### Recent Theoretical Approaches

Two recent approaches in modeling the erosive burning problem of solid propellants are described in this section. These are the turbulent boundary-layer analyses of Razdan and Kuo,<sup>40,41</sup> and Beddini,<sup>38,42</sup> and the diffusion flame bending model of King.<sup>31</sup> The approach of Razdan and Kuo,<sup>40,41</sup> and King<sup>31</sup> will be discussed in some detail. Beddini's approach,<sup>38,42</sup> due to its similarities to the approach of Razdan and Kuo, will be only briefly discussed.

Turbulent Boundary-Layer Model of Razdan and Kuo.<sup>40,41</sup> The physical model considered in the theoretical analysis consists of an axisymmetric flow of gases inside a cylindrical solid-propellant grain, as shown in Fig. 2. The analysis is limited to the combustion of ammonium perchlorate composite propellants burning in the turbulent boundary-layer region of a rocket motor. The gases form a turbulent boundary layer over the burning surface of the propellant. Both developing and fully developed regions of the flow, which is assumed to be quasisteady, are considered. The coordinate system used in the analysis is depicted in Fig. 2. Even though the model is developed for an axisymmetric flow configuration, conservation equations and boundary conditions can readily be reduced to apply to a two-dimensional flat-plate geometry.<sup>40</sup> It should be noted that the model is limited to situations where the propellant is burning under strong convective cross flow conditions such as those which exist in high performance rocket motors.

1) Conservation Equations. In the viscous flow region of the boundary layer, Reynolds' decomposition and time-averaging procedure is used to develop the conservation equations. A second-order two-equation  $K-\epsilon$  turbulence model<sup>46</sup> is used to achieve the closure of the



turbulent flow problem. Major assumptions made in the analysis are: the averaged flow properties are steady; the mean flow is axisymmetric; there is no reaction-generated turbulence; the Lewis number is unity; and Fick's law of diffusion is valid. Conservation equations of mass, momentum, species, enthalpy, turbulence kinetic energy, turbulence dissipation, and the equation of state are

$$\frac{\partial}{\partial x} (r \bar{\rho} \bar{u}) + \frac{\partial}{\partial r} (r \bar{\rho} \bar{v}^o) = 0 \quad (7)$$

where  $\bar{\rho} \bar{v}^o = \bar{\rho} \bar{v} + \bar{\rho}' v'$ .

$$\bar{\rho} \bar{u} \frac{\partial \bar{u}}{\partial x} + \bar{\rho} \bar{v}^o \frac{\partial \bar{u}}{\partial r} = \frac{1}{r} \frac{\partial}{\partial r} [r \mu_{\text{eff}} \frac{\partial \bar{u}}{\partial r}] - \frac{d\bar{p}}{dx} \quad (8)$$

$$\bar{\rho} \bar{u} \frac{\partial \bar{Y}_k}{\partial x} + \bar{\rho} \bar{v}^o \frac{\partial \bar{Y}_k}{\partial r} = \frac{1}{r} \frac{\partial}{\partial r} [r (\frac{\mu}{Sc})_{\text{eff}} \frac{\partial \bar{Y}_k}{\partial r}] + \bar{\omega}_k \quad (9)$$

$$\begin{aligned} \bar{\rho} \bar{u} \frac{\partial \bar{H}}{\partial x} + \bar{\rho} \bar{v}^o \frac{\partial \bar{H}}{\partial r} &= \frac{1}{r} \frac{\partial}{\partial r} \left\{ r \left[ \left( \frac{\mu}{Pr} \right)_{\text{eff}} \frac{\partial \bar{H}}{\partial r} \right. \right. \\ &\quad \left. \left. + \{ \mu_{\text{eff}} - \left( \frac{\mu}{Pr} \right)_{\text{eff}} \} \frac{\partial \bar{u}^2/2}{\partial r} \right] \right\} \end{aligned} \quad (10)$$

$$\begin{aligned} \bar{\rho} \bar{u} \frac{\partial K}{\partial x} + \bar{\rho} \bar{v}^o \frac{\partial K}{\partial r} &= \frac{1}{r} \frac{\partial}{\partial r} [r (\mu + \frac{\mu_t}{C_1}) \frac{\partial K}{\partial r}] \\ &\quad + \mu_t \left( \frac{\partial \bar{u}}{\partial r} \right)^2 - \bar{\rho} \epsilon \end{aligned} \quad (11)$$

$$\begin{aligned} \bar{\rho} \bar{u} \frac{\partial \epsilon}{\partial x} + \bar{\rho} \bar{v}^o \frac{\partial \epsilon}{\partial r} &= \frac{1}{r} \frac{\partial}{\partial r} [r (\mu + \frac{\mu_t}{C_2}) \frac{\partial \epsilon}{\partial r}] \\ &\quad + C_3 \mu_t \left( \frac{\partial \bar{u}}{\partial r} \right)^2 \frac{\epsilon}{K} - C_4 \bar{\rho} \frac{\epsilon^2}{K} \end{aligned} \quad (12)$$

$$\bar{p} = \bar{\rho} R_u \bar{T}/W \quad (13)$$

Turbulent viscosity  $\mu_t$  is expressed in terms of  $K$  and  $\varepsilon$  as

$$\mu_t = C_\mu \bar{\rho} K^2 / \varepsilon \quad (14)$$

Various correlations have been modeled and replaced in Eqs. (8-12). These models were discussed by the authors in Ref. 40.

In the potential flow region of the developing flow, the following equations are considered for momentum and energy:

$$\rho_c U_c \frac{dU_c}{dx} = - \frac{d\bar{p}}{dx} \quad (15)$$

$$T_c = T_{o_c} \left( 1 + \frac{\gamma-1}{2} M_c^2 \right)^{-1} \quad (16)$$

Equation (16) is a consequence of isentropic assumption. The centerline velocity  $U_c$  is calculated from Eq. (15) and the axial pressure gradient is calculated from the overall momentum balance, using the following equations:

$$- \frac{d\bar{p}}{dx} = [2\pi r_{tw} + \frac{d}{dx} (\rho_b A U_b^2)] / A \quad (17)$$

$$\frac{d}{dx} (\rho_b U_b A) = 2\pi R_p r_b \quad (18)$$

Equation (18) is obtained from the overall mass balance inside a rocket motor. The pressure gradient expressed by Eq. (17) includes the effects of change in the flow area and change in bulk density  $\rho_b$  along the  $x$  direction.

Equations (7 - 12) are reduced to two-dimensional boundary-layer equations if  $r$  is put equal to unity, and partial derivative with respect to  $r$  is replaced by partial derivative with respect to  $y$  (measured from the propellant surface). Equations (15 - 18) are not used for two-dimensional boundary-layer model of erosive burning.<sup>40</sup>

2) Modeling of Gas-Phase Chemical Reactions. When a composite solid propellant burns, solid fuel and oxidizer particles transform into gases. The gases may react in several steps. However, in this model the following global single-step forward chemical reaction is assumed:



where O and F represent the oxidizer and the fuel gases, respectively, and P represents the product gases. A possible expression for the instantaneous global reaction rate is

$$\dot{\omega}_k = -W_k k_s \prod_k (\rho Y_k / W_k)^{\nu_k} \quad (20)$$

[ $k = O, F$ , and specific reaction rate constant  $k_s$  is given by the Arrhenius law  $k_s = A_g \exp(-E_{ag}/R_u T)$ ]. The time averaging of Eq. (20) represents one of the central difficulties of turbulent combustion modeling. One can replace the exponential term by its series expansion, thereby introducing correlations such as  $\overline{Y_O Y_F}$ ,  $\overline{Y_F T}$ ,  $\overline{Y_O T}$ ,  $\overline{T^2}$ , etc. Additional conservation equations must be solved for these correlations; this procedure, however, reduces the economy significantly and introduces additional empiricism into the model.

One other approach, first proposed by Spalding,<sup>47,48</sup> is the eddy-breakup (EBU) model. In this model it is proposed that the gases in a turbulent flame, at high Reynolds numbers, be considered as lumps or eddies of unburned and fully burned gas. Spalding assumed that the rate of burning depended upon the rate at which fragments of unburned gas (eddies) were broken into still smaller fragments by the action of turbulence and that this rate was considered to be proportional to the rate of decay of turbulence energy. The EBU concept can be used to model the gas-phase reaction rate for the erosive burning problem in which fuel and oxidizer gases are unmixed as they emerge from the propellant surface.<sup>16</sup> The presence of high-lateral shear in the boundary layer forms the turbulence eddies. It is assumed that these eddies engulf the fuel and oxidizer gases, giving rise to oxidizer and fuel pockets. Following the EBU concept and the arguments of Lockwood,<sup>49</sup> the rate of consumption of fuel is taken as proportional to the rate of dissipation of the fuel-containing eddies, as characterized by the rate of diminution of energy of the fluctuations. This rate is equated to the rate of supply of energy from the large-scale motion, which can be taken as proportional to the quantity of energy involved and to the reciprocal of the eddy time scale characterized by  $\epsilon/K$ , i.e.,

$$\overline{\omega_F} \propto \overline{\rho \sqrt{g_F}} (\epsilon/K) \quad (21)$$

where  $g_F \equiv \overline{Y_F'^2}$ . Equation (21) can be used, provided  $g_F$  is known. The conservation equation for  $g_F$  (see Ref. 46) is

simplified by assuming the production and dissipation terms of the  $g_F$  equation to be dominant,

$$g_F \propto \frac{\mu_t}{\rho} \frac{K}{\epsilon} \left( \frac{\partial \bar{Y}_F}{\partial r} \right)^2 \quad (22)$$

From Eqs. (14), (21), and (22), we finally get

$$\dot{\bar{\omega}}_F = - C_\omega \bar{\rho} \sqrt{K} \left| \frac{\partial \bar{Y}_F}{\partial r} \right| \quad (23)$$

where  $C_\omega$  is a constant. Equation (23) is used together with Eq. (9) to solve the species distribution in the gas phase. It should be recognized that the reaction rate represented by Eq. (23) has some limitations. First, it is assumed that the rate of chemical kinetics is very fast, i.e., the reaction is diffusion limited. This assumption is particularly valid for gaseous reactions taking place under high pressures, such as those which exist in actual rocket situations. Second, the use of Eq. (23) is limited to turbulent boundary-layer flows. The primary reason for limiting this study of erosive burning to turbulent boundary-layer flows is that the flowfield developed over most of the solid-propellant grain in a practical rocket motor is turbulent. It may be noted that the species conservation equations are solved for  $\bar{Y}_F$  and  $\bar{Y}_{OF} \equiv [\bar{Y}_O - (\nu_{O,W_O}/\nu_{F,W_F})\bar{Y}_F]$ . The choice of the latter variable, with the assumption of Eq. (19), eliminates the nonlinear source term in the equation for this variable. No separate conservation equation is needed for  $\bar{Y}_p$ , which is defined as  $(1 - \bar{Y}_O - \bar{Y}_F)$ .

3) Boundary Conditions. At the solidgas interface, mass and energy balances lead to the following boundary conditions:

$$(\bar{\rho} \bar{v} \bar{Y}_O)_{r=R} - \rho_s r_b Y_{ox} + (\bar{\rho} \bar{D} \frac{\partial \bar{Y}_O}{\partial r})_{r=R} = 0 \quad (24)$$

$$(\bar{\rho} \bar{v} \bar{Y}_F)_{r=R} - \rho_s r_b Y_{fu} + (\bar{\rho} \bar{D} \frac{\partial \bar{Y}_F}{\partial r})_{r=R} = 0 \quad (25)$$

$$\lambda \frac{\partial \bar{T}}{\partial r} \Big|_{r=R} = \lambda_s \frac{\partial \bar{T}}{\partial r} \Big|_{r=R} - \rho_s r_b [(C_p - C_s)(T_s - \bar{T}_s) + \bar{Q}_s] \quad (26)$$

where in Eq. (26)  $\bar{Q}_s$  is defined as the net surface heat release (negative for exothermic reactions) at a reference temperature  $T_s$ . The net heat flux to the solid propellant is obtained by integrating the heat conduction equation in the solid phase,

$$-\lambda_s \left. \frac{\partial T}{\partial r} \right|_{r=R} = (T_s - T_{pi}) \rho_s C_s r_b \quad (27)$$

The burning rate of the solid propellant is expressed as a function of surface temperature through the use of the Arrhenius law of surface pyrolysis,

$$r_b = A_s \exp(-E_{as}/R_u T_s) \quad (28)$$

For  $K$  and  $\epsilon$  equations [Eqs. (11) and (12)], the boundary conditions are applied near the propellant surface, rather than directly at the surface, to avoid the low-turbulence Reynolds number region in which the application of  $K$  and  $\epsilon$  equations is inappropriate.<sup>40,25</sup> Turbulence viscosity  $\mu_t$  close to the surface is calculated from van Driest's formula, as modified by Cebeci and Chang<sup>50</sup> to include the effect of surface roughness,

$$\mu_t = \bar{\rho} [Dk(y_w + \Delta y_w)]^2 \left| \frac{\partial \bar{u}}{\partial r} \right| \quad (29)$$

where the damping coefficient,

$$D \equiv 1 - \exp \left[ - \frac{(y_w + \Delta y_w) \bar{\rho} u_*}{A^+ \mu} \frac{\tau_w}{\tau_w} \right] \quad (30)$$

$$\Delta y_w \equiv 0.9 \left( \frac{\mu}{\bar{\rho} u_*} \right) [\sqrt{R_h^+} - R_h^+ \exp(-R_h^+/6)] \quad (31)$$

$$k = 0.41, \quad R_h^+ \equiv \bar{\rho} u_* R_h / \mu, \quad u_* = \sqrt{\tau_w / \bar{\rho}} \quad (32)$$

Following the procedures used by Chambers and Wilcox,<sup>53</sup> boundary conditions for  $K$  and  $\epsilon$  obtained are

$$K = \frac{[kD(y_w + \Delta y_w)]^2}{\sqrt{C_\mu}} \left( \frac{\partial \bar{u}}{\partial r} \right)^2 \quad (33)$$

$$\epsilon = [k\mathcal{D}(y_w + \Delta y_w)]^2 \left| \frac{\partial \bar{u}}{\partial r} \right|^3 \quad (34)$$

Other boundary conditions at the propellant surface ( $r=R$ ) are

$$\bar{u} = 0, \quad \bar{T} = \bar{T}_s, \quad \bar{v} = \rho_s r_b / \rho(x, R) \quad (35)$$

and at the edge of the boundary layer ( $r=0$ ) are

$$\bar{u} = U_c, \quad \bar{T} = T_c, \quad \bar{Y}_F = \bar{Y}_O = 0, \quad \frac{\partial K}{\partial r} = \frac{\partial \epsilon}{\partial r} = 0 \quad (36)$$

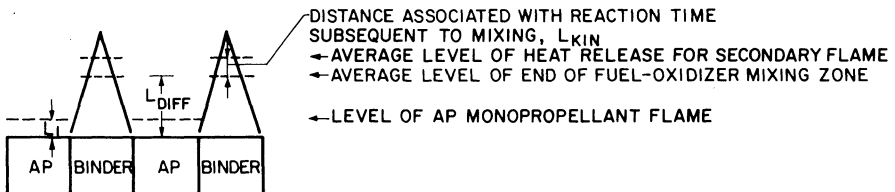
4) Numerical Solution. The coordinate transformation and numerical scheme proposed by Patankar and Spalding<sup>51</sup> was used in this study. Solutions of the differential equations were obtained by numerically integrating the equations along the transverse direction, while marching forward along the  $x$  direction (see Ref. 52 for details). Iterations of the boundary-layer solutions were performed to obtain convergence on the surface temperature.

Theoretical solutions were obtained for a composite propellant composed of 75% AP and 25% PBAA/EPON by weight. Details about the physical properties used in the calculations, the values of the constants used in the turbulence modeling, and the procedure followed in obtaining some of the parameters associated with the global single-step forward reaction may be found in Ref. 40. Computations were started at a preselected downstream  $x$  location, and starting profiles for velocity and turbulent kinetic energy and dissipation were obtained by using the same equations used by Chambers and Wilcox.<sup>53</sup> The initial centerline velocity was varied for the parametric study. Some of the results from this model are discussed in the Results section.

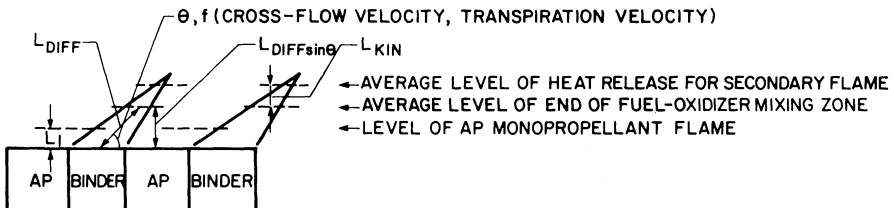
Turbulent Boundary-Layer Model of Beddini.<sup>38,42</sup> The physical model considered by Beddini<sup>38</sup> consists of a quasisteady flow of gases inside a two-dimensional, symmetric homogeneous propellant channel of constant height. The boundary layer over the propellant surface is assumed to be turbulent, and the outer boundary conditions and static pressure as specified by asymptotic matching to an isentropic one-dimensional flow. The basic equations of the boundary-layer problem are similar to those described in the model of Razdan and Kuo.<sup>40,41</sup> However, following a procedure similar to that of Johnson and Nachbar,<sup>54</sup> mass

fraction and total enthalpy are linearly related. Beddini's model differs from that of Razdan and Kuo<sup>40,41</sup> in the closure of the turbulent flow problem. Beddini has used a multiequation second-order closure approach.<sup>55</sup> Furthermore, turbulent correlations involving the chemical source term are taken to be zero in Beddini's analysis and the gas-phase reaction rate is taken as that given by the Arrhenius law [Eq. (20)] at average gas temperature.

The final system of governing equations in the model consists of coupled partial differential equations for  $\bar{u}$ ,  $\bar{v}$  (for mean continuity),  $\bar{h}$ ,  $\overline{u'u'}$ ,  $\overline{u'v'}$ ,  $\overline{v'v'}$ ,  $\overline{w'w'}$ ,  $\overline{\rho'u'}$ ,  $\overline{\rho'v'}$ ,  $\overline{h'u'}$ ,  $\overline{h'v'}$ , and  $\overline{h'h'}$ . Details of these equations may be found in Refs. 38, 42, and 55. The burning rate of the propellant is related to the propellant surface temperature through the Arrhenius pyrolysis law. The system of 12 partial differential equations was solved numerically for a parametric study. No comparison of predictions with experimental data was made. A modification of the model by Beddini<sup>42</sup> incorporated pressure gradient effect and surface roughness effect into the theoretical formulation. Beddini and Varma<sup>39</sup> also included the effects of turbulence on the mean reaction rate of AP combustion by keeping terms to second order in  $T'$  in the Taylor series expansion of  $\omega_k$ .



(a) NO CROSS-FLOW VELOCITY



(b) CROSS-FLOW,  $L_{KIN}$ ,  $L_{DIFF}$ ,  $L_1 = f(m_{burn}, P)$  ALONE, INDEPENDENT OF CROSS-FLOW ANGLE

Fig. 3 Geometrical model of erosive burning (two-flame model) developed by King.<sup>31</sup>

## Chapter 11

### Transient Burning of Solid Propellants

Kenneth K. Kuo\* and Jayavant P. Gore†

*The Pennsylvania State University*

*University Park, Pennsylvania*

and

Martin Summerfield‡

*Princeton Combustion Research Laboratories, Inc.*

*Monmouth Junction, New Jersey*

#### Abstract

Transient burning behavior of solid propellants often occurs under a rapid pressure excursion and is caused by the finite relaxation times required for the solid and/or gas phases to adjust their temperature profiles. The instantaneous burning rate under transient conditions may therefore differ significantly from the steady-state value corresponding to the instantaneous pressure. The purpose of this chapter is: 1) to report the state-of-the-art on transient burning studies; 2) to explain the detailed mechanism of transient burning; 3) to classify the existing theories to facilitate more direct comparison; 4) to point out the limitations of each model and its general validity; and 5) to summarize the important experimental observations and theoretical results. Various studies indicate that the transient burning effect is high for higher values of pressurization rates, temperature sensitivity, surface heat release, surface activation energy, and burning rate exponent and lower values of propellant initial temperature and strand burn rate.

#### Nomenclature

- A = pre-exponential factor in Arrhenius equation  
a = burning rate constant in steady burning relation,  $r_0 = a(p)^n$

---

Copyright © American Institute of Aeronautics and Astronautics, Inc., 1983. All rights reserved.

\*Professor, Department of Mechanical Engineering.

†Research Assistant, Department of Mechanical Engineering.

‡President.



$b$	= burning rate constant in pyrolysis law, $r_b = b(T_s - T_i)^k$
$C_c$	= specific heat of condensed phase
$C_g$	= constant pressure specific heat of gas phase
$D^g$	= mass diffusivity
$E$	= activation energy
$h$	= specific enthalpy (sensible plus chemical)
$k$	= power of propellant pyrolysis law, $r_b = b(T_s - T_i)^k$
$L$	= latent heat of vaporization
$L^*$	= ratio of chamber volumes to throat area
$m$	= mass burning rate per unit area
$n$	= burning rate pressure exponent
$p$	= pressure
$p'$	= small change in pressure
$Q$	= rate of generation of heat per unit volume due to subsurface chemical reactions
$Q_r$	= heat of combustion per unit mass in gaseous flame
$Q_{rad}$	= rate of in-depth radiation heat flux absorption
$Q_s$	= net exothermic heat release at propellant surface
$q$	= heat flux
$R_u$	= universal gas constant
$r_o$	= steady-state burning rate
$r_b$	= instantaneous burning rate
$T$	= temperature
$t$	= time
$u_g$	= gas velocity normal to surface
$v_i$	= diffusion velocity
$W_i$	= molecular weight of reactant gases (fuel or oxidizer)
$W$	= molecular weight of product gases
$x^p$	= distance measured from the instantaneous burning surface of the solid propellant
$Y$	= species mass fraction
$\alpha$	= thermal diffusivity
$\Delta h_f^o$	= heat of formation at reference temperature and pressure
$\delta$	= thermal wave penetration depth
$\epsilon$	= a dimensionless parameter indicating the degree of depressurization, $\epsilon \equiv [\alpha_p / (r_{eq} p_{eq})] \partial p / \partial t)_{max}$
$\epsilon$	= reaction progress variable defined in Eq. 33
$\lambda$	= thermal conductivity
$\nu$	= frequency of perturbed pressure oscillation
$\nu_f'$	= number of moles of reactant fuel gases
$\nu_o'$	= number of moles of reactant oxidizer gases
$\nu_p''$	= number of moles of product gases

$\xi$	= distance measured from a fixed frame of reference
$\rho$	= density
$\sigma$	= temperature sensitivity, $\sigma_p \equiv (\partial \ln r / \partial T)_p$
$\tau_p$	= characteristic time
$\phi$	= temperature gradient, $\phi \equiv \partial T / \partial x$
$\psi$	= dimensionless parameter defined in Eq. 25
$\dot{\omega}$	= rate of species generation in gas phase
$\dot{\omega}'$	= rate of species generation at solid surface

### Subscripts

c	= condensed phase
eq	= final equilibrium condition
g	= gas phase
f	= flame
i	= initial or pertaining to $i^{\text{th}}$ species
p	= pressure
s	= surface
o	= steady state
$\infty$	= at a large distance away from surface
+	= gas-phase side of infinitesimal control volume at surface
-	= solid-phase side of infinitesimal volume at surface

### Introduction

In solid rocket propulsion systems, the instantaneous burning rate of a solid propellant under a rapidly changing nonsteady pressure condition could be significantly different from the steady-state burning rate measured in strand burner experiments. This means that, under transient conditions, the instantaneous pressure level alone does not dictate the magnitude of the regression rate of a solid propellant.

The ability to predict the rate of burning of a solid propellant is of prime importance in the design of high-performance propulsion systems and in preventing hazards of such systems. For solid rocket motors, the burning rate has pronounced effects on the flame spreading and chamber pressurization processes, and on the maximum motor pressure. Any improper treatment of the transient (dynamic) burning phenomena may cause a significant amount of inaccuracy in predictions of system performance, especially during ignition, extinction by depressurization, and resonant burning.

The detailed mechanism of the ignition process is described by Hermance in his chapter on ignition in this

volume. In other chapters, Kumar and Kuo have discussed the overall ignition transient, while DeLuca has dealt with extinction of solid propellants under rapid depressurization. Because of the importance of the transient burning effect, it has been investigated both theoretically and experimentally by various researchers.<sup>1-82</sup> A review of the work prior to 1976 is given by Kuo and Coates in Ref. 83.

The transient burning phenomenon is caused by the finite time lags associated with adjustment of 1) temperature profiles in the solid phase, and sometimes also in the gas phase, and 2) the energy release rate and flame structure in the gaseous flame. Due to the inherent unsteady nature of events associated with transient burning, the governing equations comprise a set of time-dependent partial differential equations. Boundary conditions for the solid-phase and gas-phase equations are coupled in nature through variation in the heat feedback term from the gaseous flame zone to the solid-propellant surface. The coupling is also due to changes of the gaseous mass flux leaving the solid surface as a result of changes in burning rate. In order to evaluate the heat feedback from the flame to the surface, a detailed knowledge of the flame structure, chemical kinetics, and reaction mechanisms would be essential for a comprehensive model. However, such an extensive model may turn out to be disadvantageous, due to lack of knowledge of detailed flame structure and chemical kinetics, as well as mathematical intractability. Hence, most researchers in the past have resorted to simplifying assumptions, particularly those pertaining to the quasisteady nature of the gas phase.

It has been observed experimentally that the transient burning effect depends upon a large number of parameters, including: maximum pressurization rate and nature of the pressure-time curve; temperature sensitivity and pressure exponent of the propellant; exothermic heat release and activation energy of the propellant, together with initial temperature of the propellant and its thermal properties, etc.

### Mechanism of Transient Burning

Physically, the transient burning effect is introduced during rapid pressure changes by the finite time interval required for temperature profiles inside the condensed phase, and possibly the reaction zone, to follow transient pressure variations. The faster the pressure changes, the longer the time (relative to the characteristic time of the pressure change) required for temperature profiles to

adjust themselves to the new pressure condition. Until temperature profiles in the solid phase and the reaction zones are adjusted to the shape corresponding to the steady-state burning at the new pressure, there is an out-of-phase blowing effect of the chemically reacting gases leaving the burning surface. This blowing effect alters the temperature gradient at the surface and the heat feedback from the flame.

In order to understand the transient burning process better, let us consider events that occur when the pressure is increased according to the ramp pressurization rates of b or c as shown in Fig. 1a. The initial steady-state temperature profile corresponding to zero pressurization rate (line a in Fig. 1a) is shown by the curve IA in Fig. 1b. It should be noted that in order to facilitate the comparison of various temperature profiles, the propellant is fed at the rate equal to the instantaneous burning rate so that the instantaneous burning surface is always at a fixed location. For a very slow pressurization rate (line b in Fig. 1a), the temperature of the propellant surface will rise from A to B in a short time lag. The temperature profile can quickly adjust to the new profile IB, which

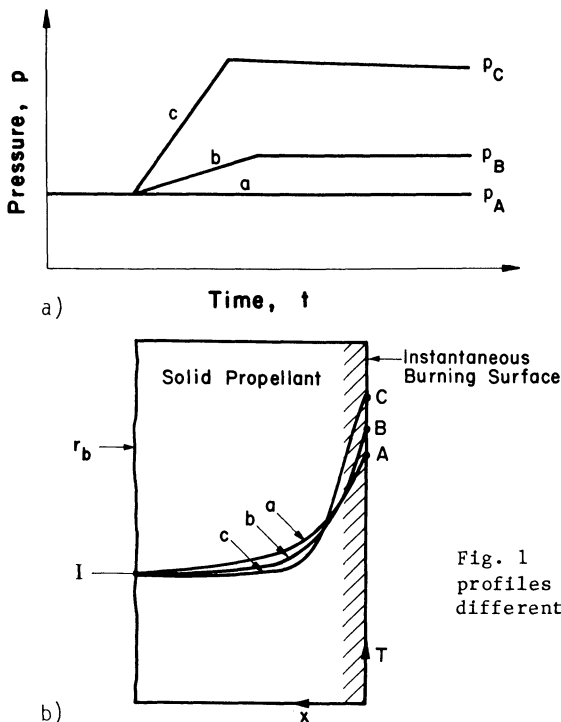


Fig. 1 Comparison of temperature profiles in the solid phase under different pressurization rates.

represents the steady-state temperature distribution at the new pressure  $p_b$ . At higher pressurization rates (line c), the steady-state temperature profile IC at the new pressure  $p_c$  differs significantly from the initial profile IA. Hence, it takes a considerably longer time lag for the temperature profile in solid phase to adjust to the new steady-state condition  $p_c$ . Furthermore, the time available for this adjustment is much shorter, due to the rapid pressurization along line c in Fig. 1a. During this rapid transient period, the temperature profile inside the solid propellant cannot keep up with the rate at which the pressure increases and hence may remain relatively close to the initial profile IA, which is above IC for a significant portion of the thermal profile. Correspondingly, this portion of the propellant is preheated, compared to the steady-state condition at  $p_c$ . As this portion of propellant is fed to the burning surface, the burning rate can substantially increase due to higher thermal energy storage. At higher burning rates, the continuity of the mass flux at the solid-gas interface may require gas velocities to be higher. The increase in gas velocities introduces a blowing effect which is opposite to the preheat effect described above.

As the blowing caused by the higher rate of gasification becomes stronger at the propellant surface, the gas-phase heat release zone becomes thicker and moves further away from the surface. For diffusion flames, the lateral species mixing above the surface is altered by the higher gas velocity normal to the surface; fuel- and oxidizer-rich gases must travel a greater distance from the surface before they react with each other. For premixed flames, the flame zone is stretched because of higher gas velocity. The magnitude of the gas velocity at the burning surface is also influenced by the local gas density which, in turn, depends upon the instantaneous pressure. As pressure is increased, the density will be higher and the gas velocity will tend to be lower. The gas velocity is determined by both the instantaneous burning rate and the local gas density. Whether the flame zone moves away from the surface or closer to it depends on the relative influence of instantaneous burning rate and gas density (net blowing effect).

No matter whether the heat release zone in the gaseous flame is confined to a thin region or is distributed over a wider area, the effective heat release location can be altered by the net blowing effect. This change of position alters the heat feedback to the solid-propellant surface. (See Ramohalli's chapter on steady-state burning of

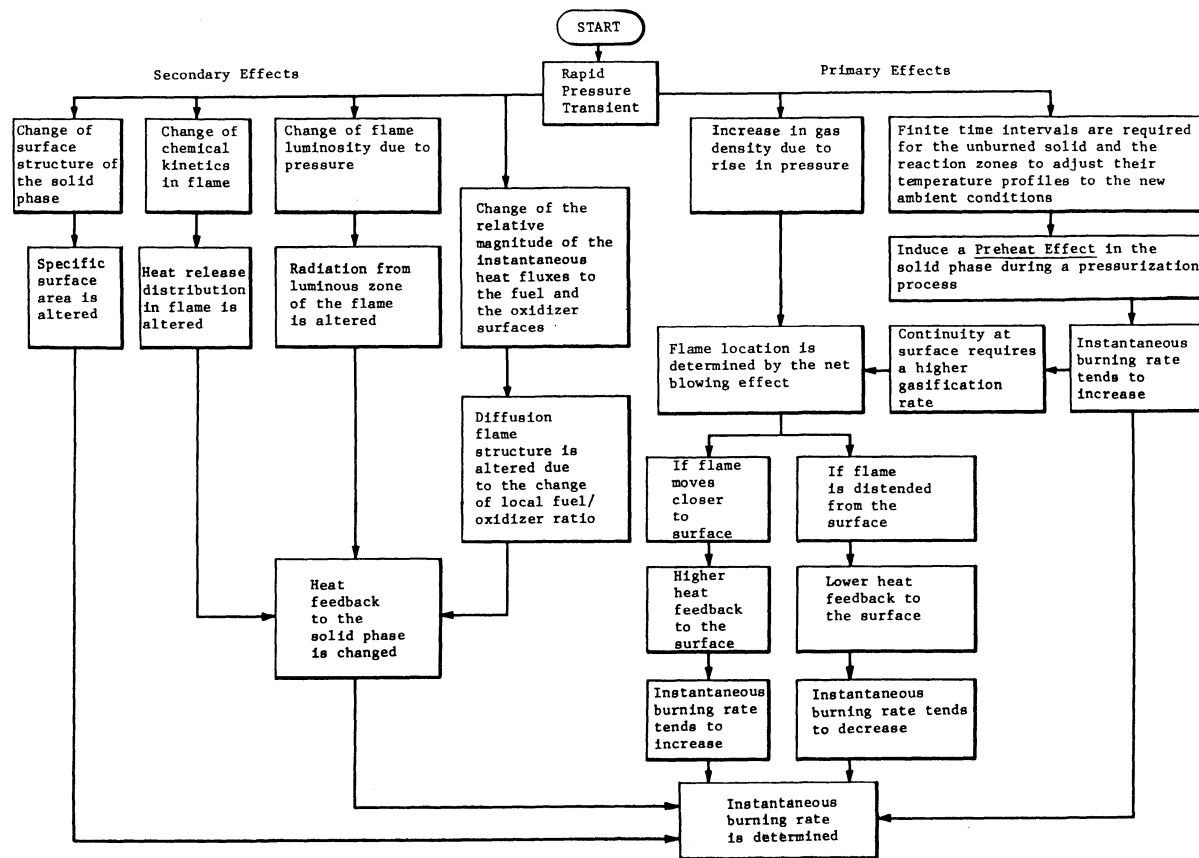


Fig. 2 Transient burning mechanism under rapid pressurization.

composite solid propellant, and the Lengellé et al. chapter on homogeneous solid propellants.)

In addition to the aforementioned primary effects, experiments indicate that there are often numerous secondary effects that may influence heat feedback to the propellant surface, and therefore alter the instantaneous burning rate. While many of the details of the actual processes are not fully understood at present, evidence tends to suggest that there is an effect of pressure upon kinetics, flame luminosity, mixing processes, change of solid-phase surface structure, etc. Figure 2 illustrates the process of determination of transient burning rate as a result of several complementary and opposing phenomena described above.

Out of the numerous secondary effects that may exist, four are depicted in Fig. 2. The effect of change of the solid-phase surface structure was recently proposed by Cohen & Strand<sup>68</sup> in consideration of dynamic burning of HMX-based composite solid propellants under high-pressure conditions.

#### Mathematical Description of the Transient Burning Phenomena

As mentioned in the previous section, the magnitude of the transient burning effect is dependent upon the characteristic times associated with the thermal diffusion process in the condensed phase  $\tau_c$ , in the surface region  $\tau_s$ , and in the gas phase  $\tau_g$ . Typical magnitudes of these time scales are calculated in Refs. 13 and 14, and are  $\tau_c \approx 0.01$  s,  $\tau_s \approx 0.001$  s,  $\tau_g \approx 0.0001$  s. This means that the surface responds 10 times faster, and the gas phase 100

Table 1 Basic Assumptions Used in Transient Burning Analysis

Appropriate basic assumptions in transient burning analysis	Steady-state in both gas and solid phases	Quasisteady in gas phase and transient in solid phase	Transient in both gas and solid phases
Relative magnitude of characteristic times	$\tau_c \ll \tau_p$ $\tau_s \ll \tau_p$ $\tau_g \ll \tau_p$	$\tau_c \sim \tau_p$ $\tau_s < \tau_p$ $\tau_g \ll \tau_p$	$\tau_c \sim \tau_p$ $\tau_s \sim \tau_p$ $\tau_g \sim \tau_p$

times faster, than the solid phase to a pressure transient. For many transient burning phenomena in rocket motors, the time scale associated with a pressure excursion  $\tau_p$  is much larger than  $\tau_g$  and  $\tau_s$ , but comparable to or smaller than  $\tau_c$ . Hence, the solid phase must be considered unsteady while a quasisteady assumption could be suitable for the surface reaction zone and the gas-phase region.

Knowledge of appropriate time scales is essential to development of mathematical models and to choice of a model to be used in predicting solid-propellant transient burning phenomena. The time scales<sup>13,14</sup> associated with the different zones are

$$\tau_c = \alpha_c / r_b^2 \quad (1)$$

$$\tau_g \approx \frac{\alpha_g}{u^2} = \left( \frac{\lambda_{gc} \rho_g}{\lambda_c \rho_{gc}} \right) \tau_c \quad (2)$$

$$\tau_s \approx \left( \frac{R_u T_s}{E} \right) \frac{\alpha_c}{r_b^2} = \left( \frac{R_u T_s}{E} \right) \tau_c \quad (3)$$

Based upon the relative magnitude of the above characteristic times as compared to  $\tau_p$ , the basic assumptions used in transient burning analysis are shown in Table 1.

#### Solid-Phase Energy Equation

The treatment of the unsteady solid-phase energy equation is common to the different approaches of various investigators. For the coordinate system shown in Fig. 3, the one-dimensional transient solid-phase energy equation can be written as

$$\underbrace{\frac{\partial T}{\partial t}}_{(A)} + \underbrace{r_b \frac{\partial T}{\partial x}}_{(B)} - \underbrace{\alpha_c \frac{\partial^2 T}{\partial x^2}}_{(C)} = \underbrace{\frac{\dot{Q}}{\rho_c C_c}}_{(D)} + \underbrace{\frac{\dot{Q}_{rad}}{\rho_c C_c}}_{(E)} \quad (4)$$

Under steady-state conditions, term (A) of the above equation can be dropped and the resulting steady-state



ordinary differential equation can be solved with the following boundary conditions:

$$x = 0, \quad r_b = r_o, \quad T = T_{s,o} \quad (5)$$

$$x = -\infty, \quad T = T_i \quad (6)$$

Using these boundary conditions to solve the temperature profiles in the solid phase, one obtains

$$T(0,x) = T_i + (T_{s,o} - T_i) \exp(xr_o/\alpha_c) \quad (7)$$

It is important to note that Eq. (7) can be used as the initial condition in some transient burning problems.

The boundary conditions for the transient energy equation are

$$T(t, -\infty) = T_i \quad (8)$$

$$\frac{\partial T}{\partial x}(t, 0_-) = \phi_{c,s}(t) \quad (9)$$

where  $\phi_{c,s}$  is related to the heat feedback from the gas phase through an energy flux balance at the gas-solid interface. In order to evaluate the heat feedback from the gas phase, conservation equations for the gas phase must be considered.

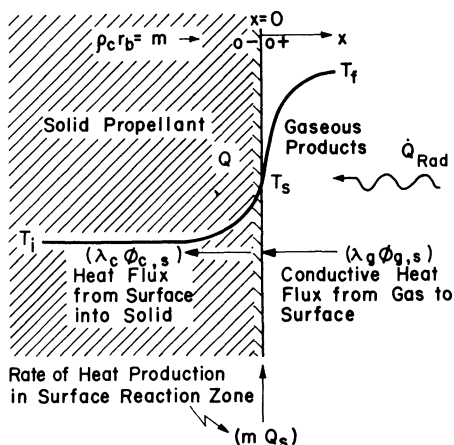


Fig. 3 One-dimensional temperature profiles in the burning of a solid propellant.

Gas-Phase Conservation Equations

The gas-phase equations in general consist of an unsteady continuity equation, an unsteady energy equation, and unsteady species equations. In the transient burning analysis, pressure distribution in the gas phase is assumed to be uniform in space, but varying with time; hence the momentum equation for the gas phase is replaced by the input  $p - t$  information which may either be externally specified or experimentally measured. It should be noted that treatment of burning rate variations due to convective effects in the gas phase is discussed by Razdan and Kuo in their chapter on erosive burning of solid propellants in this volume. Although erosive burning and transient burning effects could occur simultaneously, the analysis in this chapter deals with only transient burning phenomena.

The one-dimensional conservation equations for the gas phase can be written as follows:

continuity equation,

$$\frac{\partial \rho_g}{\partial t} + \frac{\partial(\rho_g u_g)}{\partial x} = 0 \quad (10)$$

energy equation,

$$\rho_g \frac{\partial h}{\partial t} + \rho_g u_g \frac{\partial h}{\partial x} - \frac{\partial p}{\partial t} = \frac{\partial}{\partial x} \left( \lambda_g \frac{\partial T}{\partial x} \right) + \frac{\partial}{\partial x} \left( \rho_g \sum_{i=1}^N h_i \mathcal{D}_i \frac{\partial Y_i}{\partial x} \right) \quad (11)$$

species mass fraction conservation,

$$\rho_g \frac{\partial Y_i}{\partial t} + \rho_g u_g \frac{\partial Y_i}{\partial x} - \frac{\partial}{\partial x} \left( \rho_g \mathcal{D}_i \frac{\partial Y_i}{\partial x} \right) = \dot{\omega}_i \quad (12)$$

where  $i = 1, 2, 3, \dots, N$  for  $N$  different species. In the energy equation the effects of viscous dissipation, body force work, and Dufour energy flux are neglected. It is assumed also that there is no external energy source. The heat release due to chemical reactions in the gas phase is included in change of enthalpy terms. Fick's law of mass diffusion is assumed to be valid.

An examination of the set of conservation equations reveals that these equations are coupled with each other. Detailed knowledge of the flame chemistry is needed to determine the different species to be considered in the gas phase. The energy and species equations are coupled through the production rate term in the species

conservation equations. Coupling also occurs through the transport properties. The temperature distribution in the gas phase is governed by the heat release due to chemical reactions in the gas phase. The gas-phase conservation equations are further linked with the solid-phase energy equation through energy and mass flux balances at the interface. These are discussed in the following section.

### Boundary Conditions for Gas-Phase Equations

The complexity of the problem is further increased by the complicated nature of the gas-phase boundary conditions. As we consider a 1-D system, gas-phase boundary conditions must be specified at the flame boundary ( $x \rightarrow \infty$ ) and at the burning solid surface ( $x = 0$ ). At the flame boundary, we need to specify the mass fractions of the fuel and oxidizer species and of product species; this specification requires an a priori knowledge of the reaction mechanism and of the species produced. Knowledge of how far the reaction progresses towards achieving a stoichiometrically complete combustion is also needed. If this information is available, then the boundary condition for species mass fractions can be specified in the form

$$Y_i = Y_{i,\infty} \quad \text{as } x \rightarrow \infty \quad (13)$$

The second boundary condition at  $x \rightarrow \infty$  is related to the temperature at the edge of the flame. Under adiabatic flame assumption, this boundary condition can be specified as

$$\frac{\partial T}{\partial x} = 0 \quad \text{as } x \rightarrow \infty \quad (14)$$

Sometimes, the temperature at the edge of flame is specified, i.e.,

$$T = T_\infty \quad \text{as } x \rightarrow \infty \quad (15)$$

Under transient burning conditions, the temperature of combustion products in general may not be equal to the adiabatic flame temperature of the propellant; it can vary with time and may not follow the  $T_f$  associated with instantaneous pressure if the characteristic time for pressure changes is extremely small. If the heat of reaction in the gaseous flame zone is independent of pressure, and if the rate of change of energy stored between the flame and the surface is small, the boundary

condition at the edge of the flame can be written as

$$T_f - T_s = \bar{T}_f - \bar{T}_s - \left( \frac{\phi_{g,s}}{\rho_c C_g r_b} - \frac{\bar{\phi}_{g,s}}{\rho_c C_g \bar{r}_b} \right) \quad (16)$$

where the barred quantities represent the steady-state values. Under extremely high rates of pressure variations, the instantaneous flame temperature will depend on the propellant grain geometry. In considering high-frequency ( $\sim 10,000$  Hz) pressure oscillations, T'ien<sup>15</sup> proposed that, for a 1-D situation with product gases flowing perpendicular to the burning surface, the boundary condition at  $x \rightarrow \infty$  could be specified by using an isentropic relationship for the gas phase ( $DS/Dt = 0$ ). In the case of relatively slow pressure changes, the flame temperature could be assumed to follow the adiabatic boundary condition given by Eq. (14). Krier et al.<sup>9</sup> experimentally observed near isentropic gas-phase behavior at moderately high-frequency pressure oscillations ( $\sim 200$  Hz). Entropy waves were observed at surprisingly low-frequency pressure oscillations ( $\sim 10$  Hz), while entropy waves were proposed at extremely high-frequency pressure oscillations ( $\sim 1000$  Hz). Results obtained by Krier et al.<sup>9</sup> also showed that the boundary condition for the energy equation at the flame edge is strongly dependent upon the burner geometry.

The remaining boundary conditions are associated with the propellant surface ( $x = 0$ ): the mass fluxes of different species at the surface are determined by the propellant composition; and in the case of heterogeneous propellants under transient burning, they are also determined by the amount of heat feedback to the fuel and oxidizer (this effect is shown in Fig. 2). Difference in heat feedback to different components could be caused by different thermal diffusivities and/or different optical properties. Thus the boundary conditions at the solid surface for the gas-phase conservation equations depend upon propellant composition, flame structure, and thermal properties of the propellant. The three boundary conditions that need to be specified at the propellant surface ( $x = 0$ ) pertain to the mass flux continuity, species flux continuity, and energy flux balance at the surface. Consider a control volume attached to the solid-propellant surface, as shown in Fig. 4. Figure 4a represents an overall mass flux balance at the solid surface as the interface control volume shrinks to zero. This mass flux balance yields the following boundary

condition

$$\rho_c r_b = \rho_g u_g \quad (17)$$

The boundary condition from the species flux balance at the surface is illustrated in Fig. 4b. This boundary condition takes the form given below:

$$\rho_g Y_i u_g \Big|_+ + \rho_g Y_i V_i \Big|_+ = \dot{\omega}_i + \rho_c Y_i r_b \quad (18)$$

Figure 4c shows the balance of energy fluxes at the gas-solid interface. This balance is represented by the

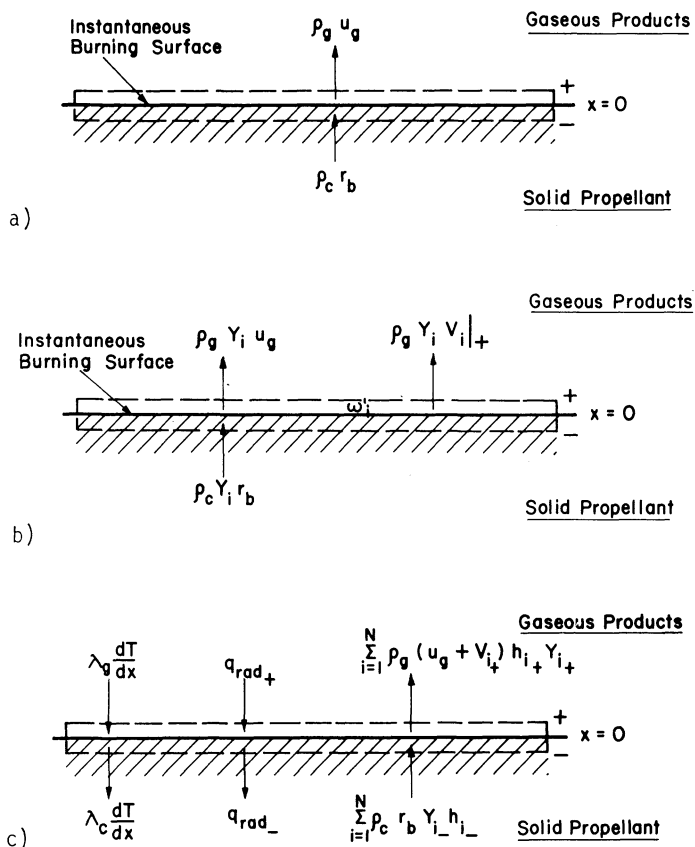


Fig. 4 Balance of mass, species, and energy fluxes at the gas-solid interface.

following equation

$$\lambda_c \left. \frac{dT}{dx} \right|_- = \lambda_g \left. \frac{dT}{dx} \right|_+ + (q_{\text{rad}_+} - q_{\text{rad}_-}) + \sum_{i=1}^N \rho_c r_{b_i} Y_{i_-} h_{i_-} - \sum_{i=1}^N \rho_{g_+} Y_{i_+} (u_g + V_{i_+}) h_{i_+} \quad (19)$$

In Fig. 4, it is assumed that the instantaneous solid-propellant surface remains stationary in space, relative to a fixed coordinate frame. This can also be looked upon as if the propellant was being fed at a velocity equal to  $r_b$ . In the absence of propellant feeding, the observer can move with the control volume at a velocity equal to the instantaneous burning rate of the propellant so that the propellant surface always remains inside the control volume.

Application of these boundary conditions requires information regarding the rates of production of different species at the surface, as functions of surface temperature. Arrhenius type expressions have been used widely for this purpose. However, use of these expressions requires knowledge of the chemical kinetics of the decomposition process. The pre-exponential factor and activation energy for decomposition of the solid are needed as input to the model. In addition to the conservation equations, boundary and initial conditions and appropriate equation of state for the gas phase need to be specified.

As is evident from the previous paragraphs, a complete mathematical description of the solid- and gas-phase conservation equations is very complicated. Information (about data for gas-phase flame chemistry, gas- and solid-phase properties, and solid-phase chemical kinetics) needed as input to the comprehensive mathematical model is usually difficult to obtain for various propellants. (The model also becomes restrictive because of the several assumptions required for specifying gas-phase boundary conditions.) As is evident from the mathematical formulation, the set of governing equations is generally a coupled, nonlinear system of partial differential equations which are nearly impossible to solve analytically, and expensive to solve numerically.

Because of these above-mentioned difficulties, several practical and ingenious assumptions have been made in transient burning studies to simplify the problem of the gas-phase behavior. These efforts are described in the next section.

### Description of the Existing Models

The treatment of the solid-phase model described in the previous section is common to most investigators, except for the difference in the heat feedback boundary condition. Investigators have simplified gas-phase equations in different ways, resulting in different expressions for the heat feedback from the gas-phase to the solid-propellant surface. As described in Table 1, the relative magnitude of characteristic times associated with the gas phase, as compared to characteristic times associated with the pressure change, determines whether the transient burning problem could be assumed quasisteady. Quasisteady assumption for the reaction regions allows the important simplification of treating the reaction zones as steady state. Existing theories on transient burning phenomena can be divided into two major categories: quasisteady flame models and unsteady flame models. Representative works during the past twenty-five years have been organized into a tabular form and presented in their proper time perspective (see Table 2).

For reasons of practical application as well as mathematical tractability, most models developed in the past are based upon the quasisteady assumption of the combustion zone. Quasisteady flame models can be further subdivided into three different approaches: 1)  $dp/dt$  approach<sup>5,6,16,35</sup>, 2) flame description approach<sup>1,8,9,11,12,17,18</sup>, and 3) Zel'dovich approach.<sup>3,4,7,13,14</sup>

With the  $dp/dt$  approach, the transient burning rate depends on instantaneous rate of pressure variation, pressure level, and properties of the propellant. Although models of this type give simple and explicit formulae for transient burning rate calculations, they oversimplify the situation by failing to consider the transient coupling between heat feedback from the flame zone and the propellant surface conditions. It must be recognized that many of the burning rate expressions were derived from small perturbation analyses of the transient heat conduction equation, and thus the use of the transient burning expressions is restricted to cases which deviate slightly from steady state.

In the flame description approach, the heat release distribution in the flame must be a specified input in order to evaluate the integrated gas-phase energy equation for determining the rate of heat feedback from the gas phase to the burning solid surface. The weakness of models of this type is the dependence of the transient burning

solution on detailed knowledge of flame structure and propellant surface reaction phenomena. Because the detailed flame structure and the surface reaction processes are extremely difficult to measure, they are usually deduced from various diagnostic experiments. Also, due to differences in flame structures and surface reactions of various propellants, and the wide range of operating conditions, it is often necessary to reconstruct and modify flame models.

Models of the third type were developed in the USSR, based upon the original work of Zel'dovich.<sup>3,21,31,62</sup> The novel idea of bypassing the uncertainties of modeling a solid-propellant flame, and using instead measurable steady-state burning characteristics to deduce the theoretically correct nonsteady feedback law, is the essence of the Zel'dovich approach. This method was not well known in the USA before its introduction and detailed elucidation by Summerfield et al.<sup>13</sup> It is now widely used in the study of dynamic responses of solid rockets<sup>14</sup> and also in closed chamber pressurization processes.<sup>61</sup> In a manner similar to that of the first two approaches, the Zel'dovich method can be applied only when the quasisteady assumption is valid for the rate processes in the gas phase and at the propellant surface. It also requires that the influence of such external forces as acceleration and erosive effects be small. Use of the Zel'dovich method is often limited by the lack of reliable surface temperature data and steady-state burning rate data over a sufficiently wide range of propellant initial temperatures. These steady-state burning rate data are necessary to the construction of the transient burning rate map (see Table 2). When the limiting situations arise, a flame description model is required.

In order to study the transient burning response at high-frequency ranges, several unsteady flame models<sup>15,25</sup> have been developed. The analysis for the solid phase is identical to that of a quasisteady flame model; however, the gas-phase analysis was extended to include the unsteadiness of the combustion zone. At present, due to the complexity of mathematical formulation and insufficient knowledge of the actual chemical processes, consideration of chemical kinetics in the flame is immensely simplified and is usually represented by a one-step global chemical reaction. It is generally believed that in order to obtain accurate quantitative predictions, future developments in unsteady flame models will immediately require further knowledge of detailed gas-phase reactions. A discussion of the three approaches used in quasisteady flame models is presented below.



Table 2 Quasisteady

Authors	Basic assumptions	Theoretical formulations
Denison and Baum (1961) (Ref. 1)	<ul style="list-style-type: none"> <li>• Homogeneous propellant</li> <li>• No subsurface reactions</li> <li>• Arrhenius expression for rate of solid propellant pyrolysis</li> <li>• Constant <math>C_p</math> for all species</li> <li>• Single-step stoichiometric reaction</li> <li>• Premixed flame in the gas phase</li> </ul>	<ul style="list-style-type: none"> <li>• Flame description approach</li> <li>• Terms A, B, C in Eq. (4) considered</li> <li>• <math>\phi_{c,s}</math> obtained from the overall energy balance in the gas phase</li> <li>• The rate of heat release in the premixed flame obtained from chemical kinetics</li> </ul>
Zel'dovich (1964) (Ref. 3)	<ul style="list-style-type: none"> <li>• <math>T_s = \text{constant}</math></li> <li>• No subsurface heat release</li> <li>• Propellant is homogeneous and isotropic</li> <li>• Functional relationship between <math>\phi_{c,s}</math>, <math>p</math>, and <math>r_b</math> is unchanged between steady-state and transient conditions</li> </ul>	<ul style="list-style-type: none"> <li>• Zel'dovich approach</li> <li>• Terms A, B, C in Eq. (4) considered</li> <li>• Heat feedback from gas phase was obtained from a Zel'dovich map constructed from steady burning data</li> </ul>
Gostintsev and Margolin (1965) (Ref. 4)	<ul style="list-style-type: none"> <li>• Same as those in Ref. 3</li> </ul>	<ul style="list-style-type: none"> <li>• Zel'dovich approach</li> <li>• Terms A, B, C in Eq. (4) considered</li> <li>• Heat feedback obtained from approximate analytical expressions for steady-state burning data</li> </ul>
G. Von Elbe (1965) (Ref. 5)	<ul style="list-style-type: none"> <li>• Gasification occurs at constant <math>T_s</math></li> <li>• Subsurface chemical reactions are neglected</li> <li>• Grain surface is flat and homogeneous</li> </ul>	<ul style="list-style-type: none"> <li>• <math>dp/dt</math> approach</li> <li>• Terms A, B, C in Eq. (4) considered</li> <li>• Term A in Eq. 4 written as <math>\partial/\partial t(dq/dt)</math>, where           <math display="block">q \equiv \int_{-\infty}^{x_s} \rho_c C_c (T - T_i) dx</math> </li> </ul>
Summerfield, Parker, and Most (1966) (Ref. 6)	<ul style="list-style-type: none"> <li>• <math>T_f = \text{const.}</math></li> <li>• <math>T_s = \text{const.}</math></li> <li>• <math>\epsilon &lt; 1</math></li> <li>• Well-stirred reactor</li> <li>• Times of reaction for transient and steady-state conditions are of the same magnitude</li> </ul>	<ul style="list-style-type: none"> <li>• <math>dp/dt</math> approach</li> <li>• Terms A, B, C in Eq. (4) considered</li> <li>• Small perturbation analysis of heat equation yields a closed-form burning rate equation</li> </ul>

(Table continued)

## Flame Models

Important conclusions by investigators	Comments
<ul style="list-style-type: none"> <li>Based upon a perturbation analysis, the stability boundary for self-excited mode was obtained. Burning will be more unstable if the surface and gas-phase reaction rates are more sensitive to temperature changes</li> <li>There exists a maximum transient response amplitude at a particular frequency for the self-excited mode</li> </ul>	<ul style="list-style-type: none"> <li>Results were obtained by small perturbation analysis, hence can only predict the tendency toward instability</li> <li>Effect of transient burning rate on pressure was not considered; therefore, results may not be directly applicable to rocket motors</li> </ul>
<ul style="list-style-type: none"> <li>For higher <math>T_i</math>, lower terminal pressure must be reached to cause extinction</li> <li>Condition for stable burning derived from steady-state relationships is <math>\alpha_c(T_s - T_i) \leq 1</math> This appears to agree with certain Russian experimental data at low initial temperatures</li> </ul>	<ul style="list-style-type: none"> <li>The overshoots of burning rate during pressurization and undershoots during depressurization are well explained</li> <li>The approach of using steady-state data to deduce the correct unsteady heat feedback law is unique</li> </ul>
<ul style="list-style-type: none"> <li>Extinction of a solid propellant is hard to achieve by short pressure pulses because the thermal layer changes only within a small depth</li> <li>Ideal conditions for extinction exist when <math>T_c \approx T_p</math></li> </ul>	<ul style="list-style-type: none"> <li>Pressure pulse functions used in extinction study are not realistic; actual extinction is usually caused by rapid depressurization</li> <li>Assumption of constant <math>T_s</math> limits the study to propellants with high activation energies</li> </ul>
<ul style="list-style-type: none"> <li>A closed-form expression for <math>r_b</math> as a function of <math>dp/dt</math>, <math>r_o</math>, <math>n</math>, and <math>\alpha_c</math> was obtained</li> <li><math>T_s</math> and the temperature profile in the solid respond to a pressure transient in the sense that <math>\phi_{c,s}</math> increases continuously during pressurization</li> </ul>	<ul style="list-style-type: none"> <li>Definition of <math>q</math> in the representation of Term A in in Eq. (4) leads to incorrect gradient of the energy flux</li> <li>The heat feedback equation used and the lack of consideration for thermal history of the propellant limit the approach to cases with small deviation from steady state</li> </ul>
<ul style="list-style-type: none"> <li>Transient burning effect shown to be negligible for pressurization rates less than <math>3.4 \times 10^3</math> atm/s</li> <li>The effect of preheating is significant in firing with a weak igniter during ignition transient</li> </ul>	<ul style="list-style-type: none"> <li>Reaction time in the flame zone may not be constant during the pressure changes</li> <li>Results may be improved by considering instantaneous thermal wave penetration depth and surface temperature</li> </ul>

on next page)

Table 2 (cont.) Quasisteady

Authors	Basic assumptions	Theoretical formulations
Novozhilov (1967) (Ref. 7)	<ul style="list-style-type: none"> <li>• All the assumptions made in Ref. 3 above except for <math>T_s = \text{const.}</math></li> </ul>	<ul style="list-style-type: none"> <li>• Zel'dovich approach</li> <li>• Terms A, B, C in Eq. (4) considered</li> <li>• Surface temperature considered as a function of pressure and heat feedback</li> </ul>
Horton, Bruno, and Graesner (1967) (Ref. 8)	<ul style="list-style-type: none"> <li>• <math>T_s = \text{const}</math></li> <li>• No subsurface reactions</li> <li>• Heat feedback from the flame to the surface is quasisteady</li> </ul>	<ul style="list-style-type: none"> <li>• Flame description approach</li> <li>• Terms A, B, C in Eq. (4) considered</li> <li>• Heat feedback from the gas phase considered solely as a function of pressure</li> </ul>
Krier, T'ien Sirignano, and Summerfield (1968) (Ref. 9)	<ul style="list-style-type: none"> <li>• Heterogeneous propellant considered</li> <li>• Heat release in the gas phase is assumed to be a step function starting at the solid surface</li> <li>• The solid phase reaction zone is infinitely thin and lumped at the surface</li> </ul>	<ul style="list-style-type: none"> <li>• Flame description approach</li> <li>• Terms A, B, C in Eq. (4) considered</li> <li>• Quasisteady gas-phase energy equation integrated to yield the heat feedback</li> </ul>
Merkle, Turk, and Summerfield (1969) (Ref. 11)	<ul style="list-style-type: none"> <li>• The heat release in the gas phase is made up of two parts: diffusion-controlled flame in the entire gas-phase reaction zone and a kinetics-controlled thin flame at the peak temperature location</li> </ul>	<ul style="list-style-type: none"> <li>• Flame description approach</li> <li>• Terms A, B, C in Eq. (4) considered</li> <li>• Quasisteady gas-phase energy equation integrated to yield the heat feedback</li> </ul>
Wooldridge and Marxman (1970) (Ref.12)	<ul style="list-style-type: none"> <li>• Negligible subsurface reactions</li> <li>• Gas-phase reaction rates expressed as two delta functions at <math>x = 0</math> and <math>x = x_f</math></li> </ul>	<ul style="list-style-type: none"> <li>• Flame description approach</li> <li>• Terms A, B, C in Eq. (4) considered</li> <li>• Quasisteady gas-phase energy equation with two flames model to obtain the heat feedback</li> </ul>

(Table continued)

## Flame Models

Important conclusions by investigators	Comments
<ul style="list-style-type: none"> <li>• For variable <math>T_s</math> the region of stable burning is increased as compared to the constant <math>T_s</math> case. The coupling between the amplitude of <math>r_b</math> and frequency of pressure variations becomes stronger with variable <math>T_s</math></li> <li>• When pressure changes sharply, <math>T_s</math> changes only slightly, but <math>\phi_{c,s}</math> and <math>r_b</math> change significantly</li> </ul>	<ul style="list-style-type: none"> <li>• Quantitative predictions depend upon the accuracy of the steady-state burning data used</li> <li>• Effects of variable <math>T_s</math> on stability domain <math>r_b</math>, extinction and ignition phenomena are important; hence, <math>T_s</math> should be treated as a variable</li> </ul>
<ul style="list-style-type: none"> <li>• Low <math>n</math> propellants are hard to extinguish. High <math>n</math> propellants under low values of <math>p_{amb}/p</math> are no easier to extinguish</li> <li>• Lowering the surface temperature or raising the heat of sublimation makes the propellant easy to extinguish.</li> </ul>	<ul style="list-style-type: none"> <li>• <math>T_s</math> may be varying during a transient</li> </ul>
<ul style="list-style-type: none"> <li>• Propellants with a high rate of surface heat release are intrinsically unstable</li> <li>• Flame temperature overshoots are predicted by the model; the higher the surface heat release rate, the higher the overshoot</li> <li>• The amplitude and phase of <math>T_f</math> depend critically on the frequency of pressure variation. Both in-phase (isentropic) and out-of-phase (isothermal) behavior was predicted for different <math>dp/dt</math>.</li> </ul>	<ul style="list-style-type: none"> <li>• The concept of quasisteadiness in the gas phase is developed</li> <li>• Power law for surface pyrolysis rate may be replaced by Arrhenius type of rate equation</li> </ul>
<ul style="list-style-type: none"> <li>• The occurrence of extinction was seen to depend more strongly on the lower end of the depressurization curve</li> <li>• Extinction boundary for a given propellant is established as a straight line on a linear plot of initial depressurization rate vs initial pressure</li> <li>• As extinction is approached, the kinetics becomes the controlling factor as opposed to diffusion-controlled flame near steady burning</li> <li>• Pressure exponent <math>n</math> is an important parameter in determining the extinction behavior</li> </ul>	<ul style="list-style-type: none"> <li>• Choice of weighting factors in combining the diffusion- and kinetics-controlled parts of the gas-phase heat release depends upon propellant formulation</li> <li>• Predicted extinction boundary is in good agreement with the data obtained</li> </ul>
<ul style="list-style-type: none"> <li>• Oscillatory burning was predicted for depressurization rates approaching the critical value. Beyond the critical rate, the burning rate oscillations are less intense</li> <li>• At depressurization rates an order-of-magnitude lower than the critical rate, oscillations are not predicted</li> </ul>	<ul style="list-style-type: none"> <li>• The two flame sheet model may be valid for a limited number of propellants. The relative magnitude of heat release in the two flames is not well known</li> <li>• The model could not predict observed undershoots in pressure</li> </ul>

Table 2 (cont.) Quasisteady

Authors	Basic assumptions	Theoretical Formulations
Summerfield, Caveny, Battista, Kubota, Gostintsev, and Isoda (1971) (Ref. 13)	<ul style="list-style-type: none"> <li>• Quasisteady gas-phase and surface reaction</li> <li>• Propellant and flame system is considered adiabatic and not influenced by external force</li> </ul>	<ul style="list-style-type: none"> <li>• Zel'dovich approach</li> <li>• Homogeneous and isotropic propellant with a uniform effective surface temperature</li> <li>• Functional relationships given by Eqs. (47-51) used</li> </ul>
Krier (1972) (Ref. 16)	<ul style="list-style-type: none"> <li>• <math>\epsilon \ll 1</math></li> <li>• <math>C_s = C_g = C</math></li> <li>• Change in pressure w.r.t. time is monotonic</li> <li>• Heterogeneous propellant considered</li> </ul>	<ul style="list-style-type: none"> <li>• <math>dp/dt</math> approach</li> <li>• Terms A, B, C in Eq. (4) considered</li> <li>• Gas-phase heat feedback expression based upon KTSS model</li> <li>• Small perturbation analysis used to derive an explicit burning rate law</li> </ul>
Kooker and Zinn (1973) (Ref. 17)	<ul style="list-style-type: none"> <li>• Homogeneous propellant</li> <li>• Single-step chemical reaction</li> <li>• The surface heat release contribution to heat feedback is given as a function of <math>r_b</math> and <math>Q_s</math> while the gaseous flame heat feedback is expressed in terms of <math>r_b</math>, <math>Q_s</math>, and <math>\omega</math></li> </ul>	<ul style="list-style-type: none"> <li>• Flame description approach</li> <li>• Terms A, B, C in Eq. (4) considered</li> <li>• Heat feedback to the propellant surface is determined from the contribution of both surface and gas-phase heat release</li> </ul>
Levine and Culick (1974) (Ref. 18)	<ul style="list-style-type: none"> <li>• Gas-phase reaction rate is a function of pressure only and more-over the functional relationship between the reaction rate and pressure is the same for steady-state and quasisteady situations</li> </ul>	<ul style="list-style-type: none"> <li>• Flame description model</li> <li>• Terms A, B, C from Eq. (4) considered</li> <li>• Gas-phase energy equation is integrated and steady-state relationships are used to obtain reaction rate as a function of pressure</li> </ul>

## TRANSIENT BURNING

621

## Flame Models

Important conclusions by investigators	Comments
<ul style="list-style-type: none"> <li>• In the absence of <math>T_{S,0} = T_{S,0}(r_0, p_0)</math> data, an approximate pyrolysis law may be employed</li> <li>• Stability and extinction characteristics are mainly dependent upon the thermal gradient in the solid phase at the surface</li> <li>• For large <math>E_s</math>, small changes in <math>T_s</math> correspond to large changes in <math>r_b</math>. Also for high values of <math>E_s</math> and <math>\sigma_p</math> the depressurization rate required for extinguishment is decreased</li> </ul>	<ul style="list-style-type: none"> <li>• Zeldovich method is superior to other methods if accurate steady-state burning rate data are available for constructing a Zeldovich map</li> <li>• Zeldovich model can be applied to different propellants with little or no modifications</li> <li>• Heat feedback to the solid phase can be determined without having a detailed knowledge of the gas-phase behavior</li> </ul>
<ul style="list-style-type: none"> <li>• The proportionality factor <math>\psi</math> is not assumed to be a constant for every propellant as opposed to previous <math>dp/dt</math> models</li> <li>• <math>\psi</math> depends on the surface heat release, pyrolysis exponent, burning-rate pressure exponent, and the ratio of the instantaneous to initial pressure</li> </ul>	<ul style="list-style-type: none"> <li>• This is an interesting small perturbation analysis which appears to be valid for slow pressure transients</li> <li>• The final burning rate expression may need experimental verification</li> </ul>
<ul style="list-style-type: none"> <li>• The pressure coupled transient burning model predicts large amplitude burning rate spikes under certain conditions. This suggests re-examination of the quasisteady flame assumption</li> <li>• Above a certain threshold amplitude of chamber disturbance, the mass generation oscillation gain phase coherency with the pressure oscillations leading to sharp burning rate spikes</li> <li>• Thermal wave near the surface is crucial in determination of <math>r_b</math></li> <li>• The mass burning rate response grows increasingly nonlinear as the amplitude of a sinusoidal pressure oscillation grows</li> </ul>	<ul style="list-style-type: none"> <li>• The model is very similar to KTSS model except for the heat feedback to the solid phase. The difference in heat feedback is due to the assumption of different specific heats for the solid and gaseous phases and a different surface pyrolysis law</li> <li>• This work represents an interesting example of the transient burning analysis coupled with the dynamic analysis of a rocket motor</li> </ul>
<ul style="list-style-type: none"> <li>• Intrinsic stability boundary defined in terms of dimensionless quantities that are functions of <math>E_s</math>, <math>T_s</math>, <math>T_i</math>, <math>C_s</math>, <math>C_g</math>, and <math>Q_s</math></li> <li>• As surface activation energy increases, stability decreases</li> <li>• At a higher amplitude pressure disturbance, the burning rate runaway can be invoked</li> <li>• Magnitude and phase of burning rate response depend strongly on the amplitude of pressure oscillations</li> </ul>	<ul style="list-style-type: none"> <li>• The model is similar to KTSS</li> <li>• Interesting results concerning the stability boundary were obtained</li> <li>• Some difficulties in obtaining the kinetic data needed in the Arrhenius law to relate the burning rate with <math>T_s</math> and <math>p</math> are likely to be encountered</li> </ul>

## Chapter 12

### Extinction Theories and Experiments

Luigi De Luca\*

*Centro di Studio per Ricerche sulla Propulsione  
e sull'Energetica, Milano, Italy*

#### Abstract

Experimental results obtained by a wide spectrum of quenching techniques are reviewed, with particular reference to dynamic extinction. Emphasis is given to combustion processes of thermokinetic character (velocity coupling is not considered). A rather general model is proposed for numerical computation of burning transients (including extinction by fast depressurization and/or deradiation) of monodimensional, heterogeneous, thin deflagration waves. Three flame models are resorted to; the validity of several of them is discussed and the relevance of the Zeldovich approach is assessed. An approximate but nonlinear burning stability theory is presented capable of predicting static and dynamic extinction boundaries for finite-size disturbances. Both boundaries are found to be property of the burning propellant (but are affected by the operating conditions).

#### Nomenclature

$a_\lambda$	= volumetric optical absorption coefficient, $\text{cm}^{-1}$
$A_M$	= constant used in MTS flame model (see Sec. V)

$b$	= constant used in nondimensional thermal conductivity law
$B_M$	= constant used in MTS flame model (see Sec. V)
$B_p$	= nondimensional pressurization rate coefficient (see Table 4)
$B_r$	= nondimensional radiation rate coefficient (see Table 4)
$C$	= specific heat, cal/g·K
$d$	= layer thickness, cm
$E$	= $E_s/\bar{Q}/T_{s,ref}$ , constant used in LC flame model (see Sec. V)
$E_s/\bar{Q}$	= activation temperature at the burning surface, K
$E_f/\bar{Q}$	= activation temperature in the gas phase, K
$f(\bar{\theta}_s - \theta_s)$	= static restoring function (see Sec. VI)
$f(X, \lambda)$	= function depending on optical properties of condensed phase and external radiation source (see Sec. V)
$F_0$	= $I_0/\dot{\phi}_{ref}$ , nondimensional radiant flux intensity impinging on the burning surface
$g(\tau, \bar{\theta}_s - \theta_s)$	= nonautonomous function (see Sec. VI)
$H$	= $Q_s/Q_{ref}$ , nondimensional surface heat release
$I_0$	= radiant flux intensity impinging on the burning surface, cal/cm <sup>2</sup> ·s
$k$	= thermal conductivity, cal/cm·s·K
$\dot{m}$	= mass flow rate, g/cm <sup>2</sup> ·s
$\bar{m}$	= average molecular weight, g/mole
$n$	= exponent in ballistic burning rate law; also order of the approximating temperature disturbance polynomial profile (see Sec. VI)
$N_t$	= transparency factor (see Sec. V)
$p$	= ammonium perchlorate percent of propellant composition, % (by weight)
$P$	= pressure, atm
$P_{ref}$	= 68 atm, reference pressure, atm
$\dot{q}_{c,s}$	= $\dot{\phi}_{c,s}/\dot{\phi}_{ref}$ , nondimensional heat flux conducted away in condensed phase
$\dot{q}_{g,s}$	= $\dot{\phi}_{g,s}/\dot{\phi}_{ref}$ , nondimensional heat flux feedback from gas phase
$\dot{q}_l$	= $\dot{\phi}_l/\dot{\phi}_{ref}$ , nondimensional heat flux lost from burning surface
$\dot{q}_s$	= $\dot{\phi}_s/\dot{\phi}_{ref}$ , nondimensional net heat flux released at the burning surface
$Q$	= $Q_f/Q_{ref}$ , nondimensional flame heat release
$Q_f$	= flame heat release, cal/g
$Q_{ref}$	= $C_{c,ref}(T_{s,ref} - T_{ref})$ , reference heat, cal/g
$Q_s$	= net surface heat release (positive if endothermic), cal/g
$r_b$	= burning rate, cm/s



$r_{b,ref}$	= $r_b(P_{ref})$ , reference burning rate, cm/s
$r_\lambda$	= surface optical reflectivity, %
$R$	= $r_b/r_{b,ref}$ , nondimensional burning rate
$R$	= universal gas constant, cal/mole·K
$t$	= time, s
$T$	= temperature, K
$T_{ref}$	= 300 K, reference temperature, K
$T_{s,ref}$	= $T_s(P_{ref})$ , reference surface temperature, K
$u$	= nondimensional finite-size disturbance of temperature (see Sec. VI)
$u_g$	= gas velocity, cm/s
$(u_x)_{c,s}$	= nondimensional finite-size disturbance of surface thermal gradient at the condensed phase side (see Sec. VI)
$U$	= $u_g/r_{b,ref}$ , nondimensional gas velocity
$w$	= power of KTSS pyrolysis law (see Sec. V)
$x$	= space variable, cm
$X$	= $x/(\alpha_{c,ref}/r_{b,ref})$ , nondimensional space variable
$Z$	= constant used in KZ flame model (see Sec. V)
$\alpha$	= thermal diffusivity, cm <sup>2</sup> /s
$\beta$	= reaction order of KZ flame model (see Sec. V)
$\delta$	= $d/(\alpha_{c,ref}/r_{b,ref})$ , nondimensional layer thickness
$\delta(X - X_f)$	= Dirac delta function located at the flame position
$\epsilon_\lambda$	= surface optical emissivity, %
$\theta$	= $(T - T_{ref})/(T_{s,ref} - T_{ref})$ , nondimensional temperature
$\xi$	= nondimensional thickness of disturbance thermal layer (see Sec. VI)
$\theta_m$	= minimum temperature for occurrence of chemical reactions in the condensed phase
$\theta_k$	= matching temperature for surface pyrolysis laws (see Sec. V)
$\theta_s$	= surface temperature
$\lambda$	= wavelength, $\mu\text{m}$
$\rho$	= density, g/cm <sup>3</sup>
$\tau$	= $t/(\alpha_{c,ref}/r_{b,ref}^2)$ , nondimensional time
$\tau'$	= $(k_{c,ref}/k_g)(C_g/C_{c,ref})(\rho_c/\rho_g)$ , nondimensional time parameter
$\bar{\tau}$	= nondimensional average diffusion time parameter used in KTSS flame model (see Sec. V)
$T$	= $T(\cdot)/T(\cdot)_{ref}$ , nondimensional temperature
$\phi_{c,s}$	= heat flux conducted away in condensed phase, cal/cm <sup>2</sup> ·s
$\phi_{g,s}$	= heat flux feedback from gas phase, cal/cm <sup>2</sup> ·s
$\phi_l$	= heat flux lost from burning surface, cal/cm <sup>2</sup> ·s

$\dot{\phi}_{\text{ref}}$	= $\rho_c c_{c,\text{ref}} r_{b,\text{ref}} (T_{s,\text{ref}} - T_{\text{ref}})$ , reference heat flux, cal/cm <sup>2</sup> ·s
$\dot{\phi}_s$	= $\rho_c r_b \dot{Q}_s$ , net heat flux released at the burning surface, cal/cm <sup>2</sup> ·s
$\Psi$	= $P/P_{\text{ref}}$ , nondimensional pressure
$\dot{\omega}$	= mass reaction rate per unit volume, g/cm <sup>3</sup> ·s
$\omega_{\text{di}}$	= constant used in MTS flame model (see Sec. V)
$\omega_{\text{ki}}$	= constant used in MTS flame model (see Sec. V)

### Subscripts and Superscripts

a	= optical absorption layer
c	= condensed phase
f	= final; also flame
g	= gas phase
i	= initial
s	= surface
v	= vaporization
cr	= crystalline
di	= diffusion
ki	= kinetic
re	= reaction
th	= thermal
ref	= reference
DL	= deflagration limit
DAM	= damped oscillations
OSC	= self-sustained oscillatory
$\xi$	= penetration depth
$\lambda$	= spectral
—	= steady-state or average value
o	= at the burning surface
— <sub>∞</sub>	= far upstream, i.e., ambient value

### Abbreviations

AFSC	= Air Force System Command
AMS	= Aerospace and Mechanical Sciences Department
AP	= ammonium perchlorate (NH <sub>4</sub> ClO <sub>4</sub> )
CTPB	= carboxyl terminated polybutadiene
CTPIB	= carboxyl terminated polyisobutylene
DB	= double-base
GDF	= granular diffusion flame
HTPB	= hydroxyl terminated polybutadiene
KTSS	= Krier-T'ien-Sirignano-Summerfield
KTSSL	= Krier-T'ien-Sirignano-Summerfield linear flame model
KTSSN	= Krier-T'ien-Sirignano-Summerfield nonlinear flame model

KZ	= Kooker-Zinn
LC	= Levine-Culick
MTS	= Merkle-Turk-Summerfield
NC	= nitrocellulose
ODE	= ordinary differential equation
PBAA	= polybutadiene acrylic acid
PBAN	= polybutadiene acrylic acid acrylonitrile
PDE	= partial differential equation
PU	= polyurethane
PVC	= polyvinylchloride

## I. Introduction

Extinction of solid rocket propellants is important from both technological and scientific standpoints. Controlled thrust termination is often a necessity, e.g., at staging times for satellite launchers or when the rocket has reached its desired velocity. Stop/restart capability of a solid-propellant rocket motor largely improves its flexibility in operations; lack of flexibility is indeed one of the main disadvantages of solid rocket motors with respect to liquid or hybrid propellants. A successful stop/restart operation requires terminating combustion rapidly on command but leaving the propellant grain ready for a new ignition. Quenching by fast depressurization or deradiation and thermal quenching by a coolant injector are the most attractive techniques. Although successfully applied in different environments, the scientific understanding of these techniques is surprisingly unsatisfactory. Unsteady as well steady burning theories have yet to be properly formulated and verified.

The purpose of this chapter is to offer such a theory. However, emphasis is given to solid-propellant combustion per se; velocity coupling with the fluid dynamic field of rocket combustion chamber is out of the scope of this chapter. The reader is urged to see the intimate connections between extinction and other burning problems. A good physical grasp will help substantially in understanding the various analytical formulations proposed in the literature and to judge the important experimental contributions.

The books by Williams,<sup>1</sup> Williams-Barrère-Huang,<sup>2</sup> and Price-Culick<sup>3</sup> are strongly recommended to readers as excellent introductions and references texts in the areas respectively of general combustion, solid-propellant rocket motors, and solid-propellant burning. Technology and research on solid-propellant burning have been developed in USSR along very autonomous and successful lines for the last 40 years. This is basically due to the pioneering and

extraordinarily advanced work performed by Ya.B. Zeldovich during World War II. Fortunately, two monographs are available containing detailed discussions of Soviet progress. The first, by Novozhilov,<sup>4</sup> was published in Moscow in 1973 and the second, by Zeldovich-Leypunskiy-Librovich,<sup>5</sup> was published in Moscow in 1975 but is based on a short course given by Librovich<sup>6</sup> in 1970 during a stay at Princeton University. Finally, a collection of specialized articles on experimental techniques in solid-propellant combustion was recently published.<sup>7</sup> This book also should be of great interest to readers.

The plan of presentation is the following. A technical background on the meaning of extinction, static vs dynamic extinction, and various techniques to practically achieve extinction is given in Sec. II. A review of theoretical and experimental contributions available in the open literature is given in Secs. III (fast depressurization and fast deradiation techniques) and IV (other quenching techniques). A mathematical statement of the problem, as accurate as possible within the presently available experimental information, is discussed in Sec. V. This formulation is too complicated to be solved analytically, so numerical integration is required. An approximate, but analytically very tractable, way to attack the problem is shown in Sec. VI. This special formulation will be used not to find actual solutions but to predict the behavior of solutions under steady or unsteady conditions. In particular, nonlinear extinction boundaries will be defined and determined. These approximate analytical predictions will be experimentally and numerically verified in Sec. VII. Finally, conclusions and suggestions for future work are given in Sec. VIII.

## II. Technical Background

Consider a monodimensional strand of solid rocket propellant, subjected to a radiant flux impinging with instantaneous intensity  $(1-r_\lambda) \cdot I_0(t)$  at its surface, burning with instantaneous rate  $r_b(t)$  in a vessel at instantaneous pressure  $P(t)$ . See the schematic in Fig. 1. It is assumed that a uniform pressure exists in a container with the instantaneous pressure level exclusively controlled from the exterior. Radiant flux is supposed to be provided by a continuous wave, external source (e.g., laser) of adjustable intensity and known properties. The ambient temperature is taken as constant in time, but it can be changed parametrically. Pressure, radiant flux, and ambient temperature will be called (external) controlling parameters of the burning processes.

For a fixed set of controlling parameters, the strand of the solid propellant is usually observed to burn steadily. If the controlling parameters change in time, the strand will usually burn with a variable but finite rate. Extinction implies quenching of all chemical activity of the strand; roughly this corresponds to the zero burning rate. Extinction can be achieved statically or dynamically. Static extinction means that, for a given set of controlling parameters, the trivial zero burning rate solution is the only allowed stable-steady solution. Dynamic extinction means that extinction occurs following an attempt to perform a combustion transition from some initial to some final set of controlling parameters for which a final stable-steady burning solution exists. Under these circumstances, extinction is due to an excessively fast change of the controlling parameters with respect to the response time of the solid propellant (time required to adjust itself to the new set of operating conditions). These ideas will be further dealt with in what follows.

Static extinction is therefore associated with excessively low values of pressure (pressure deflagration) and/or ambient temperature and/or large values of heat exchange with the exterior. Dynamic extinction is associated with fast changes of pressure (depressurization or  $dp/dt$  extinction) and/or heat exchange (usually deradiation, i.e., radiation input decrease).

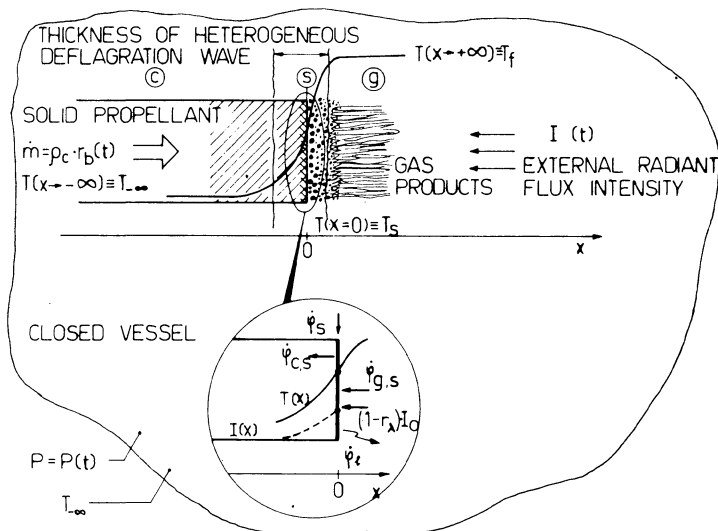


Fig. 1 Physical problem and energy balance at the surface.

Typical means to achieve the extinction of burning propellants practically are: fast depressurization, fast deradiation, injection of flame inhibitors, contact with heat sinks, reduction of the sample dimensions below some critical value, or any combination of these methods. Fast depressurization and flame inhibitor injection are currently used to intentionally stop rocket motors. Other methods are mainly relevant in improving our basic understanding of combustion, although useful applications are also conceivable. Extinction by depressurization may be realized, as a particular case, by lowering the pressure (no matter how fast or slow) below the deflagration limit; but, in this case, reignition of the rocket motor is not permitted.

It is not always obvious to distinguish between static and dynamic extinction. This is not a mere academic exercise, for different physical mechanisms and different boundaries apply. Unfortunately, great confusion exists on this point in the competent literature. While the static extinction boundary has been recognized since the beginning as a property of the propellant, the dynamic extinction boundary is usually considered to depend on the transition parameters (e.g., initial and final pressure, depressurization rate, experimental apparatus, type of forcing function, etc.). The author<sup>8</sup> showed in 1975 that the dynamic extinction boundary also is a property of the propellant, fixed by the actual set of operating conditions, but independent of initial values, experimental apparatus, type of forcing function, etc. For example, a parabolic deradiation in time to zero flux intensity at 10 atm and an exponential depressurization from 30 to 10 atm without radiation assistance feature the same dynamic extinction limit (for a given propellant). A first detailed report of this theory and some numerical verifications were included in the Ph.D. thesis of the author.<sup>9</sup> An up-to-date exposure of the theory, with further extensions, is given in Ref. 10. This also includes a wide range of numerical verifications and some preliminary experimental checks.

In the author's theory<sup>8-10</sup> extinction (static and dynamic) is studied within the framework of a general burning stability theory. Extinction boundaries, for static and dynamic burning as well, are provided for nonlinear combustion of thin<sup>+</sup> heterogeneous deflagration

---

<sup>+</sup>This nomenclature was introduced by Dr. M. Summerfield to emphasize the negligible time scales characteristic of heat release both in the gas and condensed phases as compared to thermal wave relaxation in the condensed phase. This is the physical basis for introducing the concept of partially quasisteady flames. For details, consult Chapter 11.

waves subjected to finite-size disturbances. The approach has been applied so far to several thermal flame models with a quasisteady gas phase and no distributed reactions in the condensed phase. The same approach can be applied to the Zeldovich model as well.

Before going ahead, the following terminology should be well understood. The expression "dynamic extinction" is used throughout this chapter with reference to the transient burning rate effect when extinction is observed. The expression "dynamic (or static) burning stability" is used to mean the inclusion (or not) of a forcing function when burning stability analysis is carried out.

In principle, both static and dynamic burning stability have to be analyzed by nonlinear equations and finite-size disturbances. This is particularly important for dynamic extinction, which is related to the combustion transition between two equilibrium configurations that are usually drastically different. Static stability, being related to an equilibrium configuration stability, can also be analyzed by means of linearized equations and infinitesimal disturbances. But the validity of the results is restricted: if instability is found, the fate of the burning propellant is not predictable (incipient instability); if stability is found, it is limited to infinitesimally small disturbances (linear stability).

Among the very numerous contributions (see, e.g., Refs. 11-47) to fast depressurization extinction, the only paper which clearly recognized the difference between static and dynamic extinction limits was offered by T'ien<sup>20</sup> in 1974. However, a totally different approach was followed and not all the conclusions in this excellent paper are shared by the writer. Details will be given later.

Fast deradiation extinction, being a recent discovery, has drawn much less attention (see, e.g., Refs. 48-53). The intimate connection between dynamic extinction by fast depressurization and fast deradiation was not recognized by anyone before Ref. 8 appeared.

### III. Literature Survey on Dynamic Extinction

Although much discussed in the literature, solid-propellant dynamic extinction still does not appear to be fully understood from a scientific point of view. The erroneous application of the quasisteady gas-phase assumption, the strong limitations of linearized theories, and the empirical nature of several of the proposed dynamic extinction criteria are the most serious formal drawbacks.

Furthermore, a rather fundamental but subtle error, concerning a conceptual confusion between static and dynamic extinction, is seen to permeate the literature. As explained in the previous section, static and dynamic extinction are different in nature. Static extinction received little attention in recent years; a good review can be found in standard textbooks (e.g., see Refs. 1-3). The mechanism usually accepted, but unproved, to explain static extinction invokes radiative heat loss from the burning surface. This is questionable; in any event, there is no doubt that static extinction is not directly related to changes in the externally controlling parameters. Dynamic extinction may occur under a variety of conditions. However, only dynamic extinction by fast depressurization appears largely analyzed. This is due to both its technological importance and the fact that dynamic extinction by fast deradiation is a recent finding.

#### Theoretical Results on Dynamic Extinction by Fast Depressurization

Theoretical results are reviewed prior to experimental results because the latter look scattered and may be misleading for unexperienced readers. Although basically experimental in nature, the work of Ciepluch<sup>11-13</sup> is recalled first since this was the starting point for all successive works.

In 1961 Ciepluch conducted one of the first systematic experimental studies of depressurization transients in a laboratory combustion chamber closely simulating conditions of an actual motor. Fast depressurization was obtained by suddenly opening a chamber vent hole. Initial chamber pressure in the range of 34-82 atm and ambient pressures down to 3.5 mm of mercury were explored. The burning transient was followed by measuring simultaneously combustion luminosity (primarily in the visible range) and chamber pressure. Several ammonium perchlorate (AP)-based composite propellants were tested; few data on double-base (DB) compositions were also reported. The following conclusions were reached:

- 1) A critical depressurization rate exists below which burning continues and above which extinction occurs.
- 2) The critical depressurization rate increases linearly as the chamber pressure prior to venting increases.
- 3) The critical depressurization rate is substantially affected by the propellant composition.
- 4) Reignition may follow extinction if the depressurization is not too fast and/or nozzle back pressure is not too low.



A large number of papers was offered after this study; an important critical review was given by Merkle et al.<sup>14</sup> in 1969. Since the pressure decay in Ciepluch's experiments was exponential, the maximum depressurization rate occurred at the very beginning of the transient burning. This was erroneously interpreted to suggest a tight dependence of dynamic extinction on the initial depressurization rate. Merkle et al. recognized that dynamic extinction depends on the entire  $P(t)$  curve, corrected several mistakes that had crept in the literature, and furnished a new quasisteady flame model (see Sec. V). However, Merkle et al. did not formulate an extinction criterion. For numerical simulation purposes only, a critical value of surface temperature ( $T_s = 600$  K) was empirically picked up, below which chemical reactions are considered too weak to sustain deflagration waves.

A critical review of mathematical expressions of the type

$$r_b(t) = \bar{r}_b \left[ 1 + \psi \frac{n}{P(t)} \frac{\alpha_c}{\bar{r}_b^2} \frac{dP(t)}{dt} \right] \quad (1)$$

supposed to describe transient burning rate of solid propellants was offered by Krier<sup>15</sup> in 1972. The quantity  $\psi$  was considered constant by previous investigators:

$$\begin{aligned} \psi &= 1 && \text{by Paul et al.}^{16} \\ \psi &= 1/2 && \text{by Parker and Summerfield}^{17} \\ \psi &= 2 && \text{by Von Elbe et al.}^{18, 19} \end{aligned}$$

The above expression and the the following equation

$$-\left. \frac{dP(t)}{dt} \right|_{cr} = \frac{1}{\psi} \frac{P(t)}{n} \frac{\bar{r}_b^2}{\alpha_c} \quad (2)$$

for critical depressurization rate are still being used (in particular the version with  $\psi = 2$ ) but erroneously. The use of Eq. (2) was already proved wrong, on physical grounds, by Merkle et al.<sup>14</sup> Krier analytically showed that  $\psi$  depends on the burning surface properties and pressure jump; this function can be computed a priori. Nevertheless, relationships of the type of Eq. (1), being restricted to small values of  $dP/dt$  and small excursions of  $r_b(t)$  with respect to  $\bar{r}_b$ , are just not applicable to dynamic extinction problems.

A paper by T'ien<sup>20</sup> in 1974 is the only one aimed directly at establishing an extinction criterion for fast depressurization. T'ien argues that heat losses are the

mechanism for both static and dynamic extinction of solid propellants; this view is not fully shared in this instance. However, T'ien concludes that for depressurization transients, if the instantaneous burning rate drops below the unstable burning rate solution at the final pressure, extinction will occur. T'ien derives his quantitative criterion from another study<sup>21</sup> by him of flammability limits of premixed flames under the influence of environmental disturbances.

A somewhat similar result has been found in this investigation,<sup>8-10</sup> but by a completely different approach. Several other publications<sup>22-26</sup> appear questionable. Mongia and Ambs<sup>22</sup> assumed a quasisteady heat feedback with a variable surface heat release; both the mathematical formalization and the physical motivations are questionable. However, Mongia and Ambs rightly recognized the importance of the finite time associated with the condensed-phase heat release and its dependence on the instantaneous properties near the burning surface. The importance of condensed-phase reactions was first stressed by Marxman and Wooldridge,<sup>23-25</sup> but their treatment also is suspect as already pointed out by Merkle et al.<sup>14</sup> Suhas and Bose<sup>26</sup> relaxed somewhat the quasisteady gas-phase assumption by taking into account the unsteady gas-phase continuity equation in the otherwise standard KTSS linear heat feedback law. The choice of this flame model is surprising, since the linear heat feedback law of KTSS was not intended to be used for extinction transients; in any event, the mathematical approach and the physical motivations are questionable. However, Suhas and Bose recognized the importance of the finite time associated with the gas-phase processes. Likely, the most important area of investigation in solid-propellant combustion in the near future will focus on these questions of condensed-phase reactions and unsteady gas phase (thick vs thin flames).

The line of research evolved within the framework of the Zeldovich<sup>27,28</sup> method is of limited value from the point of view of dynamic extinction. In the original Zeldovich model (constant surface temperature), extinction is assumed to occur when the instantaneous thermal state of the condensed phase can no longer be matched to the allowed values of surface temperature and thermal gradient at the condensed side of the burning surface. For example, in 1964 Istratov et al.<sup>29</sup> used an integral method to determine an approximate solution to the condensed-phase energy equation of a propellant burning with a constant surface temperature. Dynamic extinction following instantaneous or exponential pressure decay was taken to occur when the surface thermal gradient on the condensed side exceeds some critical

(maximum) value beyond which no solution can be found. This is not acceptable, since no prediction can be made (without further analysis) about dynamic combustion for burning rates outside the Zeldovich allowed range. In 1967 Novozhilov<sup>30</sup> considered variable surface temperature and recognized that dynamic combustion is permitted also in a range of parameters where statically stable solutions are not found. To explain dynamic extinction the concept was then introduced of limiting points, at constant pressure, corresponding to finite values of burning rates and surface thermal gradients on the condensed side. Combustion, steady or unsteady, is considered impossible beyond these limiting points. The latter should be experimentally established, possibly under nonstationary burning conditions. This criterion, if feasible, would rely on very delicate experimental results. However, the existence of the limiting points was never really proved. Moreover, both models (constant and variable surface temperature) assume a sudden occurrence of extinction: the burning rate immediately prior to extinction is of the order of magnitude of the corresponding steady value. In general, this does not seem plausible from a physical standpoint.

Summerfield and co-workers<sup>31,32</sup> checked the possibility that crossing the burning stability boundary, evaluated via the Zeldovich method, is sufficient to produce dynamic extinction. The answer was negative, since they found that "the dynamic conditions of extinguishment tend to shift the stability line" (Ref. 31, p. 257). Finally, in 1973 Novozhilov (Ref. 4, p. 216) observed that "for the calculation of unsteady conditions in the unstable region it is necessary to draw on certain schemes of combustion, which make it possible to predict the properties of propellants beyond the (Zeldovich) stability limit."

Further work by Soviet investigators<sup>33-37</sup> offered fresh theoretical considerations, but failed to define a physically sound extinction criterion. In 1972 Frost<sup>33</sup> considered the case of the surface temperature depending only on the mass burning rate and reached conclusions similar to those obtained by Zeldovich for constant surface temperature (extinction due to impossibility of matching the temperature distributions in the gas and condensed phases). Frost and Yumashev<sup>34</sup> later studied the problem of dynamic extinction by depressurization by numerical integration. They concluded that: 1) introduction of special extinction conditions (limiting points) is not required in order to get extinction; 2) burning rate during extinction changes smoothly; and 3) the passage of the transient burning process outside the Zeldovich limit of stability

does not necessarily imply extinction. Frost and Yumashev<sup>35</sup> in a successive work in 1976 reviewed the Princeton papers<sup>31,32</sup> and formulated criticism similar to that stated above; they emphasized that the Zeldovich stability boundary is valid only for stationary combustion and has no direct bearing on unsteady processes; however, dynamic boundaries were not provided.

### Experimental Results on Dynamic Extinction by Fast Depressurization

Experimental results are often ambiguous to interpret due to the interplay and overlapping of several factors; attention is preferably focused on data collected from laboratory burners (ranging from depressurization strand burners to simulated rocket combustion chambers) rather than actual rocket motors where fluid dynamic effects may be dominant. However, even results from laboratory burners are not easy to compare due to implementation of different extinction criteria, diagnostic techniques, and operating conditions; to scattering of results; and to confused theoretical guidelines in data handling.

The pioneering work by Ciepluch<sup>11-13</sup> was summarized at the beginning of the preceding subsection. Recall that the critical boundary between (permanent) extinction and continued burning was found with a go/no-go technique to be a straight line in the  $dP/dt$  vs  $P_i$  (initial pressure) linear plot. Experimental data were provided, among others, by Von Elbe and McHale<sup>19</sup> in effort to substantiate Von Elbe's theoretical predictions.<sup>18</sup> They tested three AP-based composite propellants in a depressurization strand burner (300 cm<sup>3</sup> internal volume) furnished with a frangible diaphragm (ruptured by a solenoid-driven plunger) and orifice plate to control the depressurization rate. Flame luminosity in time was monitored with a photodiode simultaneously to pressure decay (see Fig. 2). Initial pressures of 33 - 5 atm were used. Von Elbe and McHale plotted  $dP/dt$  vs  $P$  at extinction (as determined by zero luminosity); the critical boundary was found to be straight on a  $\lg/\lg$  plot.

Merkle, Turk, and Summerfield<sup>14</sup> produced a rather complete set of data by systematically testing several AP composite and one catalyzed DB propellants. A special laboratory combustor (see Fig. 3) was designed to minimize erosive burning effects and to cause monodimensional "cigarette" burning of the sample. Fast pressure decay was obtained by rupturing a double-diaphragm system. The exhaust gases initially pass through both a primary (large) nozzle

and a secondary (small) nozzle; the small nozzle controls the chamber pressure as long as the diaphragms remain in place. When the diaphragms are removed, the small nozzle also becomes ineffective since it was located in the double-diaphragm section. By properly combining nozzles of different diameters, the initial pressure level as well as the depressurization rate could be varied. Pressure and light emission (as seen by a photomultiplier in the visible range) were simultaneously recorded. Extinction was considered to occur when zero light emission from the flame could be observed. Initial pressures in the range of 75 - 14 atm were explored. Venting was always to atmospheric pressure; because of this, reignition was nearly always observed. The following conclusions were reached:

1) The critical boundary between extinction (permanent or temporary) and continued burning was found with a go/no-go technique to be always straight in the  $dP/dt$  vs  $P_i$  linear plot. See Fig. 4.

2) Increasing AP loading from 75 to 82.5% makes the propellant more than twice as difficult to extinguish (in terms of initial, i.e., maximum,  $dP/dt$ ).

3) Increasing AP particle size from 45 to 180  $\mu\text{m}$  (unimodal distributions) makes the propellant easier to extinguish (for a fixed loading of 75% AP).

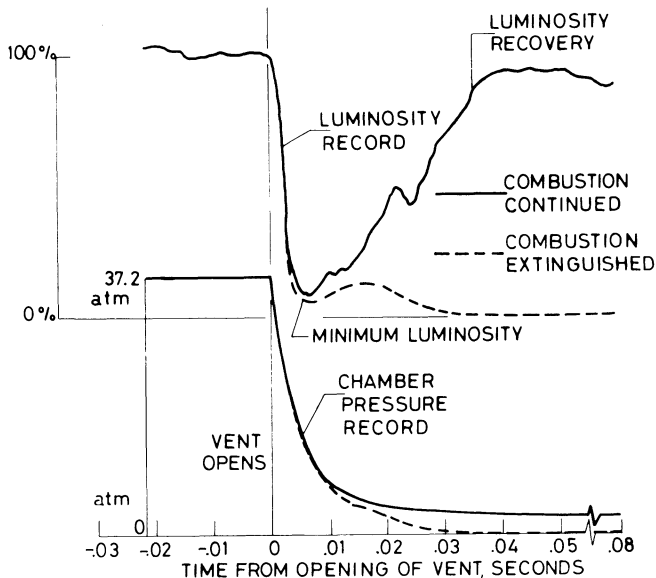


Fig. 2 Typical luminosity and chamber pressure transient records during rapid pressure decay (adapted from Ref. 10).

4) Little difference was observed when PBAA, CTPB, and PU binders (for a fixed loading of 80% AP) were tested.

5) Aluminum (16  $\mu\text{m}$  particles) addition up to 15% makes the propellant slightly more difficult to extinguish (for a fixed composition of 77.5% AP/22.5% binder); but the opposite is true for  $P_j < 27$  atm.

6) The tested catalyzed DB propellant (N-5 composition) is much easier to extinguish than any of the tested AP composite propellants.

It should be marked that some of the above conclusions on AP particle size and binder-type effects may be in conflict with other experimental studies in which permanent extinction was recorded. Merkle and Summerfield adopted the permanent extinction criterion only for tests using catalyzed DB propellants, since no visible radiation can be detected from DB burning at low pressures.

Detailed observations on the flame structure of composite propellants during depressurization were reported by Selzer and Steinz in a series of papers.<sup>39,40</sup> They showed that, regardless of the depressurization rate, the flame intensity (as seen by spectral emissions from OH, NH, CN, Na lines and carbon continuum) falls to zero soon after the impact of the first rarefaction wave on the burning surface. This event is possibly followed by the reappearance of an incipient flame, after a time span on the order of the condensed-phase thermal wave relaxation time, if the

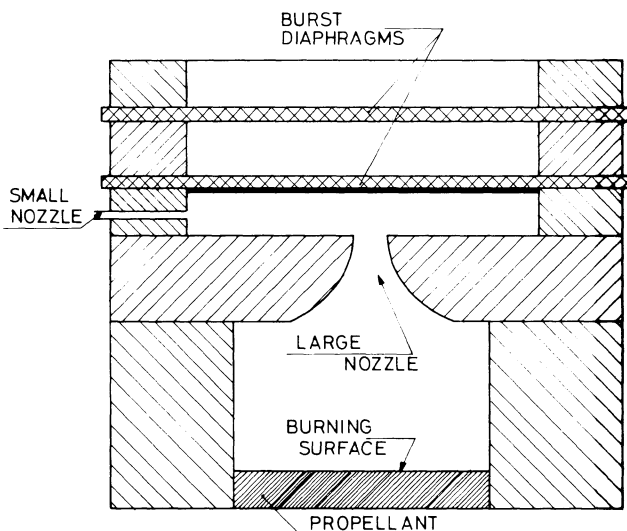


Fig. 3 Variable area combustor for depressurization tests (from Ref. 13).

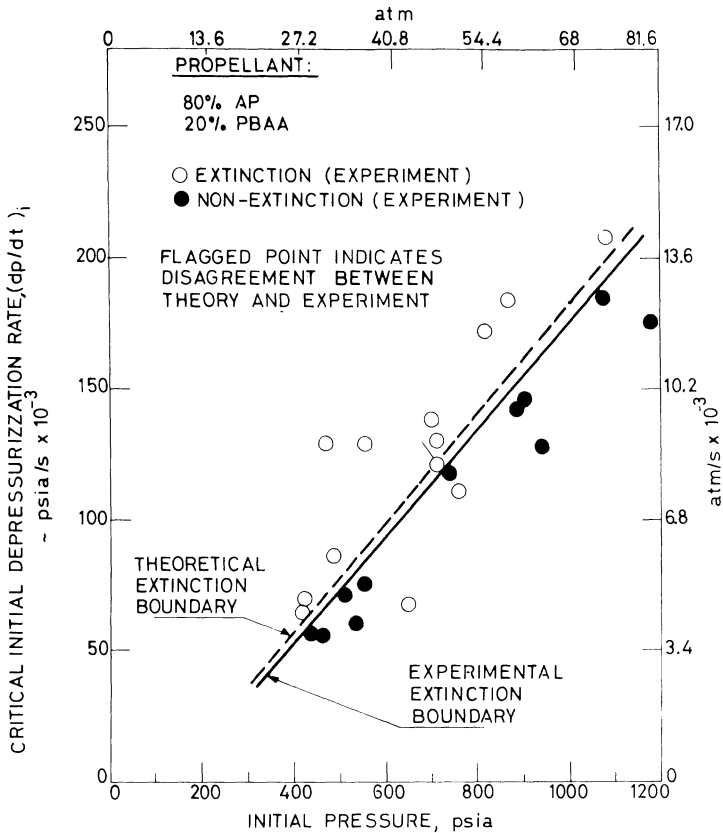


Fig. 4 Required depressurization rate for extinction: experimental and theoretical results (adapted from Ref. 13).

depressurization rate is not too fast. Marked pressure oscillations are observed when this secondary flame develops, the flame decay being otherwise exponential. The authors further claimed that the adiabatic expansion of the flame quenches the active gaseous chemical reactions; this would explain why the first zero intensity of flame radiation is noticed when the instantaneous pressure has dropped only to about 70% of the initial pressure. The average oxygen/fuel (O/F) mixture ratio was observed to be higher during some part of the transient burning than during steady state, due to preferential consumption of AP particles exposed on the propellant surface; the binder surface looked molten and not thicker than a few microns (for depressurization tests from 45 to 1 atm with 76% AP/24% CTPB composition). The implication is that the binder gasification is the first to suffer the effects of a

pressure expansion. It was finally confirmed, in agreement with Ciepluch<sup>11-13</sup> and Merkle,<sup>14</sup> that conditions at the end of the depressurization process, i.e., the final shape of the pressure history and the exhaust pressure, can be determining in extinction.

Baer and Ryan<sup>41,42</sup> also furnished detailed information on the flame structure during depressurization from about 7 atm to subatmospheric. AP-based composite propellants were tested in a rarefaction tube. Infrared spectral emissions from H<sub>2</sub>O, HCl, CO<sub>2</sub> lines and continuum (presumably from carbon particles) were detected; transient flame temperature was measured by use of an emission-absorption technique at the sodium D-lines (propellants were sodium seeded). Results obtained on the history of the gaseous mixture composition agree with those by Selzer and Steinz mentioned above.<sup>38</sup> Before the start of the pressure decay, the magnitude of the intensity of the spectral bands fluctuates, apparently as a result of almost periodic combustion irregularities. Intensities decreased rapidly as the pressure dropped and were often observed to increase prior to finally dropping to zero (for extinction transients). Plotting of H<sub>2</sub>O/CO<sub>2</sub> intensity ratio, with respect to the corresponding steady-state value, indicated that the O/F ratio increases at the beginning of the depressurization but decreases at the end, in part as a result of faster oxidizer depletion. The authors suggest that the flame might extinguish for a rich mixture limit effect, since termination of radiation emission (and extinguishment?) occurred as the intensity ratio rose above the steady burning value. The flame temperature histories reported by Baer, Ryan, and Schulz<sup>41</sup> are of greatest interest for theoretical modeling. The average steady burning temperature prior to depressurization was in excellent agreement with computed adiabatic flame temperatures. The flame temperature was observed to remain practically constant for a short while immediately after the beginning of pressure decay, then to decrease and possibly feature one or more attempts to recover before extinction. Finally, it was noticed that small pressure drops at low pressures were immediately followed by extinction.

Park, Ryan, and Baer<sup>42</sup> presented in 1973 another paper in which static vs dynamic extinction at low pressure (around 1 atm) was experimentally studied. In this pressure range, the two extinction mechanisms tend to overlap each other. Several composite propellants were tested. Propellant strands were burned in a vacuum chamber while supported on a force transducer monitoring their instantaneous weight. Extinction was detected from both the instantaneous burning



rate (obtained by differentiating the weight vs time record) and light emission. The following observations are of interest:

1) Propellants with burning rate catalysts (higher burn rate) require higher depressurization rates than the corresponding uncatalyzed propellants for extinguishment at the same pressure (in the Von Elbe sense).

2) As depressurization rates are lowered, the extinction pressure approaches a constant minimum value for each propellant (this value is, however, affected by the side burning inhibiting material, ambient gas, and the rate of heat loss).

3) Pressure deflagration limit, measured by a go/no-go technique, reveals no effect of the AP particle size for hard-to-melt binders (e.g., PBAA) while it decreases sharply as particle size increases for easy-to-melt binders (e.g., PU). This evidence suggests that AP crystals coated with molten polymer cannot participate to surface reactions, excepting those large crystals which project beyond the molten layer. The effect of molten polymer disappears at large AP loading (>80%) since not enough melt is available.

4) Extinction pressure (in the Von Elbe sense) is lowered by increasing ambient temperature (or reducing heat losses).

Further data on propellant composition effects were collected by Jensen and Brown<sup>43</sup> by testing AP-based composite propellants in two laboratory motors. They confirmed the known effects of exhaust pressure level on extinction and the overlapping effects of motor geometry. Propellants with binders degraded by endothermic thermal decomposition (thermally less stable, e.g., PU and CTPIB) were more easily extinguished than binders degraded by exothermic oxidation (thermally more stable, e.g., CTPB). The addition of aluminum made both dynamic extinction and reignition easier.

Data on condensed-phase thermal profiles during depressurization were published by Zemskikh et al.<sup>44</sup> Thin thermocouples (7-10  $\mu\text{m}$ ) were used to monitor the temperature history near the burning surface of double-base propellants in a laboratory burner. Fluctuations were observed for both extinction and reignition runs; large temperature drops could be measured following the pressure decay. Further data on double-base propellants tested in a depressurization bomb were offered by Ivashchenko and Komarov.<sup>45</sup> They claimed the importance of the dispersal of the reacting condensed layer following the expansion of the gas bubbles in response to the rapid pressure fall.

Strand and co-workers have been working for years to set up a microwave technique with the appropriate time

## Chapter 13

# Experimental Observations of Combustion Instability

E. W. Price\*

*Georgia Institute of Technology, Atlanta, Georgia*

### Abstract

The general nature of combustor instability in solid rocket motors is described, along with the implications for motor development programs. Processes contributing to stability are discussed as "gain" or "loss" mechanisms. Different types of motor instability (bulk mode, transverse acoustic mode, etc.) are described and the relevance of different gain and loss processes to each type of instability is discussed. The stability characteristics of different propellants are reviewed. The discussion includes illustrative examples and elementary descriptions of experimental results and theoretical concepts needed to understand trends of stability behavior.

### I. Introduction

The designer of a solid rocket motor normally has a design goal stated in terms of thrust level and duration of thrust, or some thrust-time program. The choice of propellant, charge geometry and nozzle throat area are tailored to meet that objective with an acceptable pressure in the motor. To make these choices, the designer uses "internal ballistic" equations based on the assumption of steady state combustion and flow in the motor. Among the equations used is the burning rate law for the propellant, which gives the dependence of the burning rate on pressure, erosive flow conditions, and bulk propellant temperature. (The "law" may be an experimentally determined dependence of the burning rate on these variables.)

Nature is no respecter of analytical approximations such as the steady-state assumption, and the designer is

---

Copyright © 1984 by E. W. Price. Published by the American Institute of Aeronautics and Astronautics with permission.

\*Professor, School of Aerospace Engineering.

often confronted by nonsteady behavior in the motor. The ignition transient is an example of nonsteady behavior that the designer accepts as an obvious design problem required to join the initial unfired state and the operational state basic to the usefulness of the motor. Nature also often donates to the designer nonsteady behavior he does not want. The most common of these is an oscillatory mode of operation, in which the pressure and combustion oscillate about a time-averaged mean pressure that may, or may not, correspond to the expected mean value. The behavior is illustrated schematically in Fig. 1. In this illustration, operation starts normally and, at some time (usually characteristic of the particular motor design), oscillations develop spontaneously at a characteristic frequency and grow to a large amplitude. In the "example," the mean pressure is seen to rise and remain high until the oscillations decrease. The high mean pressure corresponds to an enhanced mean burning rate and is accompanied by increased thrust, reduced burning time, enhanced heat transfer, and other adverse effects associated with vibrations. The consequences may range from explosion of the motor, or other modes of outright mission failure, to "mere" reduced reliability or restriction of service limits. Whenever possible, the motor developer seeks to eliminate oscillatory behavior before a motor goes into service, although there are some classic cases where this was not done and where serious (and costly) troubles developed in service use. When oscillatory behavior occurs, it is usually referred to as "combustion instability," although the oscillations would be more correctly attributed to instability of the entire combustor. The phenomenon

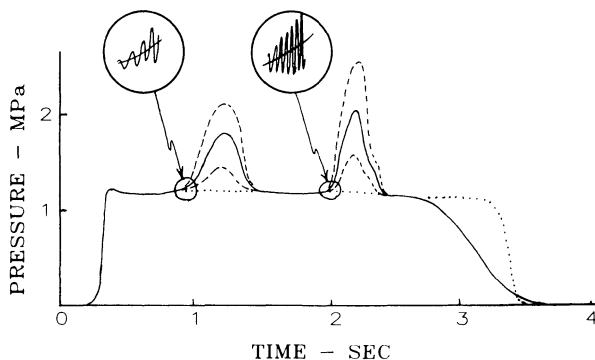


Fig. 1 Pressure-time history illustrates characteristics of combustion instability. Growing oscillations are accompanied by rise in mean pressure. Time and severity of behavior tend to shift with conditioning temperature of the motor prior to firing.

results from a very complex interaction of the combustion, the combustor flowfield, and the combustor cavity walls.

Some insight into the practical difficulties of dealing with combustion instability can be gained by some selected highlights ("low lights"?) of history of the problem. Early work with energetic propellants<sup>2,3</sup> posed a number of problems with the attainment of predictable and reproducible combustion in solid rocket motors (SRM). By 1944, there was increasing evidence that some kind of "resonance burning" was responsible for many encounters with unpredicted excursions in pressure and motor bursts, and design modifications were found to control the erratic behavior. Not until 1948 did instrumentation become available with high enough frequency response to resolve the oscillations.<sup>4</sup> By then there was a theory<sup>5</sup> for resonance, which involved dynamic response of the combustion to the gas oscillations in the natural acoustic modes of the combustor. In the ensuing 10 years, the measurements made on routine motor tests continued to be inadequate to record oscillations, so that the primary manifestations of instability were the excursions in quasisteady pressure, i.e., anomalies in the low frequency response pressure-time curve. Given the diverse modes of instability that are encountered in practice, the low frequency response instrumentation served as little more than a warning light to motor developers. However, the accumulated experiences (including specially instrumented tests for the research or diagnosis of problem cases) did show that instability was dependent on the type of propellant--there being no encounters with ammonium nitrate or potassium perchlorate composite propellants, but significant problems with ammonium perchlorate composites and double-base "ballistites." Introduction of powdered aluminum as a fuel ingredient in the late 1950's greatly reduced the incidence and severity of instability when used in smaller rocket motors, but it was found later that aluminum did not have the same effect in large rocket motors.

Systematic use was made of high-frequency response instrumentation in some programs starting with the work of Smith and Sprenger,<sup>6</sup> and it soon became evident that oscillatory behavior could occur over a very wide frequency range and was closely related to the excursions in mean pressure seen in routine testing. It was confirmed that oscillations occurred in natural acoustic wave modes of the combustor cavity, as well as in low frequency "bulk" modes. The range of frequencies observed prior to 1960 was from 10 Hz to over 50 kHz.

During the 1950's, combustion instability problems in new motor programs were quite common, but were resolved by

an array of fixes that were evaluated on a trial-and-error basis. Once stable behavior was achieved in a given design, such behavior could usually be relied upon to continue through production and service, unless some modifications in design or propellant were made.

Toward the end of the 1950's, the economics of the trial-and-error fix strategy became less acceptable. The cost of construction and testing of larger motors, the increased complexity of flight vehicles and payloads, and the increased vulnerability to oscillations usually demanded that oscillatory behavior be completely avoided, or at least be corrected with minimal full-scale motor testing. This situation was described by the conclusions of one government review committee,<sup>8</sup> which recommended that a major expansion in research be made to establish a more scientific basis for the prediction and control of instability. Since that time there has been a substantially higher level of research on instability, leading to advances in theory, analysis, and experimental methods that deserve far more comprehensive description than can be given here. To help the more determined reader, a list of review papers on combustion instability in solid rockets is provided at the end of the chapter.

## II. General Features of Instability

It was noted earlier that oscillatory behavior can develop spontaneously, often at a characteristic time during burning. This is associated with the progressive changes in geometry, pressure and flowfield that carry the system over a stability threshold. Beyond this threshold, flow disturbances are strongly enough amplified by the dynamic interaction with the combustion and mean flowfield to cause the disturbances to persist and to grow in spite of the ever-present damping processes. The disturbances are made periodic by repeated reflections from the cavity walls and can usually be identified with the natural modes of oscillation in the combustor cavity. The gas oscillations in some typical acoustic modes of a simple combustor cavity are shown in Fig. 2a, and the acoustic spectrum of a complicated configuration is shown in Fig. 2b. In a relatively unstable motor, disturbances may be unstable in several modes at once. An instructive way of summarizing the unstable oscillations is shown in Fig. 3.<sup>9</sup> This is referred to as a "waterfall" diagram produced by a Fourier analysis procedure.<sup>10</sup> In a short time interval of the high-frequency record from a pressure transducer, the spectrum is determined and plotted on a horizontal baseline in the

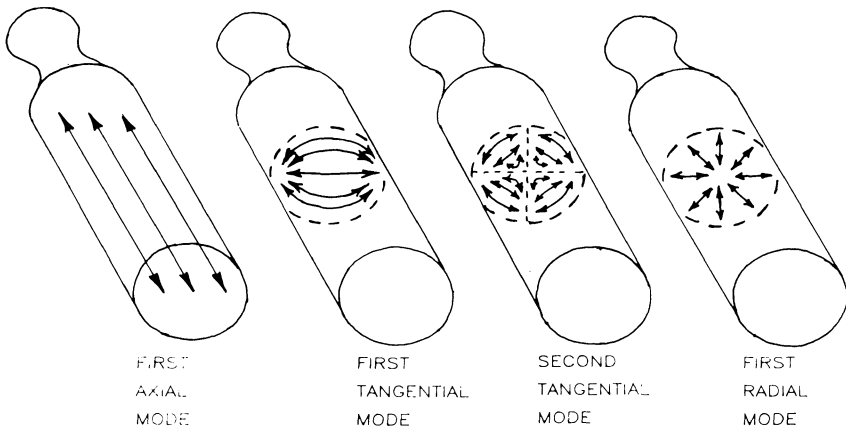


Fig. 2a Cavity modes: examples of standing acoustic modes in right circular cylinders.

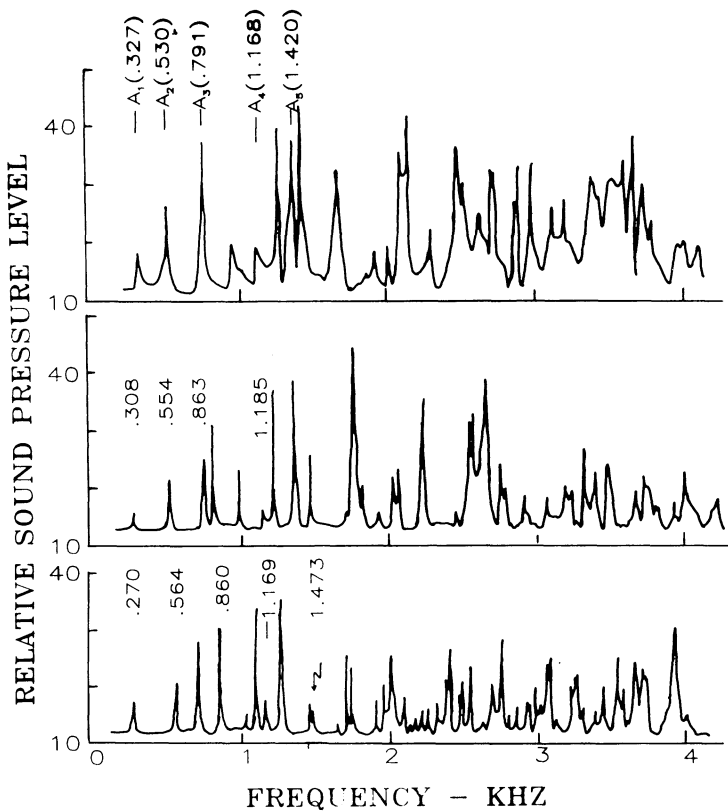


Fig. 2b Cavity modes: acoustic spectrograms from "cold" tests on scale models of a combustor of fairly complex shape (no mean flow). (The successive spectra are for geometries at successive times during burning).

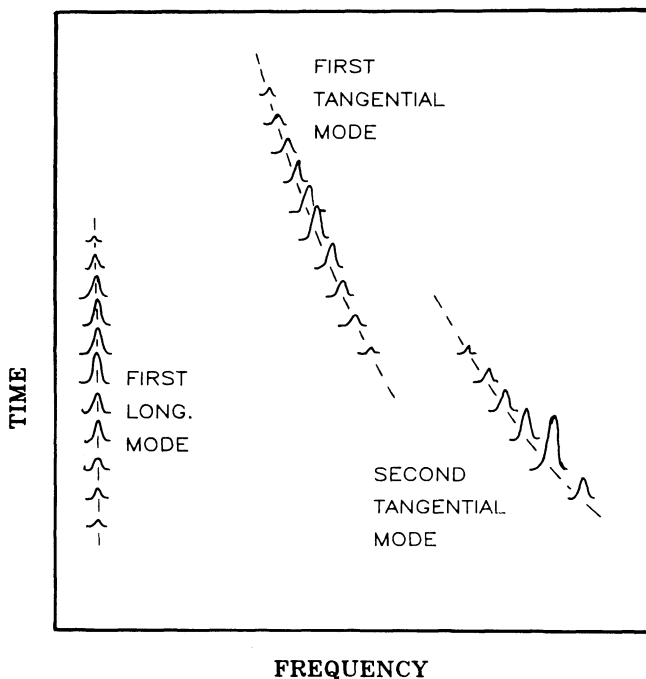


Fig. 3 Mode frequencies -- "waterfall" diagram for a motor firing.

figure. This analysis is repeated at frequent time intervals and displayed at successive locations on a time scale, providing a map of amplitude vs frequency over the entire period of oscillations. In Fig. 3, at most times during burning a low frequency is evident that corresponds to the first longitudinal mode of oscillation. Higher frequencies corresponding to transverse modes of oscillation are also evident. The frequencies of the transverse modes decrease with time due to the enlargement of the combustor cavity as the propellant burns. The map also shows the development and decay of different modes at different times during the burning, reflecting the difference in the stability of different modes and the shifting balance between the amplification and damping as conditions change during burning. Repeated tests on a particular motor design often give rather reproducible spectral histories.

The nature of the "shifting balance" between amplification and damping can be better understood by characterizing the behavior in a single mode as a function of amplitude (or mode energy level). This is indicated

schematically in Fig. 4a. The solid curve  $t_1$  shows the energy input to the oscillation per second (due to combustion and flow interactions) which would occur due to the mode oscillations, as a function of the energy levels that might be present in the mode at a particular time during burning. The broken curve  $t_1$  indicates the damping in the same mode at the same time. For the conditions of curves  $t_1$ , the damping exceeds the amplification, so that any disturbances at the mode frequency decay. Curves  $t_2$ - $t_5$  correspond to times progressively later in the burning period of the charge; thus, it can be seen that a time is

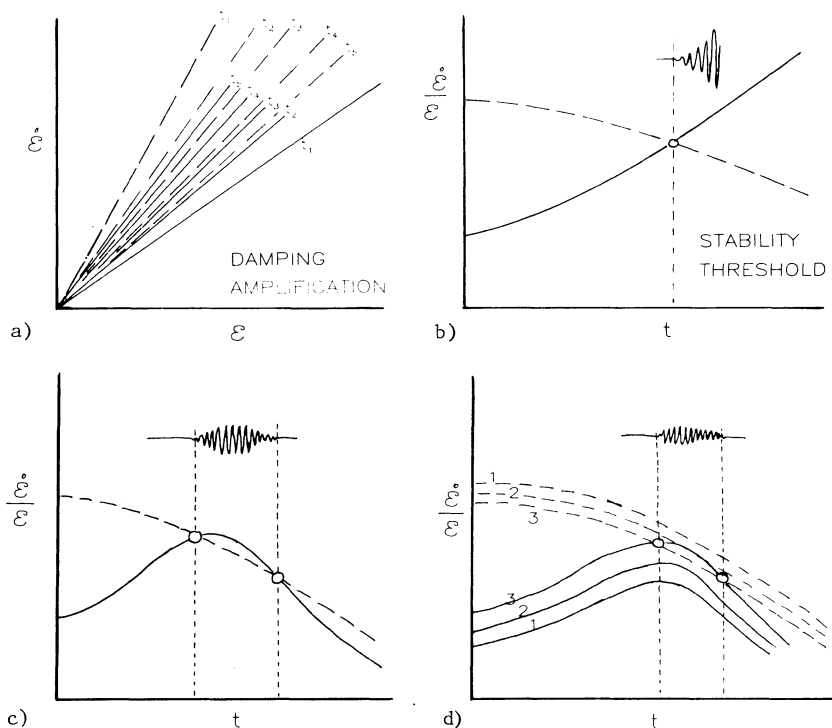


Fig. 4 Acoustic mode energies during oscillations (in a single mode).  $E$  is the mode energy level and  $\dot{E}$  are the corresponding rates of change due to driving processes (solid lines) and damping processes (broken lines); representation is for linear system: a) damping and amplification vs mode energy level for successive times during burning; b) proportional damping rates and amplification rates vs time during burning (slopes of lines in Fig. 4a); c) conditions for growth and decay of oscillations at characteristic times during burning; d) changing test conditions 1,2,3, leading to unstable conditions for curve 3. Conditions might be test temperature, nozzle size, etc.



reached for which the amplification exceeds the damping and the oscillations will grow. This trend is more concisely displayed in Fig. 4b, which shows the trends of the slopes of the lines in Fig. 4a as a function of time. Figure 4c shows a similar graph for a case where the unstable conditions prevail only briefly. Figure 4d describes the trend of Fig. 4c for a series of progressive changes in design, propellant, or operating temperature, illustrating how a stable situation (curves 1) can slip over the threshold (curves 3) due to such changes. It should be noted that, once the oscillations are sustained, they may grow to very large amplitude at a rate determined by the difference in  $\dot{\epsilon}$  for the amplification and damping curves. Oscillations will decay away quickly if the amplification later becomes lower than the damping, as in Fig. 4c.

In Fig. 4a, the ratio of  $\dot{\epsilon}$  to  $\epsilon$  was assumed to be constant, but in real systems nonlinearities give rise to the conditions represented schematically in Fig. 5. In Fig. 5a, a typical amplitude-limiting nonlinearity is illustrated. A more complex nonlinearity is shown in Fig. 5b; systems of this kind are stable to small disturbances, but exhibit growing oscillations if a large disturbance occurs. As will be seen later, the behaviors implied by Figs. 4 and 5 are readily recognized in various observed rocket motor instabilities.

In order to appreciate the "forces" at work in combustor instability, it is worthwhile to take a small detour and examine the energy levels of the oscillations implicit in Figs. 4 and 5 and where this energy might come from. Consider a rocket motor with a 100,000-kg ( $\approx 50,000$ -lb) thrust. Such a thrust corresponds to combustion of about

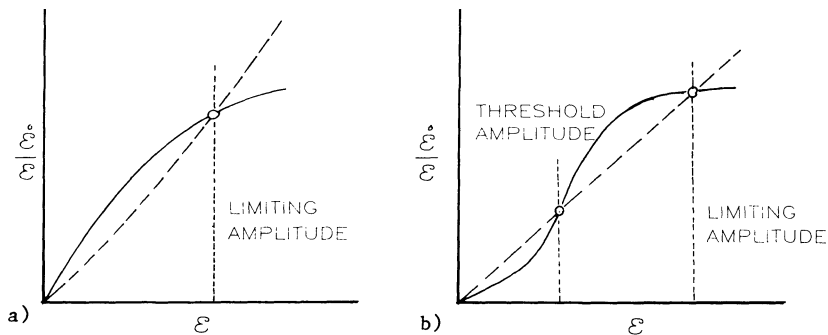


Fig. 5 Acoustic energy relations for nonlinear systems: a) illustration of amplitude limitation imposed by nonlinear aspects of damping and amplification; b) illustration of threshold amplitude (represented through  $\epsilon$ ) and amplitude limiting by nonlinear aspects of damping and amplification.

500 kg of propellant, per second or a chemical energy release rate of about  $3 \times 10^9$  J/s ( $3 \times 10^9$  W). A rocket motor of this thrust would have a combustor cavity approximated by a cylinder 8 m long and 1 m in diameter. The acoustic energy in a severe first axial mode oscillation of 1-MPa peak-to-peak amplitude at 7-MPa mean pressure would be approximately  $10^4$  J. Oscillations of this amplitude are often observed to develop in 10 cycles of oscillation, which would be about 0.10 s in a motor of this size. Thus, the energy gain of the oscillations is about  $10^5$  J/s ( $10^5$  W). While the average audio hi fi fan will recognize this as an incredibly large acoustic power, it is only a minute portion of the  $3 \times 10^9$ -W total power level of the rocket motor. Thus, severe instability can result from very modest flow-induced fluctuations in the combustion rate (0.033% in this example). This comparison may make it a little easier to understand why oscillatory behavior happens and why it can be so destructive.

### III. Gains and Losses

#### A. Processes Contributing to Stability

In the foregoing, reference was made to amplification and damping. There are a number of processes in the motor that contribute to amplification and damping. The most significant are noted below (space does not permit discussion of all in detail). Those processes that are usually amplifying are:

- 1) Dynamic response of combustion to flow disturbances (referred to as "combustion response").
  - 2) Interaction of oscillations with the mean flow.
  - 3) Fluid dynamic "noise" due to vorticity.
- and those processes that are usually damping are:
- 4) Viscous damping at walls.
  - 5) Damping by nonequilibrium of the condensed and vapor phase in the flow.
  - 6) Radiation and convection of the acoustic energy through the nozzle.
  - 7) Absorption of the acoustic energy in the solid propellant and motor structure (via stress waves and oscillatory heat transfer).

The processes that are viewed as sources of amplification can often act as "negative" amplification, depending on the phasing of the oscillations.

In linear stability theory (e.g., Refs. 10 and 11), the various contributions are found to make additive

contributions to growth or decay of oscillations, as

$$p' = P e^{\alpha t} \sin \omega t$$

$$= P (e^{\alpha_1 t} e^{\alpha_2 t} \dots e^{\alpha_7 t}) \sin \omega t \quad (1)$$

$$\alpha = \alpha_1 + \dots + \alpha_7 \quad (2)$$

where  $P$  is the amplitude of the pressure oscillation at time  $t = 0$  and  $e^{\alpha_i t}$  the proportional rate of change of amplitude of the oscillation that would occur if process  $i$  were acting alone. Terms with positive  $\alpha_i$ s are called gains and those with negative  $\alpha_i$ s are "losses"; when  $\alpha > 1$ , the oscillations are growing and the system is unstable. For convenience,  $i$  can be taken to refer to one of the seven contributions listed above.

In most motor instabilities, the behavior is significantly affected by several of the items 1-7, but the relative importance of each can depend strongly on the mode of oscillation, size of motor, type of propellant, etc. This point will be raised repeatedly in a later discussion of the classes and trends of instabilities in motors. For the present, attention will be directed to items 1 and 5. Item 1 is singled out because it is the central feature of combustion instability and item 5 because it is often the dominant source of damping. Between the two, they provide a good insight into the observational features of instability.

### B. Combustion Response

The rocket designer is well aware that the burning rate of the propellant depends on the pressure and the state of the flow near the burning surface. He uses a "burning rate law" such as

$$r = C p^n (1 + k v/a) \quad (3)$$

showing dependence of the rate on pressure ( $p$ ) and velocity ( $v$ ) in the combustor flow. If the conditions were oscillated slowly (e.g., 2 cycles/s), the burning rate would oscillate according to this "steady state" burning rate law. For ordinary propellants, such a combustion response would not cause oscillations to grow.<sup>12</sup>

If the frequency of oscillation is increased progressively, while holding the amplitude constant, burning

rate oscillations will change amplitude and phase because the conditions in the combustion wave will not be able to "keep up." This can easily be appreciated by noting the extreme example of an abrupt depressurization, which is often used to quench burning (even though the final pressure is one at which steady burning is possible). This effect is examined in more detail in the chapter "Transient Burning of Solid Propellants" by Kuo et al. Thus, one cannot expect the burning rate to follow the steady state law at high frequency. Indeed, the combustion zone oscillates in a manner that is frequency dependent, as discussed in the chapter "Theoretical Analysis of Combustion Instability" by Tien. (See also Refs. 12 and 13.) Since one cannot expect to deal rationally with the problem of combustion instability without knowledge of the dynamic response of the combustion to the gas oscillations, a great deal of effort has been devoted to its determination.<sup>14,15</sup> The present status of the problem is still somewhat tenuous, but it is good enough for the purposes of a general understanding of combustion instability and calculating stability trends.

When the gas environment oscillates near the combustion zone, the resulting combustion oscillations are called the "combustion response," usually characterized by the oscillation  $m'$  in the gassification rate of the solid about the mean value  $\bar{m}$ . (See the chapter "Theoretical Analysis of Combustion Instability" by Tien, and Refs. 10, 12, 13 and 16.) This is usually represented in nondimensional form as  $m'/\bar{m}$ , a perturbation mass flow from the surface divided by the mean mass burning rate. The information needed about this "combustion response" is its dependence on the oscillation frequency, amplitude of the flow oscillation, nature of the flow oscillation, mean pressure, propellant composition, etc. The strategies for getting (or assuming) that information are as follows:

1) The amplitude of the combustion response is assumed to be proportional to the amplitude of the gas oscillation, unless there are strong reasons to assume otherwise. Thus,  $m'/\bar{m}$  usually appears as a ratio such as  $(m'/\bar{m})/(p'/\bar{p})$ .<sup>10,12,13,16</sup> When such a quantity is available as a function of frequency, the result is called a "response function."

2) The "nature of the flow oscillations" has to do with the details of how the flow oscillations act on the combustion zone, a question that depends on the structure and scale of the combustion zone and where it is in the mean and oscillatory flowfield in the motor. A simple approach has been widely used to characterize the flow oscillations. It has been assumed that the combustion is localized near the

propellant surface and that its dynamic response can be characterized by two additive contributions, one due to the pressure oscillations and one due to the action of flow oscillations parallel to the burning surface (analogous to the pressure and erosive effects on steady-state burning noted above). The pressure effect is assumed to be the same as that which would result if the pressure oscillation were due to pressure waves perpendicularly incident on the burning surface (with no parallel flow, steady or transient). This corresponds to a one-dimensional representation that is relatively amenable to analytical<sup>13</sup> or experimental<sup>14,15</sup> examination (see the chapter "Theoretical Analysis of Combustion Instability" by Tien). In this context, the "pressure-coupled combustion response function"  $\mathcal{R}_p$  is defined as in the example above,

$$\mathcal{R}_p \equiv \frac{m'_p / \bar{m}}{p' / \bar{p}} \quad (4)$$

A "velocity-coupled combustion response function"  $\mathcal{R}_v$  is then used to represent the response attributable to the component of gas oscillations parallel to the burning surface,

$$\mathcal{R}_v \equiv \frac{m'_v / \bar{m}}{v' / a} \quad (5)$$

In this expression,  $a$  is the velocity of sound in the reaction products and  $v'$  the perturbation in velocity about the parallel component of the mean flow velocity in the region of the acoustic field adjoining the point on the burning surface corresponding to  $m'_v$ . (This definition is of heuristic origin, but a more detailed mechanistic definition has thus far been elusive.<sup>17-19</sup>) In a stability analysis, the burning rate response is then represented as the sum  $(m'_p + m'_v) / \bar{m}$ , which can be represented in terms of the acoustic variables  $p' / \bar{p}$  and  $v' / a$  when  $\mathcal{R}_p$  and  $\mathcal{R}_v$  are known. Since stability depends upon both magnitude  $R$  and phase  $\omega\tau$  of the burning rate oscillations relative to the flow oscillations,  $m'_p$ ,  $m'_v$ ,  $p'$ , and  $v'$  are represented by complex variables. The phase of  $m'$  is usually defined relative to  $p'$ , so the real part of  $\mathcal{R}$ , denoted here by  $\mathcal{R}^r$ , is the component of the mass burning rate in phase with the

pressure. Ordinarily, it is this component of  $\mathcal{R}$  that contributes to stability or instability (see Secs. III.C and III.E and the chapter "Theoretical Analysis of Combustion Instability" by Tien). The phase of  $m'$  relative to  $p'$  is denoted here as  $\omega\tau$ , where  $\tau$  is the time lead of  $m'$ .

3) The frequency dependencies of  $\mathcal{R}_p$  and  $\mathcal{R}_v$  are sought through analytical models and experiments. While not consistent in detail, the results suggest a frequency dependence of  $\mathcal{R}_p$  and  $\omega\tau$  as shown in Fig. 6. The graph shows the response as a function of nondimensional frequency

$$\Omega = \kappa\omega / \bar{r}^2 \quad (6)$$

that relates the frequency to the reciprocal of the relaxation time of the thermal wave in the solid burning surface. Here,  $\kappa$  is the thermal diffusivity of the propellant,  $\omega$  the oscillation frequency (rad/s), and  $\bar{r}$  the mean burning rate.

4) The effect of other variables, such as mean pressure and propellant variables, are encompassed in the burning rate (in  $\Omega$ ) and other parameters in the theory, but experimental determinations are preferred because of the approximate nature of the theory. [Detailed analytical modeling of  $(m'/\bar{m})/(p'/\bar{p})$  is discussed more fully in the chapter "Theoretical Analysis of Combustion Instability" by Tien, including more complete models.]

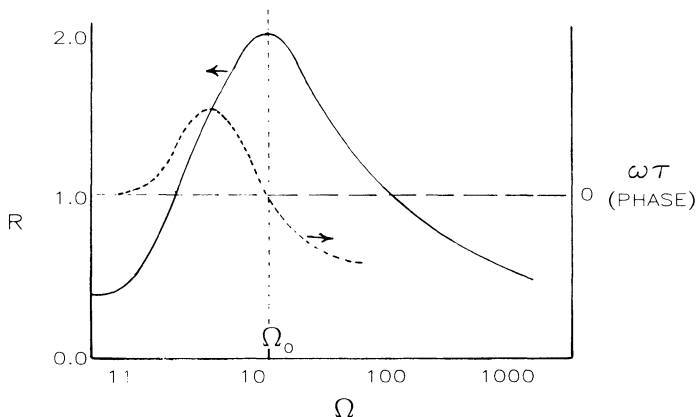


Fig. 6 Response function (solid curve is magnitude and dotted curve is phase relative to pressure).

Table 1 Laboratory burners for measurement of oscillatory combustion

Designation of burner or method	Operational mode	Operational frequency range <sup>a</sup> (Hz)	Propellant requirement	Design objective, advantages and disadvantages	References
<b>Center vented burners</b>					
1. One-dimensional	Self-excited	$10^{-2} \times 10^4$ $4 \times 10^2 - 6 \times 10^3$	Nonaluminized, two flat disks.	Unambiguous measurement of $R_B^r$ , compare propellants. Limited to use where $R_B^r$ is large enough for the burner to self-excite.	14,15,20-22
2. One-dimensional	Pulsed	$10^{-2} \times 10^4$ $2 \times 10^2 - 5 \times 10^3$	Any propellant, two flat disks	Same as above, but for conditions that do not give spontaneous oscillations.	14,15,23-25
3. Extended CVB	Self-excited	$10^{-2} \times 10^4$ $2 \times 10^2 - 4 \times 10^3$	Amount and shape chosen to produce oscillations (more than 1-D burner).	Provide added burning area to obtain spontaneous oscillations under conditions where a 1-D burner will not oscillate. Complicated geometry compromises interpretation of results.	14,15,25-27
4. Pulsed extended CVB	Pulsed	$10^{-2} \times 10^4$ $10^2 - 4 \times 10^3$	Similar to, but less than 3), above.	Use with propellants that yield high loss or low gain for which 2) and 3) are not suitable.	14,15,25,27,28
5. Variable area CVB	Self-excited, pulsed, or combination	$10^{-2} \times 10^4$ $10^2 - 2 \times 10^3$	Similar to 3), except multiple tests required per data point.	Similar to 3) and 4), but depends on different strategy of interpretation of results ("independent" check on test methods).	14,15,21,25, 29-31
6. Velocity coupled CVB	Pressure-coupled driver charge, self-excited or pulsed. May also be used with variable area strategy.	$10^{-2} \times 10^4$ $10^2 - 10^3$	Similar to 3), but with test charges on side walls, driver propellant at ends.	Expose test sample to parallel flow conditions in locations where they can induce velocity-coupled acoustic excitations	14,15,32-37

(Table continued on next page)

Table 1 (cont.) Laboratory burners for measurement of oscillatory combustion

Designation of burner or method	Operational mode	Operational frequency range <sup>a</sup> (Hz)	Propellant requirement	Design objective, advantages and disadvantages	References
<b>Modulated exhaust flow burners</b>					
7. Rotary valve burners	Forced bulk or quasi-steady axial modes. Both pressure- and velocity-coupled versions.	$10^2 - 2 \times 10^3$	Usually a short cylindrical charge, any propellant.	Exhaust modulation provides controlled oscillations in modest burner size, Potential for multiple determinations of response in each test. Provides both magnitude and phase of combustion response. Test apparatus not widely available.	14,15,38-41
8. Modulated nozzle motors	Oscillations forced in axial wave mode by nozzle flow modulation. Both pressure and velocity coupling present.	$10^2 - 2 \times 10^3$	Full length charge, any propellant.	Simulates motor-flow environment and provides controlled longitudinal oscillations and nonlinear aspects of longitudinal modes. Propellant requirement relatively large, limited availability of apparatus.	14,15,42-44
<b>Impedance tube burners<sup>b</sup></b>					
9. Forced oscillation standing wave mode	Oscillating cold gas inflow produces standing wave environment in tube. Pressure- and velocity-coupled version.	$10^2 - 2 \times 10^3$	Any propellant disk (P.C.) and cylinder or slab (V.C.).	Provides controlled mean and oscillatory environment and relatively detailed characterization of oscillatory behavior. Provides both magnitude and phase of combustion response; has potential for multiple measurements per test. Limited availability of apparatus.	14,15,45-48

(Table continued on next page)



Table 1 (cont.) Laboratory burners for measurement of oscillatory combustion

Designation of burner or method	Operational mode	Operational frequency range <sup>a</sup> (Hz)	Propellant requirement	Design objective, advantages and disadvantages	References
<b>Bulk-mode self-excited burners</b>					
10. L* burner	Self-excited	5 - 3x10 <sup>2</sup> 2x10 - 2x10 <sup>2</sup>	Any propellant, not all will oscillate. Amount small, depends on burner size.	Low cost method to study low frequency instability, elucidates class of instability exhibited by some low L motors. Will oscillate only at low pressures. Mean pressure and frequency difficult to control.	22,49-51
11. Helmholtz	Self-excited	5 - 3x10 <sup>2</sup> 2x10 - 2x10 <sup>2</sup>	(Same as above.)	Similar to 10, but range of conditions for spontaneous oscillations is less limited.	22,52
<b>Direct measurement methods</b>					
12. Microwave	Forced bulk mode oscil., time-resolved measurement of burning surface regressions.	0 - 2x10 <sup>3</sup> 10 - 10 <sup>3</sup>	Any propellant, small sample (strand).	Provides controlled pressure environment and direct measurement of pressure-coupled oscillatory burning rate. Provides magnitude and phase of combustion oscillation, continuous scan of frequency range, does not depend on back calculation from acoustic behavior. Limited availability of apparatus.	14,15,55,56
13. Other	Various	Various	Small sample.	Various methods of inducing combustion oscillations and measuring them.	57-59

<sup>a</sup>First-listed frequency range is approximate practical limit; second-listed frequency range is usual operational range.

<sup>b</sup>The impedance tube approach could be used in any standard wave mode burner, but has been developed only in classical forced-oscillation impedance tube configuration.

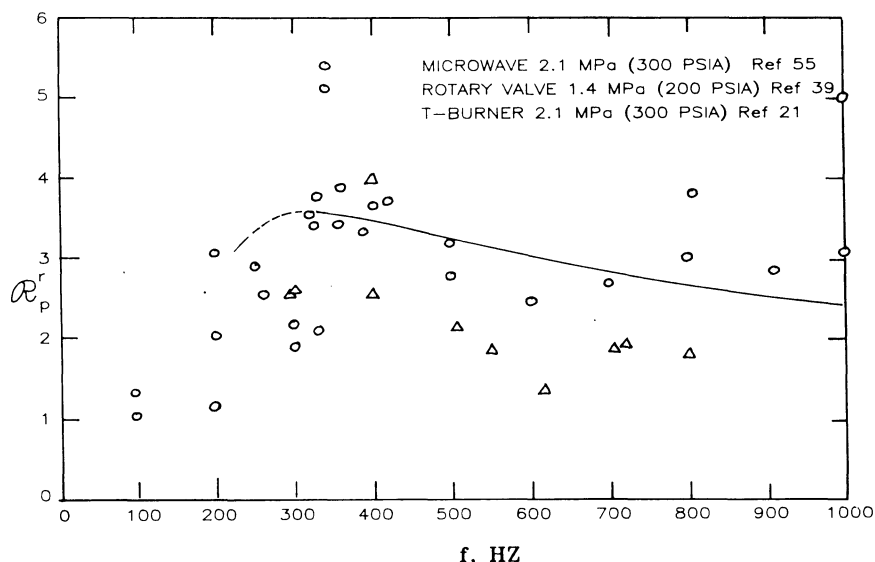


Fig. 7 Values of the pressure-coupled response function (in-phase component) measured by different methods (A-13 composite propellant).

### C. Measuring Combustion Response

The measurement of combustion response functions has been attempted by a variety of methods summarized in Table 1. Space will not permit extensive discussion of these methods here (see Refs. 10, 14, and 15) and it is unlikely that a consensus could be reached at present as to their relative merits. In limited comparisons, qualitative agreement is shown among some methods (e.g., Fig. 7). The most extensively used and evaluated method is a center-vented unstable burner (Fig. 8), commonly referred to as the "T-burner."<sup>+</sup> This burner will be discussed in some detail here, not only because of its extensive use (roughly 40,000 firings), but also because it is helpful in understanding unstable rocket motors. The design is well suited for inducing pressure-coupled combustion response, and modified designs have been used to produce velocity-coupled response. Because the method depends upon the spontaneous generation

<sup>+</sup>Since this name was acquired for reasons extraneous to the normal design or use of the burner, the more descriptive title "center-vented" or CV burner will be used here.

of oscillations, it is not well suited to measurements on aluminized propellants or to the low frequencies at which aluminized propellants are sometimes unstable. Modified versions have been used for those applications that induce oscillations, either by pulsing or by using more complex geometries that extend the domain of spontaneous oscillations (at the expense of the loss of one-dimensionality).

The arrangement in the basic one-dimensional center-vented (CV) burner<sup>10,14,15,21</sup> is shown in Fig. 8. The burner is usually connected to a surge tank that is prepressurized with nitrogen to the desired mean pressure. When the propellant disks are ignited, the propellant reaction products flush the cold nitrogen from the burner and oscillations develop and grow with exponentially increasing amplitude (Fig. 9) until nonlinear effects limit the amplitude. Particular care is exercised to assure that all propellant surfaces burn out at once. When the propellant burns out, the oscillations decay in a roughly exponential manner. In the simplest use of the center-vented burner, it is assumed that the damping is the same during the period of growing oscillations as the period of decaying oscillations, given by the observed decay rate of oscillations. Then, the initial growth rate of oscillations is the sum of a combustion contribution and the measured damping contribution; hence

$$\alpha_c = \alpha_g + \alpha_d$$

where  $\alpha_d$  is negative and  $\alpha_g$  and  $\alpha_d$  are measured from the test record (Fig. 9) or computer processing of digitized pressure-time data. The quantity  $\alpha_c$  reflects the combustion contribution to oscillations and can be determined over a range of frequencies by testing in different length burners. If one is interested in comparing propellants, a direct

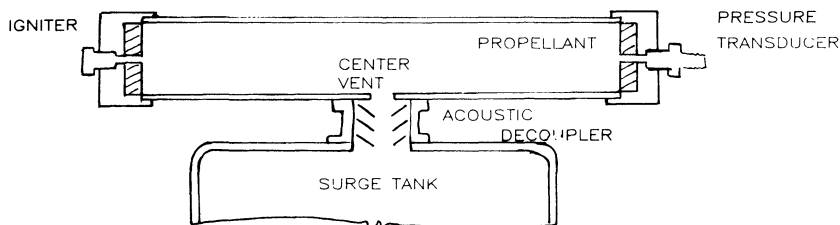


Fig. 8 Schematic arrangement of end-burning center-vented burner.

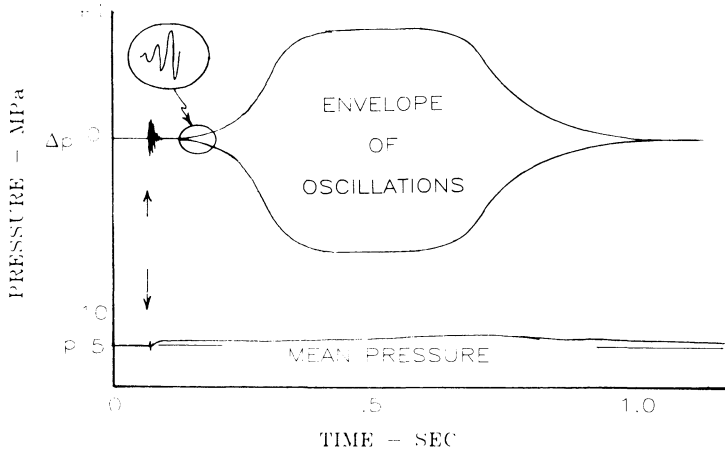


Fig. 9 Pressure-time history for a center-vented burner test. Upper trace results from filtering out dc component and amplifying pressure signal. Lower trace results from filtering out oscillations, shows slight pressure rise above surge tank, and rise in surge tank pressure during test.

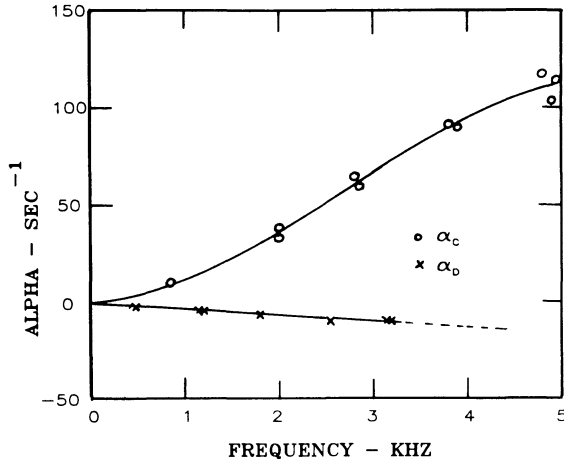


Fig. 10 Combustion alpha and decay alpha from tests in center-vented burners of type shown in Fig. 8.

comparison of  $\alpha_c$  vs frequency is often instructive (Fig. 10).<sup>60</sup> If one wants the results in a form that can be inserted in motor stability analyses, the equivalent pressure-coupled response functions must be determined. This amounts to construction of a stability analysis of the CV burner and solving for  $R^f$  in terms of the measured

quantities of  $\alpha_g$  and  $\alpha_d$ .<sup>10,14,21</sup> An approximate analysis results in the relation

$$\mathcal{R}_p^r \equiv \left( \frac{\bar{m}' / \bar{m}}{\bar{p}' / \bar{p}} \right)^r$$

$$\mathcal{R}_p^r = \frac{1}{\gamma \bar{M}_b} \frac{a_o}{a_b} \frac{S_c}{S_b} \frac{\alpha_g - \alpha_d}{4f} \quad (7)$$

where

- $\mathcal{R}_p^r$  = magnitude of the in-phase component (real part) of the oscillatory response of burning rate to pressure oscillation about the mean values
- $\bar{M}_b$  = mean Mach number of flow out of the combustion zone
- $a_o$  = average velocity of sound in the burner as indicated by the frequency ( $a_o = 2L/\tau_\omega$ ) =  $2Lf$
- $a_b$  = velocity of sound just outside the combustion zone (at the adiabatic flame temp.)
- $S_c$  = cross-sectional area of burner
- $S_b$  = burning area of propellant ( $S_c/S_b \approx 1/2$ ) for double-end burning CV burner
- $f$  = frequency of oscillation (Hz) =  $1/\tau_\omega = (\omega/2\pi)$

For quantitative results, the calculation is somewhat more complicated, even in this simple burner,<sup>21,25</sup> but Eq. (7) is often suitable for examining the effects of the systematic variations in propellant formulation designed to study or prevent instability. Repeat tests on the same propellant in different burner lengths provide  $\mathcal{R}_p^r$  vs frequency and further tests can provide such functions<sup>p</sup> over a range of pressures (see Fig. 11 and Ref. 61).

There are a number of problems with the interpretation of the results of CV burner tests, originating in the fact that the response function must be extracted from pressure oscillations that are subject to a variety of other influences, that are not accurately modeled and/or measured for the calculations of  $\mathcal{R}_p^r$ . However, the results show response function curves that are qualitatively consistent with theory and also show well-defined differences according to the propellant used. While the magnitudes of the values of  $\mathcal{R}_p^r$  calculated from the tests have only modest accuracy, comparisons among propellants are often more accurate because some of the poorly known parameters in the analysis can be insensitive to the propellant variables involved in the comparison.

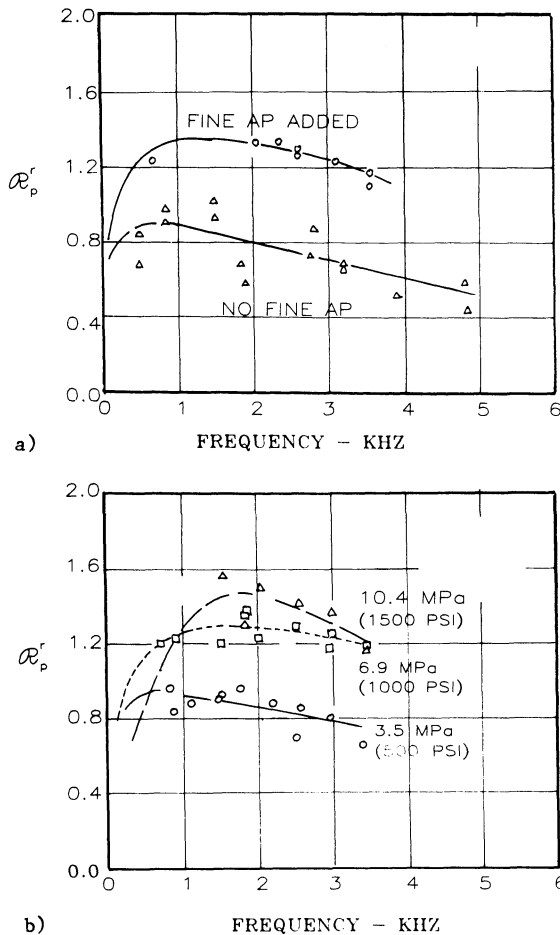


Fig. 11 Response functions as measured by the double ended, center-vented burner method, AP-HTPB propellants: a) effect of propellant change, both propellants have the same burning rate: the one with no fine AP has a burning rate catalyst; b) effect of pressure.

There are a number of variants on the basic CV burner, noted in Table 1, that are used to:

- 1) Extend the domain of applicability of the method (e.g., to lower frequency, to aluminized propellants).
- 2) Provide an alternative means of measuring  $\alpha_c$  and  $\alpha_d$ .
- 3) Allow examination of other features of combustion, such as  $R_v$ .
- 4) Permit study of the nonlinearly initiated instability depicted in Fig. 5b.<sup>11,27</sup>

## Chapter 14

# Theoretical Analysis of Combustion Instability

James S. T'ien\*

*Case Western Reserve University, Cleveland, Ohio*

### Abstract

A theoretical analysis of combustion instability in a solid rocket combustion chamber is presented in a tutorial manner. The contents include the conservation equations for wave motion in the combustor and a small perturbation analysis to study wave amplification, damping and the modes of oscillation. Models describing the solid propellant burning response to an oscillating pressure are described in detail. The acoustic damping caused by the nozzle flow and by particle velocity lag is reviewed. Examples of computations of the linear stability boundaries are given. Nonacoustic and nonlinear oscillations are discussed.

### Nomenclature

$a$	= speed of sound
$A$	= parameter in propellant response function defined in Eq. (50)
$A_t$	= nozzle throat area
$\tilde{A}_1, A_2$	= defined in Eq. (10)
$B$	= parameter in propellant response function defined in Eq. (48)
$\tilde{C}$	= defined in Eq. (22)
$D$	= diameter of combustor
$\tilde{D}$	= defined in Eq. (23)
$e$	= internal energy

---

Copyright © American Institute of Aeronautics and Astronautics, Inc., 1983. All rights reserved.

\*Professor of Engineering, Department of Mechanical and Aerospace Engineering.

$e_o$	=	$e + V^2/2$
E	=	activation energy
f	=	frequency
H	=	nondimensional propellant surface heat release defined in Eq. (40)
i	=	$\sqrt{-1}$
k	=	proportional constant between slip velocity and force on a particle in Stoke's flow
L	=	combustor length or combustor characteristic dimension
m	=	propellant pyrolysis exponent defined in Eq. (44)
M	=	Mach number
n	=	steady burning pressure exponent
p	=	pressure
P	=	nondimensional pressure defined in Eq. (40)
$Q_s$	=	solid propellant surface heat release
$r_s$	=	propellant burning rate
R	=	nondimensional burning rate defined in Eq. (40)
Re	=	real part
s	=	$\lambda + i\omega$
S	=	entropy
t	=	time
u	=	axial velocity
V	=	velocity
x	=	distance
X	=	nondimensional distance defined in Eq. (40)
Y	=	acoustic admittance defined in Eq. (18)

### Greek Symbols

$\alpha$	=	thermal diffusivity
$\beta$	=	ratio of solid thermal time to chamber wave travel time = $(\alpha_s / \bar{r}^2) / (L / \bar{a})$
$\gamma$	=	ratio of specific heats
$\delta$	=	phase angle between pressure and velocity oscillations or nondimensional gas residence time defined in Eq. (66)
$\epsilon$	=	acoustic energy density defined in Eq. (7)
$\zeta$	=	temperature ratio defined in Eq. (56)
$\theta$	=	nondimensional temperature defined in Eq. (40)
$\lambda$	=	heat conduction coefficient or wave amplification coefficient
$\mu$	=	coefficient of viscosity



$\xi$	=	temperature ratio defined below Eq. (62)
$\rho$	=	density
$\sigma$	=	dimensionless radius or dimensionless frequency defined by Eq. (60)
$\sigma_p$	=	steady-state burning rate-pressure sensitivity
$\sigma_T$	=	steady-state burning rate-temperature sensitivity
$\Sigma$	=	ratio of gas residence time in the flame to solid thermal time = $(l/\bar{u}_\infty)/(\alpha_s/r^2)$
$\tau$	=	nondimensional time defined in Eq. (40)
$\phi$	=	heat flux
$\Phi$	=	nondimensional heat flux
$\omega$	=	nondimensional frequencies (by various time scales)
$\Omega$	=	$\beta\omega$

### Script Symbols

$\mathcal{A}$	=	nozzle pressure-sensitive acoustic admittance coefficient, see Eq. (58)
$\mathcal{B}$	=	nozzle radial-velocity acoustic admittance coefficient, see Eq. (58)
$\mathcal{C}$	=	nozzle entropy acoustic admittance coefficient, see Eq. (58)
$\mathcal{L}$	=	gas flame length
$\mathcal{R}$	=	gas constant
$\mathcal{V}$	=	volume
$\mathcal{Y}$	=	acoustic admittance defined in Eq. (19)

### Superscripts

—	=	steady state
$\rightarrow$	=	vector
'	=	perturbation quantity
-	=	nondimensional quantities defined using Eqs. (20) and (21)

### Subscripts

b	=	propellant burning surface
f	=	flame
g	=	gas phase
i	=	imaginary part
p	=	particulate
R	=	real part
s	=	solid or solid surface
$\infty$	=	gas flame edge
$\perp$	=	perpendicular component to the surface
$\parallel$	=	parallel component to the surface

## I. Introduction

The purpose of the theoretical analysis is to quantify many of the important features of combustion instability described in the last chapter. This calls for the mathematical formulation of the oscillatory gasdynamic processes in the combustion chamber and near the combustor boundaries which pump in or take out the acoustic energy from the bulk gas. The physicochemical processes and the associated fluid mechanical problems are normally extremely complex. In order to make the analysis amenable to solution, many simplifying assumptions will be made in the following presentation, but the essential features of combustion instability will be retained.

When the amplitude is small, an oscillation is often approximately sinusoidal in time. When the amplitude is greater, departure from sinusoidal oscillations will occur. A large amplitude oscillation can grow out of a small amplitude one or can be triggered by a finite size disturbance. The determinations of the limiting oscillation amplitude and the possibility of triggering are clearly nonlinear problems. But the problem of incipient oscillation is a linear one. The small amplitude linear analysis is capable of determining the frequency of oscillation, the initial amplitude growth rate and the neutral stability boundary. If the perturbation method is used, the linear analysis also serves as the starting point of the nonlinear calculation. Because of the generality of its results, a great portion of the present chapter is devoted to the linear analysis.

In addition to the combustor acoustic analysis, the amplification and damping from the boundaries of the acoustic cavity are important. The solid propellant combustion response as a source of acoustic amplification is discussed in some detail. On the other hand, the nozzle acoustic response is only briefly mentioned, since the material has been extensively covered elsewhere. Other sections of this chapter cover the nonacoustic and nonlinear analyses.

Historically, many capable people have worked on combustion instability problems and there is an abundant number of references. Many of the works, such as acoustic analysis and nozzle admittance, are not specifically for solid rockets, but they are generally applicable to solid rocket application. It will not be practical in this chapter to cover all the relevant materials on the theoretical aspect of solid propellant combustion instability, but we hope the cited references can provide a more complete picture. A number of papers published by the Proceedings of CPIA (ICRPG), unfortunately, are not cited here because they are not available to the public.

There are several reference books or book chapters on combustion instability. The book by Crocco and Cheng<sup>1</sup> represents the classical work on combustion instability. Reference 2 gives a very complete description on liquid rocket combustion instability. Chapter 10 of Ref. 3 by Williams dealt with solid rocket combustion instability theory, and the recent publication by Culick<sup>4</sup> covers many up-to-date theoretical and applied aspects of solid rocket instability and is quite unique in its style of presentation.

## II. Linear Analysis of Wave Motion

### II.A. Governing Equations

In this section, the governing equations appropriate for wave analyses in the combustion chamber will be presented. The formulation of these equations follows Ref. 4, 8, and 9 by assuming that the fluid consists of a mixture of gas and condensed-phase particles of uniform size (in a solid rocket, a typical kind of solid particle is the aluminum oxide). The flow will be assumed to be inviscid and non-heating-conducting except between the gas and the particulate. The gases are assumed homocompositional, and thermally and calorically perfect.

With these assumptions, the conservation equations are conservation of mass:

$$\begin{aligned} \frac{\partial \rho}{\partial t} + \nabla \cdot (\rho \vec{V}) &= W_p \\ &= - \frac{\partial \rho_p}{\partial t} - \nabla \cdot (\rho_p \vec{V}_p) \end{aligned} \quad (1)$$

conservation of momentum:

$$\begin{aligned} \rho \frac{\partial \vec{V}}{\partial t} + \rho \vec{V} \cdot \nabla \vec{V} + \nabla p &= \vec{F} \\ &= - \rho_p \frac{\partial \vec{V}_p}{\partial t} - \rho_p \vec{V}_p \cdot \nabla \vec{V}_p + W_p (\vec{V}_p - \vec{V}) \end{aligned} \quad (2)$$

conservation of energy:

$$\begin{aligned} \frac{\partial}{\partial t} (\rho e_o + \rho_p e_{p_o}) \\ + \nabla \cdot (\rho \vec{V} e_o + \rho_p \vec{V}_p e_{p_o}) + \nabla \cdot (\rho \vec{V}) &= Q \end{aligned} \quad (3)$$

and

$$\rho_p \frac{\partial e_p}{\partial t} + \rho_p \vec{V}_p \cdot \nabla e_p = - Q_p \quad (4)$$

where  $\rho_p$  is the mass of particulates per unit chamber volume;  $R_{W_p}$  is the mass consumption rate per unit volume for the particulates; and  $\vec{F}$  is the force per unit volume exerted on the gas due to the momentum exchange with the particles. If the Reynolds number based on the slip-flow velocity is small, Stokes' formula can be used and

$$\frac{\partial \vec{V}_p}{\partial t} + \vec{V}_p \cdot \nabla \vec{V}_p = k (\vec{V} - \vec{V}_p) \quad (5)$$

from Eqs. (2) and (5) it is seen that

$$\vec{F} = (W_p + k\rho_p) (\vec{V}_p - \vec{V}) \quad (6)$$

the quantity  $Q_p$  is heat exchanged between the two phases, and  $Q$  is the rate of energy released in gas-phase chemical reactions.

With the equation of state and the proper rate expressions for  $W_p$ ,  $Q$ , and  $Q_p$ , the above system [Eqs. (1-6)] is completely specified and will be used in the acoustic analysis in the following sections.

## II. B. Acoustic Energy in a Sound Field

The growth and decay of the energy contents associated with a small amplitude oscillation in a cavity is directly related to combustion instability. The energy density of a flow is  $\epsilon + V^2/2$ . Perturbing this around the steady state and recognizing that small amplitude oscillation is isentropic in nature, the acoustic energy density is found to be<sup>11</sup>

$$\epsilon = \frac{1}{2} \frac{1}{\bar{\rho} \bar{a}^2} p'^2 + \frac{1}{2} \bar{\rho} V'^2 \quad (7)$$

In deriving the above expression, it is assumed that the maximum Mach number of the mean flow is much smaller than unity and that terms of the order of Mach number are neglected compared with terms of the order one. The terms involving first-order perturbation quantities are not included because their average value is zero. The acoustic energy given by Eq. (7) is second order in amplitudes.

To derive an expression for the time rate of change of  $\epsilon$ , Eq. (2) is written as

$$\rho \frac{\partial \vec{V}}{\partial t} + \nabla p = \vec{A}_1 \quad (8)$$

Equations (1-4) can be combined to yield

$$\frac{\partial p}{\partial t} + \rho \gamma \nabla \cdot \vec{V} = A_2 \quad (9)$$

where

$$\begin{aligned} \vec{A}_1 &= \vec{F} - \rho \vec{V} \cdot \nabla \vec{V} \\ A_2 &= -\vec{V} \cdot \nabla p + R/C_v [-\vec{V} \cdot \vec{F} + (Q + Q_p) \\ &\quad + (e_{p0} - 1/2 V^2) W_p] \end{aligned} \quad (10)$$

Seeking first-order perturbation equation in amplitude, the dependent variables are expanded as follows:

$$\begin{aligned} p &= \bar{p} + p' & \rho &= \bar{\rho} + \rho' & \vec{V} &= \bar{\vec{V}} + \vec{V}' \\ |p'/\bar{p}| &\ll 1 & |\rho'/\bar{\rho}| &\ll 1 & |\vec{V}'| &\ll \bar{a} \end{aligned} \quad (11)$$

The perturbation equations for Eqs. (8) and (9) are

$$\bar{\rho} \frac{\partial \vec{V}'}{\partial t} + \nabla p' = \vec{A}_1' \quad (12)$$

$$\frac{\partial p'}{\partial t} + \gamma \bar{p} \nabla \cdot \vec{V}' = A_2' - \gamma p' \nabla \cdot \bar{\vec{V}} \quad (13)$$

Multiplying Eq. (12) by  $1/\gamma(p'/\bar{p})$  and Eq. (13) by  $\vec{V}' \cdot$  and adding the two equations, we have

$$\frac{\partial \epsilon}{\partial t} + \nabla \cdot (p' \vec{V}') = I' \quad (14)$$

where

$$I' \equiv (1/\gamma) (p'/\bar{p}) (A_2' - \gamma p' \nabla \cdot \bar{\vec{V}}) + \vec{A}_1' \cdot \vec{V}'$$

Equation (14) can be thought of as the conservation equation for acoustic energy. Integrating Eq. (14) over the cavity volume, we get

$$\frac{\partial}{\partial t} \int_V \epsilon dV = \int_S p' \vec{V}' \cdot \vec{n} dS + \int_V I' dV \quad (15)$$

where  $\vec{n}$  is the inward unit normal vector on the surface  $S$  enclosing the volume  $\mathcal{V}$ . Clearly the first term on the right hand side of Eq. (15) represents the rate of work done to the system in volume  $\mathcal{V}$  by the surrounding through the boundary. The second term represents the rate of energy addition (if positive) or subtraction (if negative) through processes occurring in the interior of the control volume. From the definition of  $I'$ , we see that these processes include the effects of mean flow, the viscous damping due to the relative motion of the particulates and gases, the gasification or the combustion of the particulates, the heat exchange between the particle and gas, and the residue homogeneous phase combustion. If the particle gasification rate  $W_p$  is small compared with the mass addition rate from the boundary, or if  $W_p$  is well distributed in the combustor, then the magnitude of  $I'$  is smaller than that of acoustic energy  $\epsilon$  by  $O(M)$ , where  $M$  is the maximum mean flow Mach number in the combustor. It will also be shown later that under many practical situations, the surface work represented by the first term on the right-hand side of Eq. (15) is also smaller than  $\epsilon$  by  $O(M)$ . Therefore when the mean flow Mach number is much smaller than unity, Eq. (14) represents a system where the growth or the decay of the acoustic energy is only slight in one period of oscillation. This observation will be utilized in the analysis to be given later.

### II.C. Acoustic Admittance Function

The first term on the right-hand side of Eq. (15) is the rate of work done to the gas in the combustor through the surface of the control volume. Normally this control volume is drawn along the propellant surface and the nozzle entrance plane; therefore important contributions of the propellant burning and the nozzle flow to combustion instabilities are contained in this term.

For a simple harmonic oscillation, we can write

$$p' = \Delta p \cos \omega t = \text{Re} (\Delta p e^{i\omega t})$$

$$V_{\perp}' = \Delta V_{\perp} \cos (\omega t + \delta) = \text{Re} (\Delta V_{\perp} e^{i\delta} e^{i\omega t}) \quad (16)$$

where  $\Delta p$  and  $\Delta V_{\perp}$  are the amplitudes of the pressure and velocity oscillations at the surface; subscript  $\perp$  means the velocity component normal to the surface;  $\delta$  is the phase angle between the velocity and pressure oscillations; and

Re indicates the real part of the complex variable. Using Eq. (16) we get

$$p' \vec{V}' \cdot \vec{n} = p' V_{\perp}' = \Delta p \Delta V_{\perp} \cos \omega t \cos (\omega t + \delta)$$

the time average over one cycle is

$$\langle p' V_{\perp}' \rangle = 1/2 (\Delta p) (\Delta V_{\perp}) \cos \delta \quad (17)$$

Thus acoustic amplification from the surface occurs when the phase angle is between  $\pi/2$  and  $-\pi/2$  and is the maximum when the pressure and velocity oscillations are exactly in phase. On the other hand, when  $\delta$  is between  $\pi/2$  and  $3\pi/2$ , acoustic damping results.

The wave amplification and damping capability is conventionally expressed by the complex surface acoustic admittance function defined by

$$Y = \frac{V_{\perp}' / \bar{V}_{\perp}}{p' / \bar{p}} \quad (18)$$

Using the complex representation given by Eq. (16), we have

$$Y = \left[ \frac{\Delta V_{\perp} / \bar{V}_{\perp}}{\Delta p / \bar{p}} \right] e^{i\delta}$$

In comparison with Eq. (17), the real part of the acoustic admittance is proportional to  $\langle p' V' \rangle$ . Thus acoustic amplification occurs when the real part of  $Y$  is positive and the amplification power is proportional to the magnitude of the acoustic admittance function. A very important part of the combustion instability analysis is the calculation of acoustic admittances for the propellants and the nozzles.

In the acoustic analysis of the combustor in the next section, the velocities are nondimensionalized using the steady-state speed of sound. Thus an alternative definition of the acoustic admittance is given by

$$\gamma = \frac{V_{\perp}' / \bar{a}}{p' / \bar{p}} \quad (19)$$

The relation between  $Y$  and  $\mathcal{Y}$  is

$$\mathcal{Y} = (\bar{V}_\perp / \bar{a}) Y = M_\perp Y$$

where  $M_\perp$  is the Mach number based on the perpendicular velocity at the boundary. The above equation shows that when  $Y$  is of the order of unity,  $\mathcal{Y}$  is of the order of Mach number.

## II.D. Linear Analysis

Introducing nondimensional variables:

$$\tilde{t} = t / (L / \bar{a}) \quad \tilde{\nabla} = L \nabla \quad (20)$$

where  $L$  is a characteristic dimension of the combustor, and looking for solution of the type

$$p' / \bar{p} = \tilde{p} e^{s \tilde{t}} \quad \tilde{V}' / \bar{a} = \tilde{V} e^{s \tilde{t}} \quad (21)$$

where  $s = \lambda + i\omega$ ,  $\lambda$  is the wave amplification coefficient, and  $\omega$  the frequency of oscillation, then Eq. (12) becomes

$$s \tilde{V} + (1/\gamma) \tilde{\nabla} \tilde{p} = \tilde{C} \quad (22)$$

where

$$\tilde{A}_1' L / \bar{\rho} \bar{a}^2 = \tilde{C} e^{s \tilde{t}}$$

and Eq. (13) becomes

$$s \tilde{p} + \gamma \tilde{\nabla} \cdot \tilde{V} = \tilde{D} \quad (23)$$

where  $(A_2' - \gamma p' \nabla \cdot \tilde{V}) L / \bar{p} \bar{a} = \tilde{D} e^{s \tilde{t}}$ . For a given combustion chamber geometry and boundary conditions, Eqs. (22) and (23) can, in principle, be solved. However, the following alternative procedure provides more physical insight into the problem and reduces the degree of algebraic complexity. Examination of the inhomogeneous terms in Eqs.

(22) and (23) indicates that the leading terms in  $\tilde{C}$  and  $\tilde{D}$  are of the order of the maximum Mach number based on the steady gas flow or the particulates velocities, which is a quantity much smaller than unity in most applications. In addition, from the propellant and nozzle acoustic admittance



functions it will be shown that under near-resonance conditions,  $\gamma$  at the boundaries is of the order of flow Mach number (Sec. III and IVB). Thus an expansion scheme using the flow Mach number as the expansion parameter is suggested. This procedure is not required for the solution for the system [Eqs. (22) and (23)] which is already linear. Instead, it merely shows more clearly the connection between combustion instability and classical acoustic oscillations. Let

$$\begin{aligned}\tilde{p} &= p_0 + p_1 + p_2 + \dots \\ \tilde{\vec{V}} &= \vec{V}_0 + \vec{V}_1 + \vec{V}_2 + \dots \\ \tilde{\vec{C}} &= \vec{C}_1 + \vec{C}_2 + \dots \\ \tilde{D} &= D_1 + D_2 + \dots \\ s &= s_0 + s_1 + s_2 + \dots\end{aligned}\quad (24)$$

where terms with subscript zero are of the order of unity, and terms with subscript 1 are of the order of maximum mean flow Mach number, etc. The quantity  $s$  is also expanded in Mach number, since the frequency of oscillation is expected to be modified by the presence of the mean flow. Substituting Eq. (24) into Eqs. (22), (23) and the associated boundary conditions, we get for the order one system:

$$\begin{aligned}s_0 \vec{V}_0 + \frac{1}{\gamma} \tilde{\nabla} p_0 &= 0 \\ s_0 p_0 + \gamma \tilde{\nabla} \cdot \vec{V}_0 &= 0 \\ \vec{V}_0 &= 0 \text{ (on the boundary)}\end{aligned}\quad (25)$$

The above system represents an eigenvalue problem for the classical acoustic oscillation in a cavity with rigid walls. The two equations can be combined to form a Helmholtz equation which represents the spatial part of the wave equation without a mean flow. The eigenvalue  $s_0$  can be

shown to be purely imaginary, i. e.,  $s_0 = i\omega_0$ , where  $\omega_0$ 's are the natural frequencies of the acoustic modes. The system corresponding to order Mach number is

$$s_0 \vec{V}_1 + \frac{1}{\gamma} \vec{\nabla} p_1 = \vec{C}_1 - s_1 \vec{V}_0$$

$$s_0 p_1 + \gamma \vec{\nabla} \cdot \vec{V}_1 = D_1 - s_1 p_1$$

$$\vec{V}_1 \cdot \vec{n} = \gamma p_0 \quad (\text{on the boundary}) \quad (26)$$

The solution of Eq. (26) provides the first-order correction to the solution of Eq. (25), which represents a neutral oscillation. In particular,  $s_1 (= \lambda_1 + i\omega_1)$  will be determined. Here,  $\lambda_1$  is the leading term of the wave amplification coefficient. Thus the solution of Eqs. (25) and (26) yields information on the wave mode (not amplitude), oscillation frequency, and amplification coefficient. Alternatively, this information can be used to determine the neutral stability boundaries on a map of propellant or operating parameters.

The actual solution of Eqs. (25) and (26) depends on the combustion chamber geometry. For simple configurations such as cylindrical and annular shapes, analytical solutions for three-dimensional problems can be found by using eigenfunction expansion<sup>8</sup> or Green's function.<sup>4, 12</sup> For more complicated geometry, numerical solution may be necessary. In the present chapter, for illustrative purposes, computation will be performed only for the simplest configuration, i. e., an end-burning solid rocket undergoing longitudinal mode oscillation. The gasification rate of the particulates  $\dot{W}_p$ , the rate of heat exchange between the two phases  $\dot{Q}_p$ , and the gas-phase energy release  $\dot{Q}_g$  are all assumed zero, and the particulate volume density is assumed constant. In such a case, Eq. (25) is reduced to

$$s_0 u_0 + \frac{1}{\gamma} \frac{dp_0}{d\tilde{x}} = 0$$

$$s_0 p_0 + \gamma \frac{du_0}{d\tilde{x}} = 0$$

$$u_0 = 0 \quad (\text{at } \tilde{x} = 0 \text{ and } 1) \quad (27)$$

The solution of the above equation is

$$\begin{aligned} p_o &= P_{oo} \cos \omega_o \bar{x} \\ u_o &= -i (P_{oo}/\gamma) \sin \omega_o \bar{x} \\ s_o &= i \omega_o = ij\pi, \quad j = 1, 2, \dots \end{aligned} \quad (28)$$

This corresponds to a standing longitudinal wave in a tube with rigid ends. The oscillation frequency is  $\omega_o$ , where  $j = 1$  corresponds to the fundamental mode and  $j = 2, 3, \dots$  corresponds to the second, third harmonics, etc.

Note also that the velocity oscillation  $u_o$  and the pressure oscillation  $p_o$  are 90 deg out of phase. In the lowest-order solution given by Eq. (28), the oscillation is neutral, i.e.,  $s_o$  is purely imaginary and the amplification coefficient  $\lambda_o$  is zero. For the correction to the next order of the Mach number, Eq. (26) becomes

$$\begin{aligned} s_o u_1 + \frac{1}{\gamma} \frac{dp_1}{d\bar{x}} &= -\tilde{k} (u_o - u_{po}) - M \frac{du_o}{d\bar{x}} - s_1 u_o \\ s_o p_1 + \gamma \frac{du_1}{d\bar{x}} &= -M \frac{dp_o}{d\bar{x}} - s_1 p_o \\ u_1 &= \mathcal{Y} p_o \quad \text{at } \bar{x} = 0 \quad u_1 = -\mathcal{Q} p_o \quad \text{at } \bar{x} = 1 \end{aligned} \quad (29)$$

where  $\mathcal{Y}$  and  $\mathcal{Q}$  are the propellant and the nozzle acoustic admittance functions, respectively. It can be shown, by perturbing Eq. (5), that  $u_{po} = 0$ , i.e., the particle velocity is not disturbed to the first order of the oscillation amplitude and the mean flow Mach number. Substituting this result and Eq. (28) into Eq. (29), Eq. (29) can be solved for  $s_1$ , i.e.,

$$s_1 = \gamma(\mathcal{Y} + \mathcal{Q}) - \tilde{k}/2 \quad (30)$$

Separating the above expression into real and imaginary parts, we get

$$\begin{aligned} \lambda_1 &= \gamma(\mathcal{Y}_R + \mathcal{Q}_R) - \tilde{k}/2 \\ \omega_1 &= \gamma(\mathcal{Y}_I + \mathcal{Q}_I) \end{aligned} \quad (31)$$

where subscripts R and I represent real and imaginary parts, respectively. It can be seen from the above equation that the imaginary parts of the acoustic admittance functions provide a higher order (in M) correction to the oscillating frequency due to non-rigid-wall boundary conditions, while the real parts of the acoustic admittance functions and the nondimensional drag coefficient  $\tilde{k}$  determine the value of the amplification coefficient  $\lambda_1$ . Since a positive  $\lambda_1$  implies wave amplification, positive values of the real parts of the propellant and nozzle admittance functions contribute to destabilizing effects, while negative values contribute to stabilization. The particle drag is always stabilizing. It can also be shown by direct substitution of Eqs. (28) and (31) into Eq. (15) that

$$\frac{1}{\langle \epsilon \rangle} \frac{\partial}{\partial t} \int_V \langle \epsilon \rangle dV = 2\lambda_1 \quad (32)$$

The above equation is, in general, valid for more complicated three-dimensional situations, as shown by Culick,<sup>4,12</sup> Computations leading to Eqs. (28) and (31) for more complicated cases can be found in Crocco,<sup>9</sup> Culick,<sup>4-7,12</sup> and Sirignano,<sup>8</sup> for example.

The linear analysis presented so far is based on the expansion scheme given by Eq. (24). The basic assumption required, in addition to the small amplitude, includes that the maximum Mach number (gas flow and particulate) is much smaller than unity and that the surface acoustic admittance functions ( $\gamma$  and  $\alpha$ ) are of the order of Mach number. In such a case, the oscillation is close to the classical acoustic vibration with the lowest order frequency given by  $\omega_0$ . The leading term of amplification coefficient is given by  $\lambda_1$ , which is one order of magnitude (in M) smaller than  $\omega_0$ . Therefore significant wave amplification or decay will occur only over a number of cycles. When the acoustic admittance functions are of the order of Mach number, the velocity perturbation at the boundary is one order of magnitude smaller than that inside the combustion chamber, as shown by Eqs. (25) and (26). This, of course, represents a typical resonance condition that a small disturbance at the boundary excites a larger amplitude wave in the interior of the cavity.

There are situations where either the flow Mach number is not small or the surface admittance functions are excessively large. In such cases, Eq. (24) is not applicable and Eqs. (22) and (23) should be solved directly, as has been done by Crocco and Cheng in Ref. 1. In such cases, one can expect significant departure of the oscillating fre-

quency from that given by the classical acoustic mode.<sup>†</sup> But perhaps more importantly, the special case of low-frequency nonacoustic oscillation can be analyzed easily using the latter approach but not by the Mach number expansion scheme. The detailed discussion of nonacoustic instability can be found in Sec. VI.

### III. Acoustic Amplification: Propellant Response Function

#### III.A. Introduction

Since combustion processes are the major driving force for solid rocket combustion instability, analysis of propellant burnings under oscillatory conditions is of interest. Such analysis can provide more understanding to the instability driving mechanisms, and hopefully, in the long run, can help the rocket designers to select and/or to formulate solid propellants less likely to cause combustion oscillations.

Of all the elements relevant to solid rocket combustion instability, the analysis of propellant responses is perhaps the most difficult and uncertain. At the present time, theoretical analysis of unsteady combustion containing all the relevant parameters does not exist. This is partly due to the incomplete understanding of the complicated combustion processes in the burning of modern solid propellants and partly due to the mathematical intractability of such a detailed model even if all the physics and chemistry are known. Existing unsteady combustion models normally contain several selected physical/chemical processes thought to be important for a particular instability situation. Such models, being incomplete, naturally have a limited range of applications. But the important driving process that is included can be analyzed in detail and often contributes to our understanding of the instability driving mechanisms. In the following sections, some of these models will be discussed.

#### III.B. Estimate of Time Scales

Since combustion instability involves a coupled oscillation between the combustion chamber wave dynamics and the propellant combustion unsteady response, the matching of the appropriate time scales is critical. An examination of

---

<sup>†</sup> The departure from classical acoustic frequency is most severe for longitudinal or mixed longitudinal-transverse modes. It is not so severe for transverse modes.

the relevant time scales in a burning propellant is needed for formulating any simplified unsteady combustion models.

The gas residence time in the flame is defined by  $l/\bar{u}$ , where  $l$ , the flame thickness, is the distance between the propellant surface to the end of the major energy release zone, and  $\bar{u}$  is the average gas velocity normal to the propellant surface. The "overall" chemical reaction time in the gas phase should be the same as the gas residence time because of the definition of  $l$ . We emphasize the word "overall" since many of the individual elementary chemical reactions that occur in the flame can be substantially faster than that measured by the overall time. The gas-phase heat-transfer time  $\alpha/\bar{u}^2$  should be comparable or smaller than the gas residence time. The reason that some flames can have a much longer gas residence time than the heat-transfer time is because of the existence of induction zones such as in some of the double-base propellant flames.

Comparing the several time scales in the gas phase indicates that the gas residence time  $l/\bar{u}$  is the longest one.

In the solid, if the radiative-absorption and the condensed-phase reaction layers are confined near the surface, the solid temperature profile is exponential in shape as a result of the conduction-convection (due to the moving surface) balance. The characteristic thermal distance is  $\alpha_s/\bar{r}$ , and the characteristic solid thermal-relaxation time is  $\alpha_s/\bar{r}^2$ , where  $\alpha_s$  is the solid thermal diffusivity, and  $\bar{r}$  is the steady-state<sup>s</sup> propellant burning rate. If the depth of the condensed-phase reaction is given by  $l_c$ , the corresponding thermal-relaxation time is given by  $l_c/\bar{r}$ . If the radiative absorption depth is  $l_r$ , the corresponding thermal-relaxation time is  $l_r/\bar{r}$ . If the solid is heterogeneous, a heterogeneity time scale can be specified. Taking an ammonia perchlorate (AP) composite solid propellant (for example, if the AP particle size is  $l_p$ ), the local heterogeneous time can be defined as  $l_p/\bar{r}$ . Because of the random distribution of particle locations in the propellant, some sort of coherence is needed for the local heterogeneity to be important in an organized oscillation. This will be discussed further.

An examination of the estimated order of magnitudes of these time scales indicates the following. Gas residence time is the slowest one in the gas phase time scales. In

the solid, the magnitudes of the condensed-phase reaction time and the radiation-absorption time will depend on the solid properties. In ordinary cases, they are probably faster than the solid thermal conduction-convection time. In many cases, the condensed-phase reaction and solid radiation can be thought to be confined on the surface, and the solid thermal conduction-convection time is the longest and the primary time scale in the solid phase.

The magnitudes of the gas residence time and the solid thermal time depend strongly on the pressure and the types of propellant. The range of gas residence time can be from  $10^{-2}$  to 10 ms, while for the solid thermal time, it can range from 1 ms to 1 s. For a given propellant and operating pressure, the gas residence time is, in general, smaller than the solid thermal-relaxation time by at least one order of magnitude.

Therefore, for combustion instability with the period of oscillation comparable to or longer than the solid thermal time, the gas-phase time lag can be neglected. Thus a quasisteady gas phase and unsteady solid model can be applied. This simplification makes it possible to obtain a closed-form analytical solution for the propellant response under small amplitude pressure oscillatory conditions.

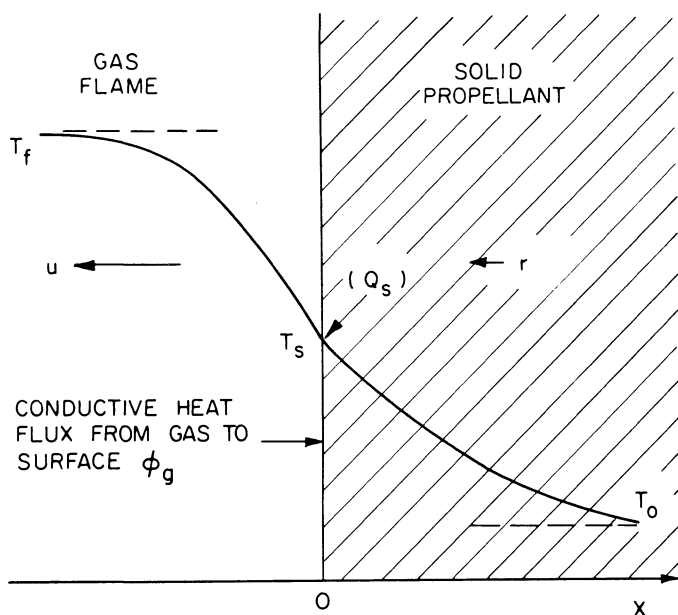


Fig. 1 Combustion model for unsteady solid-propellant burning.

Historically, Hart, McClure, and their associates<sup>15-19</sup> were credited with an extensive and pioneering effort in modeling solid propellant oscillatory burning based on physical/chemical process considerations. They are also among the first in introducing acoustic admittance function as a measure of propellant wave amplification capability.

The first quasisteady gas-phase and unsteady solid oscillatory combustion model was introduced by Denison and Baum.<sup>20</sup> In their model, a homogeneous solid propellant which decomposed into a laminar premixed flame was studied. A one-step overall gas-phase chemical reaction was assumed, and the solution in the limit of large activation energy was obtained. Their analysis triggered a number of modeling efforts, all utilizing the quasisteady gas-phase assumption.<sup>21-24</sup> As a matter of fact, this is the only class of unsteady solid propellant combustion models that has been extensively studied and tested. In the following, some general features of the quasisteady models will be outlined. These models are mainly for pressure sensitive response; velocity-coupled effect will be discussed in Sec. III E.

### III. C. Quasisteady Gas-Phase and Unsteady Solid-Phase Models

III. C. a. Model Description. Neglecting solid-phase reaction and radiation in-depth absorption (or confining them to the solid/gas interface), all the one-dimensional quasisteady flame models have the same governing equation for solid-phase heat transfer, i. e.,

$$\frac{\partial T}{\partial t} - r(t) \frac{\partial T}{\partial x} - \alpha_s \frac{\partial^2 T}{\partial x^2} = 0 \quad (33)$$

where  $x=0$  is attached to the propellant surface, and  $x$  is positive toward the interior of the solid, as indicated in Fig. 1. The propellant linear burning rate,  $r$ , is generally assumed to be related to the surface temperature  $T_s$  and/or pressure by some kind of pyrolysis relation:

$$r = r(T_s, p) \quad (34a)$$

A specific example includes the generalized Arrhenius expression:

$$r = A p^{n_s} e^{-E_s/RT_s} \quad (34b)$$



or power law <sup>24</sup>:

$$r = b(T_s - T_o)^m \quad (34c)$$

The other boundary conditions include

$$r = T_o \quad \text{as } x \rightarrow \infty \quad (35)$$

and at the solid/gas interface, an energy balance gives

$$\lambda_s \frac{\partial T}{\partial x} = \lambda \left[ \frac{\partial T}{\partial x} \right]_g - r \rho_s [Q_s + (C_p - C_s)(T_s - \bar{T}_s)] \quad (36)$$

where the subscript g means the gaseous side of the interface. The quantity  $Q_s$  is the overall heat per unit mass liberated at the surface<sup>s</sup> evaluated at the steady-state surface temperature  $\bar{T}_s$ . The value of  $Q_s$  can be positive or negative depending<sup>s</sup> on the propellant<sup>s</sup> flame models.

For quasisteady gas-phase and unsteady solid combustion model, the heat feedback from the gas phase,  $\phi_g = [\lambda(\partial T/\partial x)]_g$ , will depend on two variables which are perturbed from the steady state. These two variables can be chosen to be the instantaneous pressure and burning rate. It is worthwhile to see how this comes about. In quasisteady gas-phase laminar premixed flame theory, the burning rate  $r$  is the eigenvalue that is a function of  $T_s$ ,  $\phi_g$ ,  $T_f$ , and  $p$ , namely,

$$r = f_1(T_s, \phi_g, T_f, p) \quad (37)$$

The instantaneous flame temperature  $T_f$  is defined by

$$\phi_g = r \rho_s [Q_f - C_p(T_f - T_s)] \quad (38)$$

By combining Eqs. (37) and (38) with Eq. (34a) we get

$$\phi_g = f_2(p, r) \quad (39)$$

This conclusion is very important in the following model development. By introducing the following nondimensional

variables:

$$\begin{aligned}\theta &= (T - T_0) / (\bar{T}_s - T_0) & P &= p / \bar{p} & R &= r / \bar{r} \\ X &= x / (\alpha_s / \bar{r}) & \tau &= t / (\alpha_s / \bar{r}^2) \\ H &= Q_s / C_s (\bar{T}_s - T_0)\end{aligned}\quad (40)$$

and seeking small amplitude solution perturbed around the steady state,

$$\theta = \bar{\theta} + \theta' \quad P = 1 + P' \quad R = 1 + R' \quad (41)$$

The first-order linearized system for Eqs. (33, 35, 36) is

$$\begin{aligned}\frac{\partial \theta'}{\partial \tau} - \frac{\partial \theta'}{\partial X} - \frac{\partial^2 \theta'}{\partial X^2} + e^{-X} (m \theta'_s + n_s P') &= 0 \\ \frac{\partial \theta'}{\partial X} + A \theta' &= B P' \quad \text{at } X = 0 \\ \theta' &= 0 \quad \text{as } X \rightarrow \infty\end{aligned}\quad (42)$$

where

$$R' = m \theta'_s + n_s P' \quad (43)$$

has been used to derive Eq. (42), Eq. (43) is the linearized expression of pyrolysis Eq. (34a), where

$$m = \left[ 1 - T_0 / \bar{T}_s \right] \left[ \frac{\partial \ln r}{\partial \ln T_s} \right]_p \quad n_s = \left[ \frac{\partial \ln r}{\partial \ln p} \right]_{T_s} \quad (44)$$

If a specific pyrolysis law such as Eq. (34b) is used,

$$m = (1 - T_0 / \bar{T}_s) (E_s / R \bar{T}_s) \quad (45)$$

If Eq. (34c) is used,

$$n_s = 0 \quad (46)$$

Looking for an oscillatory-type solution using the complex variable representation (e.g.,  $P' = \exp(i\omega\tau)$ ), Eq.

(42) can be solved for the ratio  $\theta'_s/P'$ . Substituting this into Eq. (43), the propellant response function is found to be

$$\frac{R'}{P'} = \frac{2l\omega mB + mn_s \left[ \sqrt{1+i4\omega} - 1 \right]}{m+i\omega(2A-1) - (m+i\omega)\sqrt{1+i4\omega}} + n_s \quad (47)$$

In the limit of  $\omega \rightarrow 0$ , the steady-state result should be recovered. This requires

$$\frac{m(B+n_s)}{A-m-1} + n_s = \sigma_p \quad (48)$$

where

$$\sigma_p = \frac{d \ln \bar{r}}{d \ln \bar{p}}$$

is the burning rate-pressure sensitivity at steady state.

For the case  $n_s = 0$ , Eq. (47) can be written as

$$\frac{1}{\sigma_p} \frac{R'}{P'} = \frac{2l\omega m(A-m-1)}{m+i\omega(2A-1) - (m+i\omega)\sqrt{1+i4\omega}} \quad (49)$$

Equations (47) and (49) express the response function using four ( $\sigma_p$ ,  $m$ ,  $n_s$ , and  $A$ ) and three ( $\sigma_p$ ,  $m$ , and  $A$ ) parameters, respectively.<sup>‡</sup> Out of these parameters,  $\sigma_p$  is normally measured in a steady-state experiment and is usually a function of the pressure level (except when  $\bar{r} = a\bar{p}^n$ , then  $\sigma_p = n$ );  $m$  and  $n_s$  are also determined by pyrolysis experiments. The parameter  $A$  is related to the gas-phase heat feedback ( $\phi_g$ ) at the solid/gas interface. The nondimensional heat feedback defined by

$$\Phi_g \equiv \frac{\lambda_s}{\lambda_g} \left[ \frac{\partial \theta}{\partial X} \right]_g$$

is a function of  $P$  and  $R$ , as indicated earlier. Using Eq. (38) it is found that

$$A = -m \left[ \frac{\partial \Phi_g}{\partial R} \right]_P + mH + \left[ 1 - \frac{C_p}{C_s} \right] \quad (50)$$

<sup>‡</sup> The two-parameter burning response expression by Culick<sup>25</sup> is equivalent to the right-hand side of Eq. (49).

The quantity  $(\partial\Phi/\partial R)_P$  depends on gas-phase flame structure and is one of the major differences differentiating combustion models of this class. Many of the nonsteady burning models have been reviewed by Culick<sup>25</sup>, and Kuo and Coates<sup>26</sup> and we will not go into the details for these models. However, it is worthwhile to point out that in addition to the purely modeling approach, it is possible to deduce  $(\partial\Phi/\partial R)_P$  from either appropriate experiments or steady-state models using the Zel'dovich approach, which will be discussed in Sec. III.C.c.

III.C.b. Response Function and Intrinsic Instability. For a quasisteady gas flame, the acoustic admittance function is directly related to the propellant burning rate response function through the quasisteady continuity equation:

$$\rho_p r = \rho_f u_f \quad (51)$$

Perturbing the above equation and substituting it into Eq. (18), the acoustic admittance function for the propellant flame evaluated at the flame edge is

$$\gamma = \frac{R'}{P'} - \frac{\rho_f' / \bar{\rho}_f}{P'} \quad (52)$$

If ideal gas law is applicable, the above equation becomes

$$\gamma = \frac{R'}{P'} - 1 - \frac{T_f' / \bar{T}_f}{P'} \quad (53)$$

the last term in the above equation is equal to  $(\gamma-1)/\gamma$  if the flame temperature oscillation is isentropic, and is equal to zero if it is isothermal. In general this last term is small in comparison with the first two terms under instability condition. Thus the flame admittance function is predominantly determined by the burning rate response  $R'/P'$  when the gas phase is considered quasisteady.

One important property of Eq. (42) is the condition that the response becomes unbounded. This is given by setting the denominator of the first term in the right-hand side of Eq. (47) to zero, i.e.,

$$m + i\omega(2A-1) - (m+i\omega)(1+i4\omega)^{1/2} = 0$$

This complex equation defines a boundary line on the  $m$  vs  $A$  map, as shown in Fig. 2. The physical meaning of this

boundary is that, on one side of the boundary, the steady burning-rate solution (or the steady temperature field in the solid) is linearly unstable even in the absence of any pressure disturbance. This is referred to as the "intrinsic burning instability" first correctly identified by Denison and Baum.<sup>20</sup> Although from the first glance, the intrinsic instability seems unrelated to rocket motor instability, as it requires no coupling from the chamber wave dynamics, its existence on the map of propellant parameters has a profound implication on the magnitude and the peaking frequency of the propellant response function. On such a map, the closer the propellant is to the intrinsic boundary, the larger is the peak response, with the peaking frequency close to the natural frequency on the intrinsic boundary at the nearest point. This can be illustrated in

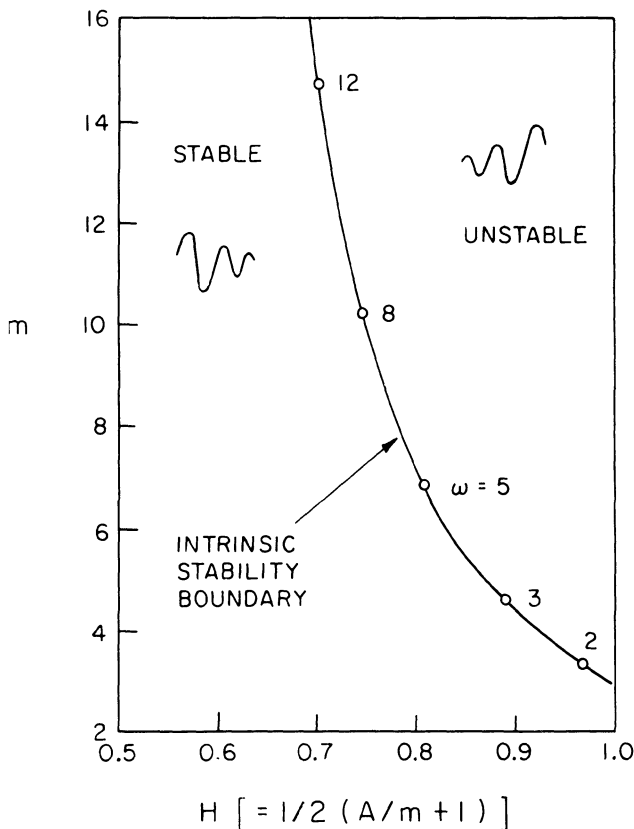


Fig. 2 Solid propellant intrinsic stability map;  $\omega$  is nondimensionalized by the solid thermal-relaxation time  $\alpha_s / r^2$ . (From Ref. 24).

Fig. 3 using the KTSS unsteady solid propellant combustion model.<sup>24</sup> In Fig. 3, the value of the pyrolysis exponent  $m$  is increased from 6 to 10. For  $m = 6$  and  $H = 0.75$ , (refer to Fig. 2), the propellant is close to the intrinsic boundary, with a natural frequency around 5; the calculated real part of the acoustic admittance shows a clear peak around that frequency. As  $m$  is increased to 7, the propellant is moving closer to the intrinsic boundary, and the peak is higher with a higher peaking frequency. For  $m = 10$ , the propellant is on the intrinsic boundary with  $\omega = 7.75$ , the response function becomes unbounded at that frequency. From a mathematical point of view, it is not difficult to understand this as a type of resonant phenomena. Referring to Eq. (47), the response function is unbounded on the intrinsic boundary at the natural frequency because of the vanishing of the denominator of the first term on the right-hand side. As we move away from the intrinsic boundary, but still close to the boundary, the denominator is nonzero, but small in the neighborhood of the resonant frequency, therefore it results in a peak in the response function. The magnitude of the peak is related to the absolute magnitude of the denominator, which, in turn, is re-

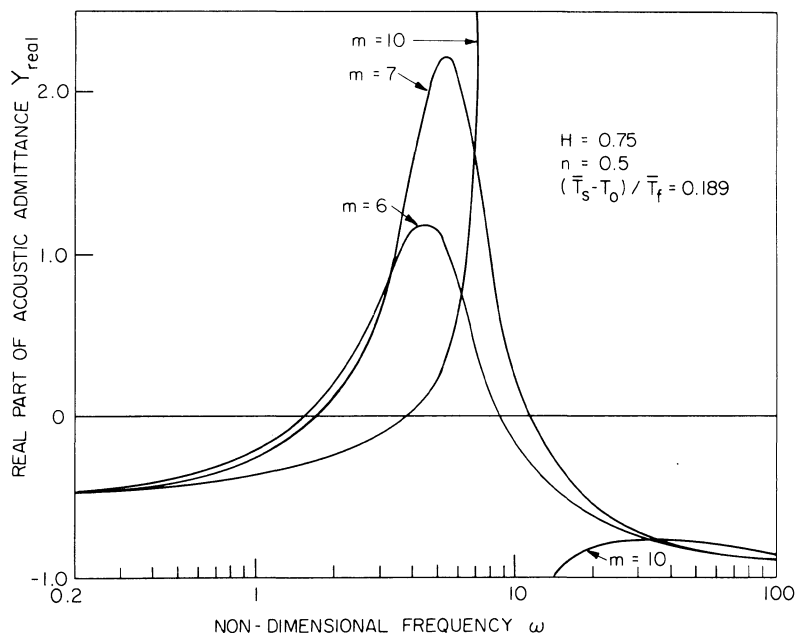


Fig. 3 Solid propellant acoustic admittance vs frequency: variation of pyrolysis power exponent  $m$ . (From Ref. 24).

lated to the closeness of the propellant parameters to the intrinsic boundary. This is analogous to the forced resonance problem in a spring-mass-dashpots system.

In addition to the propellant parameters  $m$  and  $A$ , the magnitude of the response function is directly proportional to  $\sigma_p$  when  $n_s = 0$ , as shown from Eq. (49). Therefore a more pressure-sensitive propellant (in steady burning) will generate a higher response.

**III. C. c. Zel'dovich Approach.** One way of deducing the value of parameter  $A$  in the response function [Eqs. (47) or (49)] for a given propellant without knowing its detailed gas flame structure is to use the Zel'dovich approach.<sup>27,28,81</sup> As shown by Eq. (39), the gas-phase heat flux at the solid surface can be expressed as a function of the instantaneous pressure and burning rate in the limit of a quasisteady gas phase. From Eqs. (34a) and (36), the surface heat flux into the solid  $\lambda_s(\partial T/\partial x)$  is also a function of pressure and burning rate. In order to deduce its rate of change with respect to pressure and burning rate, we note that, in the steady state

$$\lambda_s \frac{\partial \bar{T}}{\partial x} = -\bar{r} \rho_s C_s (\bar{T}_s - T_o) \quad \text{at } x = 0^+ \quad (54)$$

$$\bar{r} = \bar{r}(\bar{p}, T_o) \quad (55)$$

Since the initial bulk propellant temperature  $T_o$  is not varying in a given transient, it is not a variable in the unsteady problem. Therefore, by using Eqs. (54) and (55),  $T_o$  can be used as a parameter to effect an independent variation between the pressure and the burning rate for the surface heat flux in the steady-state experiments, which should have the same functional form as in the quasisteady state. The experiment that is needed for this information is expressed by Eq. (55), i.e., burning rate as a function of pressure and initial propellant temperature.

Applying small perturbation analysis to Eqs. (54) and (55) and using Eq. (43), it can be shown that the parameters  $A$  and  $B$  needed in Eq. (47) for the response function are

$$A = -\zeta m/\sigma_T + m + 1$$

$$B = -\zeta \sigma_p/\sigma_T + n_s (\zeta/\sigma_T - 1) \quad (56)$$

## Chapter 15

### Smokeless Propellants

Eugene Miller\*

*University of Nevada, Reno, Nevada*

#### Abstract

Secondary smoke formation in the boundary layer of a rocket plume is due primarily to the condensation of water in the form of a fog of small droplets. The presence of other soluble gases such as hydrogen chloride or hydrogen fluoride increases the amount and the rate of condensation. This smoke forms even for so-called smokeless propellants when the ambient air is sufficiently humid or cold. Secondary smoke is undesirable because of the visible signature produced and the interference of the smoke with optical guidance systems. Condensation in the plume is initiated on heterogeneous nuclei which are formed in the rocket motor. Modeling of the number, size distribution, and chemical composition of the smoke droplets as a function of radial and axial position in the plume has been achieved. The models permit computation of the plume visible signature and laser signal attenuation. The predictions compare well with experimental measurements if allowances are made for limitations of existing rocket plume models and the experimental data. Minimizing secondary smoke primarily requires reduction of water and halogen gas content of the combustion gases and potentially by modification of the condensation nuclei size and number. Some possibility exists for mechanical dispersion or chemical inhibition of smoke formation. Propellant formulation modification and possibly interior ballistic design appear to offer the most fruitful approach.

---

This paper is declared a work of the U. S. Government and therefore is in the public domain.

\*Professor and Chairman, Chemical and Metallurgical Engineering Department, Mackay School of Mines.



Improved modeling of the dynamics of smoke formation, visibility, and optical signal attenuation require further research in plume turbulence and mixing, heat and mass transport to droplets, thermal accommodation and condensation coefficients of submicron droplets, nucleation mechanisms, chemical and physical characterization of the condensation nuclei, and multiple optical scattering phenomena.

### Nomenclature

$A$	= arbitrary optical depth parameter
$c_p, C_p$	= specific heat per unit mass and mole, respectively, at constant pressure
$D$	= mass diffusivity
$E(k)$	= turbulent energy of the plume as a function of wave number
$f_k$	= optical phase function defined by Eq. (18)
$F(r), f(r)$	= Weibull cumulative and density distribution function, respectively
$H_c, H_s$	= heat of condensation and solution per unit mass, respectively
$I$	= light intensity
$i$	= osmotic coefficient
$J$	= rate of nucleation per unit volume
$K$	= Mie coefficient
$k$	= Boltzmann constant, absorption in complex index of refraction, thermal conductivity, or wave number
$L$	= mean free path of gas, optical length
$Le$	= Lewis number
$m$	= index of refraction
$M$	= molecular weight
$N$	= number of nuclei per unit volume
$N_A$	= Avogadro's number
$n$	= number of moles
$Pr$	= Prandtl number
$\bar{p}$	= saturation pressure of component of plane surface solution
$p$	= partial pressure of condensible in plume
$Q_k$	= optical quantity function defined by Eq. (20)
$R$	= gas constant, plume radius, or radiance
$Re$	= Reynolds number
$r$	= droplet radius
$\bar{r}$	= mean droplet radius
$S$	= optical distance along line of sight

$s$	= molecular speed ratio of bulk velocity normal to the droplet surface to the mean thermal speed of the gas molecules
$Sc$	= Schmidt number
$T$	= absolute temperature
$t$	= time
$u$	= average velocity
$u_r$	= root mean square gas droplet velocity difference
$u'$	= root mean square velocity fluctuation
$V$	= eye visual response
$v$	= specific volume per mole
$w$	= net condensation rate
$X$	= axial distance
$x$	= mole fraction
$\alpha$	= Weibull distribution coefficient, thermal accommodation coefficient or correlating constant
$\beta$	= Weibull distribution coefficient, condensation coefficient or correlating constant
$\gamma$	= specific heat ratio
$\lambda$	= wavelength of light
$\mu$	= gas absolute viscosity
$\nu$	= gas kinematic viscosity
$\rho$	= gas density
$\sigma$	= surface tension of the liquid-gas interface, ratio of droplet to gas density, square root of variance
$\sigma_{\text{ext}}$	= optical extinction coefficient
$\sigma_{\text{sc}}$	= optical scattering coefficient
$\tau$	= optical depth
$\Phi$	= turbulent transport coefficient, or number of nuclei per unit flow area per unit time
$\omega$	= local velocity fluctuation frequency

### Subscripts

$B$	= background
$D$	= mass
$e$	= plume edge
$f$	= film
$h$	= heat
$i$	= $i$ th component
$m$	= plume centerline
$o$	= initial or at nozzle exit
$r$	= droplet
$s$	= solvent
$\text{sol}$	= solution

$\infty$  = freestream  
t = turbulent

### Superscripts

o = pure

## Introduction

Smoke can be arbitrarily categorized as primary or secondary. Primary smoke is composed of solid particles emitted by the rocket in such a number and size as to scatter or absorb light sufficiently to be detectable in the plume. Alumina from aluminum powder added to a propellant to increase its specific impulse or to enhance its burning stability is the most common source of primary smoke. Other sources are burn rate modifiers based on salts of iron, chrome, copper, lead, tin, and carbon. Secondary smoke, or fog, is formed from the condensation of gases such as water, HCl or HF in the mixing boundary layer of the plume in the form of liquid or frozen droplets in sufficient number and size so as, again, to scatter or absorb light sufficiently to be detectable. So-called "smokeless" solid propellants are formulated with aluminum and burn rate additives reduced to a minimum compatible with interior ballistic requirements, generally less than 1-2 wt.% of the propellant. They are not truly smokeless since the exhaust contains condensable gases which will form a fog under the proper conditions of relative humidity and temperature of the ambient air. Primary smoke generally is still present in smokeless propellants but not in sufficient density to affect the mission of the rocket.

This paper is concerned with these smokeless propellants and the secondary smoke formed in the rocket plume. In what follows, it is to be understood that a reference to "smoke" is to secondary smoke or fog.

## Chemical Origin of Smoke

Modern high performance solid propellants are formulated from ammonium perchlorate (AP) and nitramine or fluoramine oxidizers with various hydrocarbon, nitrocellulose, or fluorocarbon fuel binders and hydrocarbon or nitroplasticizers. Typical nozzle exhaust gas compositions influencing the formation of smoke are given in Table 1.

Smoke may form anywhere in the plume where the thermodynamic dew point requirements of temperature and composition are met. Liquid phase solutions of H<sub>2</sub>O-HCl and H<sub>2</sub>O-HF are

Table 1 Gas composition of typical smokeless propellants

Class of propellant	Theoretical gas composition, mole %				
	CO	H <sub>2</sub>	H <sub>2</sub> O	HCl	HF
AP-hydrocarbon	13	6	42	20	-
HMX-nitrocellulose-nitroplasticizer	6	15	20	-	-
AP-HMX-nitrocellulose-nitroplasticizer	23	17	23	4	-
HMX-fluorocarbon	30	1	5	-	16
Nitrocellulose-nitroplasticizer	37	26	9	-	-

nonideal; the saturation vapor pressure of the solvent water of such solutions over a plane surface can be expressed by the following equation, neglecting nonideality in the gas phase

$$\bar{p} = p^0/(1+in/n_s) \quad (1)$$

The osmotic coefficient allows for the nonideal behavior of the solute in the liquid phase. The value can be as high as 40 for concentrated solutions of HCl dissolved in water. Hence, HF, and to a much greater extent, HCl, will depress the equilibrium vapor pressure of water over the solution more than would be predicted for an ideal solution where  $i = 1$ . Further, from the Kelvin equation which corrects for the effect of radius of curvature of a pure droplet on vapor pressure,

$$p_r^0/p^0 = \exp(2\sigma v/RTr) \quad (2)$$

Compared with a plane surface, a droplet requires a higher partial pressure of condensable gas before condensation will take place, i.e., the gas must be supersaturated relative to the plane surface saturation pressure.

Equations (1) and (2) can be combined to express the vapor pressure of the solvent of a droplet of solution

$$p_r = p^0 \exp(2\sigma v/RTr)/(1+in/n_s) \quad (3)$$

For solutions of HCl - water or HF - water for which experimental vapor pressure data are available, Eq. (3) may be

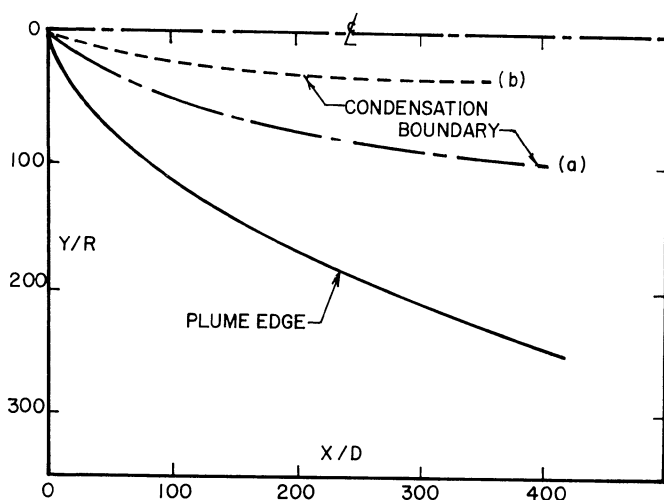


Fig. 1 Condensation boundary layer in plume.

written as

$$p_r = p_{sol}^0 \exp(2\sigma v / RTr) \quad (3a)$$

Similar equations can be written for the vapor pressure of the solute gas. Wherever the partial pressures of the solute and solvent in the plume are greater than or equal to the pressures calculated from Eqs. (3) and (3a) for a given droplet radius, condensation can take place.

In Fig. 1, a plume emitting from a 1 ft nozzle into still air for a rocket containing 86 wt.% AP - hydrocarbon rubber binder is modeled as a function of radial and axial distance. Similar temperature, composition and velocity profiles were assumed. As the plume moves downstream it mixes with the ambient air, generally increasing in water content, decreasing in temperature, and diluting the local partial pressures of the condensibles. The calculated thermodynamic dewpoint regimes for two conditions of ambient air mixing with the plume are shown, 21.1°C and 100% RH, and -40°C and 0% RH. The labelled lines, (a) and (b), respectively, define the minimum radial distance from the plume centerline at which Eq. (1) for condensing HCl and water is satisfied. At radial distances closer to the centerline, the gas temperature is too high to permit condensation to take place. The zone bounded by this limit and the plume edge defines the maximum volume of the plume in which condensation can potentially occur. For 21.1°C and 100% RH air this could occur anywhere in this volume, but for the -40°C, 0% RH air, nearer the edge of the plume the condensible gases have been diluted to below the saturation

conditions. In either case, the zone for smoke formation is more restricted than shown due to the requirements for supersaturation defined by Eq. (3) or (3a). Also at sea level, some of the  $H_2$  and CO noted in Table 1 will be oxidized to water and  $CO_2$  in the plume. This "afterburning" provides additional water and heat, modifying in general the potential saturation zone of the plume.

Qualitatively, it would be expected that the lower the water, HCl, and HF partial pressures, the lower the potential for smoke formation. Oliver<sup>1</sup> predicted from thermodynamic dew point considerations for plane surface condensation the ambient air conditions for which smoke could form. His computations considered two limiting cases - one for isothermal mixing at a fixed dilution ratio of air to propellant gas, and the other for adiabatic mixing at the limiting dilution ratio permitting condensation. Computations for typical formulations are shown in Fig. 2 as a plot of the maximum relative humidity as a function of the lowest air temperature for which smoke will not appear at sea level. Both the isothermal and adiabatic cases are shown. Smoke should form only for conditions above these limiting curves, the so-called "smoke profiles." The "smoke profiles" move up and to the left, i.e., to higher relative humidities and lower temperatures, for an increase in altitude. Oliver argues that somewhere in the plume, in the region between the adiabatic and isothermal smoke profiles, smoke will appear. Coughlin<sup>2</sup> adapted Oliver's method to the plume itself, permitting an estimate of the distance from the nozzle exit at which smoke would appear in the plume.

Calculated smoke profiles based on the vapor pressure of a plane surface are not strictly correct, but in many instances are close enough to the correct profiles based on the vapor pressure of droplets. It follows from Eq. (2) or (3) that a nucleus of radius  $r$  and supersaturation of the gas are required before condensation can occur. The nature and origin of these condensation nuclei are discussed in the next section.

#### Homogeneous and Heterogeneous Nucleation of Smoke

It may be seen from Eqs. (3) and (3a) that the saturation conditions at a specified temperature are a function of the radius of the droplet. Defining the radius of a droplet in equilibrium with the gas phase to be  $r^*$ , we obtain from Eq. (3a),

$$r^* = 2\sigma v / (RT_r \ln p/p_{so1}^0) \quad (4)$$

For multicomponent condensation, the ratio  $p/p_{so1}^0$  for each component must be the same, defining a single value of the  $r^*$  with the solution composition determining  $\sigma$  and  $v$ . At equi-

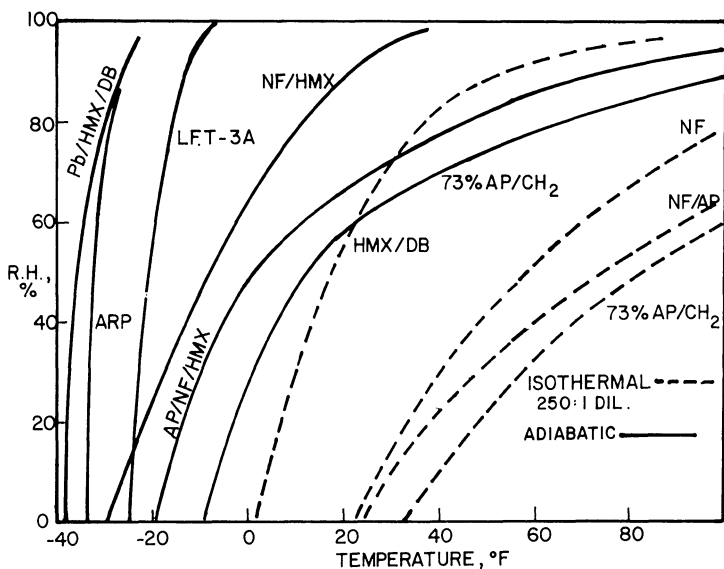


Fig. 2 Oliver fog predictions.

librium conditions, the droplet temperature will be equal to the gas temperature. If  $p = p_{sol}^0$ ,  $r^* \rightarrow \infty$ , and we have the case for a plane surface, usually defined as the thermodynamic dew point. If  $p < p_{sol}^0$ ,  $r^* < 0$  and any droplet present would spontaneously evaporate. For  $p > p_{sol}^0$  the gas is supersaturated and any droplet larger than  $r^*$  will grow by condensation. A droplet of radius  $r^*$  will be in equilibrium and will neither grow nor evaporate. It follows from this consideration that it would be impossible for a gas to condense unless there were nuclei sites present, or would subsequently be formed, that are at least as large as  $r^*$  for the environmental conditions of  $p$ ,  $T$ , and  $p_{sol}^0$ .

The condensation nuclei can form by the collision and agglomeration of a sufficient number of molecules. If the molecules that combine to form the nucleus are composed of the condensing gases, the formation is termed homogeneous. Other chemical species present or formed in the rocket, such as aluminum oxide, soot, alkali salts, lead salts, etc., which can condense homogeneously in the rocket chamber, nozzle, or plume present sites on which the water, HF, or HCl gases can condense to form secondary smoke. These sites are termed heterogeneous nuclei. Liner and insulation fragments may also serve the same function.

Homogeneous nucleation theory was developed by Becker and Doring,<sup>3</sup> Volmer,<sup>4</sup> and Frenkel<sup>5</sup> among others, based on classical

kinetic theory of gases and the Kelvin equation. As reviewed by Wegener and Wu,<sup>6</sup> the rate of nucleation, number per cubic centimeter per second, is

$$J = \sqrt{2/\pi} (N_A^{2/3}/R^2) (p/T)^2 (\sqrt{\sigma \bar{M}}/\rho_r) \exp(-n^* \ln(p/p_{sol}^0)/2) \quad (5)$$

where

$$n^* = (4\pi/3) \rho_r (N_A/\bar{M}) r^3 \quad (5a)$$

The rate of nucleation is a function of the supersaturation ratio,  $p/p_{sol}^0$ .

The classical theory has been found to be in error by factors of  $10^{-6}$  to  $10^6$  depending on the mole fraction of the condensible in the gas stream. Attempts to modify this theory by incorporating contributions to the energy of formation of the nucleus from statistical mechanical considerations and for finite rate heat transfer during nucleation have not materially corrected the large discrepancy between experimental and theoretical values. Since theoretical considerations utilizing Eq. (5) for the prediction of the number of nuclei formed are not adequate, it is necessary to obtain this information experimentally. Experimental data for the number of nuclei per cubic centimeter formed for water, alcohol, benzene condensation from the vapor phase, and for the formation of soot in methane - oxygen flames range from  $10^9/\text{cm}^3$  to  $10^{12}/\text{cm}^3$  with nuclei sizes ranging from 10 to 1000 Å. Arkhipov and Ratanov<sup>7</sup> report soot formation in solid propellants with an average diameter of 1000 Å at the nozzle exit.

Since the dynamics of secondary smoke formation depends on nucleation, information on the number, size distribution, and chemical nature of the nuclei is required. Some measurements of the nuclei for several AP and non-AP propellants have been made by the U.S. Army Missile Command in their Smoke Characterization Facility (SCF),<sup>8,9</sup> described later. Values of  $10^4/\text{cm}^3$  to  $10^6/\text{cm}^3$  with nuclei sizes ranging from 10 to 1200 Å are reported. The data support a conclusion that the nuclei for secondary smoke are heterogeneous. The experiments and their interpretation are covered later.

## Modeling of Secondary Smoke

### The Dynamics of Secondary Smoke Formation

The treatment of the dynamics of secondary smoke formation in the rocket plume is related to meteorological models



for the prediction of cloud formation and rain fall.<sup>10</sup> If the local conditions in the plume permit condensation on the heterogeneous nuclei present, the rate at which a droplet of radius  $r$  will grow may be written

$$r \, dr/dt = \Phi_D (v D_f / RT_f) (p - p_r) / (1 - p_r) \quad (6)$$

Based on Ranz and Marshall's<sup>11</sup> experimental correlation for mass transfer to spheres the turbulent mass transport coefficient is

$$\Phi_D = 1.0 + 0.3 \text{Re}_f^{1/2} \text{Sc}_f^{1/3} \quad (6a)$$

Equation (6) is satisfactory if the radius of the droplet is large compared with the mean free path of the gases in which the droplet is immersed. Typically, when condensation initiates on the nuclei this is not the case. Fuchs<sup>12</sup> showed that the classical equation for molecular diffusion should be corrected by a factor derived from the kinetic theory of gases

$$1 / \{ (2\pi \bar{M} / RT_r) (D/r\beta) + (r/(r+L)) \} \quad (6b)$$

where  $\beta$  is a condensation coefficient correcting for the molecules rebounding from the droplet surface without sticking. There has been some uncertainty over the correct value for  $\beta$ , even for water. However experimental values of  $\beta$  have increased from early values of 0.04 as experimental technique has improved. The data and analysis of Mills and Seban,<sup>13</sup> Ru Maa,<sup>14</sup> and Kroger and Rohsenow<sup>15</sup> indicate that  $\beta$  for water is equal to one. It is assumed here that  $\beta$  for HCl or HF condensation is also one.

In addition to the Fuchs correction, during net phase change the bulk vapor velocity normal to the droplet surface alters the equilibrium molecular velocity distribution. Schrage<sup>16</sup> took this into account in deriving an expression for the net condensation rate. The net condensation rate correcting the Hertz - Knudsen physical model of evaporation and condensation is

$$w = \beta \{ \Gamma (p / \sqrt{2\pi RT}) - p_r / \sqrt{2\pi RT_r} \} \quad (7)$$

where

$$\Gamma = \exp(-S^2) + \sqrt{\pi} \cdot S (1 + \text{erf } S) \quad (7a)$$

Mills and Saban<sup>13</sup> linearized  $\Gamma$  and simplified Eq. (7) to

$$w = \beta / (1 - 0.5\beta) (p / \sqrt{2\pi RT} - p_r / \sqrt{2\pi RT_r}) \quad (7b)$$

for  $0 < \text{abs}(s) < 0.001$  and

$$w = \beta / (1 - 0.523\beta) (p / \sqrt{2\pi RT} - p_r / \sqrt{2\pi RT_r}) \quad (7c)$$

for  $0.001 < \text{abs}(s) < 0.00$ .

For a  $\beta$  of 1, the coefficient of Eqs. (7b) and (7c) are 2.0 and 2.1, respectively. Incorporating a value of 2.0 into the Fuchs correction and assuming as a first approximation that these corrections can be applied to turbulent flow conditions,

$$r \, dr/dt = \Phi_D^* (vD_f/RT_f) (p - p_r) / (1 - p_r) \quad (8)$$

where

$$\Phi_D^* = 2\Phi_D / ((2\pi\bar{M}/RT_r)^{1/2} (D/r) + 2r/(r+L)) \quad (8a)$$

Equation (8) is written for single component condensation. For dilute multicomponent condensation, Eq. (8) can be used to calculate the increase in radius of the droplet produced by each condensing component.

An analogous equation can be written for the rate of temperature change of the droplet due to convective heat transfer with the ambient gas, and heats of condensation and solution:

$$mc_p dT_r/dt = \Phi_h^* k_f \cdot 4\pi r (T - T_r) + \dot{H}_c + \dot{H}_s \quad (9)$$

and

$$\Phi_h^* = \Phi_h k (2\pi\bar{M}RT_r)^{1/2} / ((C_p(\gamma+1)/2\gamma)Pr\alpha + r/(r+L)) \quad (9a)$$

From Ranz and Marshall,<sup>11</sup>

$$\Phi_h = 1.0 + 0.3Re_f^{1/2} Pr_f^{1/3} \quad (9b)$$

The turbulent transport factors,  $\Phi_h$  and  $\Phi_D$ , are dependent on the relative velocity between the droplet and the gas stream. The root mean square gas droplet velocity difference induced by turbulent gas velocity fluctuations can be predicted for a droplet which is smaller than the scale of

turbulence from Soo,<sup>17</sup>

$$u_r^2 = u^2 \int_0^\infty (\Omega^{(1)}/\Omega^{(2)}) E(k) dk \quad (10)$$

$E(k)$ , the turbulent energy spectrum of the gas stream, is a function of the turbulence wave number,  $k$ ,

$$k = 2\pi\omega/u_m \quad (10a)$$

$u_m$  is the average plume centerline gas velocity relative to the plume edge velocity. The other variables are defined by

$$\Omega^{(1)} = \{((1-\beta)/\beta)(\omega/\alpha)\}^2 \quad (10b)$$

$$\Omega^{(2)} = (1/\beta^2)(\omega/\alpha)^2 + (\sqrt{6}/\beta)(\omega/\alpha)^{3/2} + 3(\omega/\alpha) + 6(\omega/\alpha)^{1/2} + 1 \quad (10c)$$

$$\alpha = 3\nu/r^2, \quad \beta = 3\rho/(2\rho_r + \rho) \quad (10d)$$

Generalized computations<sup>18,19</sup> of  $u_r$  have been made for particle densities of 1.1, typical of HCl-water droplets, and 3.3 g/cm<sup>3</sup> (alumina) based on the turbulent spectra data of Hetsroni and Sokolof<sup>20</sup> for a subsonic plume at 20-30 nozzle diameters at low particle loading. Data from Laurence<sup>21</sup> were used for distances less than the length of the potential core. The calculated values of  $u_r/u'$  can be correlated, based on a modification of the work of Levich and Kuchanov,<sup>22</sup> as a function of  $(r^2 u_m \sigma / \nu_t)$  with  $\sigma$  the ratio of droplet to gas density.  $\nu_t = (1+f(\text{Re}))\nu$  where  $f(\text{Re})$  is an experimental factor correcting the Stokes drag coefficient for higher Reynolds numbers<sup>23</sup> and corrected for noncontinuum flow by the experimental data of Millikan.<sup>24</sup> The graphical correlation is shown in Fig. 3. Typically for a 1  $\mu$ m radius droplet in the boundary layer where condensation takes place, for an axial velocity of 300 ft/s,  $u_r/u'$  is approximately 0.4. If the turbulent behavior of relatively low velocity, cold free plumes can serve as an approximation to a rocket plume,  $u'$  would be approximately 20 ft/s - significantly greater than the velocity difference calculated from the Stokes' considerations of drag and inertial forces.

The droplets at any axial and radial position have a size distribution determined by the local condensation dynamics and the nuclei size distribution. It is convenient computationally to correlate the size distributions by means of the Weibull cumulative distribution relation,

$$F(r) = 1 - \exp(-\alpha r^\beta) \quad (11)$$

or the Weibull density distribution,

$$f(r) = \alpha \beta r^{\beta-1} \exp(-\alpha r^\beta) \quad (11a)$$

the mean of  $r$ ,

$$\bar{r} = \alpha^{-1/\beta} \Gamma(1+1/\beta) \quad (11b)$$

and the variance,

$$\sigma^2 = \alpha^{-2/\beta} (\Gamma(1+2/\beta) - (\Gamma(1+1/\beta))^2) \quad (11c)$$

with  $\alpha$  and  $\beta$  correlating coefficients.

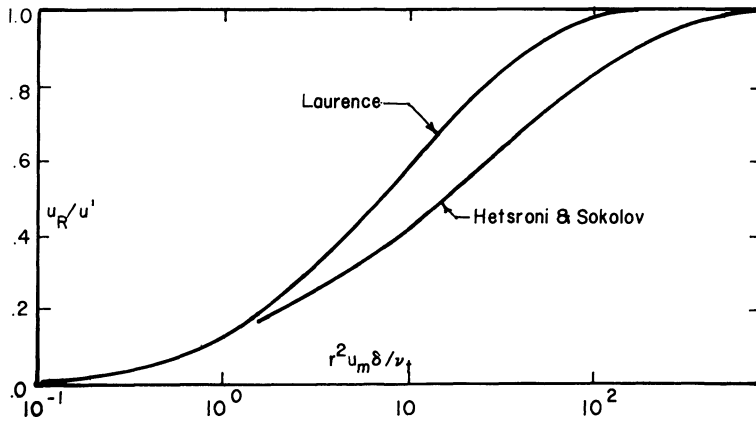


Fig. 3 Droplet relative velocity correlation.

Finally, the rocket plume itself may be modeled by the LAPP program<sup>25</sup> - defining radially and axially the velocity, mass concentration, and temperature fields. The number of droplets or nuclei per unit volume,  $N$ , at any location can be predicted as a function of the LAPP gas velocity, if it is assumed that all particles spread at a rate which is independent of their size and droplet loading, by

$$N = \Phi_0 ((u_m - u_e)/u_0^2) ((u - u_e)/(u_m - u_e))^{Sc_t} \quad (12)$$

The Lapp code permits a choice of various mixing models - Donaldson-Grey, Ting-Libby for example - which influence the resulting velocity, temperature, and concentration profiles.

The set of equations given, using the LAPP plume output, the necessary physical, chemical, and thermal properties, and the nuclei number and size distribution, are integrated using an adaptation of Gear's explicit-implicit numerical integration routine<sup>26</sup> along four streamlines simultaneously. This constitutes the DROP4 code.<sup>19,27,28</sup> The number, size, and composition of the droplets are calculated as a function of radial and axial position in the plume. It is assumed also that the droplets tracked along the streamlines are representative of the average population on that streamline. It is further assumed that the plume acts as an infinite source and sink, i.e., the mass and thermal effects on the plume due to condensation are small compared with the total mass of potentially condensible gas and enthalpy of the plume.

A dynamic model similar to DROP4 was developed by Meyer.<sup>29</sup> He neglected the effects of turbulence and nonequi-

librium molecular velocity distribution on condensation. Coupling of condensation with the plume was approximated by allowing for the removal of condensibles and the increase in plume temperature along streamtubes without diffusional compensations. Victor and Breil's model<sup>30</sup> is a simplified version of the above treatment, neglecting the same factors as Meyer, the coupling of condensation with the plume, and uses a simplified plume code.

Equilibrium models<sup>1,2</sup> consider only that when the concentration of condensibles exceeds the thermodynamic requirements, smoke can form. As an indicator of the incidence of secondary smoke, they are useful. They do not describe any details of number, size distribution, and chemical composition of the droplets. Consequently they cannot quantify plume visibility nor optical signal attenuation through the plume.

In this analysis, it has been tacitly assumed that the effects of coagulation of droplets due to Brownian motion, turbulent diffusion, and relative velocity due to turbulence are negligible. From Levich,<sup>31</sup> these may be estimated, assuming each collision leads to agglomeration. The change of the number of droplets per unit time,  $dN/dt$ , for an  $N$  of  $3 \times 10^5/\text{cm}^3$  by Brownian motion is about 100/s and would predominate for droplet diameters smaller than  $0.4 \mu\text{m}$ . At a diameter of  $1 \mu\text{m}$   $dN/dt$  by turbulent diffusion would be approximately 1500/s and would predominate for droplet diameters up to  $6 \mu\text{m}$ . At a  $10 \mu\text{m}$  diameter,  $dN/dt$  caused by relative velocity due to turbulence would be about 2500/s. Coagulation effects would be important therefore for relatively long periods of time, minutes to an hour, depending on the mode of coagulation that is dominant. According to Langmuir,<sup>32</sup> it may be noted that the coagulation efficiency is much smaller than unity. As will be seen in succeeding sections, the formation of smoke in the plume generally occurs in the millisecond to decisecond time period, and coagulation is not important in smoke development in the boundary layer of a rocket plume. Consideration of the stagnant contrail or postfire cloud formation and dissipation however would have to include collisions and agglomeration. This regime is not included in the DROP4 model nor any of the other referenced models.

### Opacity Theory for Visible Light

Light Scattering. The theory of scattering of light by spheres is available in several texts,<sup>33-35</sup> and only the elements relevant to secondary smoke in the rocket plume will be reviewed here. A suspension of particles removes energy from an illuminating beam by scattering, and also by absorp-

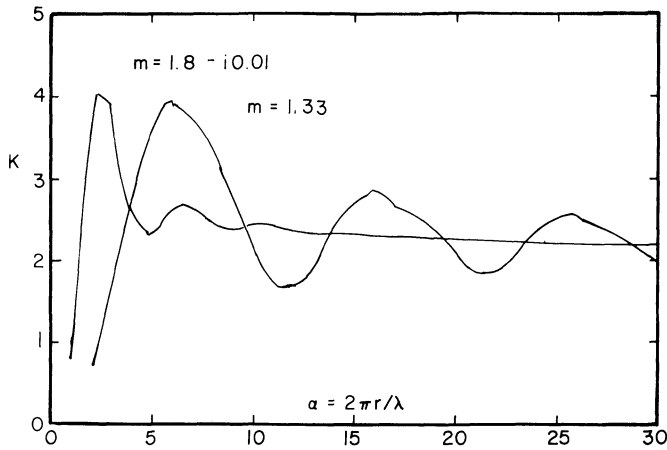


Fig. 4 Variation of Mie coefficient with  $m$  and  $\alpha$ .

tion if the particles absorb in the frequency of the beam. If in a unit volume of the suspension there are  $N$  particles of uniform radius,  $r$ , and a particle extinction coefficient (Mie coefficient),  $K$ , the Beer-Lambert-Bouguer law describes the light attenuation

$$I/I_0 = \exp(-N\pi r^2 K L) \quad (13)$$

The Mie coefficient is a function of a particle size parameter  $\alpha = 2\pi r/\lambda$  and may be predicted from the Mie theory for spherical particles, for monochromatic light of wavelength  $\lambda$ , and the index of refraction of the droplet. It is convenient to assign to absorbing materials, such as carbon and alumina found in primary rocket smoke, a complex refractive index  $m = m_0(1 - ik)$ , where  $k$  is the absorption coefficient of the material at that wavelength. For secondary smoke in visible and near-visible light, extinction is dominated by scattering and we need only deal with the real portion of the refractive index. Typical variations of  $K$  with  $\alpha$  and  $m$  are given in Fig. 4. Since a monochromatic beam traversing through the plume scatters from droplets of varying number density, size, and index of refraction, it is necessary to modify Eq. (13) to describe the extinction. In terms of the DROP4 output

$$\ln I/I_0 = -\int_0^L \int_0^\infty N K f(r) \pi r^2 dr dX \quad (14)$$

$N$  and  $f(r)$  are functions of the radial and axial position of the plume. For a given DROP4 output and plume geometry, values of  $N$ ,  $K$ ,  $\alpha$ ,  $\beta$  are stored in a matrix as a function of radial

and axial position in the plume. Equation (14) is then integrated numerically to determine the attenuation of the light signal. A computer code, acronym OSA, computes this for any geometry of the beam relative to the plume, for a beam whose diameter is small compared with the diameter of the plume.

As defined by Eq. (14), the equation will be incorrect when the particles are spaced closer than a few droplet diameters. They then interact electromagnetically and the value of  $K$  is modified. For the case of a plume geometry given by the following equation<sup>35</sup> for the plume radius as a function of axial distance

$$R = 0.2 + \sqrt{0.5X}$$

with a water droplet size distribution of

$$N_r = A \exp(-8.944\sqrt{r}) / (1+r^2+x^2)$$

an incident unpolarized light beam of 1 cm in diameter, and  $\lambda = 0.5 \mu\text{m}$ , Hoshizaki et al.<sup>36</sup> found that the effect of multiple scattering becomes important for an optical depth  $\tau \geq 0.4$ . For the Beer-Lambert-Bouguer equation, this is equivalent to an  $I/I_0 \leq 0.67$ .

Plume Visibility. This portion is drawn from Hoshizaki et al.<sup>36,37</sup> who developed a model for predicting the probability of visual detection of a smoky rocket plume. The 50%

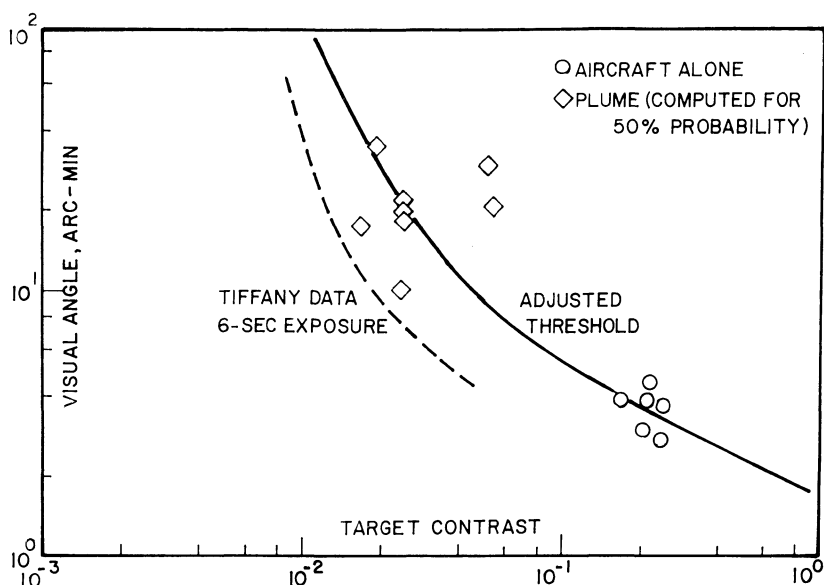


Fig. 5 50% probability of detection visual threshold.

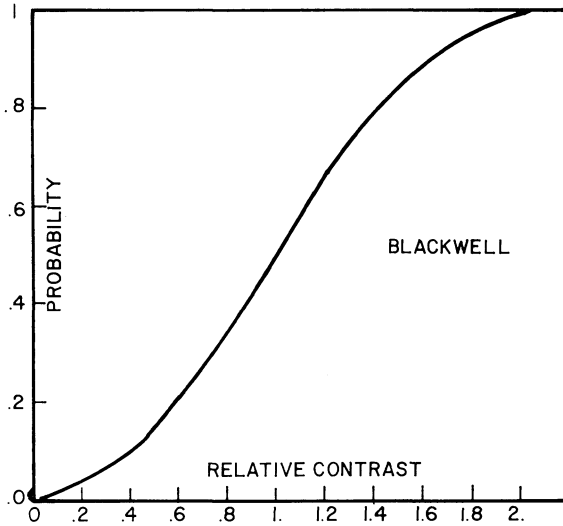


Fig. 6 Probability of detection as a function of relative contrast.

probability of detection is based on field data from the U.S. Air Force Compass Ghost Program<sup>38</sup> of observations of jet aircraft and jet plumes for both sunlit and shaded conditions. The data obtained for nonsmoking aircraft, and plume visibility points computed by a model developed by Hoshizaki et al.,<sup>39</sup> are shown in Fig. 5 where visual angle is plotted as a function of target contrast. The probability of detection for any other target contrast relative to the 50% probability point is determined from Blackwell<sup>40</sup> who gives an average probability of visual detection as a function of relative contrast of various target shapes, sizes, and backgrounds. His data are shown in Fig. 6.

Plume contrast is related to the plume and background radiance by

$$\text{plume contrast} = (\int (R_p - R_B) V_\lambda d\lambda) / \int R_B V_\lambda d\lambda \quad (15)$$

In this study,  $R_p$  and  $R_B$  are calculated with respect to a given observation point. From this, the field of view that encompasses the plume is determined. Selected points on the plume surface that are within the field of view are chosen. The direction of the light ray is calculated at each point and the intensity at the observation point is computed from radiation-transfer equations. The plume radiance is then obtained by integrating the selected points over the plume surface. In the background calculation, the volume occupied by the plume is replaced by the background medium, e.g., clear sky, haze,



etc. The field of view and the selected points on the plume surface are identical to those used in the plume radiance computation. Schematics of the relation of the plume to the sun and background scattering is shown in Figs. 7 and 8.

Using the approximate method of Chou,<sup>41</sup> the general radiation-transfer equation is solved based on Hartel's work.<sup>42</sup> Hartel proposed that the scattering intensity at a given point in the medium may be written as the summation of various scattering levels,  $k$ , each having a known phase function,  $f_k$  (as determined from the phase function of single scattering), and a quantity function (or energy density)  $Q_k$ . First-order intensities are the intensities that have been scattered once; the second-order intensities are all the intensities that have been scattered twice, etc.

The general radiation equation is expressed by

$$\delta I / \delta s + \sigma_{\text{ext}} I = \sigma_{\text{sc}} (Q_0 f_i(\cos \psi_0) + \int_0^{2\pi} d\phi' \int_0^\pi I f_l(\cos \psi) \sin \theta' d\theta') \quad (16)$$

See Fig. 8 for the coordinate system.

The total intensity is expressed as:

$$I = \sum_k Q_k f_k(\cos \psi_0) = \sum_k I_k \quad (17)$$

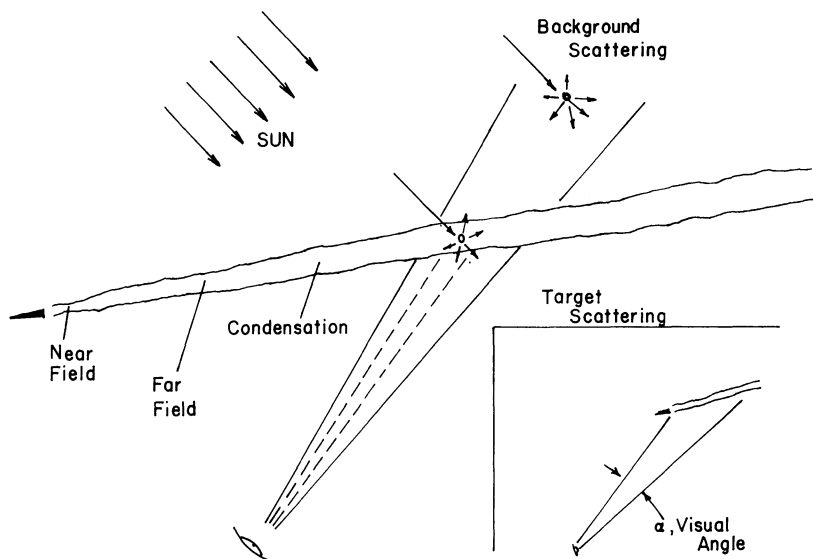


Fig. 7 Formation of secondary smoke and rocket plume visibility.

where  $\psi_o$  is the scattering angle relative to the direction of a ray.

$$f_k \cos \psi_o = (1/4\pi) \sum_{n=0}^N (2N+1) (\Lambda_n / (\Lambda_o (2n+1)))^k \quad (18)$$

$$\times p_n \cos \psi_o$$

$$Q_o = \exp(-\int_{L_o}^o \sigma_{\text{ext}} dL) \quad (19)$$

and

$$f_1 \cos \psi_o = (1/4\pi) \sum_{n=0}^N (\Lambda_n / \Lambda_o) P_n \cos \psi_o \quad (19a)$$

$P_n \cos \psi_o$  are the Legendre polynomials of order  $n$  and  $\Lambda_n$  are coefficients derived from Mie theory by Dave.<sup>43</sup>  $f_1 \cos \psi_o$  is normalized such that integration over all solid angles around the incident direction yields the value of unity. The quantity function is given as

$$Q_{k-1} = \int d\phi \int I_{k-1}(\theta, \phi) \sin \theta d\theta \quad (20)$$

$\theta$  and  $\phi$  are the polar and azimuthal angles of the light ray.

The droplet size distribution and number density are determined from the model described above. For a given droplet size, light wavelength, and index of refraction, using the

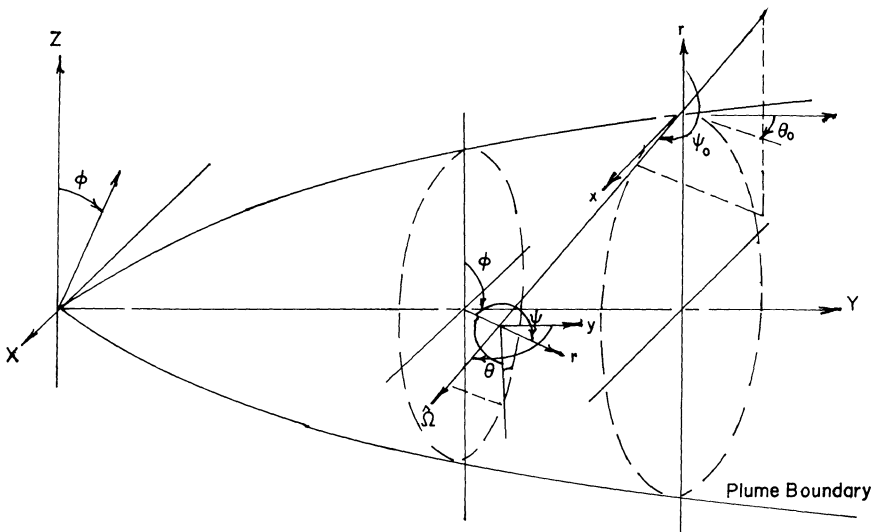


Fig. 8 Coordinate system and geometry.

method of Dave,<sup>43</sup> the extinction coefficient, the scattering coefficient, and the Legendre coefficients needed to calculate the phase function  $f_k$  are computed. At any point in the plume, the total values are found by

$$\sigma_{\text{ext}} = \int \sigma_{\text{ext}}(r) f(r) dr \quad (21)$$

$$\sigma_{\text{sc}} = \int \sigma_{\text{sc}}(r) f(r) dr \quad (21a)$$

$$\bar{\Lambda}_n = \int \Lambda_n(r) f(r) dr / \int f(r) dr \quad (21b)$$

These, together with the plume size, completely define the plume medium.

### Experiments in Secondary Smoke Formation

Secondary smoke produced by various solid propellants has been characterized under controlled ambient conditions using subscale motors in the U.S. Army Missile Command's and U.S. Air Force Arnold Engineering Development Center's test facilities. Additional data have been obtained from high-altitude and sea level flight tests at Eglin Air Force Base, and from static motor tests at the U.S. Army Missile Command. Measurements of condensation nuclei in the plumes from several propellants were also made at the U. S. Army Missile Command.

### Facilities

U.S. Army Missile Command Smoke Characterization Facility (SCF). The SCF is a 19.6 cm<sup>3</sup> insulated environmental chamber in which small-scale rocket motors containing 65-75 g of propellant are statically tested. The chamber temperatures are controllable in the range of -40°F to 140°F with relative humidities of 20-100%. The chamber has multiple access ports for instrumentation. The motors utilize a smokeless igniter and are fired inside the conditioned chamber. A schematic diagram of the SCF is shown in Fig. 9. The exhaust gases from the rocket are mixed with fans, and transmission and droplet counting measurements are made after several minutes to characterize the smoke.

The SCF equipment used for smoke analysis consists of Anderson cascade impactor, a Climet particle analyzer, and several transmissometers operating at discrete wavelengths in the visible and near infrared. Details of the SCF and instrumentation are available in Refs. 8 and 9.

U.S.A.F. Arnold Engineering Center Ballistic Range. This range, Fig. 10, consists of a 10 ft diam, 1000 ft long tank through which a small-scale rocket (9-1/2 in long by 1-1/4 in diam) is flown. The rocket is gun launched and ignited in flight. The test range can be evacuated and the pressure controlled to simulate high altitude flight. For condensation studies, a climatic chamber for temperature and humidity control is installed about 100 ft from the range entrance. Doors on the chamber are dropped just before model launch. Tests for condensation can only be made at atmospheric pressure. The range is instrumented with visible and x-ray shadowgraphs,

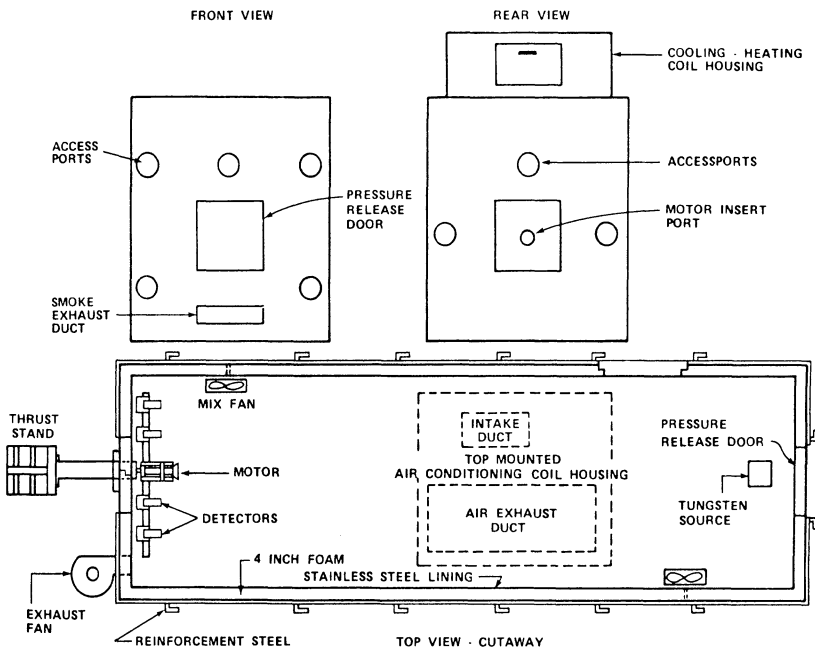


Fig. 9 Schematic of U. S. Army Missile Command Signature Characterization Facility (SCF).

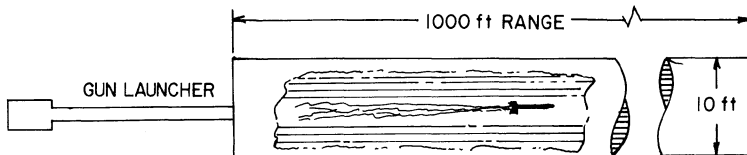


Fig. 10 U. S. Air Force Arnold Engineering Development Center Ballistic Range.

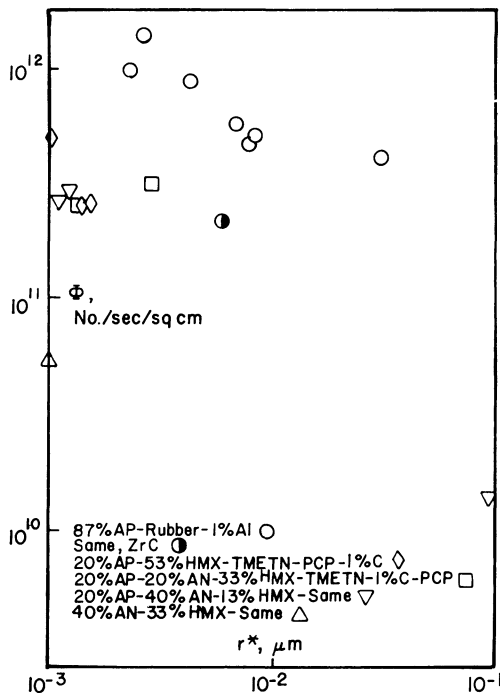


Fig. 11 Experimental cumulative number of condensation nuclei exiting rocket nozzle as a function of nucleus radius.

Schlieren, high-speed photograph, laser scattering, temperature rakes, radiometers, and particle collection devices.

### SCF Results and Comparison with Models

Condensation Nuclei. If a multitude of nuclei ranging in size and number is produced in the rocket, as the supersaturation in the SCF chamber is increased by increasing the humidity or decreasing the temperature, it may be seen from Eq. (4) that ever smaller nuclei will be activated to grow by condensation. The greater the number of nuclei activated to grow, the greater the density of the smoke. If it is assumed that each droplet counted has grown from a single nucleus, the number of droplets counted is identical to the number of activated nuclei present. Thus the total number of droplets in the chamber for a given supersaturation ratio is the number of nuclei larger in radius than  $r^*$  calculated from Eq.(4).

If it is assumed that the droplets are spherical, and that after 5 min the droplets are all or close to the same size, the attenuation of a light beam passing through the smoke can be described by the Beer-Bouguer-Lambert equation given before - using an average droplet radius. From light

transmission measurements made at 0.52, 0.63, 0.85, 0.95, and 1.06  $\mu\text{m}$ , knowing  $L$ , the theoretical values of the Mie coefficient, the equilibrium temperature in the SCF, and the partial pressures of the condensible gases, values of  $N$ , average radius, and the chemical composition of the droplet are derived.

The results of the measurements are shown in Fig. 11 as a cumulative distribution plot of  $N$  vs  $r^*$  for two classes of propellant - an 87 wt.% ammonium perchlorate - rubber binder propellant with 1% aluminum or ZrC additive, and TMETN - PCP propellant with varying amounts of HMX, ammonium nitrate, and ammonium perchlorate plus 1 wt.% carbon. The smoke droplets for the non-AP propellant were frozen at the test conditions, and the point plotted represents the total number of nuclei assuming that all nuclei are activated under freezing conditions. Only the calculated results based on an assumption of complete afterburning of hydrogen to water are presented. The correlation for nonafterburning resembles the one for afterburning displaced to larger  $r^*$  values. The degree of displacement depends on the oxidation ratio of the propellant. Several general observations may be made:

- 1) The number of nuclei increases as the nucleus radius decreases, as expected from the discussion above.
- 2) The higher the concentration of AP in the propellant, the larger the number of condensation nuclei.
- 3) No effect of binder, HMX, nor ammonium nitrate on the number of nuclei can be discerned.
- 4) Assuming that the microrocket used in these tests delivers a specific impulse of 200 lbf-s/lbm, or an exhaust velocity of 6440 ft/s, the total number of nuclei emitted from a high-AP propellant is approximately  $1.3 + 11/\text{ft}^3$  of gas or  $4 + 06/\text{cm}^3$  of gas. The number of nuclei per unit volume measured is 3 to 6 orders of magnitude smaller than observed for homogeneous nucleation of water or water-alcohol in a nozzle or for soot formed in rich methane-oxygen flames. The non-AP or low-AP propellants produce significantly lower nuclei concentrations. The nuclei sizes calculated from the data are in the same range as for the other nuclei data reported in the literature. The data do not permit the computation of a size distribution. Counts of the number of droplets made with the Climet agree with the light attenuation counts within a factor of 1.5 to 2.5.

Additional tests were made in the SCF at air temperature and relative humidity conditions which avoided formation of secondary smoke, and the condensation nuclei counted directly with an electrical aerosol analyzer (EAA). The EAA scans through 11 size channels from 0.0032  $\mu\text{m}$  to 1  $\mu\text{m}$  diam. The

instrument measurements are less accurate at either extreme, but it permits the measurement of particles to at least 1 order of magnitude smaller than the Climet which is limited to about  $0.3 \mu\text{m}$  diam. EAA counts were all made after the 5 min mix period in the SCF from samples diluted by 100:1 with dry nitrogen to avoid coagulation during counting - about 1 min. The EAA measurements for the high-AP propellant yielded a count of  $6 + 06/\text{cm}^3$  for particles larger than  $50 \text{ \AA}$  with some indication that the count could be as high as  $5 + 07/\text{cm}^3$  for nuclei radii larger than  $30 \text{ \AA}$ . A similar experiment with a double-base propellant containing 2 wt.% lead salts and carbon produced a count of  $2.5 + 06/\text{cm}^3$ . The nuclei size distribution, as obtained from the EAA data, was found to be Gaussian with  $\alpha = 0.5865 + 03$ ,  $\beta = 2.4625$ ,  $\sigma = 0.3000 - 01$ , and  $\bar{r}$  is  $0.0610 \mu\text{m}$ . Background count of the nuclei in the SCF prior to the motor firings was of the order of  $10^3/\text{cm}^3$ . Both the optical and EAA counts are faulted by the sample time of 5 min and by the action of the mixing fans.

From the Einstein equation for diffusion, Smolochowski<sup>44</sup> predicted for the agglomeration of a unimodal distribution of particles in Brownian motion, assuming that each collision leads to agglomeration

$$1/N - 1/N_0 \approx (4/3)(kT/\mu)t = K_0 t \quad (22)$$

For air at room temperature,  $K_0 = 1.8 - 08 \text{ cm}^3/\text{min}$ . From Eq. (22) an estimate can be made of the nuclei concentration at time zero. For the optical counts on the AP propellant,  $N_0$  is  $3.1 + 05$  and for the EAA,  $N_0$  is  $1.3 + 07$  (based on  $N = 6 + 06$ ).  $N_0$  by either method should be precise within a factor of 2.

If from Cadle,<sup>45</sup> based on experimental data for a carbon aerosol,  $K_0 = 1.41 - 07 \text{ cm}^3/\text{min}$  is used,  $N_0$  for the optical measurement is  $3.8 + 05$ .  $N_0$  for the EAA measurement would be indeterminate but much higher and possibly closer to the  $10^9$  to  $10^{12}/\text{cm}^3$  found by other investigators. The optical data from SCF tests are more extensive than the EAA data and believed to be more reliable.

Since the counts made with the EAA were made under conditions prohibiting the formation of secondary smoke, it may be concluded that the smoke for AP and double-base propellants initiates on heterogeneous nuclei. No satisfactory data presently exist for the chemical composition of these nuclei but they probably comprise soot, alumina, calcium, potassium, lead, or tin salts produced in the rocket chamber.

No explanation can be given at this time for the difference in nuclei counts from the optical and EAA measurements.

However, as will be shown later, secondary smoke predicted by the derived dynamic model is consistent with a concentration of  $10^5$  to  $10^6/\text{cm}^3$ . Since the rate of droplet growth on the heterogeneous nuclei is very rapid, of the order of milliseconds to droplet radii larger than  $0.2\text{ }\mu\text{m}$ , the local supersaturation ratio should be depressed sufficiently to prevent homogeneous nucleation from being a significant factor in smoke formation in the plume. Smoke formation in the relatively stagnant but well-mixed postfire cloud, however, would be expected to be affected by both heterogeneous and homogeneous nucleation.

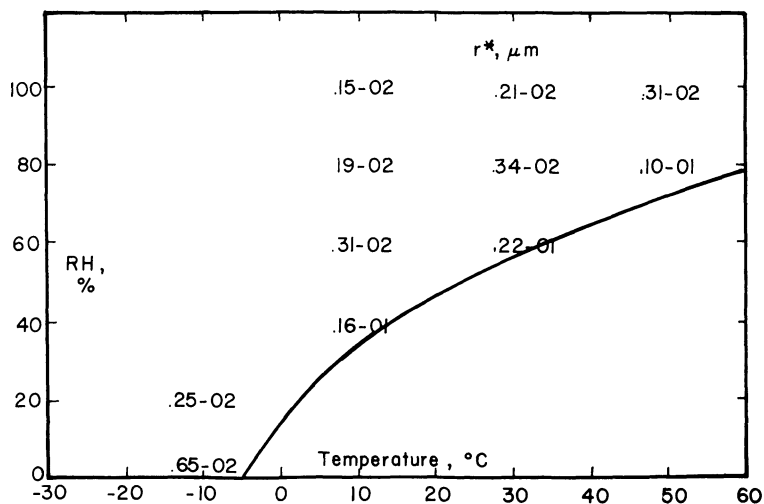


Fig. 12 Isothermal fog computation for AP/rubber binder propellant.

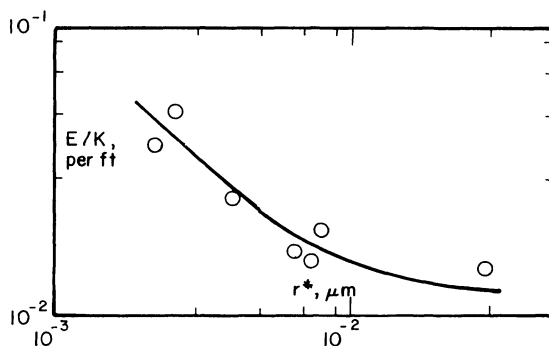


Fig. 13  $E/K$  as a function of the critical nucleus radius.



**List of Contributors to Volume 90**

Bizot, A. . . . .	361
Boggs, T. L. . . . .	121
De Luca, L. . . . .	661
Duterque, J. . . . .	361
Fifer, R. A. . . . .	177
Gayathri, V. . . . .	53
Gore, J. P. . . . .	599
Hermance, C. E. . . . .	239
Kishore, K. . . . .	53
Kubota, N. . . . .	1
Kumar, M. . . . .	305
Kuo, K. K. . . . .	305, 515, 599
Lengellé, G. . . . .	361
Miller, E. . . . .	841
Price, E. W. . . . .	479, 733
Ramohalli, K.N. R. . . . .	409
Razdan, M. K. . . . .	515
Summerfield, M. . . . .	599
T'ien, J. S. . . . .	791
Trubert, J. F. . . . .	361